AEDC-TR-79-2

EXPERIMENTAL STUDY OF THE PLUME CHARACTERISTICS OF AN AGED MONOPROPELLANT HYDRAZINE THRUSTER

W. D. Williams, T. D. McCay,
H. M. Powell, D. P. Weaver, et al.
ARO, Inc., a Sverdrup Corporation Company

VON KÁRMÁN GAS DYNAMICS FACILITY
ARNOLD ENGINEERING DEVELOPMENT CENTER
AIR FORCE SYSTEMS COMMAND
ARNOLD AIR FORCE STATION, TENNESSEE 37389

April 1979

Final Report for Period 13 August 1976 — 5 April 1977

Prepared for

AIR FORCE ROCKET PROPULSION LABORATORY/PACP
EDWARDS AIR FORCE BASE, CALIFORNIA 93523

NOTICES

When U. S. Government drawings, specifications, or other data are used for any purpose other than a definitely related Government procurement operation, the Government thereby incurs no responsibility nor any obligation whatsoever, and the fact that the Government may have formulated, furnished, or in any way supplied the said drawings, specifications, or other data, is not to be regarded by implication or otherwise, or in any manner licensing the holder or any other person or corporation, or conveying any rights or permission to manufacture, use, or sell any patented invention that may in any way be related thereto.

Qualified users may obtain copies of this report from the Defense Documentation Center.

References to named commerical products in this report are not to be considered in any sense as an indorsement of the product by the United States Air Force or the Government.

This report has been reviewed by the Information Office (OI) and is releasable to the National Technical Information Service (NTIS). At NTIS, it will be available to the general public, including foreign nations.

APPROVAL STATEMENT

This report has been reviewed and approved.

STANISLAUS L. LUDWIG, Captain (CF)
Project Manager, Research Division
Directorate of Test Engineering

Approved for publication:

FOR THE COMMANDER

ROBERT W. CROSSLEY, Lt Colonel, USAF
Acting Director of Test Engineering
Deputy for Operations

UNCLASSIFIED

REPORT DOCUMENTATION PAGE		READ INSTRUCTIONS BEFORE COMPLETING FORM
1 REPORT NUMBER AEDC-TR-79-2	2 GOVT ACCESSION NO.	3 RECIPIENT'S CATALOG NUMBER
4 TITLE (and Subtitle) EXPERIMENTAL STUDY OF THE PLUME CHARACTERISTICS OF AN AGED MONOPROPELLANT HYDRAZINE THRUSTER		5 TYPE OF REPORT & PERIOD COVERED Final Report, 13 August 1976 - 5 April 1977
		6 PERFORMING ORG REPORT NUMBER
7 AUTHOR(s) W. D. Williams, T. D. McCay, H. M. Powell, D. P. Weaver, et al., ARO, Inc., a Sverdrup Corporation Company		8 CONTRACT OR GRANT NUMBER(s)
9 PERFORMING ORGANIZATION NAME AND ADDRESS Arnold Engineering Development Center Air Force Systems Command Arnold Air Force Station, Tennessee 37389		10. PROGRAM ELEMENT, PROJECT, TASK AREA & WORK UNIT NUMBERS Program Element 62302F
11. CONTROLLING OFFICE NAME AND ADDRESS Air Force Rocket Propulsion Laboratory/PACP, Edwards Air Force Base, California 93523		12. REPORT DATE April 1979
		13. NUMBER OF PAGES 245
14 MONITORING AGENCY NAME & ADDRESS(if different from Controlling Office)		15. SECURITY CLASS. (of this report) UNCLASSIFIED
		15a. DECLASSIFICATION DOWNGRADING SCHEDULE N/A

16 DISTRIBUTION STATEMENT (of this Report)

Approved for public release; distribution unlimited.

17 DISTRIBUTION STATEMENT (of the abstract entered in Block 20, if different from Report)

18 SUPPLEMENTARY NOTES

Available in DDC

19 KEY WORDS (Continue on reverse side if necessary and identify by block number)

hydrazine
monopropellants
operation
exhaust plumes

20 ABSTRACT (Continue on reverse side if necessary and identify by block number)

An experimental study of the exhaust plume of an aged (200,000 pulses), 0.44 N (0.1 lbf), hydrazine monopropellant thruster was performed with the goal of characterizing both the gas dynamic and contamination properties of the vacuum plume expansion. The thruster was operated in a high vacuum chamber over a thrust range from 0.44 to 1.10 N (0.1 to 0.25 lbf) with a nominal 0.14-sec-on/ 9.86-sec-off duty cycle using initial catalyst bed (Shell 405)

DD FORM 1473 1 JAN 73   EDITION OF 1 NOV 65 IS OBSOLETE

UNCLASSIFIED

20. ABSTRACT (Continued)

temperatures of 367 K (200°F), 478 K (400°F), and 589 K (600°F).
Exhaust plume diagnostic systems employed included a mass
spectrometer probe, a quartz crystal microbalance (QCM), a laser-
Raman/Rayleigh scattering system, an electron beam fluorescence
system, and a particle collection network. These systems de-
termined plume species number densities and temperature, mass
deposition rates, and the level of particulates in the plume;
they also permitted visualization of the plume. Traditional
engine performance parameters were also determined in order to
relate performance and exhaust plume properties.

AFSC
Arnold AFS Tenn

PREFACE

The work reported herein was conducted by the Arnold Engineering Development Center (AEDC), Air Force Systems Command (AFSC) for the Air Force Rocket Propulsion Laboratory (AFRPL/PACP), AFSC. The results of the research were obtained by ARO, Inc., AEDC Division (a Sverdrup Corporation Company), operating contractor for the AEDC, AFSC, Arnold Air Force Station, Tennessee, under ARO Project Numbers V34S-B3A, V34S-R9A, and V321-P4A. Project monitors for AFRPL were Capt. John Williams and Lt. Eric Lund; Maj. K. B. Harwood (CF) and Capt. Stanislaus L. Ludwig (CF) were the Air Force project managers at AEDC. The data analysis was completed on January 23, 1978, and the manuscript was submitted for publication on November 11, 1978.

In addition to those listed on the cover, L. L. Price, J. H. Jones, and J. W. L. Lewis are coauthors of this report.

CONTENTS

ILLUSTRATIONS

7

TABLES

APPENDIXES

1.0 INTRODUCTION

The use of monopropellant thrusters for attitude control and station keeping functions has stimulated interest for several years in the characteristics of the thrusters' plume exhausts. The reasons are as follows:

(a) Particulates (catalyst fines, fuel droplets, or condensate clusters) in the plume can increase background noise or provide false target information for satellite-borne sensors.

(b) Deposition of particulates and/or gaseous exhaust plume species on sensitive surfaces such as solar panels, thermal control coatings, and optical surfaces can degrade satellite performance.

Experimental studies with regard to "a" above were begun in FY73 under Program CONSCAT and have continued to the present under Program CONSET. Both programs have been sponsored by the Air Force Rocket Propulsion Laboratory (AFRPL). The objectives of the AEDC experiments under these programs were to study condensation in pure gas and gas mixture expansions from sonic orifices and nozzles utilizing noninterfering diagnostic techniques to develop scaling laws for condensation onset and growth. Results of these experiments can be found in Refs. 1 through 9. In the final part of CONSET the same noninterfering diagnostic techniques were to be applied to study condensation in the flow field of an actual monopropellant thruster.

With regard to "b" above, during the same time that the AEDC Program CONSET experiments were conducted, AFRPL-sponsored studies were being made at the Jet Propulsion Laboratory (JPL) on the contamination properties of monopropellant exhaust plumes. These studies are adequately summarized in Refs. 10 through 13. The primary diagnostic used at JPL was the quartz crystal microbalance (QCM) for determining mass deposition rates. The purpose of the measurements was to provide experimental verification of the CONTAM computer code (Ref. 14) developed by McDonnell Douglas Astronautics Corporation (MDAC), also under sponsorship of the AFRPL. It should be noted that a subprogram (KINCON) of CONTAM attempted to predict the condensation properties in thruster plumes.

As the time approached for the thruster experiments at AEDC, it seemed highly cost effective to include contamination measurements as a part of the condensation studies program. A most ambitious, multiple diagnostic program was planned. A QCM device was to be used for forward-flow mass deposition measurements, and a mass spectrometer axial centerline probe (Ref. 15) was to be used for species mole fraction measurements in the far field of the exhaust plume. An electron beam fluorescence system (Ref. 16) was to be

11

used for species density and temperature measurements in the far field as well as to provide luminescence for flow-field visualization using an image intensifier/camera system. Near-field species densities and temperatures were to be measured using a laser-Raman scattering system (Refs. 6 and 17). Laser-Rayleigh/Mie scattering (Refs. 1 through 9) was to provide information on particulate levels in the plume, and a special particle collection apparatus was also to be used to determine the nature of the particulates in the plume. The usual engine parameters, inlet pressure, combustion chamber pressure, catalyst bed wall temperature, and fuel mass flow rate, as well as test cell pressure, were also to be monitored.

This report presents a detailed description of the experimental techniques employed in this investigation of a monopropellant thruster exhaust plume. Exemplary data are presented, and comparisons are made with CONTAM predictions (Ref. 10) as well as other predictions (Ref. 18) and measurements (Ref. 13). (A complete set of the experimental data is available from AFRPL in the form of a 260-page data package.) In addition, a description of a catastrophic increase in plume contaminants which occurred during the thruster study is presented along with a documentation of thruster performance changes after this occurrence. Table 1 presents a matrix of the test conditions and data obtained during these experiments. A total of 18 test periods of two days' duration each was necessary to complete the experimental study.

2.0 DESCRIPTION OF RESEARCH CELL

The thruster was contained within the 4- x 10-ft Research Vacuum Chamber (RVC), a stainless steel vacuum chamber nominally 4 ft (1.3 m) in diameter and 10 ft (3.3 m) long. The chamber is constructed in two sections: a movable section approximately 4 ft (1.3 m) long and a stationary section, approximately 6 ft (2 m) long. For this test an additional spool piece 1.5 ft (0.49 m) long was used to provide eight instrumentation ports. Another movable section approximately 3 ft (0.99 m) long was also added, and it was in this section that the thruster was mounted. Figure 1 is a schematic of the engine installation in the RVC.

Initial pumping capabilities were supplied by a 300-cfm mechanical pump for rough pumping and a 6-in.-diam oil diffusion pump with a baffle refrigerated by liquid nitrogen (LN_2) for intermediate pumping. Pumping during testing was provided by a gaseous helium (GHe)-finned cryoliner at 20 K with a liquid nitrogen (LN_2) cryoliner radiation shield and a 37-liter capacity liquid helium (LHe)-filled cryopump (Ref. 15) with LN_2-cooled radiation shields. This configuration is depicted in Fig. 1. The gaseous helium was supplied by a closed loop, 4-KW refrigeration system, and the liquid helium was supplied from a 500-liter portable dewar near the end of the vacuum chamber.

The engine was mounted on a traversing table with three linear degrees of freedom which allowed all flow-field instrumentation to be stationary. Distances of travel were approximately 25 cm parallel to the test chamber axial centerline, 13 cm vertically, and 38 cm transverse to the axial centerline. The vertical motion was used only for alignment purposes. The precision of the movements was 0.013 cm. Test chamber instrumentation is discussed in Appendix A.

The RVC operating procedures for each test period were begun after completion of instrumentation and engine alignments and prechecks. Generally, the RVC was maintained at an approximate pressure of one atmosphere of bone-dry nitrogen during the nonuse and precheck periods. Upon completion of prechecks the 300-cfm Stokes mechanical pump was employed to evacuate the chamber to a pressure of approximately 30 millitorr. During the roughing period the chamber diffusion pump was heated, and the liquid helium pump was purged with dry gaseous helium. The heated diffusion pump was then valved into the chamber, and the Stokes pump was valved out. When the chamber pressure reached the 10^{-5} torr scale, the system was considered sufficiently leak-tight for testing, and the LN_2 heat shield cryoliners were filled. Approximately 8 hr before testing the GHe cryosystem was valved in to bring the chamber to test conditions. The blank-off chamber pressure achieved was $\approx 1 \times 10^{-7}$ torr.

Prior to the initiation of testing and after all other systems had been rechecked, the liquid helium pump was filled and the diffusion pump was isolated from the chamber. After a sequence of thruster pulses had been completed, the diffusion pump was employed to aid the LHe pump in removing hydrogen from the cell. Even for the highest engine thrust condition studied the chamber background pressure remained less than 7.0 $\times 10^{-4}$ torr (9.3 x 10^{-2} Pa), which corresponds to a simulated altitude of approximately 94 km.

Chamber operation during testing was routine except for the occasional overloading of the LHe pump with H_2. When the LHe pump becomes overloaded, additional hydrogen injected by the thruster reduces the chamber vacuum; this results in more heat conduction losses, which cause more warming of the pump, which in turn results in more hydrogen desorption from the pump. This process takes place very rapidly and is referred to as the "avalanche" effect. When avalanche occurred, the mechanical and diffusion pumps had to be used for restoring test conditions. The large H_2 partial pressures which occurred during the avalanche necessitated the installation of N_2 bleeds into the exhaust lines to decrease the safety hazard.

Upon completion of a testing period the RVC was brought to atmospheric conditions by first forcing the remaining LHe from the pump by pressurizing the pump

with warm GHe. The GHe cryogen flow was then terminated, and the LN_2 supply was valved off. Two internal, 1-KW heat lamps were turned on to hasten the removal of the cryoload. The diffusion and mechanical pumps were used to remove the cryoloads as they sublimated. Once the cryodeposits were removed, the chamber was alternately backfilled to one atmosphere with bone-dry N_2 and then evacuated several times (usually three). Finally, a 1-atm pressure of bone-dry N_2 was established in the chamber, and the system was isolated.

3.0 DESCRIPTION OF ROCKET ENGINE AND FUEL SYSTEM

3.1 THRUSTER

The thruster used in this experimental program was a Hamilton-Standard REA/CTS 10-18 monopropellant hydrazine thruster which employs a 30 to 35 mesh Shell 405 ABSG spontaneous catalyst with a preloaded packed bed design. The injector was a short core penetrant composed of 85-mesh inner screen and 325-mesh outer screen. The propellant valve was a normally closed, coaxial solenoid, poppet type with TFE Telfon® for the seat. The valve was mounted perpendicular to the thrust chamber axis, and a pressure tap was located just downstream of the catalyst bed. The thruster was originally designed to provide 1.24 N (0.28 lbf) thrust at a steady-state chamber pressure of 1.55×10^6 Pa (225 psia). The exhaust was provided by a conical nozzle with a 0.030-in. (0.76-mm) throat diameter and an exit area ratio of 55. A complete description of the engine properties, as stated by the manufacturer, is included in Table 2, and a schematic of the engine is shown in Fig. 2. The engine was operated without the heat shield shown in Fig. 2. As originally designed, the thruster was expected to supply up to 500,000 pulses at thrust levels less than 0.28 lbf. Since the thruster was tested at JPL prior to delivery to AEDC, the exact pulse history was unknown. It is believed, however, that the engine had been pulsed at least 150,000 to 200,000 times.

The thruster was originally equipped with an internal catalyst bed heater, which was inoperative when delivered from the Jet Propulsion Laboratory. The JPL had replaced this heater with an external heater by wrapping with insulated heater (nichrome) wire the section of the engine body which contained the bed. During the course of experiments it was necessary to replace the heater twice. The chamber temperature sensor which the manufacturer supplied with the engine was also inoperative upon receipt.

High pressure, flexible 304 stainless steel tubing was used to connect the engine to the propellant system. The inlet pressure transducer was located on the engine traversing mechanism to minimize the distance to the valve inlet. Propellant lines internal to the RVC were wrapped with heater tape to maintain the fuel temperature in the range from 283 to 300 K (510 to 540°R). A schematic of the engine system installation is shown in

Fig. 3. For temperature control, thermocouples were attached at two positions along the fuel line underneath the heater tape, and a Honeywell controller was used to maintain a selected temperature within ±6 K.

3.2 FUEL SYSTEM

The hydrazine propellant system used in these experiments was a nitrogen gas-pressure-regulated system with a maximum operating pressure rating of 5.2 MPa (750 psig). The system material was entirely stainless steel except for aluminum flame savers used to improve fitting seals. A schematic of the system is shown in Fig. 4. Fuel flow rate measurements utilized a Viscojet® which could be valved in as desired. The propellant system was operated in both the regulated and blowdown modes. Since the propellant tank volume was fairly large (about 3.8 liters or 1 gallon) and flow rates were small (0.45 gm/sec or 0.001 lbm/sec), no discernible pressure loss was experienced during use of the blowdown mode. Because of its better stability, the blowdown mode was used on all runs where total pulses were less than 70.

The propellant system was pressurized for an engine firing by raising the propellant tank pressure to approximately 2 atm with Matheson prepurified-grade gaseous nitrogen which was filtered to 2 μ. A high point bleed valve was opened momentarily to remove trapped gas from the system, and then the valve inlet pressure was increased to the required value through the pressure regulator. In the regulated mode the pressure regulator was left open and set, whereas in the blowdown mode it was closed for the duration of the pulse sequence. Since nitrogen is soluble in hydrazine (see Fig. 5 and Ref. 19) and the system was cycled between low and high pressures, dissolved nitrogen was prone to being trapped in the system. To avoid this situation, a tank depressurization was performed approximately every half hour through an air-operated vent valve which directed the pressurant to a roof relief. The hydrazine was permitted to vent its trapped gas to atmospheric nitrogen for 5 to 10 min during these vent periods.

The fuel employed throughout the testing of the thruster was standard monopropellant grade hydrazine, MIL-P-26536C. All fuel came from one drum obtained from the Rocky Mountain Arsenal. Water concentration in the fuel was measured periodically to ensure that excessive moisture was not absorbed. The Olin Corporation performed a detailed analysis on two drums from the same fuel batch from which the fuel in this investigation was drawn; the results of that analysis and the required military specifications are given in Table 3.

3.3 FUEL SYSTEM/ENGINE INSTALLATION PROCEDURE

Prior to operation the fuel system was broken down into components, cleaned, and reassembled in its operating configuration except for the engine, which was replaced with a flexible line. The system was then flushed in place with freon, water, isopropyl alcohol, and again with water through a recirculating system until particulate requirements (see Table 4) were met with each fluid. The engine was then installed in place of the flexible line and flushed and dried.

Alignment of the engine with the chamber centerline was critical. This was accomplished by covering the nozzle exit with a paper cover and locating and marking the center of the exit plane. The engine was then installed on the previously orthogonally-aligned traversing mechanism. Pairs of crosshairs located on both ends of the vacuum chamber were used to set up an optical telescope aligned with the chamber centerline. The telescope was employed to establish that the engine nozzle center was on the chamber centerline. The axial traverse mechanism was aligned with the chamber by traversing along the chamber axis and making adjustments necessary to keep the nozzle exit aligned. The telescope was replaced with a 0.5-mW He-Ne laser, and the marked exit cover was replaced with a flat mirror sealed against the nozzle exit. The engine adjusting screws were employed to bring the reflected laser beam back onto the incident laser beam outside the chamber. The mirror was removed, and the laser beam was observed to pass through the center of the nozzle exit into the throat of the engine.

3.4 THRUSTER OPERATION

Normally the thruster was operated in a pulse mode with a nominal 0.14 sec on/9.86 sec off duty cycle and a nominal 25 to 30 pulse sequence. The prepulse catalyst bed temperature was systematically varied over the range from 367 to 589 K (200 to 600°F), and the thruster chamber pressure was systematically varied from 5.86×10^5 to 14.1×10^5 Pa (85 to 205 psia). Table 1 should be consulted for the matrix of thruster test conditions and their nomenclature.

Exceptions to pulse mode operation occurred for two reasons. Whenever mass flow rate measurements were made, the engine was operated in a 60-sec continuous burn. Also, on a few occasions short range spectral scans were made of the electron beam-induced fluorescence in the plume, and whenever these scans were made the engine was operated in a 60-sec continuous burn.

4.0 LASER SCATTERING AND ELECTRON BEAM DIAGNOSTICS

4.1 LASER SYSTEM

The experimental arrangement for all special diagnostic instrumentation is shown in Fig. 6. The engine plume flow is into the plane of the figure. It can be seen that all eight equally-spaced viewports on the instrumentation spoolpiece were utilized, and the laser system is shown mounted at 45 deg from the top. The laser was a Holobeam 600 series, pulsed ruby laser which was utilized to provide excitation for Raman and Rayleigh/Mie scattering. The 6- by 3/8-in. ruby rod was oriented to provide a horizontally polarized beam, and the laser was operated in the conventional mode, providing a nominal pulse width of 1 msec and an energy of 35 J per pulse at 6,943 Å. After expansion in the ratio 4:1, the laser beam was focused by a 1,000-mm focal length, hard-coated, fused silica lens onto the thruster axial centerline. The port through which the beam passed into the chamber was also made of fused silica. As shown in Fig. 6, the beam was trapped by a laser dump to prevent reflections from entering the viewing area.

At the rear of the laser an energy monitor system was installed to provide a means of correcting the scattered light intensity for variations in laser energy. These variations were typically ±3 percent. The monitor consisted of a photodiode, a 35-Å bandpass filter centered at 6,943 Å, and HN-22 Polaroid sheets. Before each test period the energy monitor was calibrated by placing a Quantronix energy receiver/meter unit directly at the laser output to measure laser energy as a function of laser power supply voltage settings. The photodiode energy monitor output which was electronically integrated over the laser pulse duration was simultaneously recorded through the data acquisition system. In this manner a calibration curve of actual laser energy versus energy monitor-reading was obtained, and a typical curve is shown in Fig. 7. Although the curve is not completely linear throughout the full energy range, it was treated as linear for the nominal ±3-percent variations of the laser energy encountered.

Alignment of the laser beam with cell centerline and engine nozzle was accomplished through several steps. A He-Ne laser beam was transmitted through the ruby laser system, and adjustments were made so that the beam passed through the center of the entrance and laser dump ports. The He-Ne laser beam was then repositioned so that it was transmitted through the mass spectrometer system and along the axial centerline of the RVC. A plumb line was dropped from the electron beam exit orifice, and adjustments were made in the He-Ne laser beam so that it intersected the plumb line. The engine nozzle was then traversed to the plumb line and adjusted so that the beam passed through the center of the nozzle and into the nozzle throat. Adjustments were then made on the ruby laser system to bring the focus of the ruby laser beam to the point of

intersection of the plumb line and the He-Ne beam. The position and focus of the ruby laser beam were checked by operating the laser at low energy and taking "burn" patterns on developed but unexposed Polaroid film. Ruby laser light reflected from the focal point by the plumb line was used for alignment of collection optics systems. The engine nozzle was then traversed axially until the focal point of the ruby laser beam impinged on the edge of the nozzle. This was defined as the axial zero position of the engine with respect to the laser scattering optical systems.

The laser focal volume is an axially symmetric irradiance distribution, and, ideally, 80 percent of the total laser power is contained in a cylinder of diameter $d = 2.4$ $\lambda_o (F_L/D_L)$ and length $\ell = 16 \lambda_o (F_L/D_L)^2$ (Ref. 20). The ideal diameter of the focal volume is calculated to be ≈ 44 μm. In practice, however, it was ≈ 600 μm. This difference is easily accounted for by lens aberrations and multiple laser modes (Ref. 21). The length of the focal volume is calculated to be ≈ 0.8 cm. Nominal power density at the focal point is estimated to be $\approx 1.24 \times 10^7 W/cm^2$.

4.2 ELECTRON BEAM SYSTEM

The electron source was an RCA Model VC2126 V4 electron gun mounted in a stainless steel housing at the top of the chamber, and the beam was directed vertically downward as shown in Fig. 6. Electrons were produced from a button-type thoriated-tungsten filament operated at 20 amperes current. The beam was injected into the chamber and flow field through a 1.0-mm-diam orifice. Direction of the beam through the orifice was accomplished with an alignment yoke. The orifice was located 50 cm from the chamber centerline, and the beam was magnetically focused to provide a small diameter beam source at the chamber centerline. The orifice provided the necessary pressure drop needed for a 15-cm-diam diffusion pump with an LN_2-cooled baffle to maintain the electron gun pressure at less than 6×10^{-6} torr (8×10^{-4} Pa) under nominal chamber vacuum conditions. An isolation valve installed between the gun and the chamber provided independence between the gun system and chamber pressure conditions when necessary. For number density and temperature measurements the beam remained stationary with 30 Kev energy and 1.0 ma current.

Experimental configurations for obtaining plume visualization photographs are shown in Figs. 8a and b. A sweep-deflection coil located below the orifice permitted sweeping the beam through any angle up to 30 deg either side of vertical, or the beam could be repetitively swept through any angle about any mean deflection angle with a constant angular velocity. In these experiments the starting point of the sweep was adjusted so that the electron beam just grazed the thruster nozzle.

Undeflected beam currents were collected by a cylindrical Faraday cup 35 cm long and 4.5 cm in diameter fitted with two screen grids for suppression of secondary electrons and monitoring of beam spreading and deflection. The distance from the plume axial centerline to the external collector cup screen was 27 cm. A potential of 45 volts was applied to the inner screen, and the external screen was grounded. A rectangular copper trough 38 cm long, 6 cm wide, and 13 cm deep surrounded the cup and was electrically connected with the inner cup screen. The trough provided current collection during flow visualization experiments, and it was aligned axially with the chamber. Orifice, gun emission, and collector currents were continually monitored.

Coarse vertical alignment of the electron gun exit orifice, rocket engine, and collector cup was performed with a plumb bob after the engine position relative to the laser beam focal volume was established. Final axial alignment of the electron beam assumed correct alignment of the laser and spectrometer system, and a detected electron beam fluorescence signal was then maximized by axial deflection of the beam. A check of the engine's axial zero position was accomplished by translating the engine into the beam until half the collector cup current remained, and excellent agreement with that position determined by the laser system was obtained. Radial alignment of the electron beam was accomplished by performing a radial density scan of the flow field near the nozzle exit plane.

The visible optical fluorescence produced by the collision of the electron beam with the plume gas constituents was focused onto the photocathode of a microchannel plate image intensifier by a lens that included an 8.75-in. (3.44-cm)-diam field of view at the chamber centerline. The intensified image was photographed by a Minolta camera. This experimental arrangement is shown in Fig. 8a.

The image intensifier and the camera were electronically operated and under computer control. The camera shutter was opened 0.5 sec before a thruster pulse. Approximately 30 msec after engine ignition the image intensifier was gated on for 100 msec of the thruster pulse duration, and the electron beam swept across the field of view. At the end of the pulse the camera shutter was closed, the film advanced one frame, and the shutter was armed for the next thruster pulse.

In addition to the image intensifier system a simple arrangement utilizing a camera alone was implemented to obtain both black and white and color photographs of the exhaust plume utilizing either the electron or laser beam to provide flow-field radiation. The electron beam was swept along the chamber axis beginning at the nozzle exit plane and ending in the plume far field during each thruster pulse. It should be noted that electron beam impingement on the nozzle prior to each sweep produced a hot area at the

top of the nozzle seen in each photograph. The resulting photographs represent an integration of the induced plume radiation over the length of a given exposure. Exposures of both single and multiple thruster pulses were made. In each case, the camera shutter was opened just prior to the thruster pulse and held open for the desired number of thruster pulses. For electron beam visualization photographs the entire extent of the plume intersected by the beam during its sweep is outlined. For laser beam visualization only that cross section of plume intersecting the beam is visible.

A schematic of the camera system experimental arrangement is given in Fig. 8b. The camera was positioned at the same viewing port used by the image intensifier system. The view axis for the camera system was along a line centered on the viewing port and perpendicular to the plane defined by the chamber centerline and the electron beam. Color photographs were obtained using a Honeywell Pentax Spotmatic single lens reflex camera with a 50-mm, f/1.4 lens. Black-and-white photographs were obtained using the same camera with a 105-mm, f/3.5 lens or a standard Polaroid camera with a 50-mm lens. The color film used was Eastman Kodak High Speed Ektachrome with an ASA number of 160. Black-and-white photographs were produced with Kodak Tri-X film with an ASA rating of 400.

4.3 SPECTROMETER SYSTEM

Light collection for the electron beam and laser systems was provided by a 3-in. (7.62-cm)-diameter, 12-in. (30.5-cm)-focal length fused silica lens mounted on an optical rail inside the RVC. The lens was located approximately 12 in. (30.5 cm) from the axial centerline of the RVC, and it therefore provided a nearly collimated light beam out to the imaging lens. The imaging lens was 3 in. in diameter and had a 20-in. focal length; it focused an image of the electron beam or laser focal volume onto the entrance slit of the spectrometer.

Spatial resolution was achieved with an iris aperture at the spectrometer entrance slit. The aperture was adjusted so that a 2.75-mm length of either electron or laser beam was observed. The slit widths nominally used for both electron beam and laser beam measurements were 1 mm, and the magnification of the optics system was 1.67; therefore, the nominal electron beam volume observed was ≈ 1.65 mm^3, and the nominal laser beam volume observed was ≈ 1.39 mm^3.

The spectrometer was a 0.5-m focal length Spex 1301 double spectrometer with 1,200 groove/mm gratings blazed at 5,000 Å. The collection aperture was f/7, and the mounting arrangement was Czerny-Turner. The spectral coverage of the instrument was 24,000 cm^{-1} (4,167 Å) to 11,400 cm^{-1} (8,772 Å), and the dispersion was approximately

16.9 cm^{-1}/mm (8.3 Å/mm) at 14,286 cm^{-1} (7,000 Å) and 43.5 cm^{-1}/mm (8.5 Å/mm) at 22,645 cm^{-1} (4,416 Å). Table 5 lists the wavenumbers (wavelengths) used for both signal and background measurements. The molecular species responsible for the observed signal radiation are also listed. Selection of wavenumber was accomplished remotely by the operator of the data acquisition system which electronically controlled the spectrometer scanning system.

The detector for all Raman and electron beam radiation dispersed by the spectrometer was a cooled RCA-C31034A photomultiplier. At -26°C and a supply voltage of 2,200 VDC the dark count rate of the tube and Ortec photon-counting system was 2,000 counts per second. The photon-counting electronics consisted of a Model 454 amplifier, a Model 436 discriminator, and a Model 772/773 100-MHz counter which was gated on for a preset 1 to 5 msec time period for Raman or electron beam data acquisition, respectively.

The spectrometer system sensitivity as a function of wavelength was determined by placing a tungsten strip standard lamp of known spectral radiance at the laser beam focal volume. The result of this calibration is presented in Fig. 9 as a relative spectral sensitivity curve.

4.4 RAYLEIGH/MIE SCATTERING SYSTEM

The Rayleigh/Mie scattering optical system is shown in Fig. 6 mounted on an optical rail at a port 45 deg from the bottom port. A positive-negative collection lens system provided a collimated beam of scattered laser light that passed through two narrow band (15-Å FWHM) filters centered at 6,943 Å and through a sheet of HN-22 Polaroid in a rotatable mount. This collimated beam was then focused on an iris diaphragm which was set to define the 2.75-mm spatial resolution required. The volume observed was ≈0.986 mm^3. A lens focused the image at the aperture through a narrow band (30-Å FWHM) filter centered at 6,943 Å and onto the photocathode of a cooled RCA-8853 photomultiplier with a supply voltage of 1,300 VDC. Output pulses from the photomultiplier were processed by a boxcar integrator that presented integrated values of the pulses to the data acquisition system.

4.5 RAMAN-RAYLEIGH/MIE DIAGNOSTIC TECHNIQUES

When a gas is irradiated by an incident laser beam consisting of photons of energy $h\nu_0(\nu_0 = c/\lambda_0)$ whose frequency is such that it is not absorbed by the gas, the majority of the beam traverses the gas virtually unaffected. A small fraction of the beam is scattered by molecular constituents in a direction other than that of the incident beam.

The majority of this scattered light is at the same frequency as the laser beam, ν_0, and is the result of an elastic scattering phenomenon referred to as Rayleigh scattering. References 22, 23, 24, and 25 give excellent theoretical treatments of Rayleigh scattering, and Refs. 1 through 9 describe the utilization of Rayleigh scattering in the study of condensation processes in expansion flow fields. For a fixed scattering angle and laser frequency the Rayleigh scattered intensity normalized to the incident laser beam intensity is

$$I_{Ry} = C_{F_{Ry}} \sum_{i=1}^{j} n_i \sigma_{Ry_i} \qquad (1)$$

in which n_i is the number density (molecules/cm³) of the molecular species i with Rayleigh scattering cross section σ_{Ry_i}, and $C_{F_{Ry}}$ is a constant that includes detection sensitivity. The temperature variation in the Rayleigh scattering cross section can be neglected for the temperature range in the thruster plume (Ref. 26). Equation (1) can be rewritten as

$$I_{Ry} = C_{F_{Ry}} n_T \sum_{i=1}^{j} \left[X_i \right] \sigma_{Ry_i} \qquad (2)$$

in which n_T is the total number density of the gas mixture and $[X_i]$ is the mole fraction of the ith species. Since the species mole fractions of the plume were unknown, it was decided to reduce Rayleigh scattering data based entirely on calibrations in pure N_2 because it was expected that N_2 would be a major constituent of the plume. Calibrating in pure N_2 allowed $C_{F_{Ry}}^{N_2}$ to be determined from

$$C_{F_{Ry}}^{N_2} = n^\circ(N_2)/I_{Ry}^\circ \qquad (3)$$

Measured intensity values are presented as

$$\hat{I}_{Ry_1} = \frac{I_{Ry_1}}{n_o} = \frac{I_{Ry}' C_{F_{Ry}}^{N_2}}{n_o} \qquad (4)$$

in which I_{Ry}' represents raw data values and n_o is the measured thruster combustion chamber number density. Following determination of the plume species mole fractions, corrections can be made to the $\hat{I}_{Ry_1}$ values from the following relation:

$$\epsilon_{Ry} = \left[\frac{\sum_{i=1}^{j} \left[X_i \right] \sigma_{Ry_i}}{\sigma_{Ry_1}} \right]^{-1} \qquad (5)$$

where $i = 1$ indicates nitrogen. If the exhaust plume were a gas mixture, then an axial plot of $\epsilon_{Ry} \hat{I}_{Ry_1}$ and an axial plot of n/n_0 for the plume expansion should be in perfect agreement.

Equation (1) can also be written (Ref. 1) in the form

$$I_{Ry} = C_{F_{Ry}}^{\alpha} \, n_T \sum_{i=1}^{j} \left[X_i \right] \alpha_i^2 \qquad (6)$$

in which α_i is the polarizability of the scatter.

The polarizability of each scatterer can be written classically in terms of its relative index of refraction, m, and its radius, a, as

$$\alpha = \left[(m^2 - 1) \big/ (m^2 + 2) \right] a^3 \qquad (7)$$

From Eqs. (6) and (7) it can be seen that the Rayleigh scattering intensity will be extremely sensitive to the size of the scatterer. For example, if condensation processes began in the exhaust plume, then molecules would begin to stick together. As the clusters grew, they would make a significant contribution to I_{Ry} and provide a method for detection of both condensation onset and level of condensation (see Refs. 1 through 9). That is, an axial plot of $\hat{I}_{Ry_1} \, \epsilon_{Ry}$ for the plume will no longer agree with an axial plot of n/n_0.

In the preceding relations it has been assumed that the ratio of the spherical scatterer radius to the incident wavelength, a/λ_0, is

$$a/\lambda_0 \lesssim 0.05 \qquad (8)$$

which generally permits use of the Rayleigh scattering relations, depending upon the index of refraction of the scatterer (Ref. 27). For molecules and plume condensate the assumption of $a/\lambda_0 \lesssim 0.05$ should be reasonable (Ref. 1). However, for fuel droplets and/or catalyst fines in the plume a/λ_0 could well be greater than one. In this case only the general Mie scattering relations can be used. With the single scattering angle and single wavelength setup utilized in these experiments it cannot be determined whether Rayleigh or Mie relations are applicable. In either case, however, disagreement of $\hat{I}_{Ry_1} \epsilon_{Ry}$ with predictions of n/n_0 will surely indicate the presence of condensate or particulate matter in the plume. Subsequent experiments are planned with particulate-free simulated plume expansions whereby the contribution of condensate scattering alone can be estimated.

A small portion of scattered light is at frequencies other than that of the laser beam, and it is the result of an inelastic scattering phenomenon known as Raman scattering.

23

Inelastic collisions between the laser beam photons and the plume molecules may cause the molecules to undergo transitions to higher or lower energy levels with the result that light is scattered at lower or higher frequencies, resepctively, than ν_0. Only the lower frequency (longer wavelength) Raman scattering was utilized for diagnostic purposes in these experiments. Complete reviews of Raman scattering theory may be found in Refs. 22, 28, 29, and 30; therefore, only the methods by which species density and temperature measurements are determined from the Raman spectra are discussed here.

Figure 10 is a partial synthetic spectrum generated by a Raman scattering program (Ref. 17) for a simulated thruster plume at ≈ 200 K, and only the long wavelength Raman bands or lines (the Stokes spectrum) are shown. This spectrum is a prediction of the spectrum which would be generated by the 0.5-m focal length spectrometer used in these experiments. Located at approximately 8,284 Å is the Q-branch of the N_2 vibration-rotation band. For a temperature range of 100 to 300 K, which includes the anticipated range of plume temperatures for the axial positions at which Raman measurements were to be made and the large spectral bandpass employed, the intensity of the N_2 band is essentially independent of temperature. It is, however, directly proportional to the number density of N_2, $n(N_2)$. Therefore,

$$n(N_2) = C_{F_{N_2}} \, I_m(N_2, Q) \tag{9}$$

in which $I_m(N_2,Q)$ is the measured N_2 band, deadtime-corrected, laser energy-normalized intensity, and $C_{F_{N_2}}$ is a calibration constant obtained from

$$C_{F_{N_2}} = n^\circ(N_2) \Big/ I_m^\circ(N_2, Q) \tag{10}$$

The $n^\circ(N_2)$ and $I_m^\circ(N_2,Q)$ values were obtained from a series of calibration measurements in the RVC. The procedure required evacuation of the RVC to a pressure less than 0.1 torr and the subsequent filling of the RVC to 100 torr with prepurified N_2. A series of five laser shots was used to determine an average $I_m^\circ(N_2,Q)$ value. The procedure was repeated for N_2 pressures of 200, 400, and 600 torr. A plot of $C_{F_{N_2}}$ values versus $n(N_2)$ was made to check the system linearity and the deadtime (τ_D) value employed. The $C_{F_{N_2}}$ values were always in close agreement, and a straight line of zero slope was fit along the points to give an average value of $C_{F_{N_2}}$ to be used for data reduction in Eq. (9).

Shown in Fig. 10 at 7,121 and 7,240 Å are the two lowest level H_2 rotational lines, commonly referred to as the J = 0 and J = 1 lines, respectively. The intensity of these rotational lines can be written (see Ref. 6) as

$$I_m(J, H_2) = \frac{C_J \, n(H_2) \, e^{-J(J+1)87.5/T_R}}{q_r} \tag{11}$$

where J is the rotational level quantum number, T_R is the rotational temperature, C_J is a quantum number-dependent parameter, and q_r is the rotational partition function. As pointed out in Ref. 6, particular attention must be paid to the ortho-para modifications when the H_2 rotational temperature drops below ≈ 300 K. The even-numbered rotational levels belong to the para species, and the odd-numbered levels belong to the ortho species (Ref. 31). Therefore, the partition function must be defined for each of the separate modifications as

$$q_{ro} = \sum_{J=1,3,\ldots} (2J+1)\, e^{-J(J+1)87.5/T_R} \tag{12}$$

and

$$q_{rp} = \sum_{J=0,2,\ldots} (2J+1)\, e^{-J(J+1)87.5/T_R} \tag{13}$$

In these experiments the $J = 1$ rotational line can be used to determine H_2 density, $n(H_2)$, from the following relation:

$$n(H_2) = C_{F_{H_2}}\, I_m^t\, (J = 1, H_2)\, C_F\, (T_R) \tag{14}$$

in which the temperature-dependent correction factor, $C_F(T_R)$, is determined from

$$C_F(T_R) = e^{175(1/T_R - 1/T_R^\circ)}\, q_{ro}(T_R)\, /\, q_{ro}(T_R^\circ) \tag{15}$$

The sum over rotational levels in q_{ro} was limited to $J_{max} = 29$. The superscript $^\circ$ indicates that T_R° is the temperature value of H_2 during calibration measurements performed in the RVC at a hydrogen pressure of 100 torr. A plot of $C_F(T_R)$ for $T_R^\circ = 300$ K is shown in Fig. 11. The $C_{F_{H_2}}$ calibration factor was determined from

$$C_{F_{H_2}} = n^\circ(H_2)\, /\, I_m^\circ (J = 1, H_2) \tag{16}$$

In order to shorten calibration time preceding each test period the relative sensitivity of the H_2 and N_2 density calibration factors was determined as

$$C_{F_{H_2}}/C_{F_{N_2}} = C_{F_R} \tag{17}$$

and this permitted calibrations with only N_2 prior to most test periods. The stability of the relative spectral sensitivity of the system is assumed.

The rotational temperature was determined by comparison of the measured ratio of the $J = 0$ and $J = 1$ line intensities to calculated values obtained from

$$R^c = \frac{10}{54} e^{175/T_R} \; q_{ro}/q_{rp}(T_R) \tag{18}$$

A plot of R^c versus T_R is shown in Fig. 11. The measured value of the intensity ratio obtained at calibration conditions, R_m^o, was used to obtain a correction factor, C_{F_T}, from

$$C_{F_T} = \frac{R^c(T_R^o)}{R_m^o} \tag{19}$$

The measured value of the intensity ratio obtained in the plume was then

$$R_m^t = C_{F_T} \; I_m^t(J = 0, H_2) \, / \, I_m^t(J = 1, H_2) \tag{20}$$

The correction factor, C_{F_T}, was necessary because of relative spectral sensitivity differences between 7,121 and 7,240 Å. It is noted that the measured rotational temperatures should be equal to the gas kinetic temperature because of the relatively high density of the plume at the axial positions at which Raman scattering data were obtained.

The NH_3 rotational Raman lines had to be used to measure NH_3 number densities since the most prominent vibration-rotation band was located at 9,035 Å, which was in a relatively insentitive region for the spectral system employed. Figure 12 is a spectral scan of the NH_3 rotational spectra obtained with 4,880-Å laser excitation at $\approx$300 K in pure NH_3, and Fig. 13 is a rotational spectral scan of a mixture of NH_3 and N_2 at a temperature of 216 K. The NH_3 to N_2 mole fraction ratio was 1.93. The rotational spectrum of NH_3 consists of two branches (designated R and S) as indicated in Figs. 12 and 13. For the spectral resolution of the system employed the lines of the S-branch overlap with the even-numbered lines of the R-branch. An integer L (not a quantum number) was used to designate the lines for purposes of intensity calculation. It can be seen from Figs. 12 and 13 that lines $L = 10$ and $L = 12$ (shown also in Fig. 10) are sufficiently far from any interfering N_2 rotational lines. Furthermore, the $L = 11$ line is at least an order of magnitude less than the $L = 10$ line at room temperature, and with decreasing temperature it will practically disappear relative to the $L = 10$ line (see Fig. 13). For these reasons the $L = 10$ line was chosen for NH_3 density measurements and any spectral interference at this position could only be from Rayleigh light leakage caused by internal scattering by the spectrometer optics.

The intensity of the ammonia lines can be written as

$$I_m(L, NH_3) = C_L \, n(NH_3) \, f(T_R, L)/q_r \tag{21}$$

Information on the NH_3 rotational Raman line intensities is available from Ref. 32 and 33, and using this information with the assumption of moderate spectral resolution such that the S-branch lines completely overlap with the even R-branch lines, the relative intensity of the even L lines can be written as

$$
\begin{aligned}
C_L f(T_R, L) = \left(\frac{\nu_L}{\nu_o}\right)^4 e^{-\frac{hc}{kT_R}[BL(L+1)]} &\left\{ \frac{1}{L(L+1)(L+2)} \left[\sum_{M=1}^{L} M^2[(L+1)^2 - M^2] g_M \, e^{-\frac{hc}{kT_R}(A-B)M^2} \right] \right. \\
+ &\left. \frac{e^{-\frac{hc}{kT_R}B\left[-\frac{3}{2}\left(\frac{L^2}{2}+2\right)\right]}}{L\left(\frac{L}{2}+1\right)(L+1)} \left[\sum_{M=0}^{\frac{L}{2}-1} \left[\left(\frac{L}{2}\right)^2 - M^2\right]\left[\left(\frac{L}{2}+1\right)^2 - M^2\right] g_M \, e^{-\frac{hc}{kT_R}(A-B)M^2} \right] \right\}
\end{aligned}
\tag{22}
$$

The term ν_L/ν_o is the ratio of Raman line wavenumber to laser line wavenumber. The constants A and B used in Eq. (22) were A = 6.29 cm^{-1} and B = 9.96 cm^{-1}. The weighting factor "g_M" is as follows:

$$g_M = 2 \qquad \text{for } M = 1, 4, 7, 10, \ldots$$

$$\text{for } M = 2, 5, 8, 11, \ldots$$

$$\text{for } M = 0, \ L = 2$$

$$g_M = 4 \qquad \text{for } M = 3, 6, 9, 12, \ldots$$

A plot of $I(L = 12, NH_3)/I(L = 10, NH_3)$ calculated using Eq. (22) is shown in Fig. 14 as a function of T_R. Measured values are also shown to demonstrate the validity of Eq. (22) for the spectral system employed.

For the temperature range expected for these measurements the classical value of the partition function (Ref. 32) could be adequately used, and it can be represented as

$$q_r = b \, T_R^{3/2} \tag{23}$$

in which "b" is a constant. For the L = 10 line the density was determined from

$$n(NH_3) = C_{F_{NH_3}} I_m^t(L = 10, NH_3) \, A(T_R) \tag{24}$$

in which the temperature-dependent correction factor, $A(T_R)$, is determined from

$$A(T_R) = \frac{f(T_R^o, L = 10)}{f(T_R, L = 10)} \left(\frac{T_R}{T_R^o}\right)^{3/2} \tag{25}$$

27

A plot of $A(T_R)$ versus T_R for $T_R^\circ = 300K$ is shown in Fig. 15.

The $C_{F_{NH_3}}$ calibration factor was determined from

$$C_{F_{NH_3}} = n^\circ(NH_3) \ / \ I_m^\circ (L = 10, NH_3) \tag{26}$$

Again, in order to shorten calibration time for each test period, the relative sensitivity of the NH_3 and N_2 density calibration factors was determined to be

$$C_{F_{NH_3}} \ / \ C_{F_{N_2}} = B_{F_R} \tag{27}$$

Table 6 is a compilation of all the calibration factors periodically obtained throughout the experiments for reduction of Raman/Rayleigh scattering data.

All Raman/Rayleigh intensity values measured during the thruster pulses were obtained over a 1-msec data gate located 90 msec into the thrust interval (see Appendix A). For all Raman/Rayleigh measurements the thruster was pulsed a nominal 30 times. The first five pulses were ignored since other thruster experiments (Refs. 34 and 18) indicated that at least five pulses were needed before the thruster temperatures and pressures would begin to stabilize. The Raman/Rayleigh intensity values were determined as an average over the last 25 pulses. Background values for the Raman intensities were obtained by setting the spectrometer wavenumber just outside the Raman bandpass region (see Table 5) and again pulsing the thruster 30 times with laser firing. Average background intensities were also averaged over the last 25 pulses, and in this manner the influence of laser-induced background radiation was removed from the Raman signals. Rayleigh scattering background was obtained from the average of 10 laser pulses, but the thruster was not fired. All Raman signals and background were corrected for photon-counting system deadtime effects, and details of this correction process are found in Appendix B. During data reduction any signal whose value relative to the mean was plus or minus twice the standard deviation was discarded.

4.6 ELECTRON BEAM DIAGNOSTIC TECHNIQUE

For the plume expansion region for which the species density was too low to permit use of Raman scattering, the electron beam fluorescence technique (Ref. 16) was used to measure local values of $n(N_2)$ and T_R. The axial distance region investigated was $78 \leqslant \hat{x} \leqslant 300$, and at selected axial points radial profiles of both $n(N_2)$ and T_R were obtained.

One result of the interaction between moderate energy electrons and gaseous atoms or molecules is electronic excitation followed by light emission. The electron beam utilizes spectroscopic analysis of the emission to obtain number density and rotational

temperature of the gas. In N_2 the vibration-rotation bands of the N_2 First Negative System emission are quite intense, and the measured intensity and intensity distribution of the rotational lines within a band permit determination of the number density and rotational temperature of N_2.

The excitation and emission processes are

$$e^-_p + N_2 (X\ ^1\Sigma) \xrightarrow{\text{excitation}} N^+_2 (B\ ^2\Sigma) + e^-_p + e^-_s$$
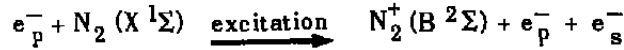
in which e^-_p is a primary electron and e^-_s is a secondary electron, and

$$N^+_2(B\ ^2\Sigma) \xrightarrow{\text{emission}} N^+_2(X\ ^2\Sigma) + h\nu \quad (\text{First Negative System})$$
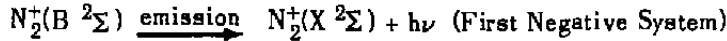
The photon emission rate at 4,275.3 Å, a position in the unresolved P-branch of the (0,1) band, was monitored for the number density measurement. The detected photon emission rate $S(v',v''_2)$ from vibrational band (v',v''_2) is, neglecting other excitation and emission processes,

$$S(v',v''_2) = \frac{\omega}{4}\ T\ [\lambda(v',v''_2)]\ C\ [\lambda(v',v''_2)]\ \beta(v',v''_2)\ \sigma\ (v''_1,v')\ i_B L\ n(N_2) \qquad (28)$$

Here, ω is the detection solid angle; $C[\lambda(v',v''_2)]$ denotes the effect of spectral intensity variation of the system; $\beta(v',v''_2)$ is the branching factor of the v' to v''_2 transition; v''_1 is the ambient gas vibrational state quantum number ($v''_1 = 0$ for the vibrational temperature $T_v \leqslant 800°K$, which is the case for the thruster plume); $\sigma(v''_1, v')$ is the excitation cross section to state v' at the particular electron beam energy utilized; i_B is the beam current; L is the length of beam observed (2.75 mm); and $T[\lambda(v', v''_2)]$ is the spectrometer transmission function. Since the band shape is dependent on rotational temperature (Ref. 16), $T[\lambda(v', v''_2)]$ and $C[\lambda(v', v''_2)]$ introduce a temperature dependence into Eq. (28) which can be rewritten as

$$S_m(0,1) = S_{N_{F_2}}\ F(T_R)\ n\ (N_2) \qquad (29)$$

in which $S_m(0,1)$ is the measured beam-current-normalized photon rate, $F(T_R)$ is a temperature-dependent correction factor, and $S_{F_{N_2}}$ is a calibration factor. The variation of $F(T_R)$ with T_R as predicted by an electron beam fluorescence spectral program is shown in Fig. 16. Except for several continuous thruster burns during which the R-branch rotational lines were scanned and fully resolved, T_R was measured by computing the ratio of $S_m(0,1)$ to the measured photon rate at one of two wavelengths in the R-branch tail and comparing to a prediction of the variation of the ratio with T_R. These wavelengths were 4,264.8 Å and 4,267.5 Å, and they were chosen to cover high and low temperature regions. The calculated variation of the ratios versus T_R is shown in Fig. 17.

The calibration factor $S_{F_{N_2}}$ was obtained by performing calibrations of count rates in nitrogen flows of known number density for each test period. The flow source was a small conical nozzle mounted on the traversing mechanism and adjacent to the thruster. Method-of-characteristics calculations of the number density and temperature variation on the axial centerline were utilized (Ref. 35). To complete the calibration the flow's rotational temperature was measured, since the effect of T_R on band shape had to be included. Therefore, $S_{F_{N_2}}$ was determined as follows:

$$S_{F_{N_2}} = S_m^o \ (0,1) \ / \ F(T_R^o) \, n^o(N_2)$$

$$(30)$$

All electron beam plume data acquisition employed a 5-msec data gate beginning 90 msec into the thrust interval. For the electron beam measurements the thruster was nominally pulsed 25 to 40 times. The first 5 to 10 pulses were ignored, and those remaining were used to determine an average signal level. Any signal whose value relative to the mean was plus or minus twice the standard deviation was discarded. Corrections were made for stray background radiation, which was located at the wavelength of interest of the electron-beam-induced radiation, and also for the detection system noise; therefore, off-band radiation at 4,315 Å was periodically measured with the thruster firing. A slight excess of detector counts was observed over the background continuously obtained on-band but between thruster pulses. This off-band excess was assumed to exist on-band during thruster firings and to be proportional to the net signal magnitude. With these assumptions background correction relations were developed including thruster measurements with neutral density filters which were employed at high count rate conditions to minimize nonlinear detection system response. Again, all signals were corrected for counting system deadtime effects (see Appendix B).

Another important correction had to be made to the number density data to account for collisonal de-excitation or quenching processes in which electron-excited molecules are de-excited by collisions with gas molecules before First Negative System emission can occur. That is, Eq. (29) is linear only for densities below 10^{15} cm^{-3} (Ref. 36). Except for ground state nitrogen, values of the rate constants for N_2 B $^2\Sigma$ state quenching by other thruster plume species are not available, and it is assumed that all rate constants are equal to that of nitrogen and that the constant is temperature-independent. Using a predicted nitrogen mole fraction, x_{N_2}, in the plume, the corrected number density is

$$n^{(2)} (N_2) = n^{(1)}(N_2) \ / \ 1 - \left[n^{(1)}(N_2) \ k\tau' x_{N_2} \right] \Big\}$$

$$(31)$$

in which $k = 3.0 \times 10^{-10}$ cm^3/sec/molecule (Ref. 36) and $\tau = 6.6 \times 10^{-8}$ sec (Ref. 37).

4.7 PRESENTATION OF LASER SCATTERING AND ELECTRON BEAM DATA

The laser-Raman results of species number density and temperature in the near-field plume ($\hat{x}$ = 18.5 and 28.5) are tabulated in Table 7 and plotted in Figs. 18 through 22. Average values of density and temperature for test conditions 3A, 2A, 2B, 2C, and 2S are given in Table 8 along with values of γ calculated using the number density values. The laser-Rayleigh results are tabulated in Tables 9, 10, and 11 and plotted in Figs. 23 through 29. The Raman results in Figs. 18 through 21 are compared to γ = 1.2 and 1.3 MOCS predictions for the plume (Ref. 35). Figures 23, 25, and 26 are plots of I_{Ry_1} versus axial position in the plume, and Figs. 24 and 27 are radial plots of I_{Ry_1} for $\hat{x}$ = 28.5, test condition 2A and $\hat{x}$ = 78.5, test condition 2S, respectively. Figure 28 is a plot of I_{Ry_1} as a function of reservoir density n_o for an axial position of $\hat{x}$ = 28.5, and Fig. 29 is a plot of I_{Ry_1} for test condition 2A and $\hat{x}$ = 28.5 as a function of test period.

Electron beam results are tabulated in Tables 12 and 13, and axial and radial plume surveys are presented in Figs. 30 through 41. Figure 42 is a plot of measured N_2 number density at $\hat{x}$ = 278.5 as a function of thruster chamber pressure with an initial catalyst bed temperature of 400°F. Figure 43 is a plot of $n(N_2)$ at $\hat{x}$ = 278.5 as a function of thruster chamber pressure for initial catalyst bed temperatures of 200, 400, and 600°F. Figure 44 is a plot of $n(N_2)$ versus thruster chamber pressure for four different axial positions with an initial catalyst bed temperature of 400°F. Figure 45 is a plot of T_R as a function of thruster chamber pressure for four different axial positions with an initial catalyst bed temperature of 400°F.

Figures 46 through 49 are N_2^+ (1^-)(0,1) R-branch rotational scans obtained with the electron beam system during continuous thruster firings, and Fig. 50 shows the Boltzmann plots (Ref. 16) of these scans. Figure 51 is an N_2 isodensity plot obtained from the electron beam data for test condition 2A. Figures 52 and 53 are diagrams depicting $n(N_2)$ and T_R, respectively, obtained in the backflow region by the electron beam system.

For electron beam measurements the overall uncertainty of $n(N_2)$ values is in the range from ±4 to ±9 percent, while that for T_R values is in the range from ±13 to ±30 percent with a typical value of ±18 percent. For laser-Raman measurements the overall uncertainty of number density values is as follows:

$$n(N_2) \longrightarrow \pm 19 \text{ percent}$$
$$n(H_2) \longrightarrow \pm 12 \text{ percent}$$
$$n(NH_3) \longrightarrow \pm 50 \text{ percent}$$

The overall uncertainty for T_R values is ±16 percent. For laser-Rayleigh measurements the overall uncertainty of $\hat{I}_{Ry_1}$ values is ±22.5 percent. Detailed discussion of measurement uncertainties is presented in Appendix C.

In order to reduce publication costs, flow visualization photographs have been omitted from this report. A large number of photographs were included in a previous data package transmitted to the AFRPL.

5.0 MASS SPECTROMETER DIAGNOSTICS

5.1 MASS SPECTROMETER SYSTEM

The cryogenically pumped mass spectrometer used in these experiments was developed for rocket engine exhaust plume studies (Refs. 15 and 38) under DARPA sponsorship. The gaseous helium (GHe)-cooled probe (see Fig. 54) was fabricated from stainless steel in two separate sections. The probe face was conical with a cone half angle of 30 deg. A 15-deg conical half-angle, pure nickel skimmer with a 0.020-in.-diam eloxed orifice was soldered to the probe body. Three flat Minco heaters with a total output power of 10 W were attached to the outside of the nickel skimmer. The probe's two sections were thermally insulated from each other by a Kel-F® gasket placed between machined knife edges on each section. The forward section was cooled by circulating GHe between its concentric cylindrical walls. The aft section was uncooled, and it contained the electrical feedthrough, CO_2 injection port, roughing pumpout port with solenoid-operated valve, and an ionization gage for pressure measurement and automatic arcing pressure shutdown.

The mass spectrometer system employed in the probe included an EAI circular rod quadrupole mass filter and Extranuclear Laboratories ionizer assembly and paraxial electron multiplier. A close-coupled, high frequency response preamplifier was used with the system in addition to the normal power supplies and electronics. The mass spectrometer assembly was mounted to the uncooled section probe wall with the ionizer and filter sections protruding into the cold section.

The probe functions under the same principle as a molecular beam system. In effect, the probe serves as the second stage of a two-stage, miniature, high-performance, molecular beam-mass spectrometer system. For free jets (exhaust plumes) with little condensation this gives practically an unperturbed measurement of plume species (Ref. 15). Basic operation consists of the probe's skimming a molecular beam from the plume centerline and directing the beam onto the ion source entrance aperture that serves as a collimator. The collimated beam passes through the ion source, where a small percentage of the molecules is ionized. The ions are extracted and focused by the ion lens assembly

prior to entry into the mass filter. The mass-selected ions which pass through the quadrupole section are extracted by the negative potential of the first dynode of the 17-stage copper-beryllium paraxial multiplier, and the resultant signal is recorded.

Operation of a molecular beam or a quadrupole mass spectrometer requires very high vacuum conditions. The probe pressure maximum was thus required to be less than 1×10^{-6} torr. The use of cryopumping alone to meet this requirement was insufficient as a result of the high percentage of H_2 (a noncondensable at GHe temperatures) in the monopropellant thruster plume. This problem was alleviated by injecting CO_2 into the probe prior to testing. The CO_2 adhered to the GHe-cooled surface and functioned as a sorption pump for H_2 in the plume. The Minco heaters were used to ensure that CO_2 or other condensables would not deposit around the skimmer orifice and reduce the total signal.

5.2 ALIGNMENT, CALIBRATION, AND OPERATION

Because the mass spectrometer probe is a streamline-sampling device, it was necessary to align the probe very accurately to ensure proper sampling. The He-Ne laser system used to align the thruster was employed to accomplish the alignment. The probe was positioned on its unistrut mount as near the chamber centerline as practical. The probe end plate was removed, and the mass spectrometer was taken out. Wire crosshairs were installed at the rear of the probe, and the probe was adjusted until the laser beam struck the crosshairs and passed through the skimming orifice. The mass spectrometer was installed on its internal mount and adjusted until the beam passed through the multiplier housing, the ion source orifice, and then out the skimmer orifice. The mass spectrometer was locked in place, the end plate reinstalled, and the alignment checked through the open solenoid valve on the end plate.

An extensive calibration of the mass spectrometer system was not performed; rather, the following procedures were followed for extracting necessary composition information from the raw data.

From past experience with the EAI mass spectrometer-sampling probe system it was known that if (and only if) standard operating conditions were maintained, standard published quadrupole calibrations could be used. Because it was not possible to recalibrate the probe system for all species of interest and since standard published calibration data had been established as acceptably accurate, these data were used to ascertain relative species compositions for all mass spectrometer data obtained.

Because mass spectrometer data were taken during pulse mode operation of the thruster and long time periods were involved in the data acquisition, the mass spectrometer probe background pressure and, hence, background signal changed with time. This did not affect the calibrations, but it did require recording and subtracting the background signal for appropriate pulses.

An absolute number density measurement with the mass spectrometer was attempted by using a calibration obtained by expanding N_2 through the auxiliary nozzle attached to the traversing mechanism. The electron beam system was used to measure the number density in the flow, and then that value was extrapolated to the mass spectrometer position using the standard $1/x^2$ far-field approximation (Ref. 39). Operating parameters for the mass spectrometer were set to be consistent with normal operation except for multiplier voltage and emission current, which were necessarily adjusted day-to-day to account for sensitivity changes of the overall system. Sensitivities were found to shift too much to allow confidence in absolute number densities unless calibrations were taken prior to each data run. This was not deemed practical due to the excessive time required. However, relative concentrations were not noticeably affected by the sensitivity shifts.

Prior to the pumpdown for any test period in which the mass spectrometer was to be utilized, all electrical connections to the probe were checked for continuity. The probe coolant lines were connected in series with the main header of the GHe-cooled, finned cryoarray and therefore began cooling whenever the GHe flow to the cryoarray was begun. During cooling the probe solenoid valve was operated periodically to decrease the amount of cryopumped gas on the probe walls, and the internal electrical devices were activated to prevent their excessive cooling. The probe pressure was monitored during the cooling, and the mass spectrometer ion source was kept warm but operated without current.

If sensitivity calibrations with the auxiliary nozzle nitrogen flow were to be performed, they were begun when the probe pressure reached the 10^{-7} scale and the RVC pressure level reached 10^{-6} torr or less. If calibrations were not to be performed, as was generally the case, the probe pumping system was made ready for operation with the thruster. Special preparation was required since the probe walls were not cold enough at 12 to 20 K to pump the hydrogen from the plume. Carbon dioxide for cryosorbing the hydrogen was deposited through the CO_2 injection port at a rate which maintained the probe pressure at 1×10^{-4} torr during injection. The skimmer heaters were activated during this period, and the skimmer temperature was controlled thereafter. The initial injection of CO_2 during a test period lasted 5 min, but the injection time was increased by 2 min each time injection was required during the test period. The need for additional

injection of CO_2 became apparent as a result of sudden rises in the probe background pressure when the quantity of CO_2 in the probe became saturated with H_2. Upon completion of each CO_2 injection a 15-min delay was allowed to permit the CO_2 which may have been cryopumped onto intermediate temperature surfaces to evaporate and migrate to the 20-K surfaces.

To permit a relationship to be established between operation of the quadrupole system on different days, optimum settings for most electronic components were determined during the first mass spectrometer test period and maintained throughout the entire test schedule. Constant values of lens potentials, electron energy (75 eV), ion energy, and resolution were maintained throughout testing. Multiplier voltage and ion source current were adjusted periodically to account for required sensitivity shifts. The low mass range, less than 55 amu, was normally examined with the spectrometer.

The mass spectrometer data were taken in two basic modes: either the entire mass range was recorded and repeated as many times as possible during a pulse, or a limited sweep was used over 4 amu, permitting detailed intrapulse data to be obtained in the 4-amu band of interest. Entire mass range sweeps limited the number of times a given mass number signal could be monitored for a particular engine pulse to approximately two. Limiting the mass range sweep to 4 amu confined the number of sweeps per thruster pulse to approximately 20. This mode of operation still permitted the adjacent peaks for hydrazine and ammonia to be monitored for cracking pattern purposes. A description of the Visicorder® oscillograph and remaining data acquisition-related components of the system can be found in Appendix A.

5.3 PRESENTATION OF MASS SPECTROMETER DATA

The ratio of ammonia to nitrogen mole fractions ($[NH_3]/[N_2]$) was monitored throughout the test periods in which the mass spectrometer was installed and operating. Tabulated results which were averaged over Test Periods 6 through 11 are shown in Table 14. These ratios can be used to infer equilibrium ammonia dissociation levels from the relation

$$([NH_3] / [N_2])_{equil} = 4(1 - x)(1 + 2x) \qquad (32)$$

in which x = ammonia dissociation fraction. Table 15 gives the dissociation fraction assuming equilibrium dissociation for the average pulse values given in Table 14.

The intrapulse variation of ammonia to nitrogen was not generally monitored; however, limited data were taken in anticipation of possible later interest. The results for pulses 11 through 25 (average) for Test Condition 2A are shown in Fig. 55.

During the mass spectrometer test periods the five species of primary interest (H_2, NH_3, H_2O, N_2, and N_2H_4) were monitored as functions of pulse number for several of the test conditions. In most instances all of these species were monitored, but in many cases the hydrogen peak signal-to-noise ratio was so poor that the hydrogen data could not be used. This high background noise was associated with the large quantities of H_2 absorbed into the CO_2 frost used as pumping in the probe. Cases for which five species data were obtained are presented in Figs. 56, 57, and 58 for Test Conditions 2A, 2B, and 2C, respectively. Data for two additional test conditions are shown in Fig. 59.

Species' variation within a pulse was obtained for Test Condition 2A by sweeping over limited mass ranges. These data are presented in Figs. 60 and 61 for pulse numbers 1 and 25, respectively.

For the first thruster pulse in a sequence the amount of N_2H_4 in the plume varied significantly with inlet pressure (and hence thrust level). The first-pulse relative variation of hydrazine in the plume as a function of pressure measured at the valve inlet for an initial catalyst bed temperature of 204 K ($400°F$) is shown in Fig. 62.

Because of the lack of detailed calibration data for the mass spectrometer system and the large variations caused by engine fluctuations, no good evaluation of the error in the mass spectrometer measurements will be offered. A cursory analysis does indicate that the variations in species proportions are within ±20 percent for the major species, but the correctness of the values is undefinable at present.

6.0 QUARTZ CRYSTAL MICROBALANCE AND PARTICLE—SAMPLING DIAGNOSTICS

6.1 QUARTZ CRYSTAL MICROBALANCE

A quartz crystal microbalance (QCM) was utilized in this study for measurements of the mass deposit rate and total mass deposit in the thruster plume. Measurements were made for crystal surface temperatures in the range from 90 to 200 K at a variety of radial and axial positions in the forward flow region of the thruster for the complete range of engine operating conditions.

The QCM consists of a quartz crystal, an electronic oscillator, and connection to the data processing/recording system. The piezoelectric effect of the quartz crystal is used to stabilize the resonance frequency of the oscillator. The term piezoelectric refers to the generation of an electromotive force between the faces of the crystal when pressure is applied. Conversely, application of voltage to the crystal faces produces a corresponding mechanical distortion. An alternating voltage applied to the crystal produces mechanical vibrations of the quartz, and at the resonant frequency the vibrations are particularly

strong. From an electronic viewpoint the crystal assembly appears as a sharply resonant circuit capable of stabilizing the frequency of oscillations. This resonance frequency, depending on the angle of the crystal cut, is found to be a function of the mass deposited on the crystal surface and the crystal surface temperature. The relationship for the change in frequency, Δf, that results when the crystal experiences a mass change, ΔM, and temperature change ΔT, is given by

$$\Delta f = C_m \Delta M + C_T \Delta T \tag{33}$$

(Ref. 13) where C_m is the mass coefficient and C_T is the temperature coefficient of the quartz crystal.

Since a measurement of the variation of QCM frequency with deposited mass is required, the influence of temperature on the observed frequency should be minimized. Therefore, a QCM of the temperature-compensating variety developed by JPL (Ref. 40) was utilized. For this type of QCM, a doublet crystal is cut and the electrode suitably arranged so that two independent crystal oscillators are obtained. If the two crystals are of identical piezoelectric properties and are constrained to identical temperature environments, the following relation results (Ref. 13):

$$\Delta f = \Delta f_1 - \Delta f_2 = C_{m_1}(\Delta M_1 - \Delta M_2) \tag{34}$$

where Δf is the beat frequency shift. When one of the crystal surfaces is protected from mass deposition with a transparent strip, the beat frequency shift is

$$\Delta f = C_{m_1} \Delta M_1 \tag{35}$$

For an AT crystal cut of $35°10'$ an evaluation of C_{m_1} (Ref. 13) using a quartz density of 2.28 gm/cm^3 yields the desired mass deposition rate expression

$$\frac{dM}{dt} (gm/cm^2 - sec) = 1.524 \times 10^{-8} \frac{df}{dt} (Hz/sec) \tag{36}$$

This particular crystal cut and the JPL doublet crystal design provided effective temperature compensation in the range from 85 to 200 K.

A schematic of the QCM doublet from Ref. 13 is shown in Fig. 63. The QCM (Model No. 2397) was equipped with a gold wire brush mount to absorb thermal stresses and resistance heaters controlled by copper-constantan thermocouples. Three thermocouples were monitored during thruster firings. The first was mounted in the proximity of the heaters, while the second was at one corner of the crystal doublet

37

surface. A third thermocouple was located in the crystal mounting block to assess the temperature difference between crystal doublet and the crystal mounting block. The crystal doublet was covered by a Teflon® block collimator assembly provided with two circular apertures, one over each crystal surface. One aperture was utilized to collect oncoming contaminants, and the second aperture was covered with a mylar strip.

The experimental configuration for both phases of the thruster study is shown in Fig. 64. In Test Phase A the QCM crystal surface was located 387.7 cm (15.2 in.) from the center of the thruster exit plane at an angle of 30 deg from the chamber centerline; in this position the thruster axis was centered on the chamber centerline, and the thruster was in the forwardmost axial position. Cooling was provided by thermal contact via an aluminum bracket attached to the RVC gaseous helium cryoheader and to an aluminum bolt through the QCM mounting block. Indium was used as gasket material between the bracket and header and between the bolt and QCM mounting block. For Test Phase B the QCM crystal surface was positioned on the (thruster) chamber centerline at a distance of 113.4 cm (44.6 in.) from the thruster exit plane measured with the thruster in the rearmost position. Cooling was provided by thermal contact via a copper braid conduction path with the RVC gaseous helium cryoheader and the QCM aluminum mounting bolt. For both experimental configurations QCM position and surface angle (θ) with respect to the thruster exit plane will be referenced in terms of an axial position (z) from the thruster exit and a radial distance (x) perpendicular to the thruster axial centerline. Figure 65 outlines these relationships.

The QCM resistance heaters, controlled by the thermocouple at the crystal surface, maintained the operating temperature of the unit. The range of crystal temperatures utilized in this study was 90 to 200 K.

6.2 QCM DATA ACQUISITION

Two channels of QCM data were acquired during each thruster firing sequence. First, QCM surface temperature measurements (T_{QCM}) yield information contributing to the identification of species in the trapped cryodeposit. Second, as outlined previously, a measurement after each thruster pulse of the shift in QCM beat frequency provides a measure of the mass deposition rate. In addition, summation of total beat frequency variation yields information about the total deposited mass.

A block diagram of the QCM data acquisition system is given in Fig. 66a. Signals from the QCM were amplified and directed to a counter which displayed the beat frequency for each thruster pulse. As each data cycle was completed, the PDP-8

computer system read and stored the contents of the frequency counter along with its identifying thruster pulse number and a sample from all three QCM temperature measurement thermocouples. At the conclusion of a thruster firing sequence, the stored QCM data from all channels were listed using a teletype unit while a magnetic tape record was made for subsequent data processing. While the digital data acquisition was taking place, an analog system monitored the QCM beat frequency by having a portion of the QCM signal directed to a ratemeter, the output of which was recorded on a strip chart. The analog system provided a real-time monitor of the QCM beat frequency during the course of a thruster firing sequence.

The QCM digital data sequence is shown schematically in Fig. 66b. Prior to each thruster pulse in a given sequence, the QCM data gate was opened for a period of 3 sec. During this period the beat frequency was counted, and upon closing of the data gate the computer system read the frequency counter, sampled the QCM thermocouples, and stored these data as a function of thruster pulse number. The computer then initiated the counter and continued with the thruster firing sequence and other data acquisition tasks. After a period of 7 sec, the QCM data cycle was again initiated.

In order to establish a mass deposition rate, some representative characteristic time of thruster operation was required. A representative thruster pulse duration of 138 msec, determined from observation of the pressure transducer traces (outlined in Section 7.4) and denoted as the thruster deposition time, τ_d, was selected for use as the characteristic time. Mass deposition computations were made as follows:

$$\dot{m} \ (\mathrm{g\,m/cm^2-sec}) = 1.524 \times 10^{-8} \left[\frac{C_2}{\tau_{Q2}} - \frac{C_1}{\tau_{Q1}} \right] \Big/ \tau_d \qquad (37)$$

in which C_1 and C_2 are the contents of the frequency counter before and after each thruster pulse, respectively, and τ_{Q1} and τ_{Q2} are the 3-sec QCM data gates before and after each pulse, respectively.

It should be noted that no value of $\dot{m}$ is recorded for the last thruster pulse in each data sequence since no sample of the QCM frequency is made after the last thruster pulse.

Mass deposition rates may also be computed in terms of gm/sec · steradian as follows:

$$\dot{M} \ (\mathrm{gm/sec\text{-}sr}) = \dot{m}\,r^2 \Big/ \cos\phi \qquad (38)$$

39

where r is the distance from the QCM surface to the center of the thruster exit plane and ϕ is the angle between the direction of flow and the normal to the surface of the QCM (see Fig. 65).

Predictions of deposition rates for the thruster can be obtained by following the method outlined in Ref. 18. The mass flux from the thruster can be estimated as

$$\dot{M}_T = 2.3 \left(\frac{1.0}{0.1}\right) F_T \doteq 23 \, F_T \; \text{(gm/sec·sr)} \tag{39}$$

in which F_T is the thrust and a mass flux of 1 gm/sec·sr is used for a 0.1-lbf thrust. The mass flux for a particular species can be estimated as

$$\dot{M}_i = 23 \, X_i F_T \tag{40}$$

in which X_i is the species mass fraction. To predict the mass flux at the QCM surface the following relation is used:

$$\dot{m}_i \; \text{(gm/cm}^2\text{·sec)} = \frac{23 \, X_i F_T f(\theta)}{r^2/\cos \phi} \tag{41}$$

in which $f(\theta)$ for these experiments is the Hill-Draper approximation (Ref. 41).

Predicted fluxes from Eq. (41) must be corrected for evaporation of the species trapped on the QCM surface (i.e., a net deposition must be calculated). Again, the procedures outlined in Ref. 18 are used, and the evaporation rate curves for the species of interest from Ref. 18 are reproduced in Fig. 67.

6.3 PARTICLE-SAMPLING SYSTEM

The sample collecting system used during these experiments was completely passive. It consisted of two basic components, an aluminum housing and the collectors themselves. The housing was made of eight strips of 1-in.-wide aluminum bolted together at one common point and welded to form a web (see Fig. 68). A series of holes was drilled 5/8-in. apart along the entire length of each strip, and the stubs on the collecting disks were placed through these holes and secured with alligator clips.

The sampling disks were standard scanning electron microscope (SEM) disks made of aluminum with glass cover slides added to the top surfaces. The glass was covered with a vacuum-deposited copper substrate. There were three types of collecting surfaces used to

capture samples: the vacuum-deposited copper alone, beeswax melted onto the copper, and SEM quality Microstick® glue dripped onto the copper and spread by moving the disks to and fro. A total of 84 disks (9 with wax, 16 with glue, and 59 with just copper) were distributed throughout the web.

The sampling was accomplished by installing the web in the vacuum chamber so that the engine exit was located in the center of the plane of the open end of the web. The axis of the engine nozzle was located along the centerline of the web length. The engine was pulsed into the web approximately 1,000 times before the web was removed from the RVC. The SEM disks were carefully removed and placed on stands in dust-free boxes for subsequent viewing by the SEM.

The disks with their captured samples were screened under an optical microscope to discern which disks were most interesting and worthy of further examination by an SEM. The disks thus selected were then examined with a mini SEM scanning electron microscope, and, in addition, an x-ray subsystem was used to perform an energy dispersive x-ray analysis. A microprocessor with the capability of automatic element identification from the x-ray analysis was utilized to search each of the selected disks for possible catalyst bed and nozzle material which may have been collected.

6.4 PRESENTATION OF PARTICLE-SAMPLING AND QCM RESULTS

The attempted collection of particles was very successful with large quantities of submicron and larger particles captured on all three types of disks. In addition, there was evidence of fuel droplet impingement upon the particle sampling disks. Discussion with the AFRPL personnel revealed that proof of catalyst bed particle capture required the identification of iridium among the collected particles. Extensive x-ray analysis of the collected samples failed to reveal the presence of iridium; therefore, it was assumed that no particulate matter from the bed itself was actually collected. However, the x-ray analysis in conjunction with microscopic examination did reveal alumina spheres in large quantities. Information given by AFRPL indicated that these were not from the catalyst bed. It is believed that the aluminum particles were eroded from the aluminum cryoliners of the RVC or the aluminum particle sampling web itself. Another possibility is that the particles could have been introduced through the thruster as a result of the use of aluminum flare savers in a few locations in the fuel system connections. This possibility is extremely remote, however, because of the stringent requirements on particulate levels that were met during engine/fuel system preparation.

Microscopic examination of the disks did reveal that near the centerline of the plume copious quantities of fuel droplets had impinged. These droplets badly etched the pure copper disks; very similar patterns were observed in a laboratory study in which copper disks were sprayed, using a nebulizer, with pure N_2H_4. The similarities were sufficient to infer that large quantities of fuel were present near the plume centerline.

The disks near the centerline were obviously subjected to high heat loads; the collectors without wax were blackened, and those with wax were whitened. Disks just outside the direct impingement area showed the etching effects, but these effects were not observed for the disks nearest the centerline because the intense stagnation heating was dominant.

In addition to the observations reported in the preceding discussion, an interesting shadowing effect on the sampling disk mounting device was observed. Areas shielded from the plume by being behind disks were very dark. Some areas that had been underneath disks appeared dark, but these were noted to correspond to disks which were not pressed flat against the mounting device.

It should be noted that the particle sampling experiments under discussion were conducted after a catastrophic increase in plume contaminants was observed during test period 15. Further discussion of this phenomenon can be found in Section 7.0.

Tables 16 through 23 present average deposition rates on the QCM, $<\dot{m}>_n$, where "n" indicates the final number of thruster pulses over which the average was taken. The parameters which were varied include T_{QCM}, engine position, and test conditions for all data runs made during Test Periods 1 through 11 (Phase A). Similar data for test periods 13 through 16 (Phase B) are presented in Tables 24 through 19.

Figures 69 through 76 are exemplary plots of mass deposition rate versus thruster pulse number with either T_{QCM} or thruster test condition as parameters. Only exemplary plots are shown since plots of all QCM data were included in the data package previously transmitted to the AFRPL. Figures 77 through 89 are plots of $<\dot{m}>_n$ as functions of either test condition, T_{QCM}, or effective angular position of the QCM. Table 30 is a tabulation of $<\dot{m}>_n$ values for various T_{QCM} values and test conditions, predicted values from the method of Ref. 18, and measured values obtained by JPL (Ref. 13).

7.0 DATA ANALYSIS AND DISCUSSION

7.1 LASER SCATTERING AND ELECTRON BEAM RESULTS

Several theoretical calculations were performed to provide a basis for comparison with the experimental results. Figure 90 is a plot of specific heat ratio (γ), hydrogen-to-nitrogen mole fraction ratio, and ammonia-to-nitrogen mole fraction ratio as a function of ammonia dissociation fraction, x. The following relations were used for the calculations:

$$[NH_3] / [N_2] = R_1 = \frac{4(1 - x)}{1 + 2x} \tag{42}$$

$$[NH_3] / [H_2] = R_2 = \frac{2(1 - x)}{3x} \tag{43}$$

$$[H_2] / [N_2] = R_1/R_2 \tag{44}$$

$$\gamma = (0.2087 \ x) + 1.1556 \ \text{(Data Fit)} \tag{45}$$

MOCS calculations (Ref. 35) were also used to provide axial variation plots of n/n_0 and T/T_0 for the thruster plume. The thruster nozzle exit plane conditions were the MOCS input data and were determined using the method of Whitfield (Ref. 45) for calculating the internal nozzle flow field with boundary-layer corrections. For the underexpanded flow field it was assumed that the subsonic portion of the boundary layer was accelerated so that the Mach number, M, at the exit plane nozzle wall was 1.01; this value of M was faired into the calculated M distribution interval to the nozzle for the region where $M \geqslant 2$. The exit plane static pressure distribution and the entirely supersonic M distribution were then used as the starting line input for the MOCS. The expansion was assumed isentropic with constant specific heat ratio, γ, and the calculations were made for both $\gamma = 1.2$ and $\gamma = 1.3$. The species mole fractions used for the MOCS calculations were determined from Fig. 90, and they are presented in Table 31. A tabulation of MOCS values at selected axial positions is presented in Table 32. Average thruster combustion chamber number density, n_0, and temperature, T_0, values are given in Table 33. These average values were obtained by averaging the last 20 or 25 P_{INLET} and T_{CATB} values of a thruster pulse sequence. The average P_{INLET} values were converted to average P_c values using thruster calibration plots, and the average T_{CATB} values were converted to T_0 values using the following relations:

43

$$T_o(K) = (5/9)(1.0267)\left[T_{CATB}^{(°F)} + 460\right], \text{ Test Condition 2S} \tag{46}$$

$$T_o(K) = (5/9)(1.0553)\left[T_{CATB}^{(°F)} + 460\right], \text{ Test Condition 2A} \tag{47}$$

$$T_o(K) = (5/9)(1.0631)\left[T_{CATB}^{(°F)} + 460\right], \text{ Test Condition 2B} \tag{48}$$

$$T_o(K) = (5/9)(1.0712)\left[T_{CATB}^{(°F)} + 460\right], \text{ Test Condition 2C} \tag{49}$$

The CONTAM II computer code (N2H4) was also used to predict species mole fractions for test conditions 2S and 2A, and these results are given in Table 31. The values given are averages over the last 20 pulses in a 25-pulse train calculation. Furthermore, the values are for a time of 90 msec into the thruster pulse, which corresponds to the time at which laser scattering and electron beam data were acquired.

Measured axial temperature variations are compared to MOCS predictions in Figs. 18 through 20 and 30, 32, 33, and 34. The Raman T_R/T_o values fall between the $\gamma = 1.2$ and $\gamma = 1.3$ predictions, and these values are always closer to the $\gamma = 1.2$ curve at the $\widehat{x} = 18.5$ position. The Raman values at $\widehat{x} = 28.5$ and the electron beam T_R/T_o values in the far field tend to move toward the $\gamma = 1.3$ curve. Furthermore, the electron beam values of T_R/T_o show a trend of decreasing temperature values in the far field as more test periods were completed.

Laser-Raman measured values of total number density normalized by combustion chamber number density are shown in Fig. 21 compared to MOCS predictions. The measured values are in fair agreement with the predictions; however, the values are widely scattered as a result of the large dependence on the measured NH_3 number density, which is the least reliable of the laser-Raman number density measurements (see Section 4.7).

The variation of the hydrogen-to-nitrogen mole fraction ratio with test condition is shown in Fig. 22, and a decrease with combustion chamber pressure is evident. This implies a decreasing plume γ with increasing combustion chamber pressure (or thrust), and this is verified by the averaged values of $n(H_2)/n(N_2)$ and γ given in Table 8. The γ values were obtained using Fig. 90. The $n(H_2)/n(N_2)$ values give a plume γ of 1.24 for the plume near-field region, whereas the CONTAM II code predicts $\gamma \approx 1.2$ in the near

field. Also shown in Fig. 22 is the variation of nitrogen mole fraction with combustion chamber pressure, and it can be seen that the nitrogen mole fraction is approximately 0.20 on the average, which is to be compared to CONTAM II predictions of $\approx$ 0.30.

Using both electron beam and laser-Raman measurements of $n(N_2)$ and T_R, one can compute a graphical variation of the static pressure P with T_R (or T) for the test condition 2A plume expansion. The result is shown in Fig. 91, and, using the isentropic relation $PT^{\gamma/1-\gamma}$ = constant, a simple computation yields γ = 1.24 for the overall plume expansion.

Averaged values of ammonia-to-nitrogen mole fraction ratios based on results from Table 8 give $n(NH_3)/n(N_2)$ $\approx$ 2.2, and this value can be compared to the mass spectrometer values given in Table 14 which are, on the average, $n(NH_3)/n(N_2)$ = 1.8 for the 10th through 25th thruster pulses. Again, it should be noted that $n(NH_3)$ values determined by Raman scattering have an uncertainty of $\pm$50 percent, which is the highest uncertainty of all laser-Raman values. Furthermore, the mass spectrometer measurements are made in the far-field plume, and NH_3 condensation is almost certain to occur to some degree before the mass spectrometer location is reached by the molecules.

Radial variations of rotational temperature were obtained only with the electron beam technique, and these variations are plotted in Figs. 31 and 35. The most interesting aspect of these plots is the off-axis temperature peaks, which could possibly be an indication of off-axis plume condensation as observed in Ref. 5.

Axial variations of nitrogen number density determined by both laser-Raman and electron beam measurements are shown in Figs. 36 and 39. The electron beam results show agreement with the γ = 1.2 MOCS predictions for $\hat{x}$ > 100 when the N_2 mole fraction is assumed to be 0.3, as predicted by CONTAM II; however, for $\hat{x}$ < 100 both electron beam and laser-Raman values fall well below the γ = 1.2 MOCS prediction. With the assumption of an N_2 mole fraction $\approx$ 0.2 (see Fig. 36), the measurements for $\hat{x}$ < 100 agree fairly well with the γ = 1.2 MOCS prediction; however, the measured values for $\hat{x}$ > 100 then show a tendency toward the γ = 1.3 prediction, but this is consistent with the trend of the temperature measurements. Radial surveys of $n(N_2)$ by the electron beam technique are shown in Figs. 37, 38, and 41. An isodensity map for $n(N_2)$ as determined from the radial surveys is shown in Fig. 51.

Variations of $n(N_2)$ with combustion chamber pressure show a general linear trend as seen in Figs. 42 through 44. Variation of rotational temperature with combustion

chamber pressure as determined with the electron beam technique and shown in Fig. 45 depicts a steady decrease with comubstion chamber pressure until test condition 2C is reached and a sudden increase in temperature is observed. The only explanation for this behavior that can be offered at present is that increased condensation in the plume has released sufficient heat to cause an increase in plume static temperature (Ref. 5).

Electron beam measurements of $n(N_2)$ and T_R in the backflow region are shown in Figs. 52 and 53. A word of caution is applicable to these measurements, because the region of the RVC behind the thruster was not cryogenically pumped, and the quantitative effect of the background gas is not known.

The axial variations of normalized Rayleigh/Mie scattering intensity, $\widehat{I}_{Ry1}$, are shown in Figs. 23, 25, and 26. Comparison with the MOCS predictions of n/n_0 as shown in Fig. 36 shows that the $\widehat{I}_{Ry1}$ values are no less than approximately two orders of magnitude greater than the n/n_0 predictions. However, the axial variations of $\widehat{I}_{Ry1}$ do show the same trend as that exhibited by the MOCS predictions of n/n_0. Figure 25 is particularly interesting, because for an approximately constant chamber pressure an order of magnitude increase in $\widehat{I}_{Ry1}$ is observed as the initial catalyst bed temperature is decreased from 589 to 367 K. Quite probably liquid fuel is being observed. Furthermore, as shown in Fig. 28, at an initial catalyst bed temperature of 478 K, the $\widehat{I}_{Ry1}$ values increase with an increase in n_0; as n_0 increased by a factor of approximately 1.4, the $\widehat{I}_{Ry1}$ increased by a factor of 1.6, which may possibly be the result of NH_3 condensation.

Radial variations of $\widehat{I}_{Ry1}$ are shown in Figs. 24 and 27. The most interesting feature is the extreme narrowness of the distribution as compared to the measured $n(N_2)$ distribution determined by the electron beam and normalized to the axial centerline value of $\widehat{I}_{Ry1}$ as shown in Fig. 24. Whatever the cause, the extremely high values of $\widehat{I}_{Ry1}$ are concentrated on the plume axial centerline.

Figure 29 shows a variation of $\widehat{I}_{Ry1}$ with test period for test condition 2A and axial position $\widehat{x}$ = 28.5. $\widehat{I}_{Ry1}$ definitely showed an accelerating increase with thruster use, and when the thruster "catastrophe" was observed in test period 15 the Rayliegh/Mie scattering was so intense that the detector was saturated. Furthermore, the passage of the laser beam through the plume was quite readily observed with the eye, and this was not possible prior to the "catastrophe." Electron beam measurements of temperature and nitrogen number density showed no significant changes as a result of the "catastrophe"; this can be seen by comparing the results of Figs. 39 and 40 and Figs. 34 and 32.

7.2 MASS SPECTROMETER RESULTS

The measured ammonia-to-nitrogen mole fraction ratios are given in Table 14 for pulses 1, 5, 10, 15, and 25 for eight test conditions. The results indicate a decreasing ratio with pulse number, which is the result of an increasing ammonia dissociation (see Table 15) caused by thruster heating. The first pulse data are somewhat inconsistent due to the large concentrations of hydrazine and generally erratic behavior of the thruster during first pulses. The average ammonia dissociation fraction for pulses 10 through 15 is 0.293, which gives a plume γ of 1.217 in the far-field region. Intrapulse variation of $[NH_3]/[N_2]$ is shown in Fig. 55 for test condition 2A, and these data represent an average over pulse numbers 11 through 25. The same trend of decreasing ratio is observed as the pulse duration increases. Furthermore, the results in Fig. 55 are consistent with the values in Table 14 which were taken at 0.090 sec into the pulse.

Figures 56 through 59 show mole fractions of the five major plume species as a function of pulse number. The most noteworthy aspects are the large mole fraction of N_2H_4 present during pulse one of each case and the small number of pulses necessary to reduce N_2H_4 significantly. It is obvious from these figures that hydrazine is present primarily during the first few pulses of a pulse sequence and that the percentage increases with thrust level. The N_2 mole fractions are in good agreement with laser-Raman and electron beam measurements, but there is a glaring disagreement between laser-Raman and mass spectrometer determinations of H_2 mole fraction. The mass spectrometer hydrogen-to-nitrogen mole fraction ratio is approximately a factor of three lower than the laser-Raman values. It should be remembered, however, that H_2 measurements taken with the mass spectrometer generally have a poor signal-to-noise ratio because of the high background noise associated with large quantities of H_2 absorbed in the CO_2 frost, as pointed out in Section 5.3.

The data of Fig. 59 are of particular interest since they present an opportunity to observe the effects of initial catalyst bed temperature. These data are consistent with the data of the previous figures but are presented as ratios since hydrogen data were not available to permit calculation of mole fractions. The initial catalyst bed temperature is seen to have a major effect on the first pulse; that is, the hydrazine concentration is greatly reduced with increased temperature. After the first few pulses a major difference in thruster behavior is not observed as a result of higher initial bed temperature.

Data showing species variation within a pulse were obtained for test condition 2A, and these data are shown in Figs. 60 and 61 for pulses 1 and 25, respectively. The data

demonstrate the combination of pressure buildup and heating effects within the combustion chamber. Again, the data are not presented in terms of mole fractions since hydrogen data were not obtained. The N_2H_4 signal is seen to be very large for pulse number one as for all other data presented previously. The hydrazine concentration does decrease as the interstitial temperature increases during the remainder of the pulse, and the hydrazine concentration is essentially zero for pulse number 25. In addition to the hydrazine decrease with pulse time, the increased dissociation of ammonia and the resulting increases in N_2 and H_2 can be observed in Figs. 60 and 61. Since a direct experimental determination of interstitial temperature was not made, no attempt was made to correlate the species data with temperature and pressure data.

Since the amount of hydrazine in the plume was of significant interest, a calibration sequence was run in which the amount of hydrazine at 0.090 sec into the pulse was recorded as a function of valve inlet pressure. The results are shown in Fig. 62 for the first thruster pulse. The change in slope of the apparently linear variation with inlet pressure (and hence thrust level) was observed for more than the one calibration sequence shown, but no explanation can be offered at this time.

7.3 QCM RESULTS

Figures 69 and 70 show the variation of the mass deposition rate, $\dot{m}$, detected by the QCM for a range of surface temperatures, T_{QCM}, at test conditions 2A and 2S, and the variation of $\dot{m}$ with both T_{QCM} and thruster pulse number is obvious. Operation of the QCM at various temperatures enabled a qualitative characterization of the deposit species. Figure 67 indicates that for $144\ K < T_{QCM} < 160\ K$ only N_2H_4, H_2O, and trace impurities should be permanently deposited. The results shown in Figs. 69 and 70 show that as T_{QCM} decreased from 130 K to approximately 110 K some ammonia begins to be permanently deposited and drastically increases the mass deposition rate.

Further examination of Figs. 69 and 70 reveals several additional properties of the mass deposition. The first few thruster pulses exhibit extremely large deposition rates for the temperature region where a permanent deposition of hydrazine, water, and other trace impurities is expected. After approximately ten thruster pulses a steady state is reached with respect to mass deposition, and this rate is nearly an order of magnitude less than that for the first pulse. When the T_{QCM} is adjusted so that in addition to the aforementioned species some NH_3 is permanently deposited, the mass deposition rate becomes more uniform throughout the pulse sequence.

Figures 71 through 76 show the variation of $\dot{m}$ with the different engine test conditions. Figures 71 and 72 demonstrate the variation of mass flux with thrust level for $T_{QCM} = 161$ and 144 K, respectively, for an initial catalyst bed temperature of 477 K (400°F). The mass deposition rate, as well as the number of pulses required to reach the steady deposition rate, is observed to increase with increasing engine thrust. Figure 73 shows the variation of $\dot{m}$ with thruster pulse number for three catalyst bed temperatures. For these data the thruster inlet pressure was maintained at 17 atm (230 psia) and T_{QCM} = 143 K. The deposition rate is observed to increase with decreasing catalyst bed temperature throughout the pulse sequence, and the most striking difference occurs in the first few thruster pulses. The number of pulses required to reach a steady deposition rate is also seen to decrease with increasing catalyst bed temperature.

Figures 74 and 75 show the variation of $\dot{m}$ with thrust level for $T_{QCM} = 144$ K and initial catalyst bed temperatures of 366 K (200°F) and 589 K (600°F), respectively. Again the overall increase in mass deposition with decreasing initial catalyst bed temperature can be observed.

Figure 76 depicts the variation of $\dot{m}$ with pulse number over a wide range of thruster inlet pressure. The results of Fig. 76 are used to compute the average of the mass deposition rate over the last five thruster pulses, $\langle\dot{m}\rangle_5$, and Figs. 77 and 78 show the variation of $\langle\dot{m}\rangle_5$ with inlet pressure. Figure 78 demonstrates the nearly linear variation of $\langle\dot{m}\rangle_5$ with inlet pressure.

Figures 79 through 82 present normalized mass deposition rates as functions of thruster inlet pressure. The deposition rates in Fig. 79 were normalized to the $\langle\dot{m}\rangle_5$ value at test condition 2A, with T_{QCM} = 104 K. It can be observed that both normalized first pulse rates and $\langle\dot{m}\rangle_5$ values are linear with inlet pressure. Figure 80 presents first pulse deposition rates normalized to $\dot{m}$ at test condition 3A for T_{QCM} = 144 K. The linear variation with inlet pressure is again evident, as is the nearly factor-of-two increase in mass deposition when initial catalyst bed temperature is changed from 589 K (600° F) to 366 K (200°F).

Figure 81 presents data similar to those of Fig. 79, but T_{QCM} = 144 K and the deposition rates are normalized to $\langle\dot{m}\rangle_5$ at test condition 2S. When Fig. 81 is compared to Fig. 79, the dramatic increase in the ratio of first pulse rates to $\langle\dot{m}\rangle_5$ values when T_{QCM} is increased to 144 K is quite evident.

Figure 82 also presents mass deposition rates normalized to $<\dot{m}>_s$ at test condition 2S for T_{QCM} = 144 K. However, the results of Fig. 82 were obtained on the axial centerline. Compared to the off-axis data of Fig. 81 the $\dot{m}_1/<\dot{m}>_s$ values are markedly decreased as a result of the on-axis position of the QCM.

Figure 83 shows average mass deposition rates, $<\dot{m}>_s$, as a function of inlet pressure for three values of T_{QCM}. Again, the linear variation with inlet pressure is evident as well as the large increase in mass deposition when T_{QCM} is lowered to 104 K. Figure 84 also presents $<\dot{m}>_s$ values versus inlet pressure at two different off-axis positions and, thereby, demonstrates the linear pressure behavior at different off-axis positions.

Figure 85 presents $<\dot{m}>_s$ and $\dot{m}_1/<\dot{m}>_s$ values as a function of initial catalyst bed temperature. The $<\dot{m}>_s$ values are shown to decrease with increasing catalyst bed temperature as seen previously (Fig. 73, for example). Furthermore, it is observed in Fig. 85 that the first-pulse deposition rates are much more dependent on initial catalyst bed temperature than the steady deposition rate values.

Figure 86 presents first pulse mass deposition rates normalized to $\dot{m}_1$ at test condition 3A for T_{QCM} = 144 K as a function of initial catalyst bed temperature for two T_{QCM} values. At T_{CATB} = 589 K (600°F) there is little difference in deposition rates; however, as T_{CATB} is lowered, the mass deposition for T_{QCM} = 144 K is significantly more than that for T_{QCM} = 170 K.

Figure 88 is a presentation of average measured mass deposition rates as a function of T_{QCM}. The average rates are normalized by $<\dot{m}>_s$ at T_{QCM} = 144 K. For comparison purposes prediction of mass deposition rate by CONTAM II from Ref. 18 is shown as well as values measured by JPL (Ref. 18). Predictions are also presented using the method proposed by Davis and Wax (Ref. 18). For these predictions the mole fractions generated by CONTAM II and given in Table 31 were used, and a water mole fraction of 0.005 was assumed. The experiments reported here show a considerably higher mass deposition than either that measured by JPL or that predicted by CONTAM for T_{QCM} < 160 K. However, the prediction method of Davis and Wax gives results in close agreement with the results of these experiments for T_{QCM} > 160 K. For $T_{QCM} \leqslant$ 130 K the JPL measurements, the CONTAM II predictions, and the measurements reported herein are in fair agreement, but the predictions by the method of Davis and Wax greatly overestimate the mass deposition rate for $T_{QCM} \leqslant$ 130 K.

Averaged QCM results are presented in Table 30; that is, several sets of data with the same QCM position and temperature were averaged to give the results shown in Table

30. Predicted values using Ref. 18 are also presented, and the good agreement with measurements for $T_{QCM} > 130$ K is observed. Measured JPL values are also presented in Table 30, but these values have resulted from multiplication of the original JPL values by (10.1/0.15) to eliminate inclusion of thruster-off time and by 3.9 to account for JPL values having been determined from thruster pulse sequences of $\approx 1,000$ (Fig. B-2, Ref. 13).

Figure 89 is a plot of the angular variation of average mass flux normalized to the θ = 30-deg value. For comparison purposes the Hill-Draper relation (Ref. 41) is plotted in Fig. 89 using δ = 9.59 as was used by Baerwald in Ref. 13, and reasonable agreement is observed for the off-axis data. However, the centerline mass deposition is clearly a factor of two higher than expected on the basis of the Hill-Draper relation.

It should be noted that during the thruster "catastrophe" the QCM indicated deposition rates so large that saturation of the QCM occurred during the first few pulses of a sequence. Since the saturation occurred for $T_{QCM} \approx 160$ K, indications were that the contaminant was raw hydrazine.

7.4 THRUSTER AND RVC DATA

A very important consideration in employing an engine such as the 0.45 N (0.1-lbf) thruster considered here is the establishment of its operating condition. The thrust level of the engine is so small that it could not be effectively measured for the pulsed mode which was of primary interest. In addition, the volume of the combustion chamber is such that operation of the thruster in the pulsed mode with an attached pressure transducer could significantly alter the behavior of the engine. This, therefore, precluded the investigation of the engine exhaust properties with an attached combustion chamber pressure transducer. Hence, the engine was calibrated at the outset of the testing by installing a close-coupled, small volume, 17-atm (250 psia) Tabor pressure transducer on the combustion chamber and recording the combustion chamber pressure levels for both pulsed and steady-state firings as a function of the fuel line pressure. The fuel pressure was measured at the engine propellant valve inlet with a 34-atm (500 psia) Tabor transducer. In addition, for the steady-state firings a Viscojet® differential pressure device was employed in conjunction with a 20.4-atm (300 psid) Tabor differential pressure transducer to measure the fuel flow rate. This technique gave poor resolution for pulsed firings; therefore, fuel flow rates were measured only for steady-state firings (several seconds' duration).

The results of the original thruster calibration are shown in Fig. 92 for pulsed operation. The pressure shown in Fig. 92 is the peak chamber pressure which occurred at

any point during the 25th pulse of a sequence. The aged thruster was operated with a nominal duty cycle of 0.14 sec on and 9.86 sec off; the catalyst bed temperature was set at 477 K (400°F) prior to the first pulse. The calculated thrust is also presented in Fig. 92 for reference purposes.

After the conclusion of testing on the engine (including observance of a marked change in thruster exhaust behavior as discussed previously) a second calibration was performed to determine the extent of pressure degradation of the thruster. As can be seen in Fig. 93, the pressure calibration for the pulsed mode had changed very little, and, for all practical purposes, it could be considered unchanged. The same statement cannot be made regarding the thrust since it depends upon mass flow rate and the combustion process itself. A calculation similar to that used to establish thrust levels for Fig. 92 yielded an estimated increase in thrust level of between 2 and 5 percent for the posttest calibration with respect to the pretest calibration.

In addition to combustion chamber pressure, the temperature at the external lower wall of the catalyst bed was recorded during each pulse. Values of this temperature are given for both pretest and posttest calibration runs in Fig. 94. The lower values for the posttest data are consistent with the increased thrust levels. The mass flow measurement will be discussed in a subsequent section.

A posttest calibration of the thruster was also conducted by the engine manufacturer, but the results are not available at this time.

On the basis of the results of the calibration presented a set of thruster operating conditions was selected for investigation. In addition to the hot-pulse data, startup data for approximately the first 15 pulses before the thruster reached quasi-equilibrium were also of interest. For these pulses the initial catalyst bed temperature prior to any pulsing is significant; therefore, each hot-bed thrust level selected for investigation was examined with three different initial catalyst bed temperatures: 367 K (660°R), 478 K (860°R), and 589 K (1,060°R). The total test condition matrix is shown in Table 1.

Although it is important to know the peak pressure and thrust levels of the engine at its operating condition, the pressure pulse shape is also of significance, for the impulse bit is directly related to the instantaneous levels of pressure and mass flow. An additional desired parameter is the number of engine pulses which are required to produce an operating condition for which the bed temperature is independent of pulse number. For the nominal duty cycle of this study, 0.14 sec on/9.86 sec off, it was found that 15 pulses are required to establish this operating condition.

The pulse shape of the engine combustion chamber pressure was investigated for the baseline duty cycle by employing the close-coupled, small-volume Tabor pressure transducer in conjunction with a Visicorder oscillograph for data output. Figure 95 demonstrates the appearance of the trace for a typical pulse. The combustion chamber pressure and the valve current are both given to show the relative sequence of events. The initiation of a pulse was made by the PDP-8F minicomputer when it energized the firing relay. Relay delays caused approximately 35 msec delay in the opening of the thruster valve as indicated in Fig. 95. Once valve current began to flow, another approximately 7-msec delay ensued before any measurable pressure was recorded within the combustion chamber. A relatively slow rise time, characteristic of an aged thruster, was observed as it took approximately 80 msec to reach 90 percent of the eventual peak chamber pressure. The thrust clock, the time sequencer for data taking, was obtained from the waveform eductor and was initiated at approximately 50-percent peak pressure; at approximately 90 msec into the thrust clock sequence the data gate was provided for acquisition of the electron beam and laser data; this time location corresponds closely to the beginning of the closing of the valve. The tail of the pressure curve was quite long and somewhat variable depending upon inlet pressure, but the total time for recordable combustion chamber pressure was generally about 320 msec with the thruster valve fully open for 119 msec ±1 msec from one run to the next. The pressure response unfortunately is coupled very strongly to the pressure transducer configuration; therefore, direct comparison of the chamber rise times for different transducer configurations is not recommended.

Considering the pretest calibration the temporal dependence of the pressure pulse for various engine conditions is shown in Figs. 96 through 106. Pulse numbers 1, 10, and 25 are selected for these exhibits to show the variation observed within a given pulse train. It is seen that, although the pulse shape is essentially the same for the three, pulse numbers 10 and 25 differ in magnitude from pulse number 1. It should be noted that although some pressure irregularities or fluctuations can be observed in Figs. 96 through 106, much larger pressure fluctuations or spikes were occasionally observed. Although no data are known to exist for other pulsed, aged thrusters operating with the same duty cycle as this work, similar data obtained for this same, aged engine but with a different duty cycle were provided by Hamilton-Standard; these data are shown in Fig. 107. It is seen that the pressure rise-time and operating condition value data of Fig. 107 are very similar to those of the present study; any differences which exist may be attributed, at least in part, to slight differences in pressure transducer volumes used in the two studies.

Shown in Fig. 108 is the time-related behavior of the lower wall temperature for pulse numbers 1, 10, and 25 for two different inlet pressures. The near-independence of this temperature with time during a pulse is observed.

The mass flow rates during pulsed operation were randomly monitored using a Viscojet pressure drop device. The relative changes in flow rate were discernible, but the actual measurement of mass flow rates was performed only in the steady-state mode, as discussed in the following paragraphs.

In general, the published data on thrusters are for steady-state firings of the engines. Steady state is defined for the purpose of this report as continuous firings in excess of 10 sec, although, in the strictest sense, steady conditions are not established in that time. The quasi-steady-state operation of the 0.45 N (0.1 lbf) thrust Hamilton-Standard engine was examined in some detail for comparison with other data. The combustion chamber pressure, lower-wall catalyst temperature, nozzle throat temperature, and fuel mass flow rate were measured for several valve inlet pressures. Once again it should be emphasized that, in general, this engine is not operated with a combustion chamber pressure transducer, but since the burns of long duration do reach a near "steady state," the discrepancy caused by this excess volume is small.

The behavior of the thruster for continuous firings is demonstrated in Figs. 109 and 110 for 60-sec burns during the first calibration period and in Fig. 111 for a 60-sec burn during the second calibration period. Included on the figures are Viscojet measurement results for the mass flow rate. The Viscojet was calibrated with JP-4 at the AEDC calibration laboratory prior to use in the propellant system. The calibration curve and resultant calibration equation are given in Fig. 112. Figure 109 demonstrates the general behavior of the engine for the low thrust condition with a chamber pressure of 6.46 atm (95 psia) and a lower-wall chamber temperature of approximately 920 K. Temperature data of Figs. 109 through 111 are given in terms of thermocouple voltage, but conversion to degrees Fahrenheit may be performed with the Chromel®-Alumel® calibration curve given as Fig. 113. The figures shown as 109 through 111 are tracings of the Visicorder output at the beginning and ends of the long burns. Viscojet flow rate values are given for the end of the burn since the slow-responding system did not permit time-resolved studies of flow rate to be conducted. The pressure excursions during the three runs are small; however, occasionally at ±15-percent variation in chamber pressure would occur as a sharp spike. It is not certain, but occasional noise spikes, rather than actual pressure excursions, appear to be the cause of this observed behavior. Comparison of the data presented in the three figures reveals the expected behavior, namely increased chamber pressure, mass flow rate, and chamber temperature with inlet pressure. The data for test period 17 do indicate that the thruster is not performing quite at the level of test period 10, but the results are very similar for these 60-sec firings. It should be noted that the results compare very well with results published by the Jet Propulsion Laboratory for the same model thruster. The data published by Hamilton-Standard indicate that combustion

chamber pressures are low for given inlet conditions but that mass flow rates are approximately 5 to 8 percent higher than those expected for a new engine.

Since interest existed in comparing some of the thruster data with results from previous firings of the engine in the JPL MOLSINK space chamber, the thermal environment of the engine was examined during the steady-state burns. The MOLSINK and the RVC 4- by 10-ft chamber are cryogenically pumped vacuum chambers; thus high radiation cooling rates from the engine wall can be expected. The cooling rate in the 4- by 10-ft chamber was measured by operating the Visicorder for a sufficient length of time after engine shutdown. The results of that measurement are given in Fig. 114 for a condition 2A run. It is notable that the temperature attained is somewhat higher than that for runs during period 10. Occasional deviations such as this were observed, but, as was the case for this run, no more than 5- to 6-percent deviations were normally observed. For reference purposes, a facsimile of the JPL cooling curve is included in Fig. 114.

As indicated previously, the pulse variations in thruster parameters were of major concern in this investigation. The variation with number of pulses was of concern for all the exhaust measurements since: 1) it was necessary to have knowledge of such behavior to ensure that proper interpretation was given to the exhaust data, and 2) pulse to-pulse changes were of inherent interest from a contamination point of view.

In general, it was found that the properties (catalyst temperature and pressure) of the engine for a particular pulse number during a pulse sequence were reasonably reproducible for a particular test period. The results unaccountably did vary somewhat from one test period to another. The fact that the thruster normally operates without a chamber pressure transducer prohibits detailed performance studies during each period; thus, only periodic performance checks were made. The initial performance check for pulse number behavior was conducted in test period 1, but a malfunction of the equipment required this to be repeated in test period 10.

The results for test period 10 are shown in Figs. 115 through 118 for the four inlet pressure conditions investigated. The data presented are for the combustion chamber pressure and lower wall chamber temperature, which were measured approximately 110 msec into the pulse. After pulse number twenty-five, the variation in chamber temperature is minute, and the average chamber pressure does not change. It is expected that the chamber temperatures would coalesce regardless of these starting values, and results from several 400-pulse runs bear this out.

Regarding the lower-wall temperature determination, the measurement was made with a Chromel-Alumel thermocouple attached to the outer wall of the combustion

chamber. For pulsed operation with long off-times compared to on-times it is obvious that the wall temperature will not be the same as the interstitial gas temperature. A calculation must be employed which accounts for the thermal characteristics of the thruster to predict the end-of-bed intersitial temperature based on the lower wall temperature. Since the CONTAM II computer code was being employed at AEDC during this research effort and the calculation mentioned is included in the CONTAM II code, the results of those calculations were employed to estimate interstitial temperatures. Results of calculations for conditions 2S and 2A are shown as examples in Figs. 119 and 120. The agreement between calculations and measurements is reasonably good, and these theoretical curves demonstrate the differences between T_o and T_{c1w}.

The behavior of the thruster was necessarily monitored with the combustion chamber lower-wall thermocouple, which is a good qualitative indicator for the combustion process. A marked change did occur for thruster behavior during the latter test periods, 13 through 18. A plot of typical thruster wall temperatures during the 25th pulse of a sequence as a function of test period number indicates this behavior and is shown as Fig. 121. Significant events which occurred during each test period are noted in Fig. 121 as well, including fuel refills, etc. It should be noted that Fig. 121 has an expanded temperature scale and accentuates the actual variations in T_{c1w}. During test period 15 the exhaust measurements began to indicate (for the first time) that copious quantities of fuel were present in the exhaust. The observance led to the recalibration of the engine in test period 17. During test period 17 the only major difference in thruster combustion performance was indicated in the pulse number variation of the properties. Figure 122 presents these results, and it can be noted that, although chamber temperatures are slightly reduced, the combustion chamber pressure behavior is similar to the test period 10 behavior.

Now that the performance characteristics of the engine have been presented, it is appropriate to discuss briefly the behavior of the vacuum chamber into which the plume exhausts. Cryopumping of the RVC "4 by 10" was achieved by the simultaneous use of LN_2, GHe, and LHe, the last being required to cryopump gaseous H_2. Prior to the first thruster pulse in any test period the "4 by 10" chamber pressure was on the order of 1 x 10^{-7} torr. Following the first few pulses in the initial pulse train the chamber pressure rose to the pressure range of 5 x 10^{-7} to 2 x 10^{-6} torr, which corresponds to a simulated altitude of greater than 150 km. However, as shown by Fig. 123, within approximately 50 msec after pulse initiation the pressure in the chamber increases to approximately 10^{-4} torr: this corresponds to a decrease in the simulated altitude to approximately 100 km. It is to be noted that Fig. 123 shows the temporal behavior of the chamber pressure for both high- and low-thrust cases; in addition, the variation of the chamber pressure

with pulse number is of interest. Generally, this behavior was characteristic of the performance of the chamber for several thousand engine pulses, at which time the cryopumping of H_2 ceased and an avalanche-type sublimation of H_2 occurred and the chamber pressure rose dramatically.

8.0 CONCLUSIONS AND SUMMARY

8.1 CONCLUSIONS

1. The noninterfering plume diagnostic techniques employed in this investigation were demonstrated to be applicable and valuable. The data base obtained with these systems is directly applicable to interpreting engine behavior and contamination production.

2. The electron beam/laser-Raman measurements of species number density and temperature are consistent with each other within experimental error.

3. The CONTAM II code does not adequately predict the species mole fractions in the aged thruster plume as measured by the electron beam and Raman systems.

4. Rayleigh scattering measurements indicate a significant quantity of particulates (fuel droplets or condensate, because catalyst fines were ruled out as a result of the particle-sampling experiments) in the forward-flow region and particularly concentrated near the axial centerline for all test conditions of the aged thruster. During the initial pulses of a pulse train the amount of particulates is much larger than during later pulses.

5. Measured Rayleigh scattering axial variations and measured values of $n(N_2)/n_0(N_2)$ generally follow the variation predicted by the MOCS.

6. The mass spectrometer indicates large quantities of hydrazine are in the forward-flow plume region for all operating conditions during the first few pulses of a pulse train from an aged thruster.

7. QCM mass deposition measurements also indicate significant amounts of N_2H_4 and H_2O present in the initial pulses from an aged thruster at all operating conditions.

8. Angular variation measurements (12 to 30 deg) of mass deposition rate indicate a flux distribution adequately described by the Hill-Draper approximation with $\delta = 9.59$ as found by the Jet Propulsion Laboratory.

The centerline mass flux was found to be approximately a factor of 2.5 higher than expected for a Hill-Draper distribution.

9. QCM mass deposition measurements indicate a near-linear variation with inlet pressure and therefore thrust. Initial catalyst bed temperature also has a significant effect on the mass deposition rates.

10. Electron beam, Raman, and mass spectrometer measurements of species mole fraction ratios indicate an average plume specific heat ratio of 1.25.

11. The thruster "catastrophe" observed during these experiments and the subsequent engine performance measurements indicate that copious quantities of hydrazine may be present in the forward-flow region of the exhaust plume without a serious performance degradation or "washout" of the thruster occurring.

8.2 SUMMARY AND FUTURE EXPERIMENTS

A most ambitious measurements program has been completed for a 0.45 N (0.1 lbf) monopropellant thruster. The thruster exhaust plume has been characterized by a battery of noninterfering plume diagnostic techniques.

A similar investigation for the same thruster with an unaged catalyst bed will be conducted, and the results compared to the results of the aged thruster investigation. Furthermore, experiments will be conducted on a simulated monopropellant exhaust plume, and these results will be compared to thruster measurements.

REFERENCES

1. Limbaugh, C. C., Lewis, J. W. L., Kinslow, M., et al. "Condensation of Nitrogen in a Hypersonic Nozzle Flow Field." AEDC-TR-74-31 (AD919337L), May 1974.

2. Lewis, J. W. L., Williams, W. D., Price, L. L., and Powell, H. M. "Nitrogen Condensation in a Sonic Orifice Expansion Flow." AEDC-TR-74-36 (AD783254), July 1974.

3. Lewis, J. W. L. and Williams, W. D. "Argon Condensation in Free-Jet Expansions." AEDC-TR-74-32 (AD782445), July 1974.

4. Lewis, J. W. L., Williams, W. D., and Powell, H. M. "Laser Diagnostics of a Condensing Binary Mixture Expansion Flow Field." Proceedings of Ninth International Rarefield Gas Dynamics Symposium, Vol. II, edited by M. Becker and M. Fiebig. DFVLR Press, Porz Wahn, West Germany, 1974, pp. F7.1-F7.8.

5. Lewis, J. W. L. and Williams, W. D. "Profile of an Anisentropic Nitrogen Nozzle Expansion." The Physics of Fluids, Vol. 19, No. 7, July 1976, pp. 951-959.

6. Williams, W. D. and Lewis, J. W. L. "Rotational Temperature and Number Density Measurements of N_2, O_2, CO, and CO_2 in a Hypersonic Flow Field Using Laser-Raman Spectroscopy." AEDC-TR-75-37 (ADA012877), July 1975.

7. Williams, W. D. and Lewis, J. W. L. "Rayleigh Scattering Studies of CO_2 Expansion Flow Fields." AEDC-TR-75-146 (ADA019386), December 1975.

8. Williams, W. D. and Lewis, J. W. L. "Condensation Scaling Laws for Reservoir and Nozzle Parameters and Gas Species as Determined by Laser Scattering Experiments." AEDC-TR-76-67 (ADA029733), September 1976.

9. Williams, W. D. and Lewis, J. W. L. "Experimental Study of the Reservoir Temperature Scaling of Condensation in a Conical Nozzle Flowfield." Progress in Astronautics and Aeronautics, Rarefied Gas Dynamics, Vol. 51, Part II, edited by J. Leith Potter. American Institute of Aeronautics and Astronautics, 1977.

10. Chirivella, J. E. "Operation of Small Rocket Engines in the JPL High-Vacuum Molecular Space Simulator (Molsink)," JPL Quarterly Technical Review, Vol. 3, No. 1, April 1973, pp. 1-13.

11. Chirivella, J. E. "Molecular Flux Measurements in the Back Flow Region of a Nozzle Plume." NASA-CR-133602, July 15, 1973.

12. Chirivella, J. E. "Hydrazine Engine Plume Contamination Mapping." AFRPL-TR-75-16, October 1976.

13. Baerwald, R. E. and Passamaneck, R. S. "Monopropellant Thruster Plume Contamination Measurements." AFRPL-TR-77-44, September 1977.

14. Hoffman, R. F., et al. "Plume Contamination Effects Prediction: The CONTAM Computer Program, Version II." AFRPL-TR-73-46, August 1973.

15. McCay, T. D., Powell, H. M., and Busby, M. R. "Development of a Cryogenically Pumped Mass Spectrometer Probe for Rocket Plume Studies." AEDC-TR-76-55 (ADA026136), June 1976.

16. Williams, W. D., Hornkohl, J. O., and Lewis, J. W. L. "Electron Beam Probe for a Low Density Hypersonic Wind Tunnel." AEDC-TR-71-61 (AD727004), July 1971.

17. Williams, W. D., et al. "Emitted Radiation from Special Engines (ERASE), Part III: Determination of Temperature and Species Number Density in the Exhaust Plume Utilizing Laser-Raman/Rayleigh Scattering." AEDC-TR-76-121 (ADB023356L), November 1977.

18. Davis, Larry P. and Wax, Steven G. "Verification of Contamination Predictions for Monopropellant Thrusters." AFRPL-TR-77-56, October 1977.

19. Chang, E. T., Gokcen, N. A., and Poston, T. M. "Thermodynamic Properties of Gases in Propellants: Solubility of He, N_2, and Ar in Hydrazine, Methylhydrazine, and Unsymmetrical Dimethylhydrazine." Aerospace Corp. Report No. TR-0158(3210-10)-2 (AD664885), El Segundo, California, October 1967.

20. Schwiesow, R. L. "Optimum Illumination Geometry for Laser Raman Spectroscopy." Journal of the Optical Society of America, Vol. 59, No. 10, October 1969, pp. 1285-1287.

21. Roberge, K. K. "Application of an Interference Free Method for the Measurement of Velocities in Supersonic Flows." Deutsch Luft-und Raumfahrt, Forshungsbericht 74-38, 1974.

22. Placzek, G. "The Rayleigh and Raman Scattering," translated from a publication of the Akademische Verlagsgesellschaft G.m.b.H., Leipzig, 1934, Handbuch der Radiologie, Heft 6, Teil 2, pp. 209-374.

23. Hulst, H. C. van de. Light Scattering by Small Particles. John Wiley and Sons, New York, 1957.

24. Born, M. and Wolf, E. Principles of Optics. Pergamon Press, New York, 1965 (Third Edition).

25. Kerker, M. The Scattering of Light and Other Electromagnetic Radiation. Academic Press, New York, 1969.

26. Graham, S. C., Grant, A. J., and Jones, J. M. "Transient Molecular Concentration Measurement in Turbulent Flows Using Rayleigh Light Scattering." AIAA Journal, Vol. 12, No. 8, 1974, pp. 1140-1142.

27. Kerker, M., Scheiner, P., and Cooke, D. "The Range of Validity of the Rayleigh and Thomson Limits for Lorenz-Mie Scattering." Journal of the Optical Society of America, Vol. 68, No. 1, January 1978, pp. 135-137.

28. Placzek, G. and Teller, E. "Die Rotationsstruktur der Ramanbanden Mehratomiger Molekule." Zeitschrift für Physik, Vol. 31, March 1933.

29. Sushchinskii, M. M. Raman Spectra of Molecules and Crystals. Israel Program for Scientific Translations, New York, 1972.

30. Anderson, A., Ed. The Raman Effect, Vol. 2. Marcel Dekker, Inc., New York, 1973.

31. Rushbrooke, G. S. Statistical Mechanics. Oxford University Press, London, 1964.

32. Herzberg, G. Infrared and Raman Spectra, D. Van Nostrand Company, Inc. Princeton, New Jersey, 1960.

33. Lewis, C. M. and Houston. W. V. "The Raman Effect in Ammonia and Some Other Gases." Physical Review, Vol. 44, December 1933, pp. 903-910.

34. Moynihan, P. I., and Bjorklund, R. A. "Performance Characterization Tests of Three 0.44-N (0.1-lbf) Hydrazine Catalytic Thrusters." JPL/CIT-TR-32-1584, September 1973.

35. Prozan, R. J. "Development of a Method of Characteristics Solution for Supersonic Flow of an Ideal, Frozen, or Equilibrium Reacting Gas Mixture." Lockheed Report No. HREC/0082-8 (LMSC/HREC A782535), April 1966.

36. Price, L. L. and Lewis, J. W. L. "Collisional Quenching of Atomic and Molecular Nitrogen: I. Experimental Results." AEDC-TR-75-151 (ADA018780), December 1975.

37. Bennett, R. G. and Dalby, F. W. "Experimental Determination of the Oscillator Strength of the First Negative Band of N_2." The Journal of Chemical Physics, Vol. 31, No. 2, August 1959, pp. 434-441.

38. McCay, T. D. and Powell, H. M. "Direct Mass Spectrometric Measurements in a Highly Expanded Rocket Exhaust Plume." Journal of Spacecraft and Rockets, Vol. 15, No. 3, May-June 1978, pp. 133-138.

39. Sibulkin, M. and Gallaher, W. H. "Far-Field Approximation for a Nozzle Exhausting into a Vacuum." AIAA Journal, Vol. 1, 1963, pp. 1452-1453.

40. Bartera, R. E. "Quartz Crystal Oscillator Apparatus for Measuring Mass Accretion and Temperature Independently of Each Other." JPL Patent Case 11274, Jet Propulsion Laboratory, Pasadena, California, April 29, 1975.

41. Hill, J. A. F. and Draper, J. S. "Analytical Approximation for the Flow from a Nozzle into a Vacuum." Journal of Spacecraft and Rockets, Vol. 3, No. 10, October 1966, pp. 1552-1554.

42. Klobuchar, R. L., Ahumada, J. J., Michael, J. O., and Karol, P. J. "Details of Dead Time Losses in Scaling and Multiscaling." Review of Scientific Instruments, Vol. 45, No. 9, September 1974,, pp. 1073-1076.

43. Scott, H. E., Frazine, D. F., and Lund, E. G. "Bipropellant Engine Plume Contamination Study," presented at the Joint NASA/USAF International Spacecraft Contamination Conf., USAF Academy, Colorado Springs, Colorado, March 7-9, 1978.

44. Beers, Y. Introduction to the Theory of Error. Addison-Wesley Publishing Co., Inc., Reading, Massachusetts, 1953.

45. Whitfield, D. L. "Viscous Effects in Low-Density Nozzle Flows." AEDC-TR-73-52 (AD761489) June 1973.
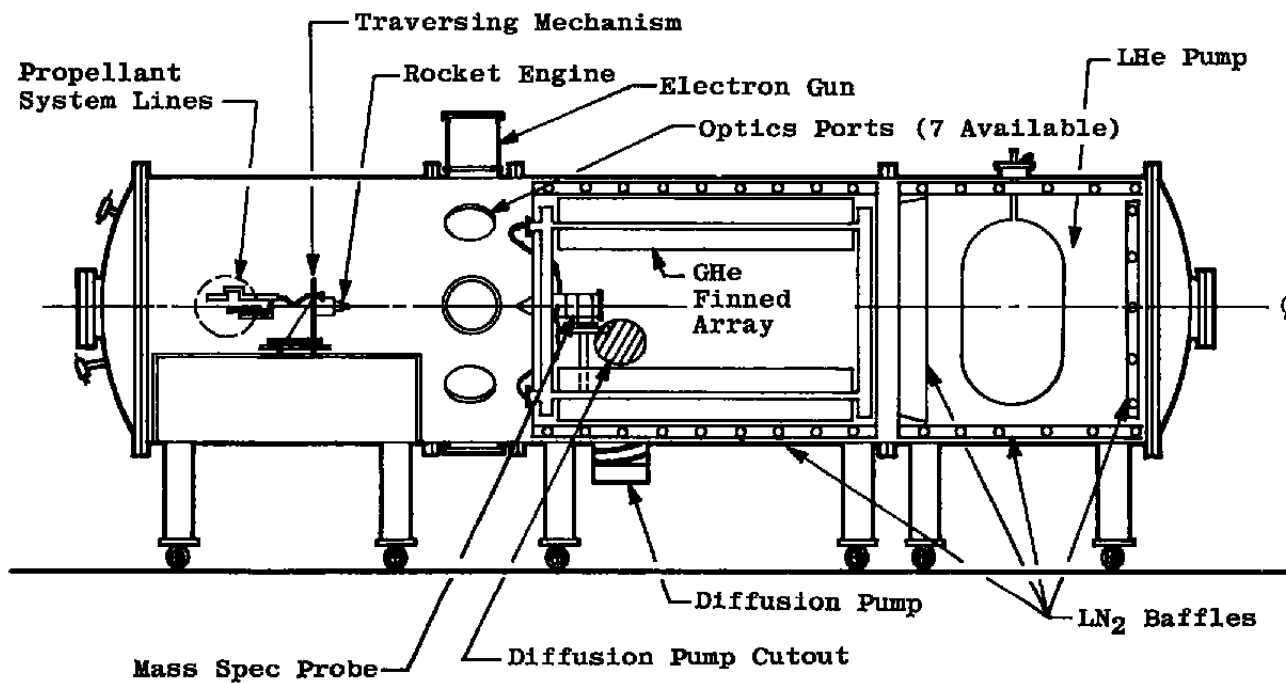
Figure 1. Thruster installation in the RVC.
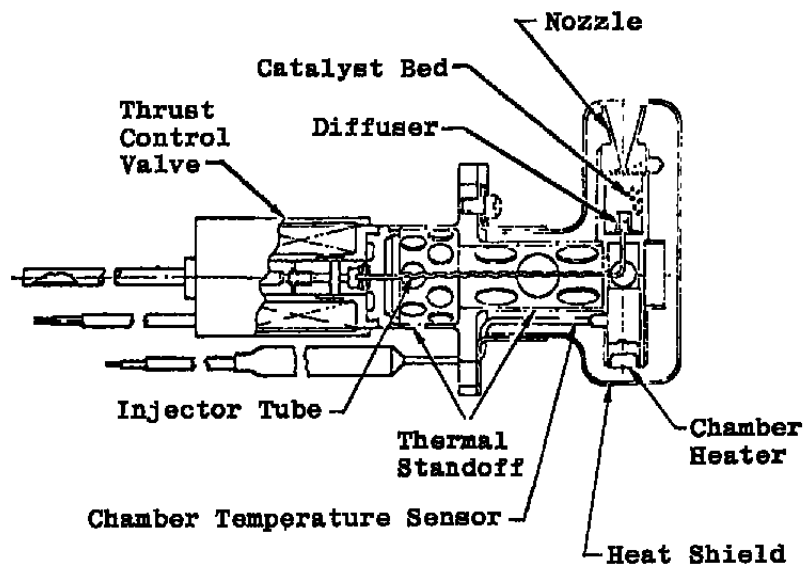
Figure 2. 0.1-lbf-thrust monopropellant engine.

Centerline of Vacuum Chamber

Up-Down Traverse Motor

All Lines Wrapped with
Heater Tape up to Valve
Inlet

Mounting
Block
of
Traverse
Mechanism

500-psia
Inlet
Pressure
Transducer

GN_2 Purge

Mounting
Bracket

Fuel

Mounting Bracket

Check
Valve

Align-
ment
Screws

Thruster Valve

Alignment Screws

5-μ
Filter

250-psia Combustion
Chamber Pressure
Transducer

Engine

Top View (Not to Scale)

Figure 3. Engine system installation schematic.
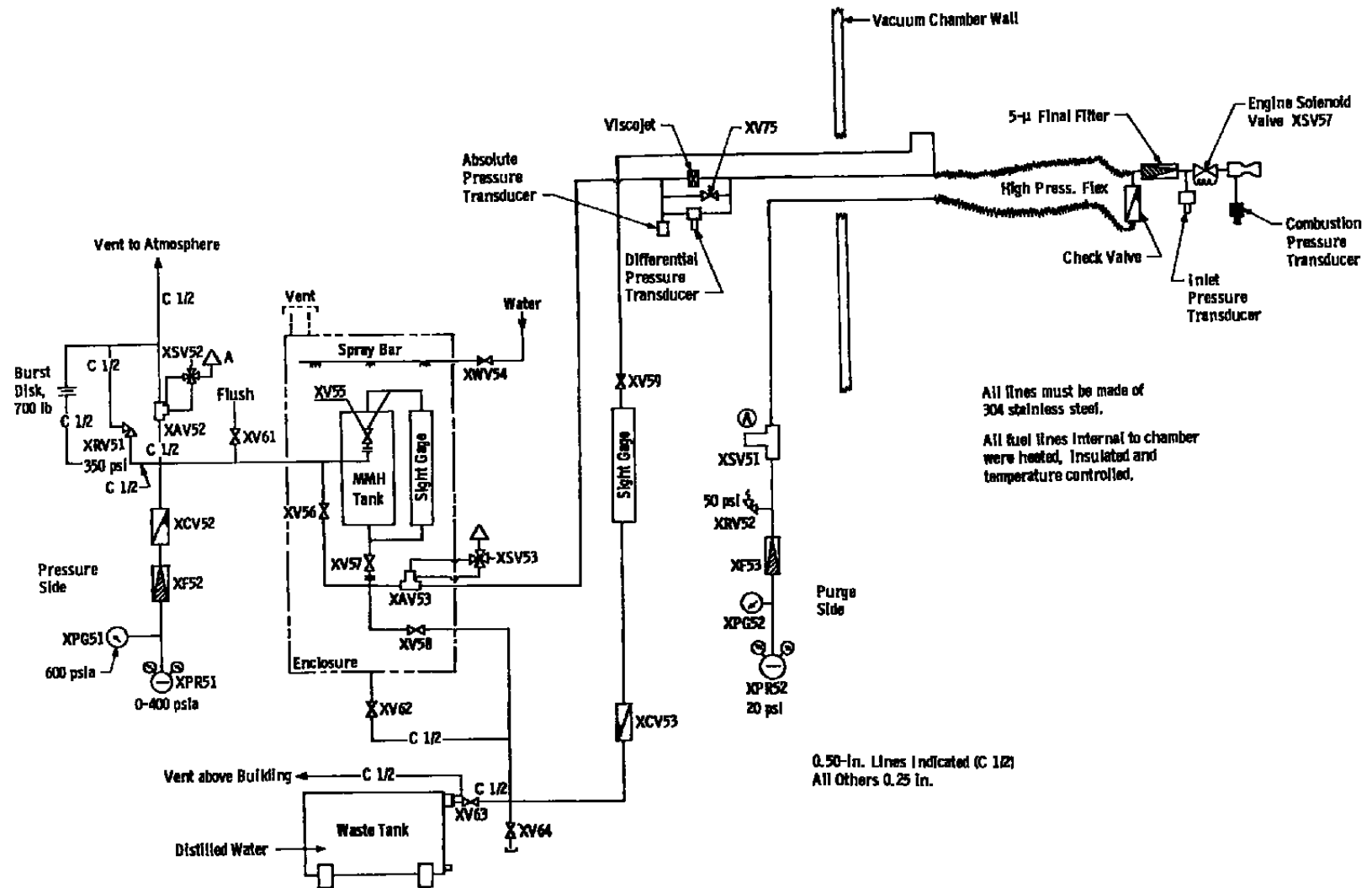
Figure 4. Hydrazine propellant system.
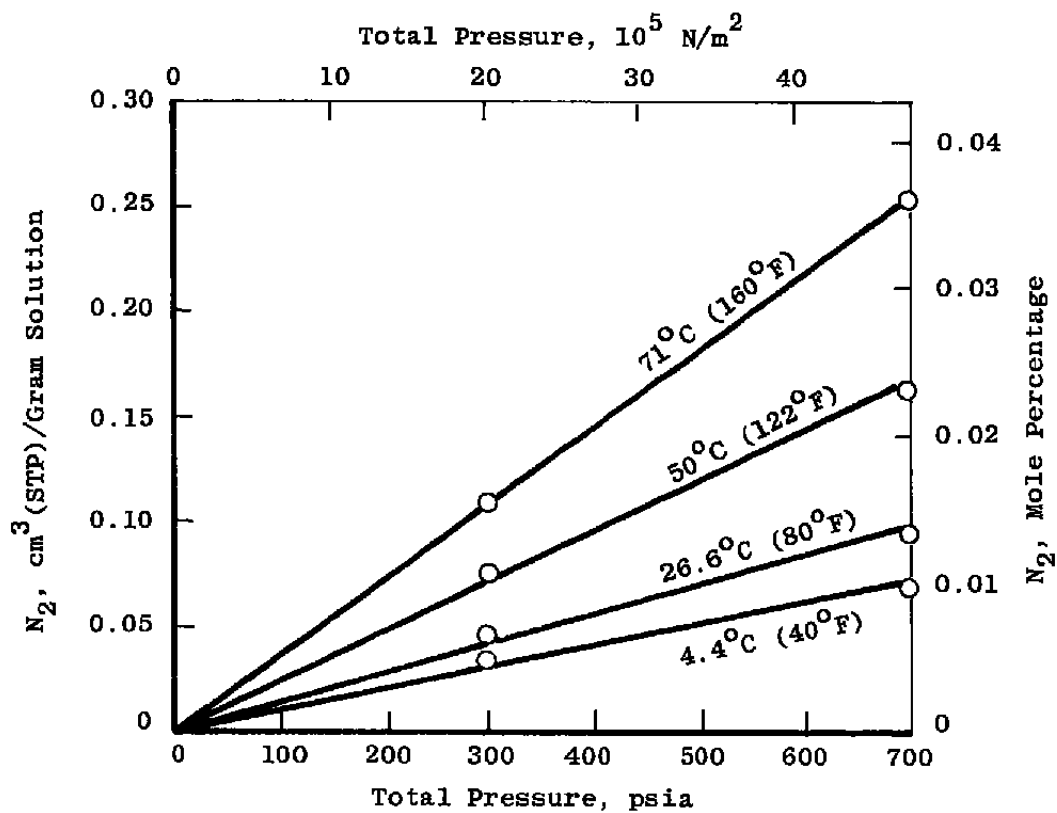
Figure 5. Quantity of N_2 in a saturated N_2-N_2H_4 solution as a function of temperature and pressure.
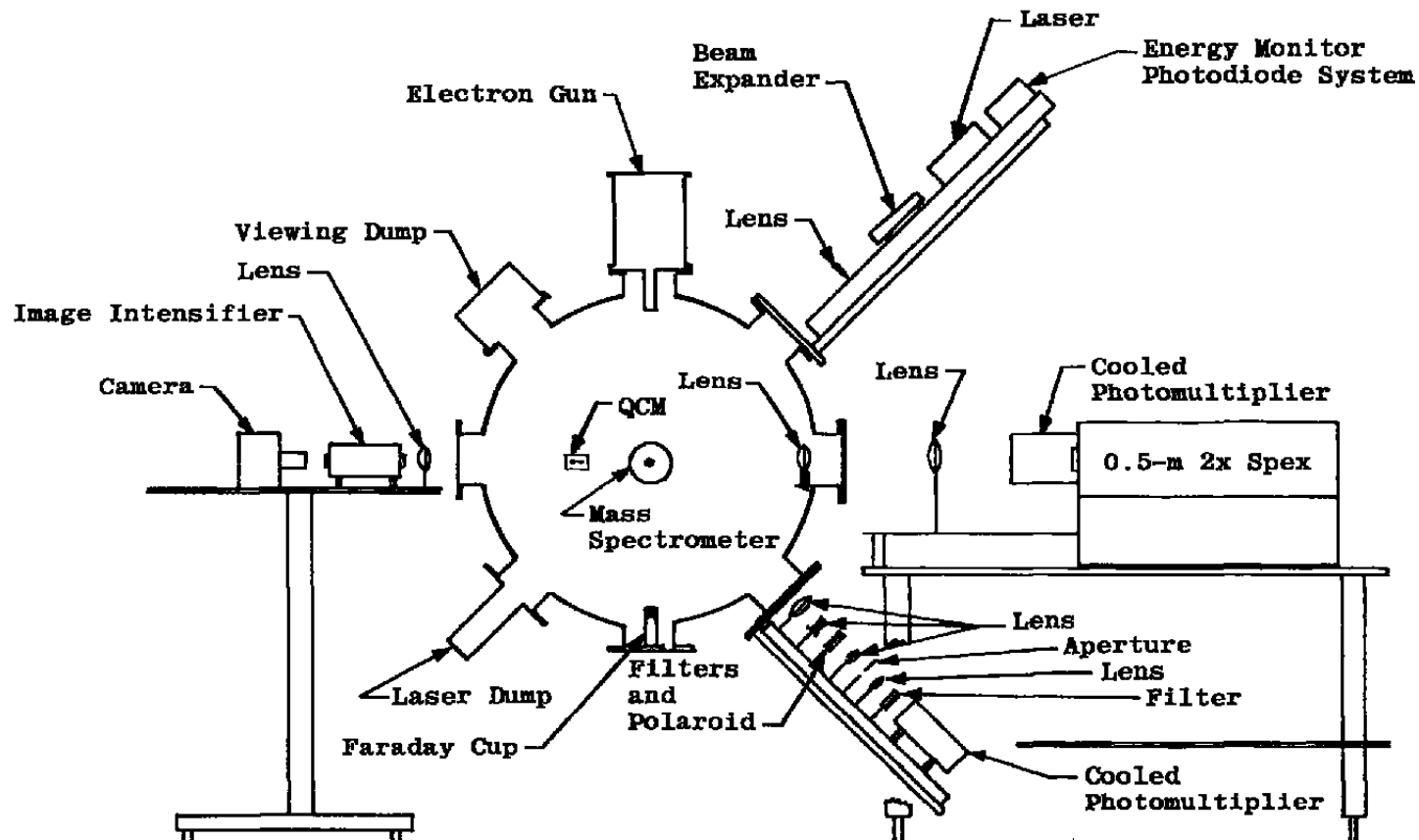
Figure 6. Experimental arrangement for special diagnostic instrumentation.
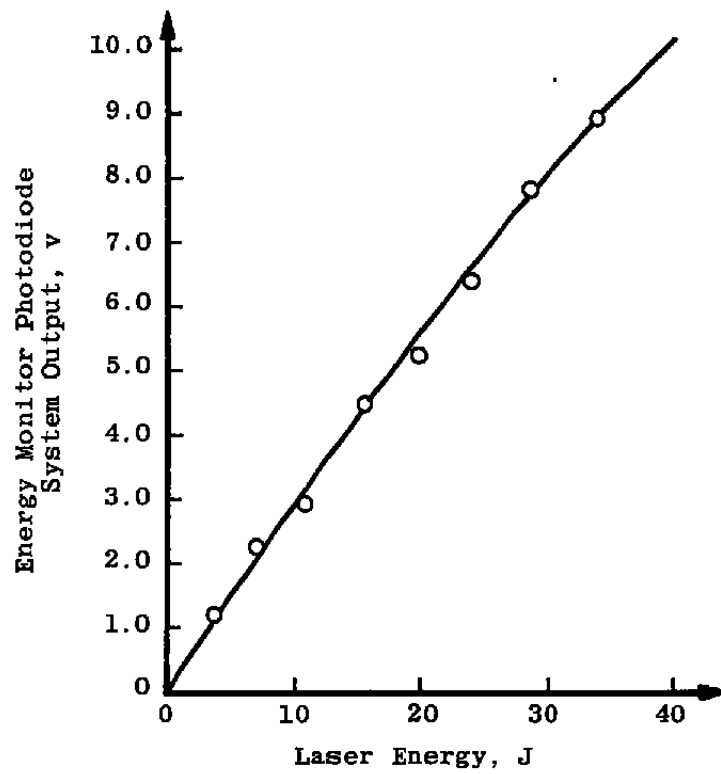
Figure 7. Typical laser energy monitor calibration.

e⁻ Beam

e⁻ Beam
Deflection
Coil

Axial
Centerline

0.1-lb
Rocket
Engine

Lens

Micro-Channel Plate
Image Intensifier

Faraday
Trough

Minolta
Electronic
Camera

Vertical
Centerline
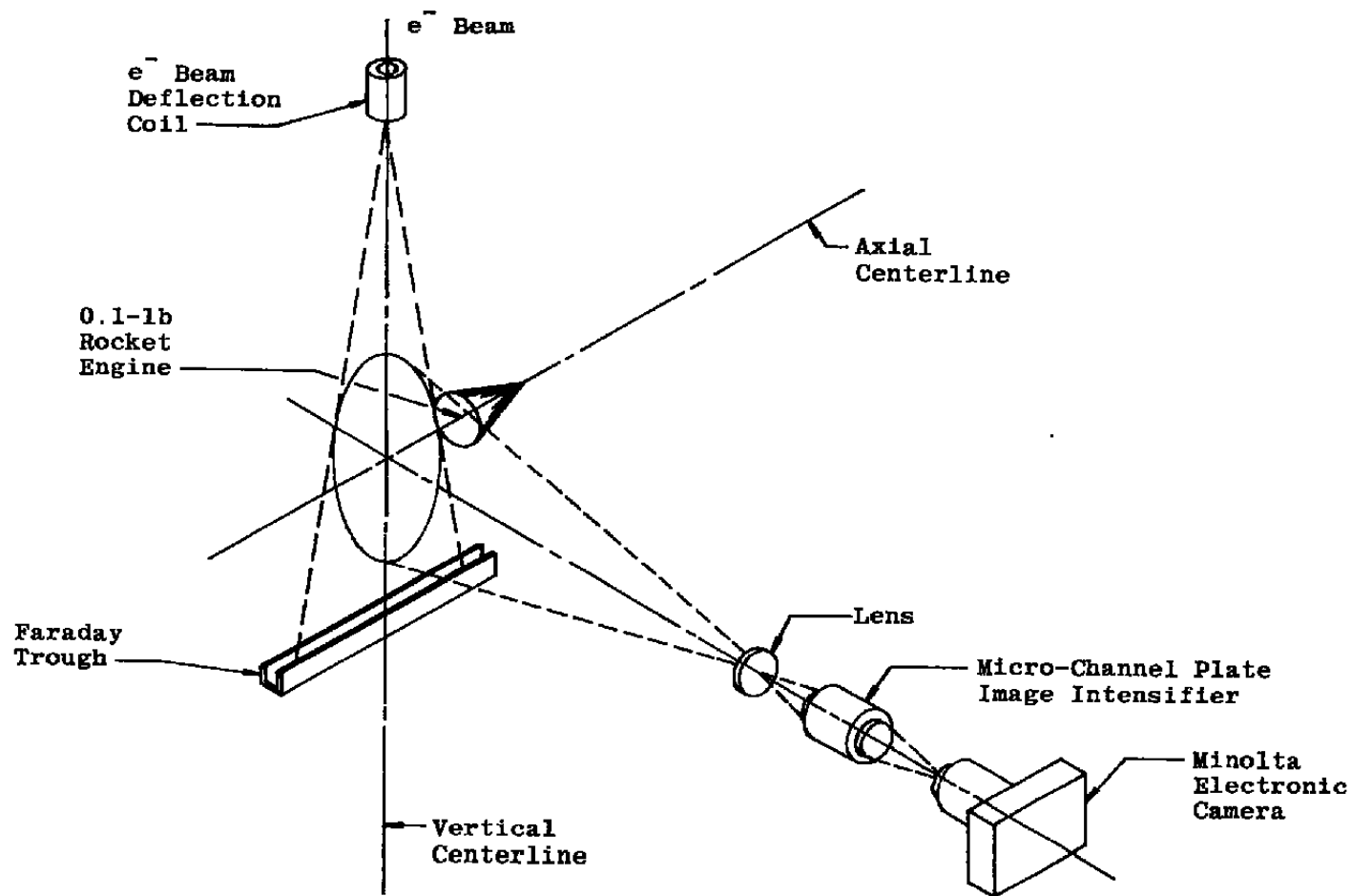
a. Intensifier system
Figure 8. Flow visualization experimental configuration.

e⁻ Beam

e⁻ Beam
Deflection Coil

Axial
Centerline

≈36 in.

0.1-lb
Thruster

Lens

Pentax
Camera

Faraday Trough

Vertical Centerline
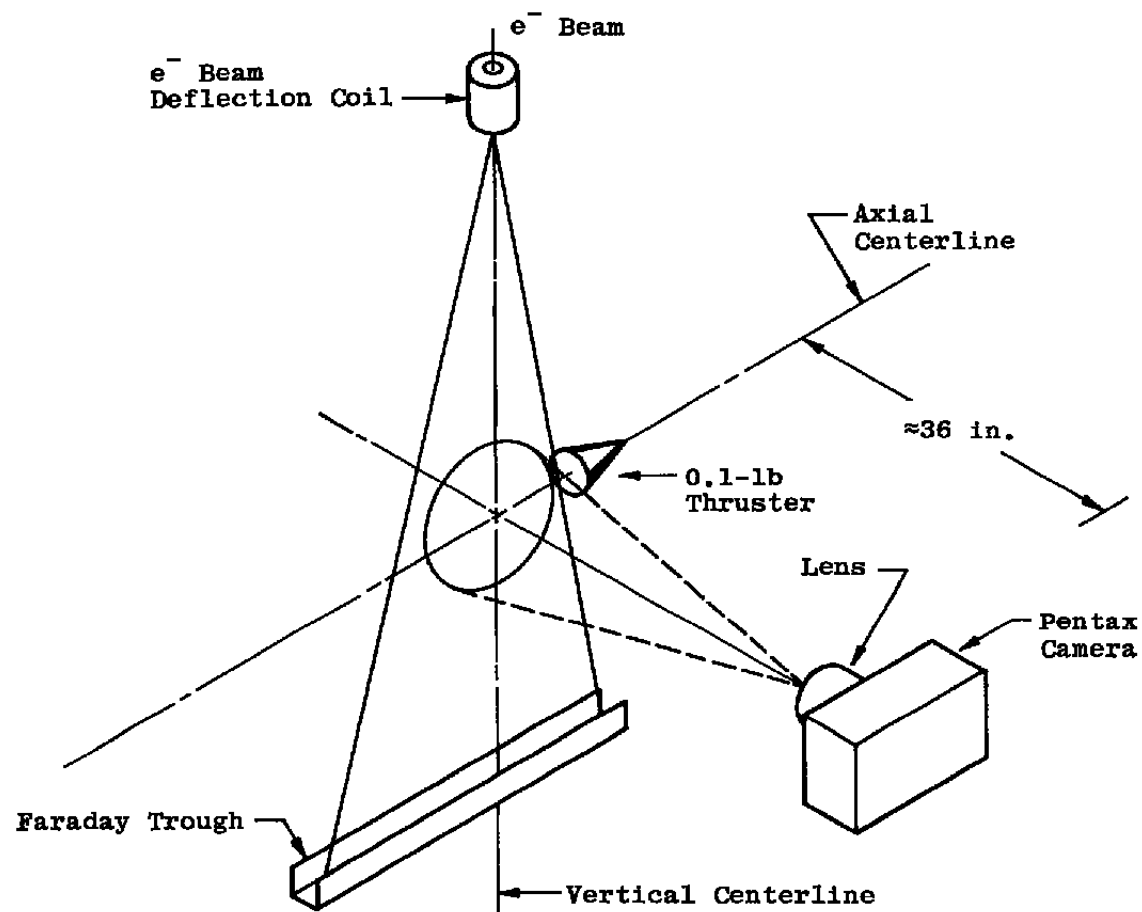
b. Camera system
Figure 8. Concluded.
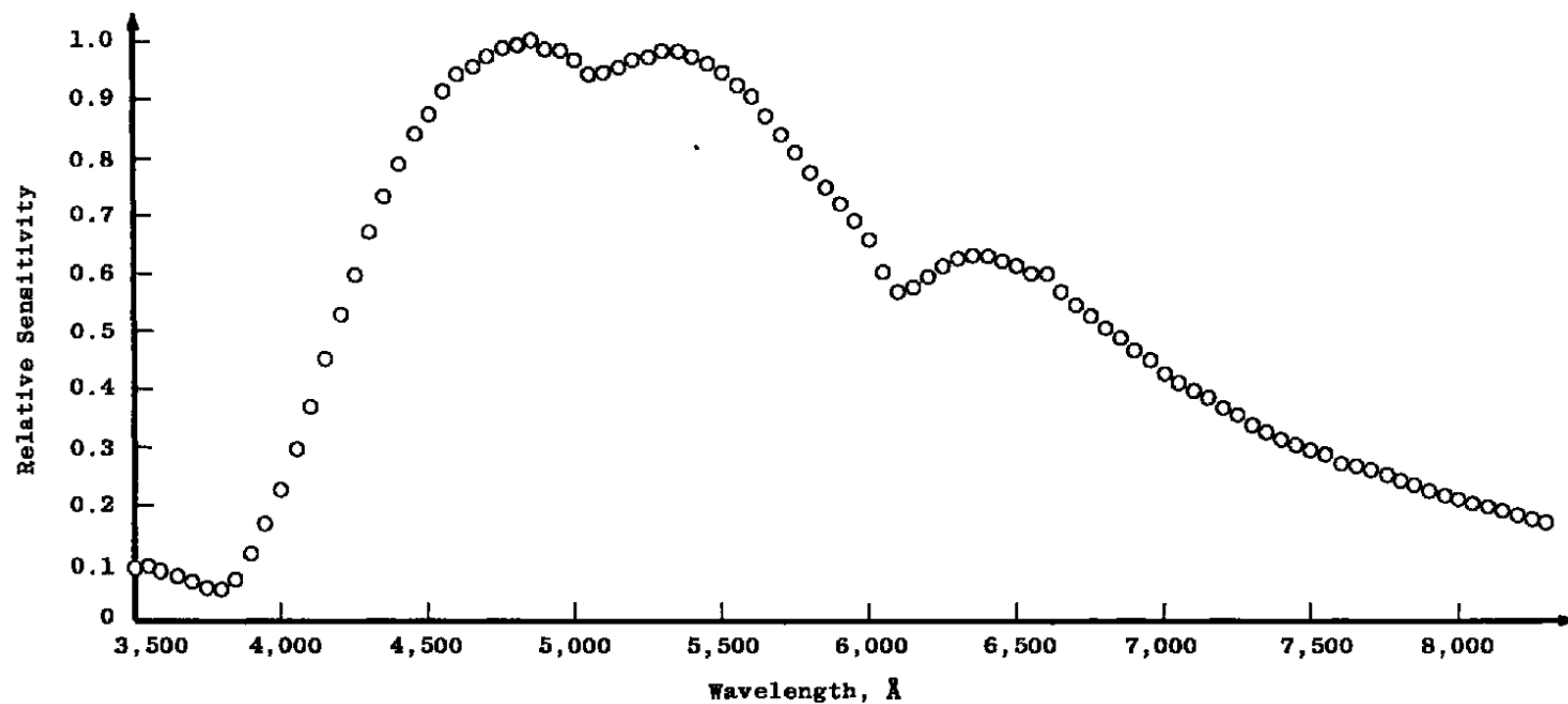
Figure 9. Spectral sensitivity calibration of spectrometer optical system.
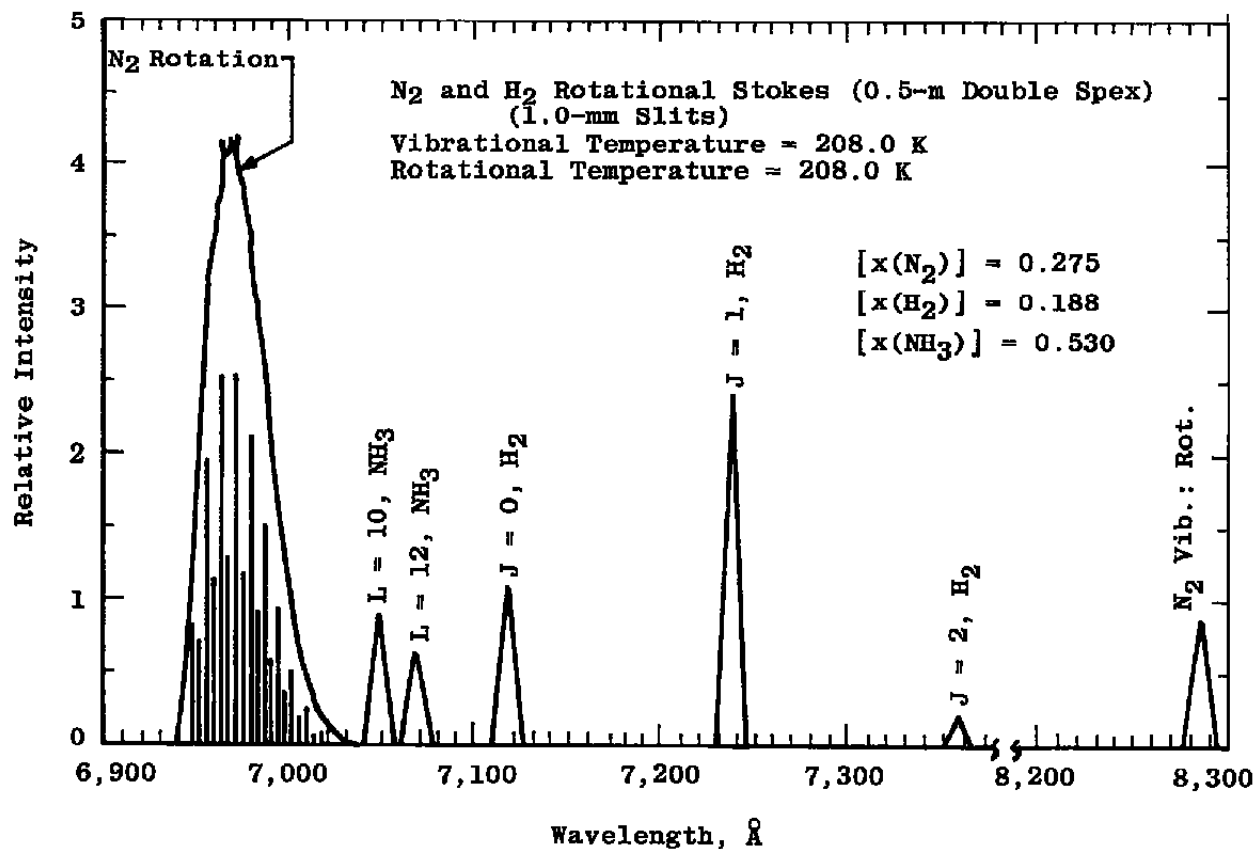
Figure 10. Raman scattering synthetic spectrum.
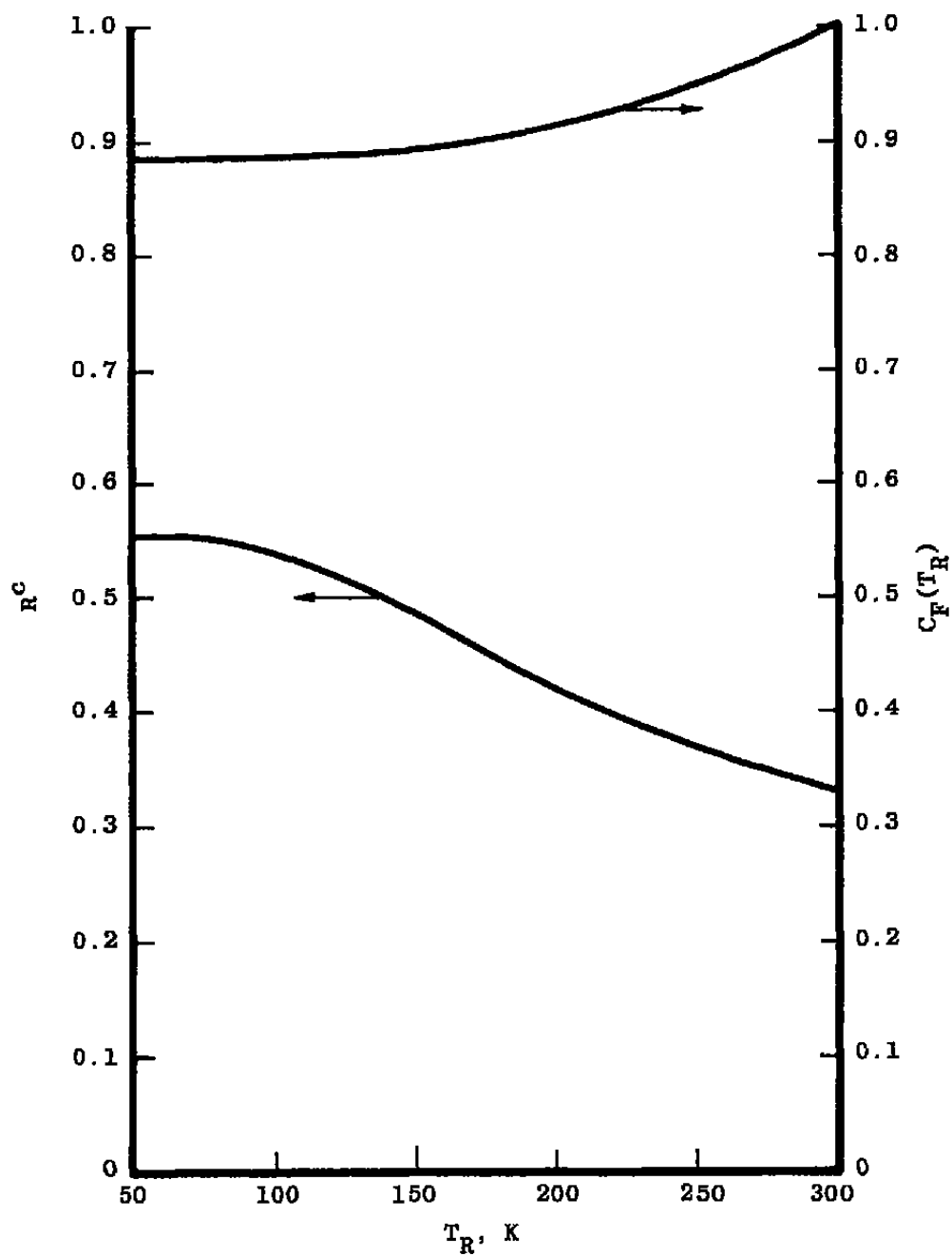
Figure 11. R^c and $C_F(T_R)$ versus T_R.

0.5-m, 2x Spex Spectrometer
200-μm by 10-mm Slits
P = 12.3 psia, T = 75°F
1-w Laser Power at 4,880 Å

Relative Intensity

$\vdash$30 cm^{-1}

0

R-Branches: 2 3 4 5 6 7 8 9 10 11 12

J = 1

λ →

S-Branches: J = 0   1   2   3   4   5   6   7   8   9   10
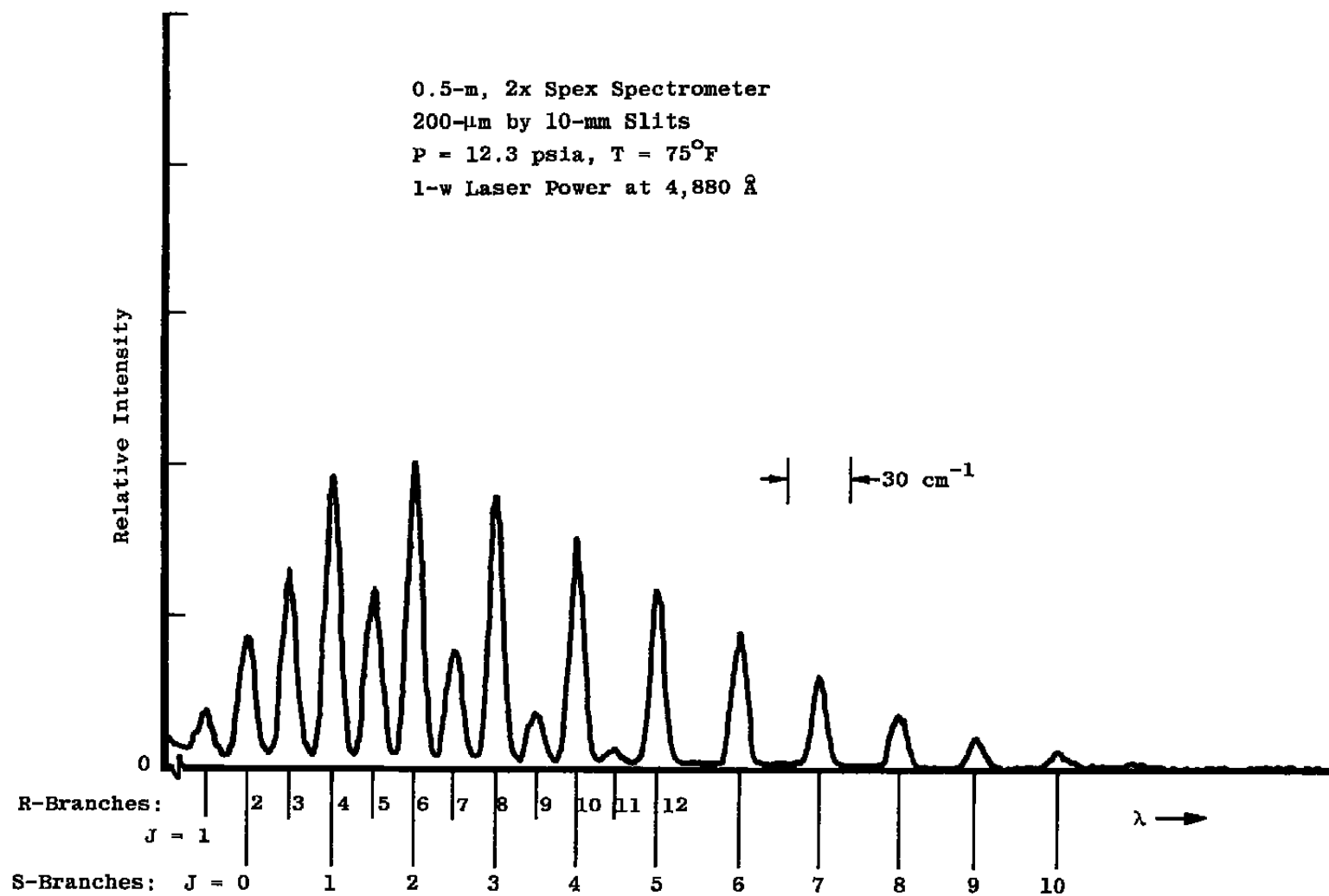
Figure 12. NH$_3$ rotational Raman spectrum.
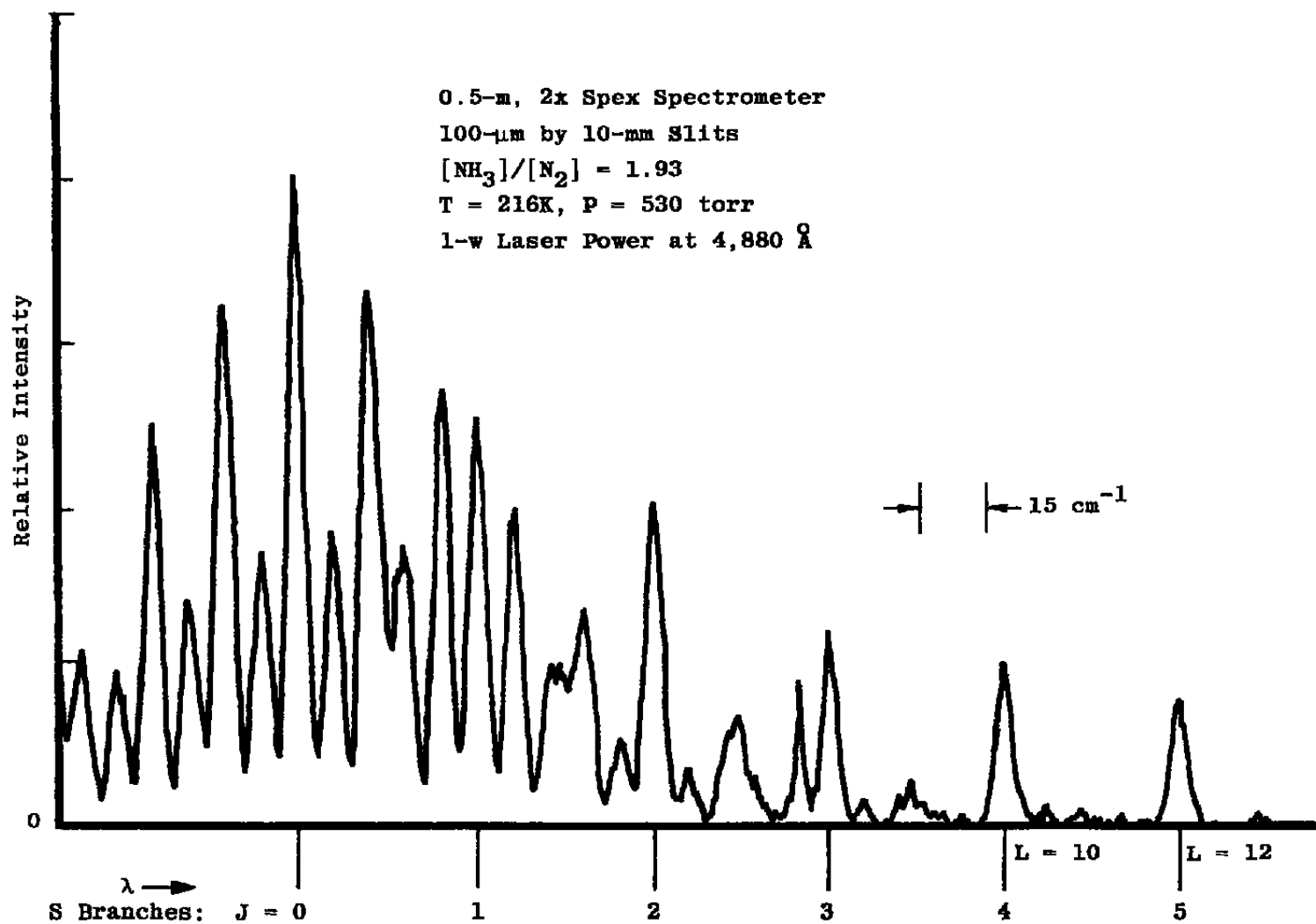
Figure 13. NH$_3$/N$_2$ rotational Raman spectrum.
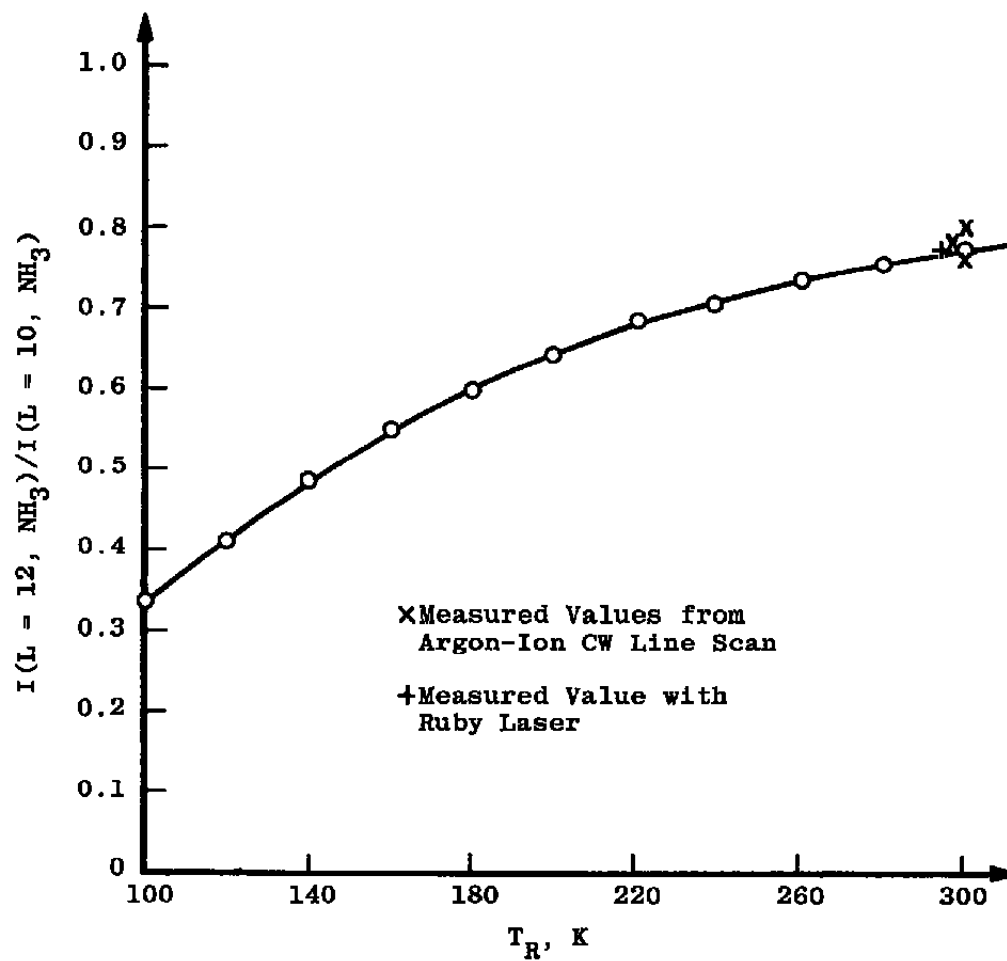
Figure 14. Calculated ratio of NH₃ rotational line intensities
versus temperature.
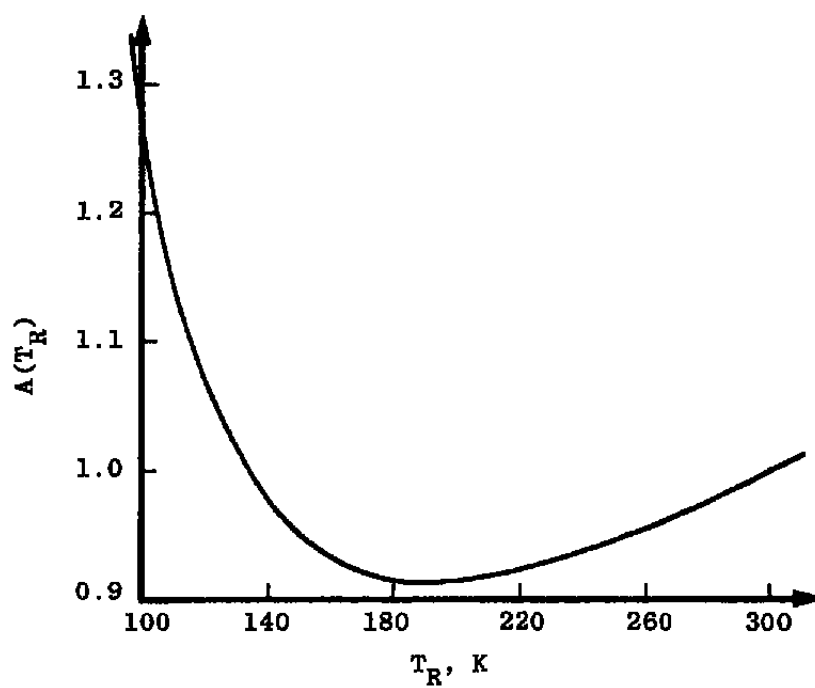
Figure 15. $A(T_R)$ versus T_R.
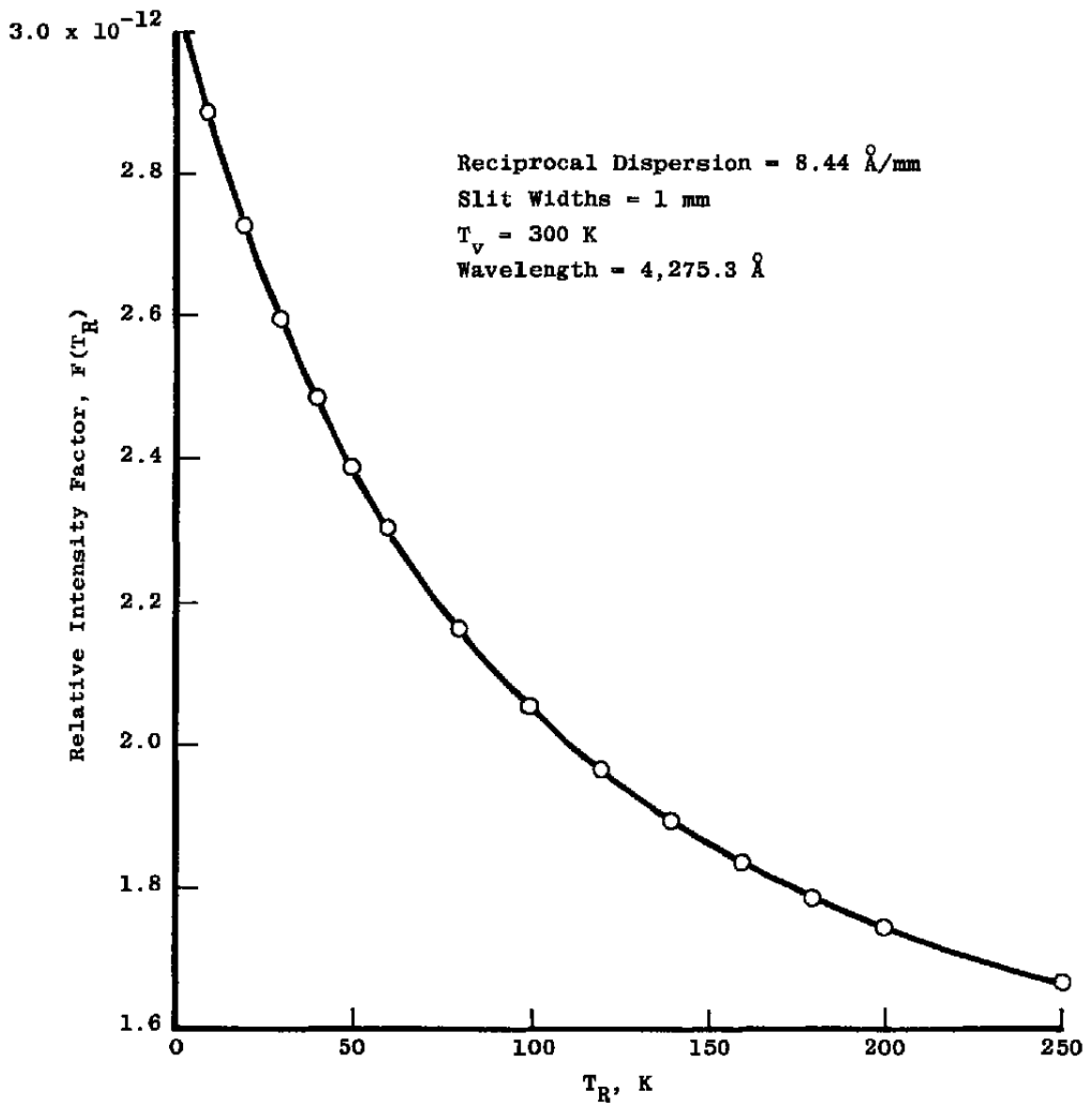
Figure 16. N_2^+ (1⁻)(0,1) band intensity at 4,275.3 Å.
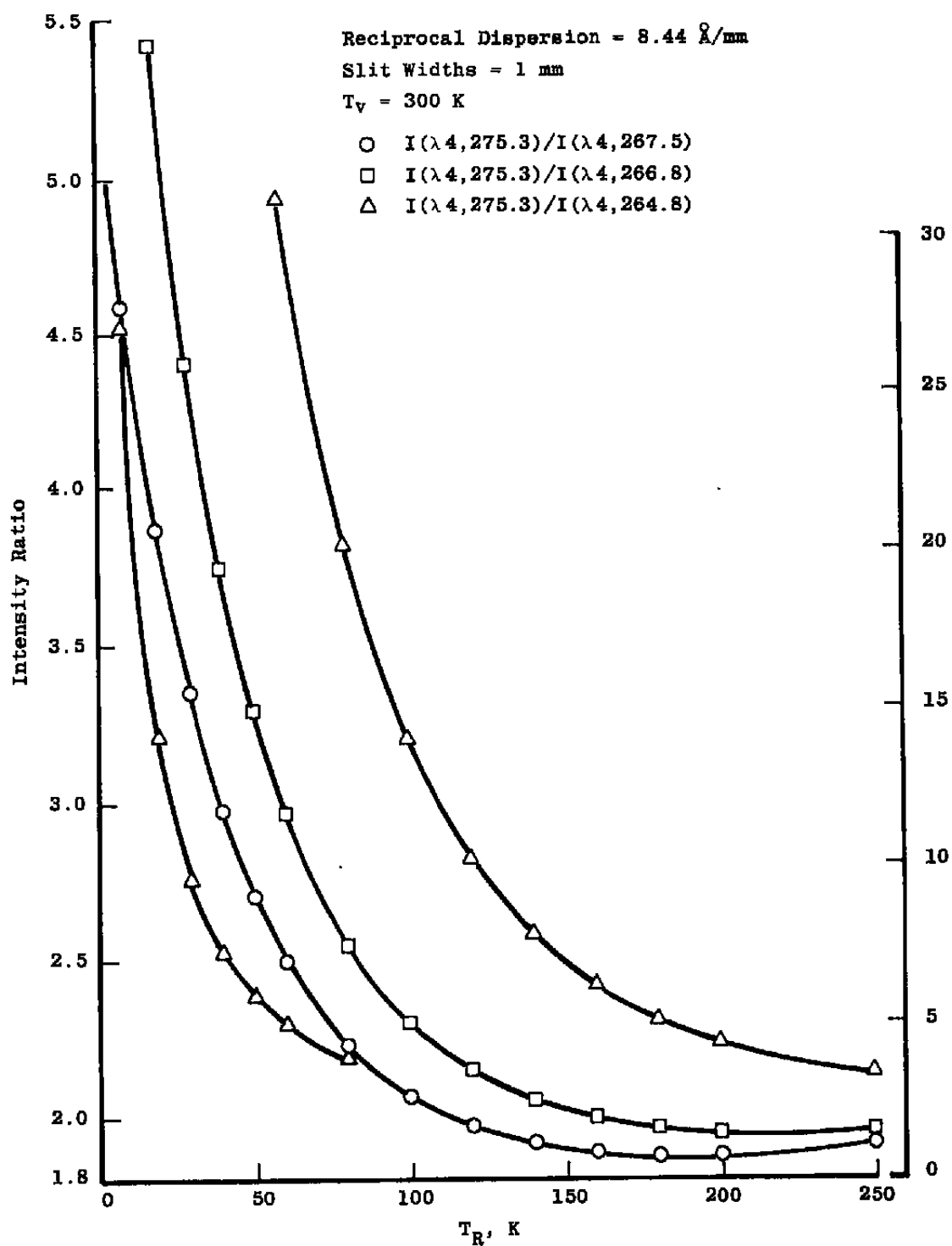
Figure 17. R-branch intensity ratios for $N_2^+(1^-)(0,1)$ band.
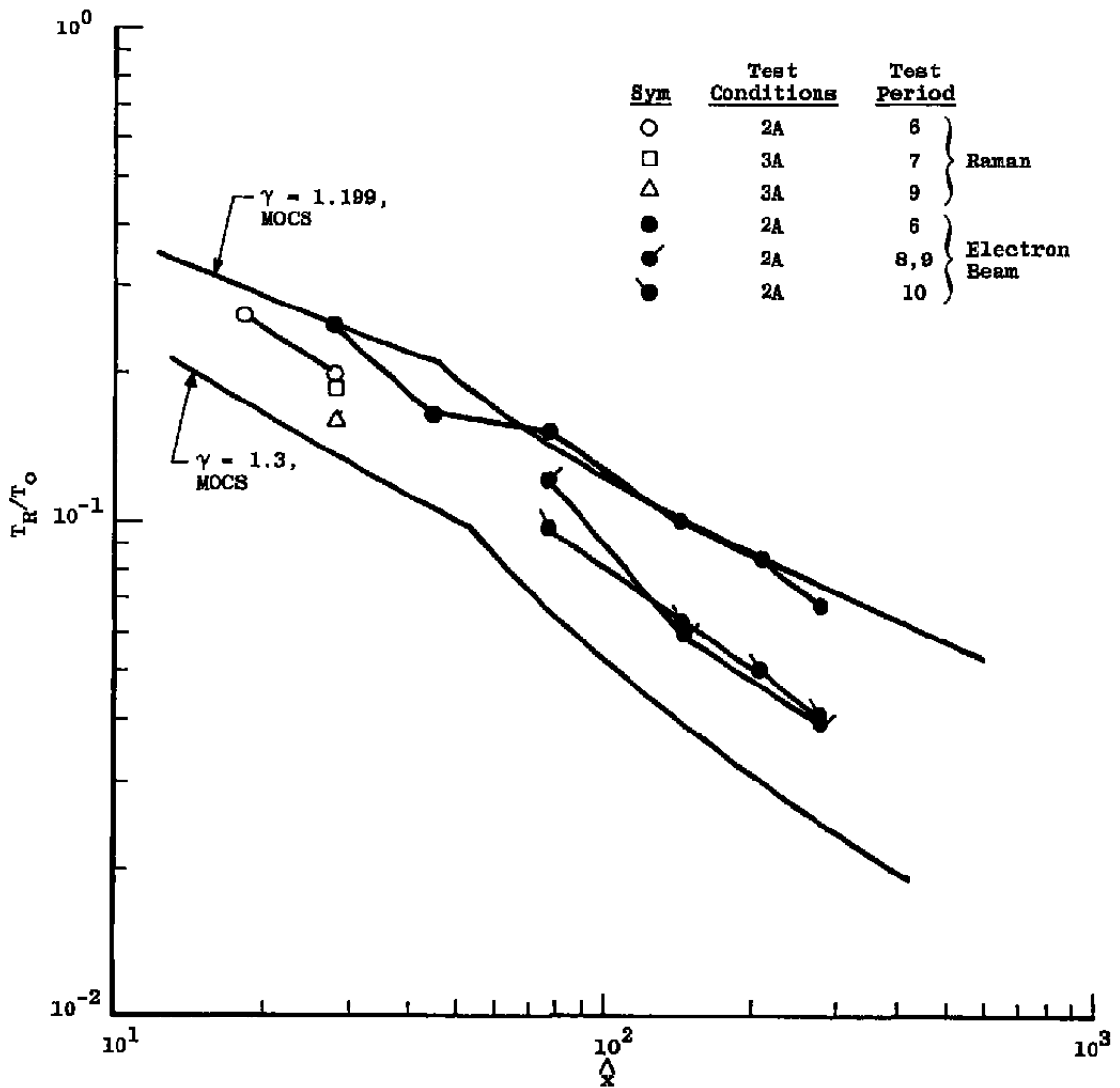
Figure 18. Axial variation of rotational temperature, test periods
            6 through 10.
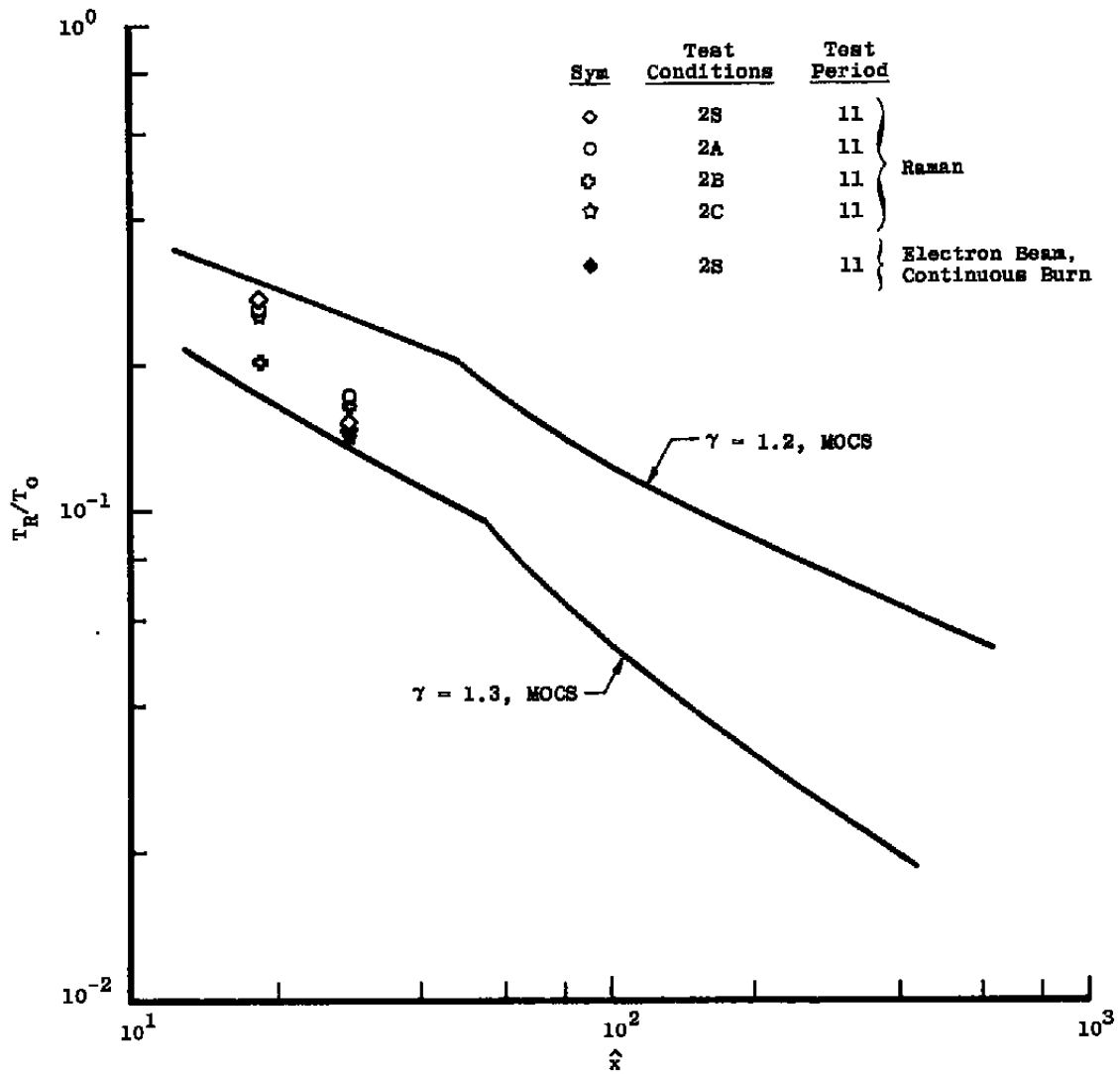
Figure 19. Axial variation of rotational temperature, test period 11.
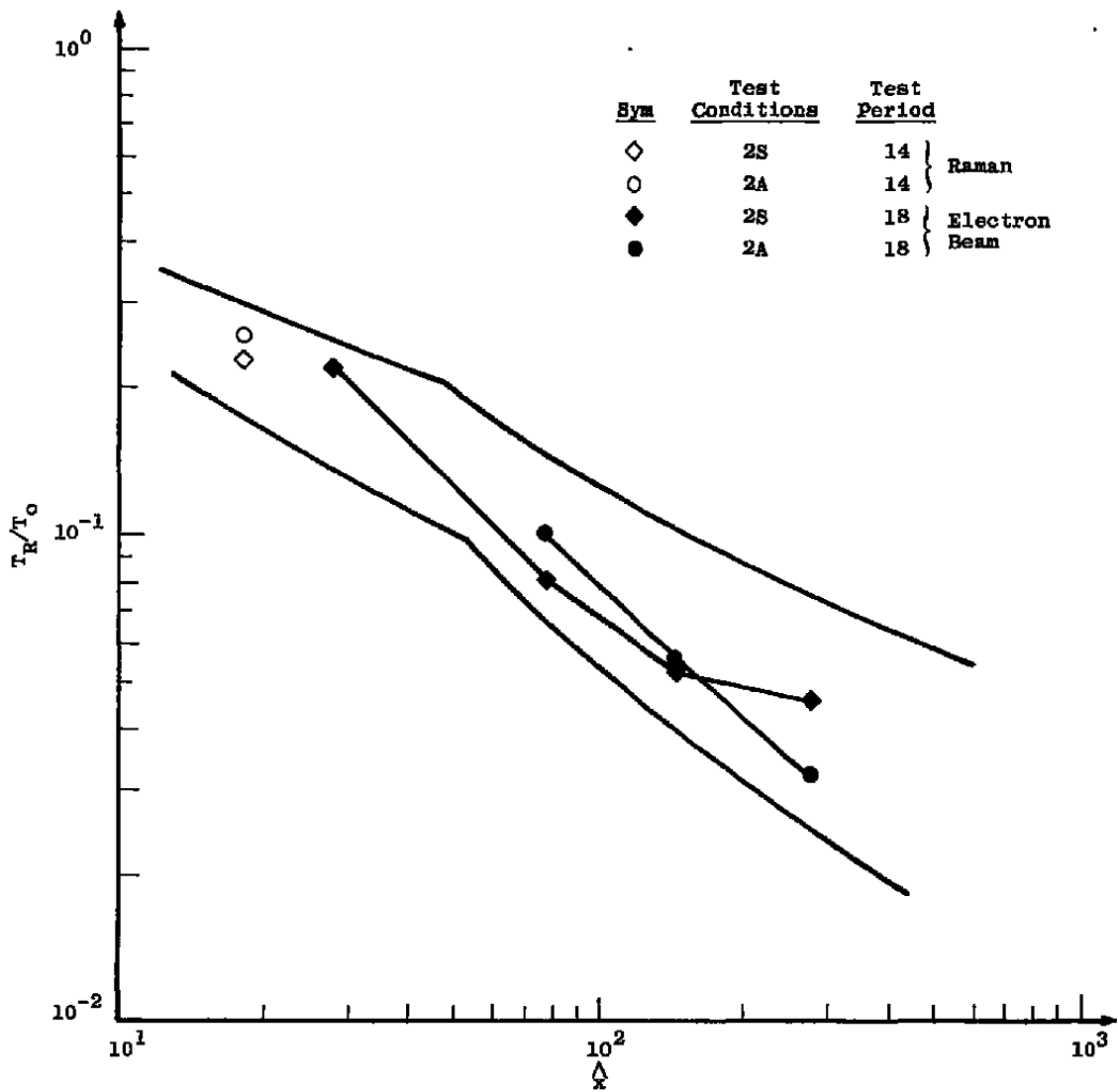
Figure 20. Axial variation of rotational temperature, test periods
14 and 18.
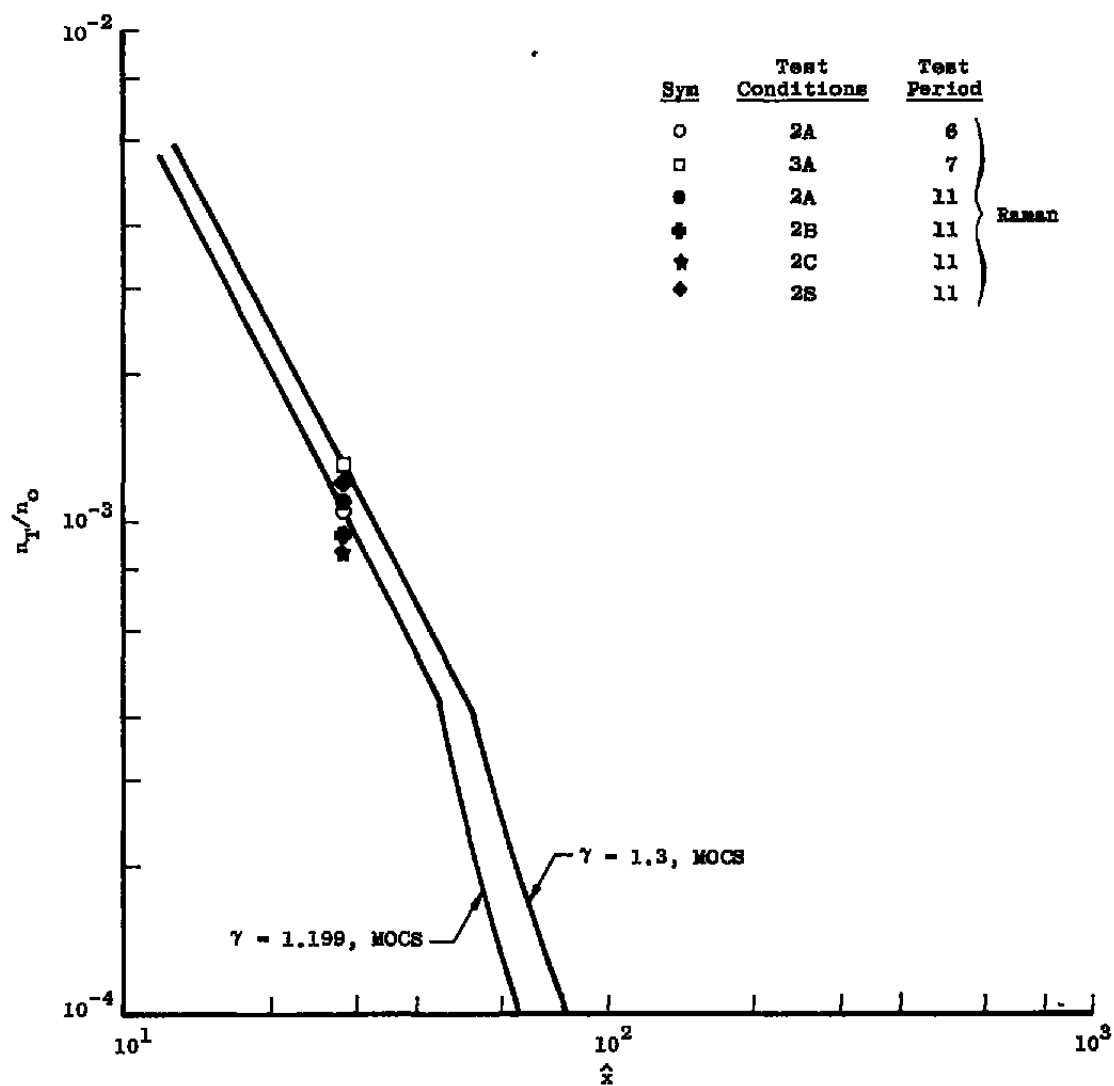
Figure 21. Axial variation of total number density.

Sym	Test Period	$\overset{\triangle}{x}$	$n(H_2)/n(N_2)$	$n(N_2)/n_T$
○	11	28.5	x	
□	11	18.5	x	
■	14	18.5	x	
☆	11	28.5		x
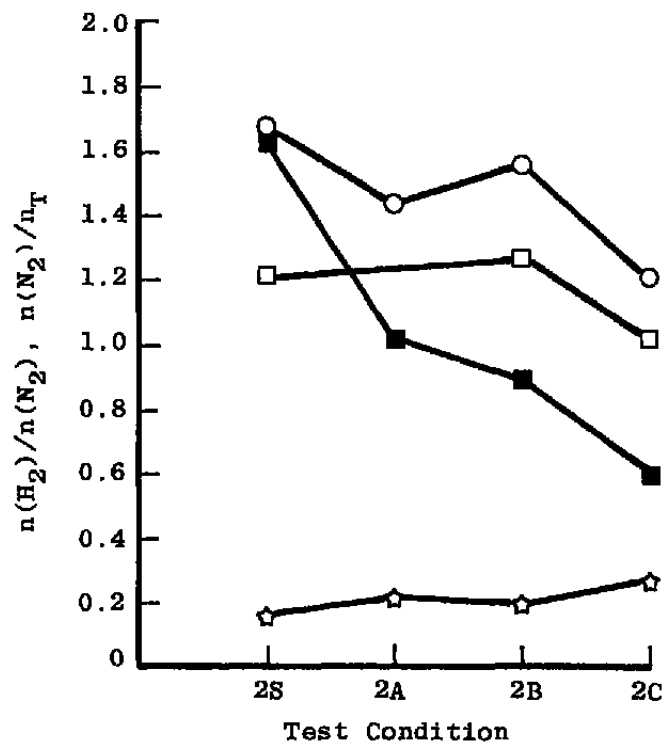
Figure 22. $n(H_2)/n(N_2)$ and $n(N_2)/n_T$ as a function of test condition.

85
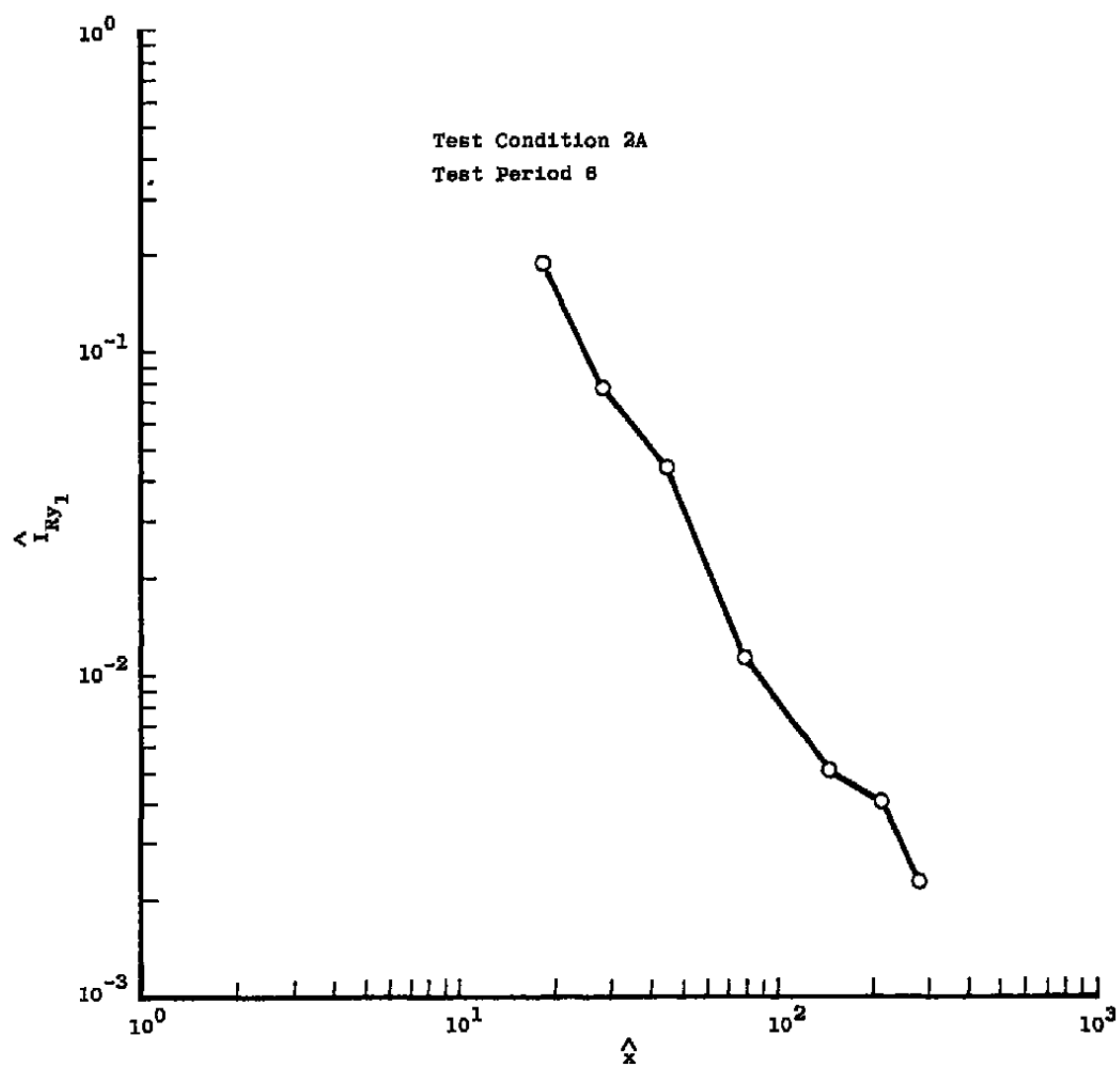
Figure 23. Axial variation of $\widehat{I}_{Ry_1}$, test condition 2A, test period 6.
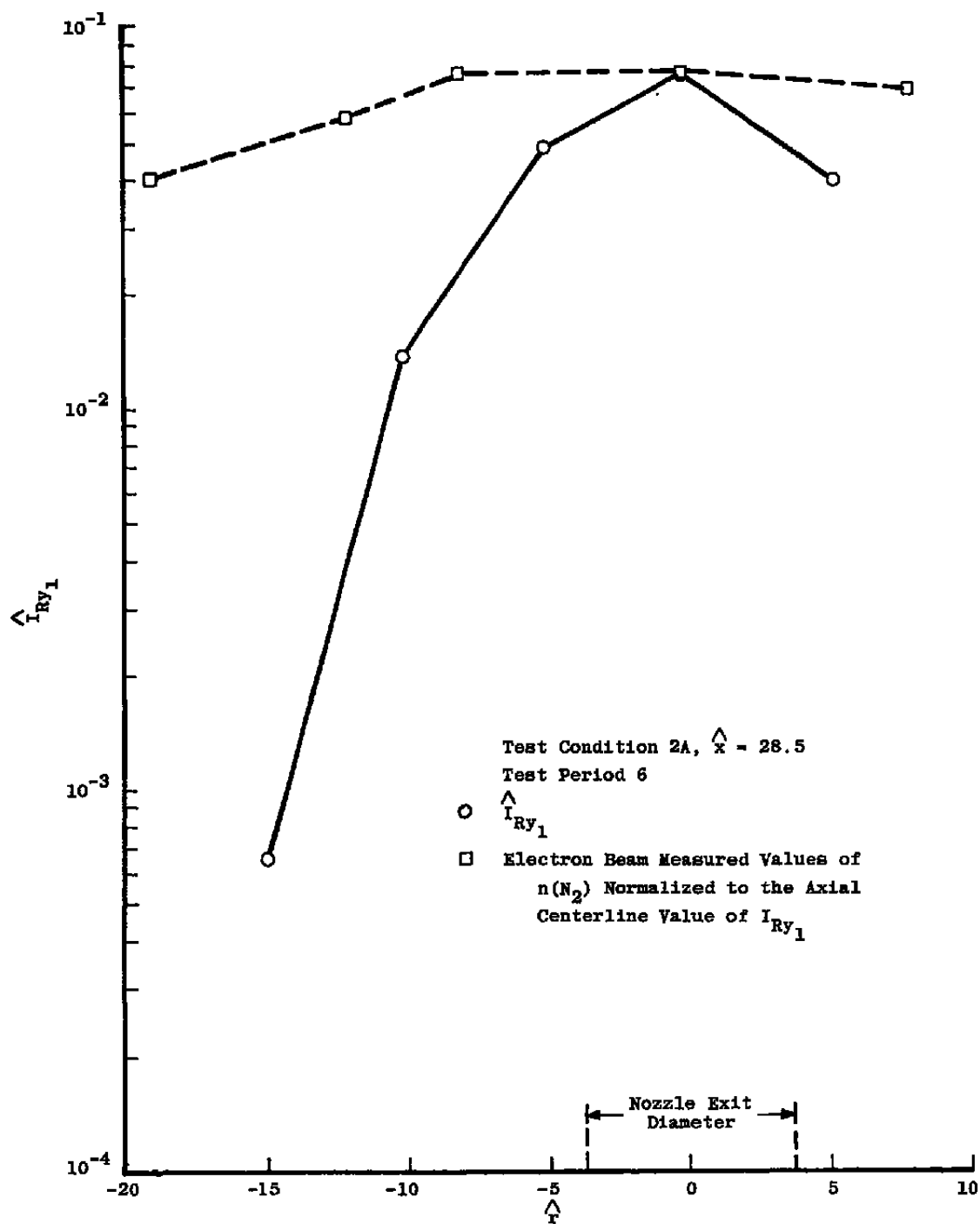
Figure 24. Radial variation of $\widehat{I}_{Ry_1}$ at $\widehat{x} = 28.5$, test condition 2A,
test period 6.

10^0

10^{-1}

$\widehat{I}_{Ry_1}$

10^{-2}

Sym	Test Conditions
○	2A
□	3A
△	1A

Test Period 9

10^{-3}

10^0 10^1 10^2 10^3

$\widehat{x}$
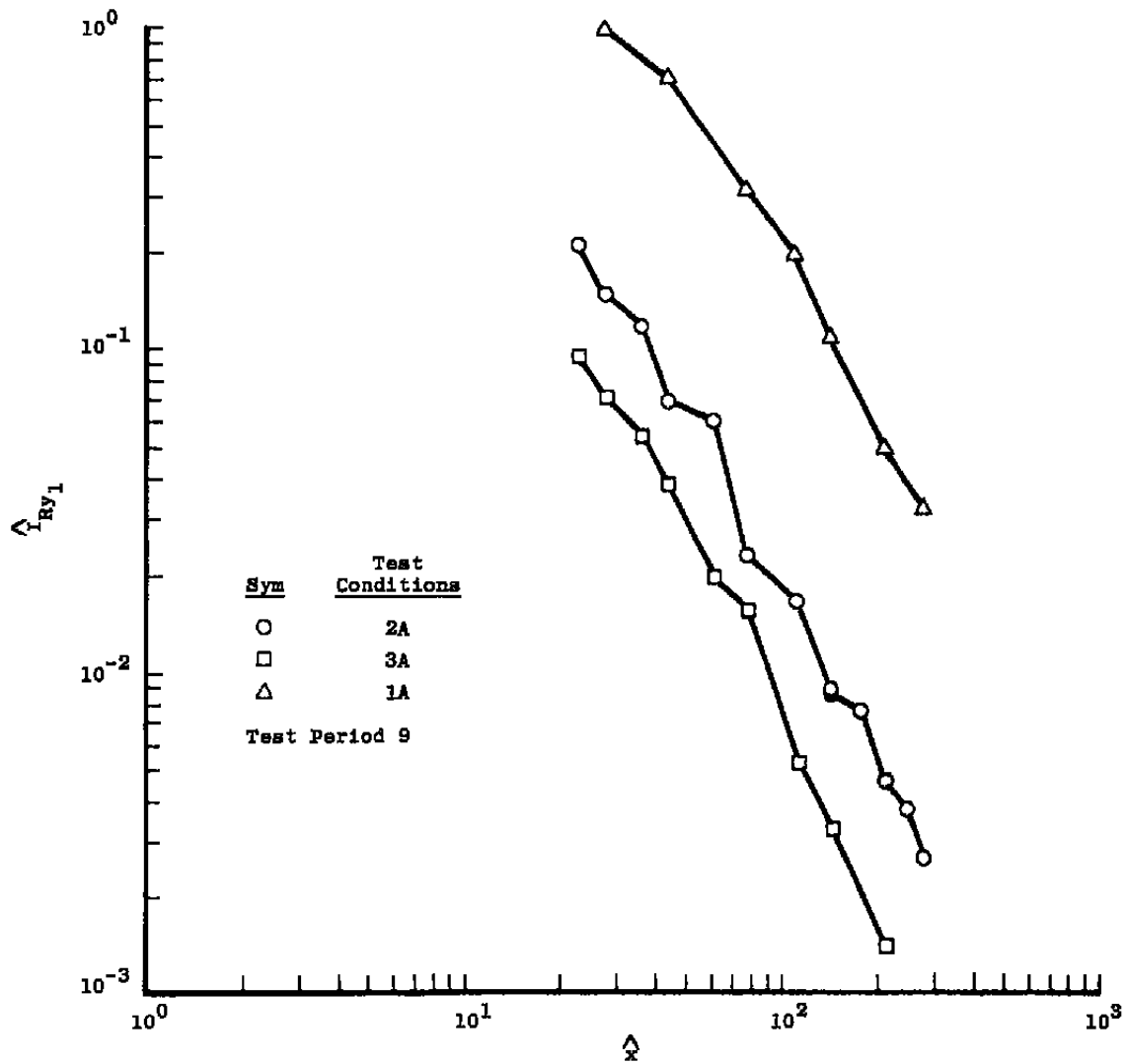
Figure 25. Axial variation of $\widehat{I}_{Ry_1}$, test conditions 1A, 2A, and 3A, test period 9.
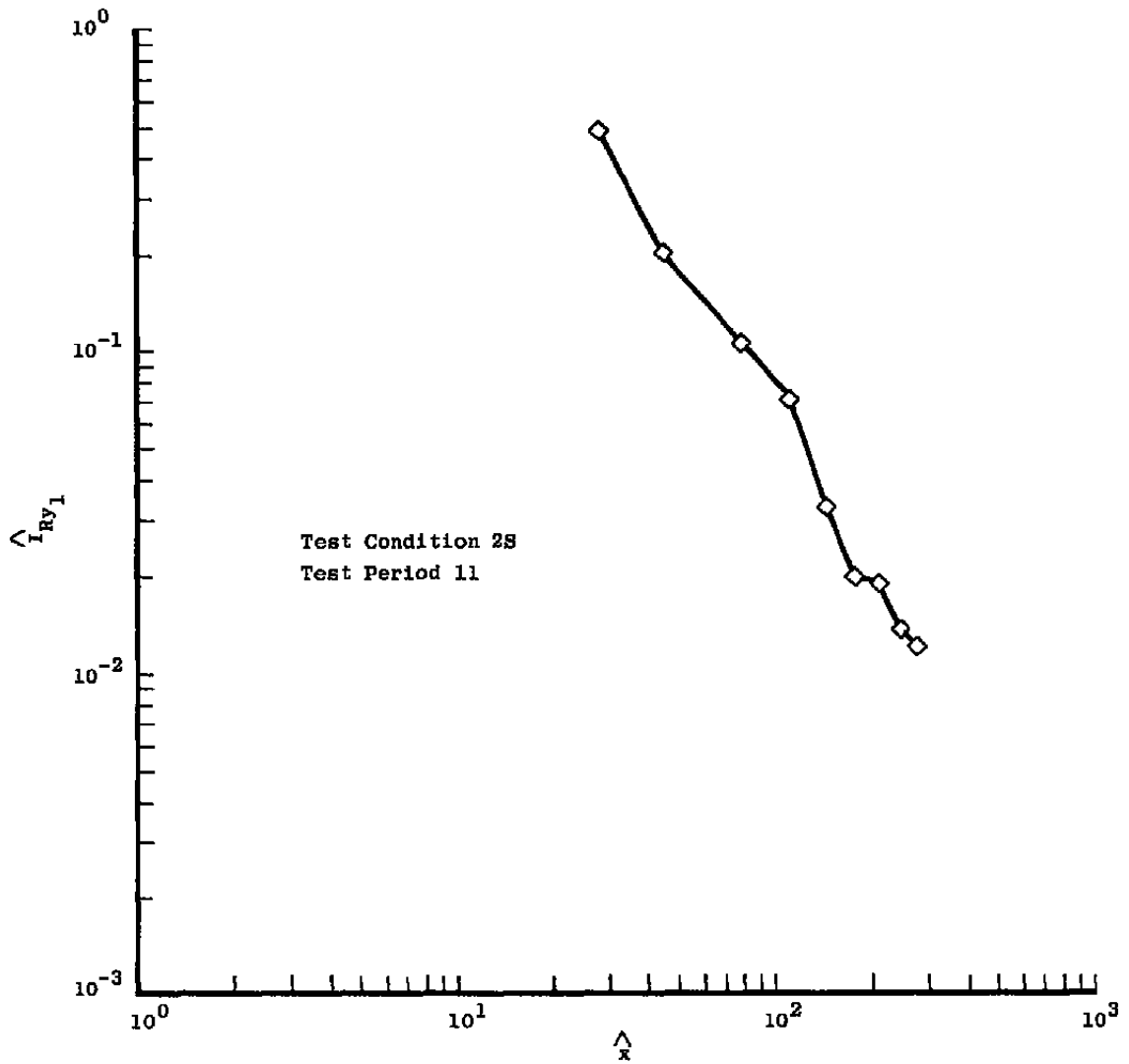
Figure 26. Axial variation of $\widehat{I}_{Ry_1}$, test condition 2S, test period 11.
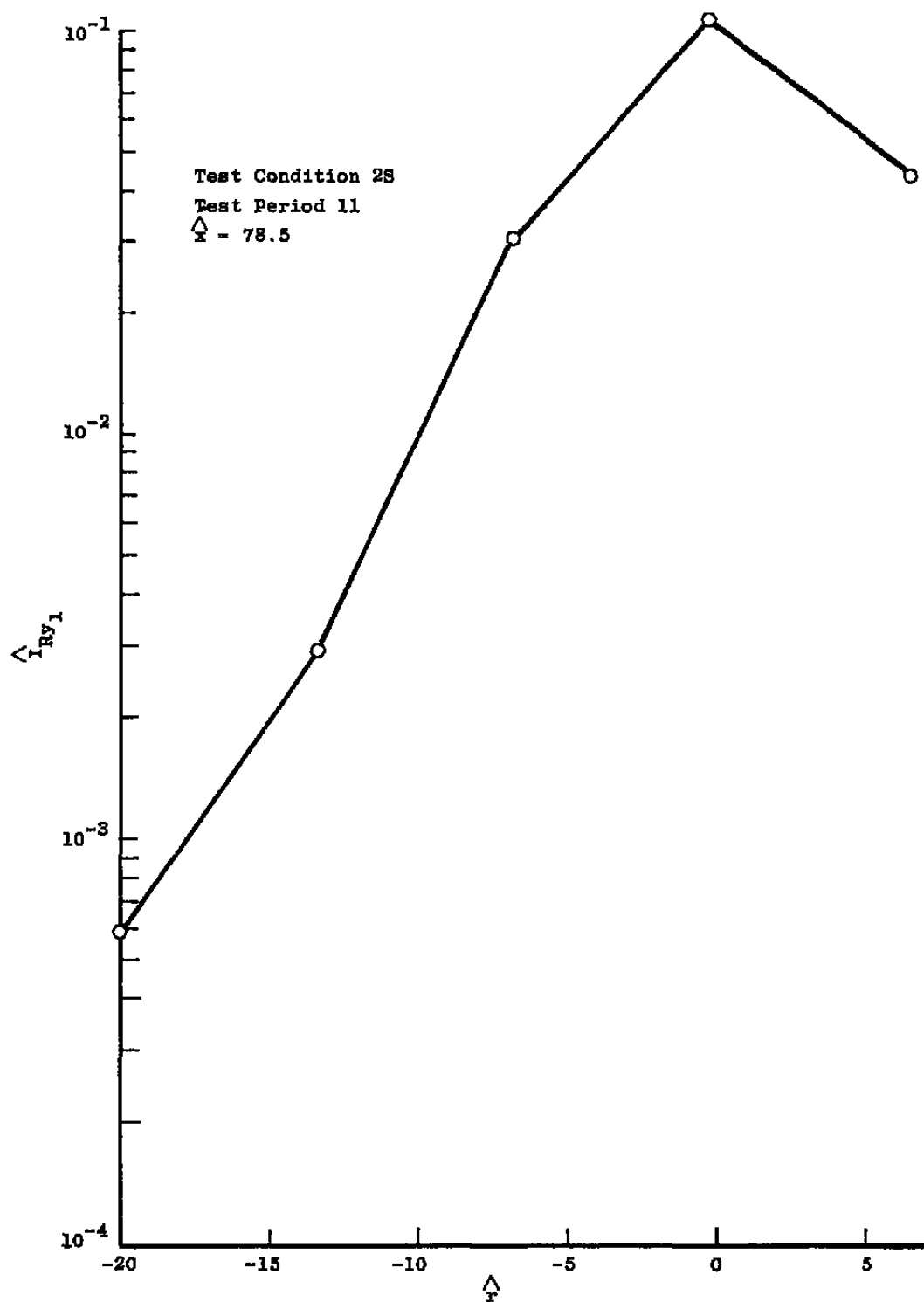
Figure 27.   Radial variation of $\widehat{I}_{Ry_1}$ at $\widehat{x}$ = 78.5, test condition 2S, test period 11.
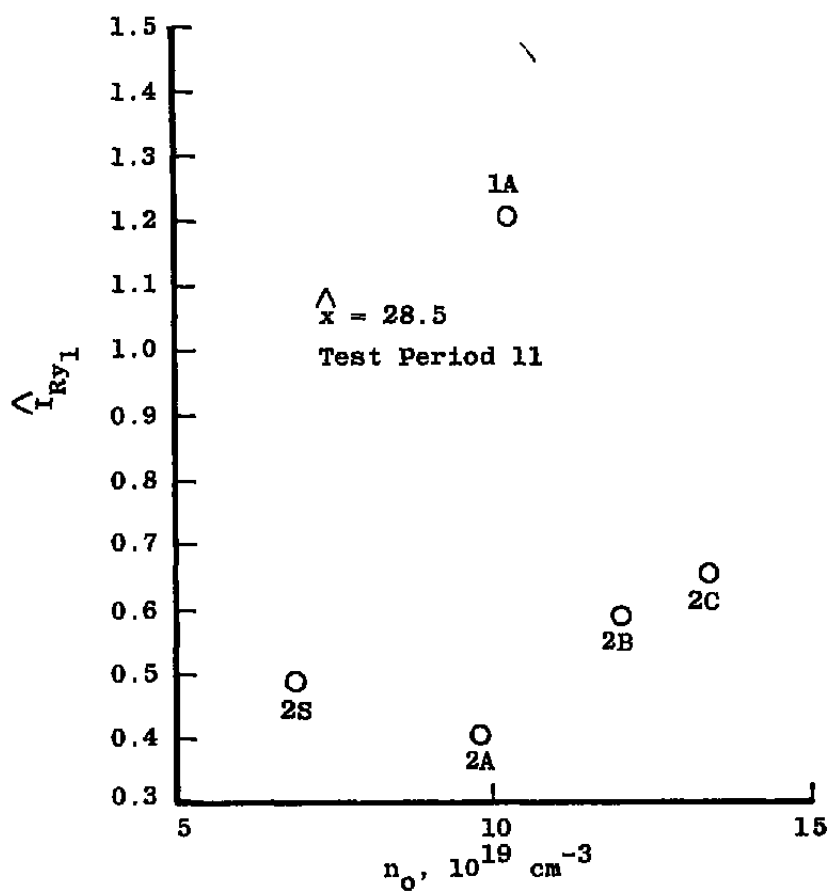
Figure 28. Variation of $\hat{I}_{Ry_1}$ with combustion chamber number density, $\hat{x}$ = 28.5, test period 11.
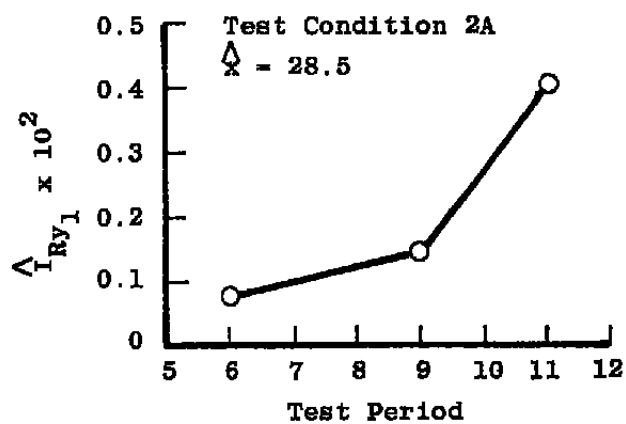
Figure 29. Variation of $\hat{I}_{Ry_1}$ with test period, $\hat{x}$ = 28.5, test condition 2A.
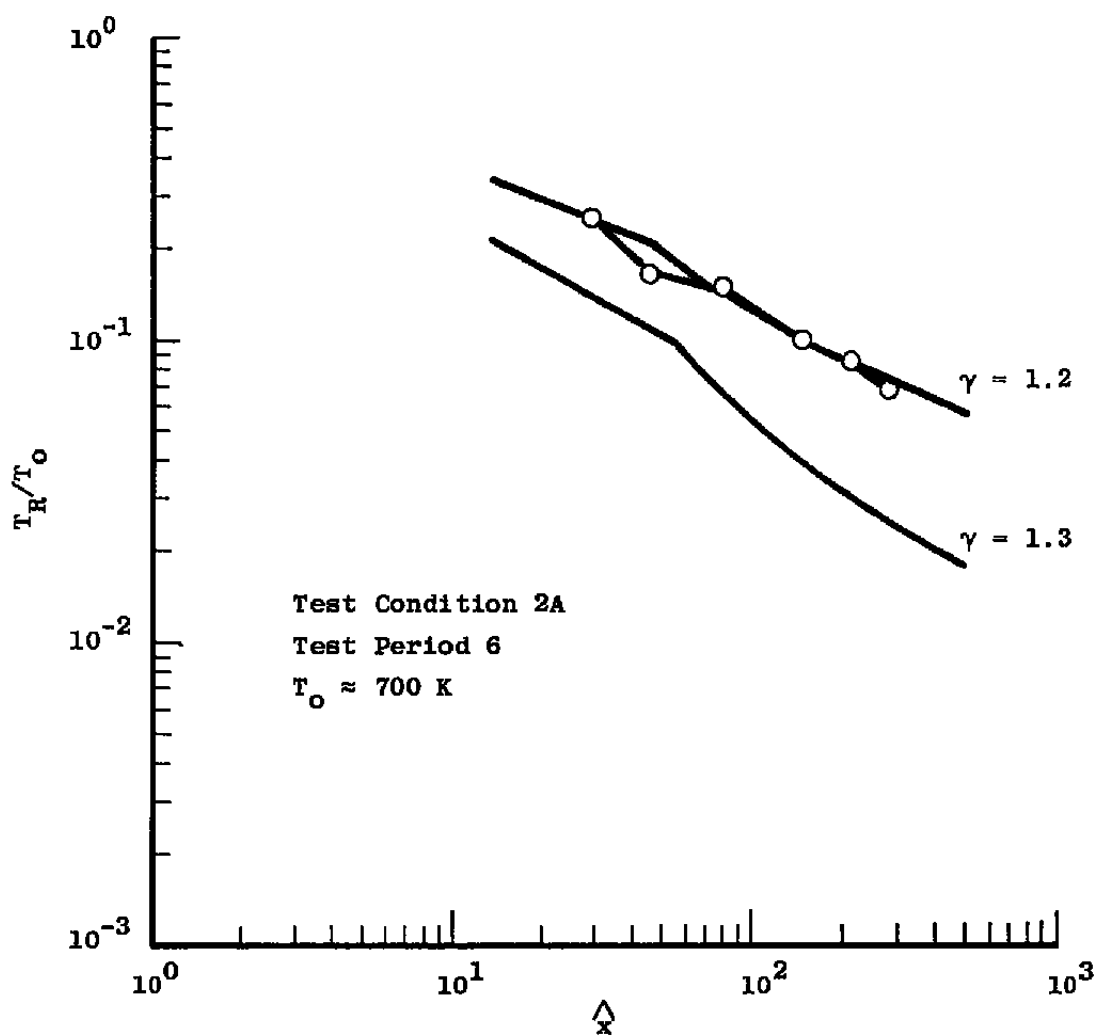
Figure 30. Axial variation of rotational temperature, test condition 2A, test period 6.
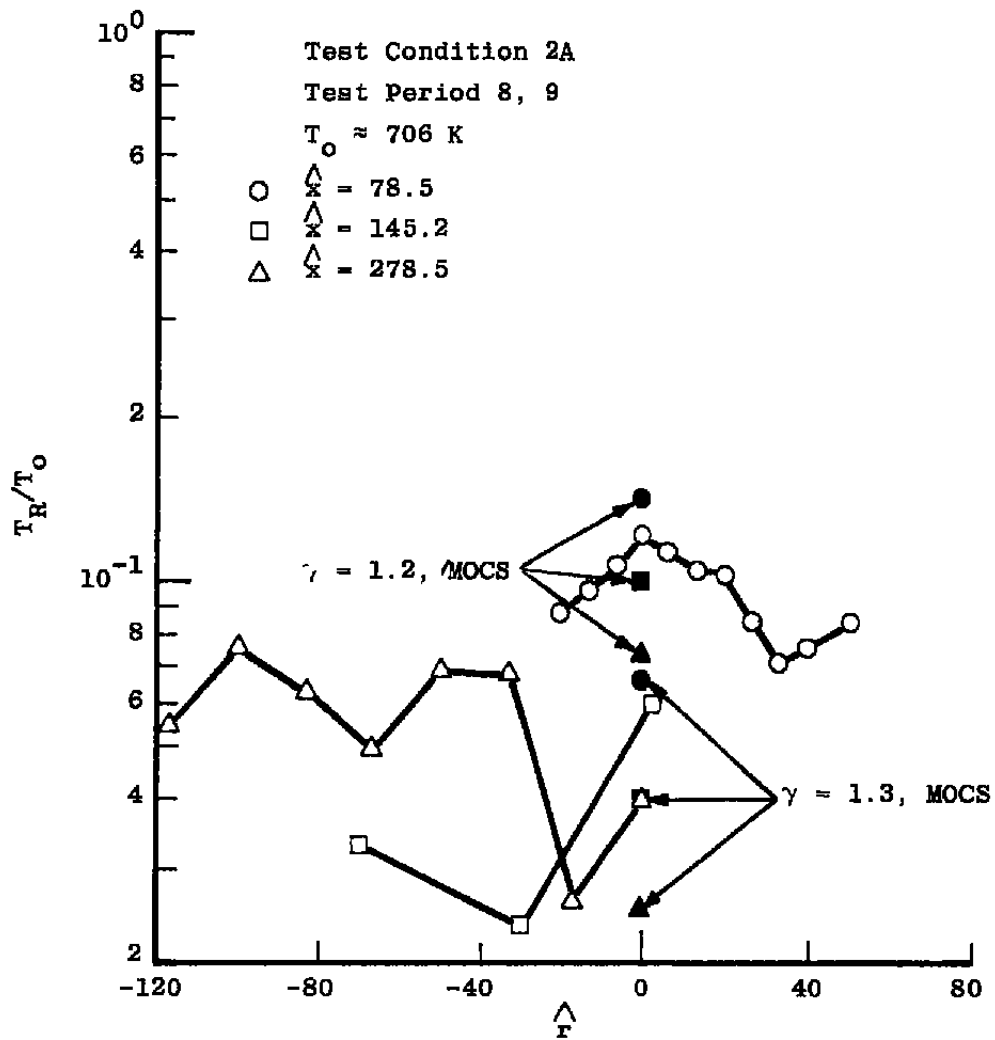
Figure 31. Radial variation of rotational temperature, $\hat{x}$ = 78.5, 145.2, and 278.5, test condition 2A, test periods 8 and 9.
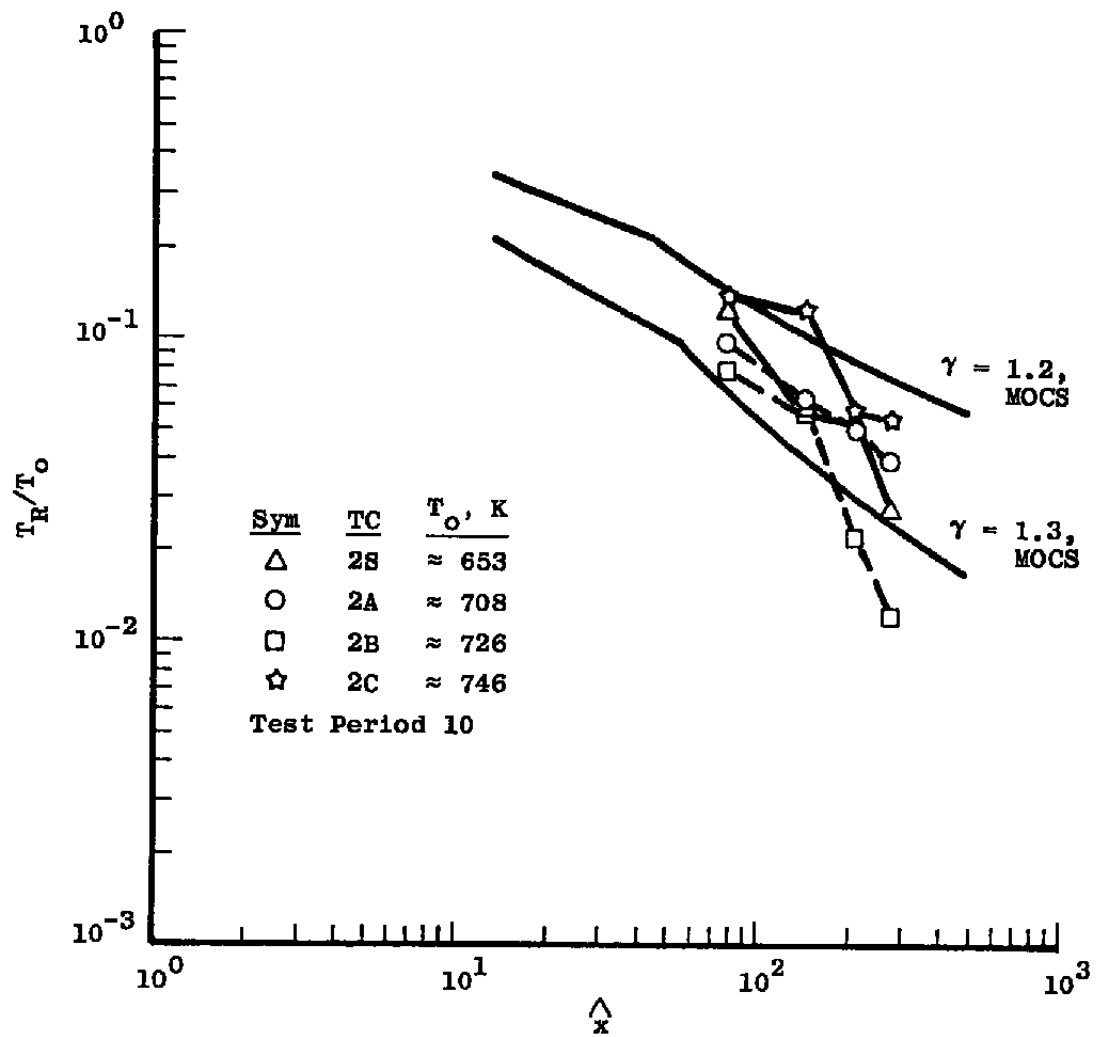
Figure 32. Axial variation of rotational temperature, test conditions 2S, 2A, 2B, and 2C, test period 10.
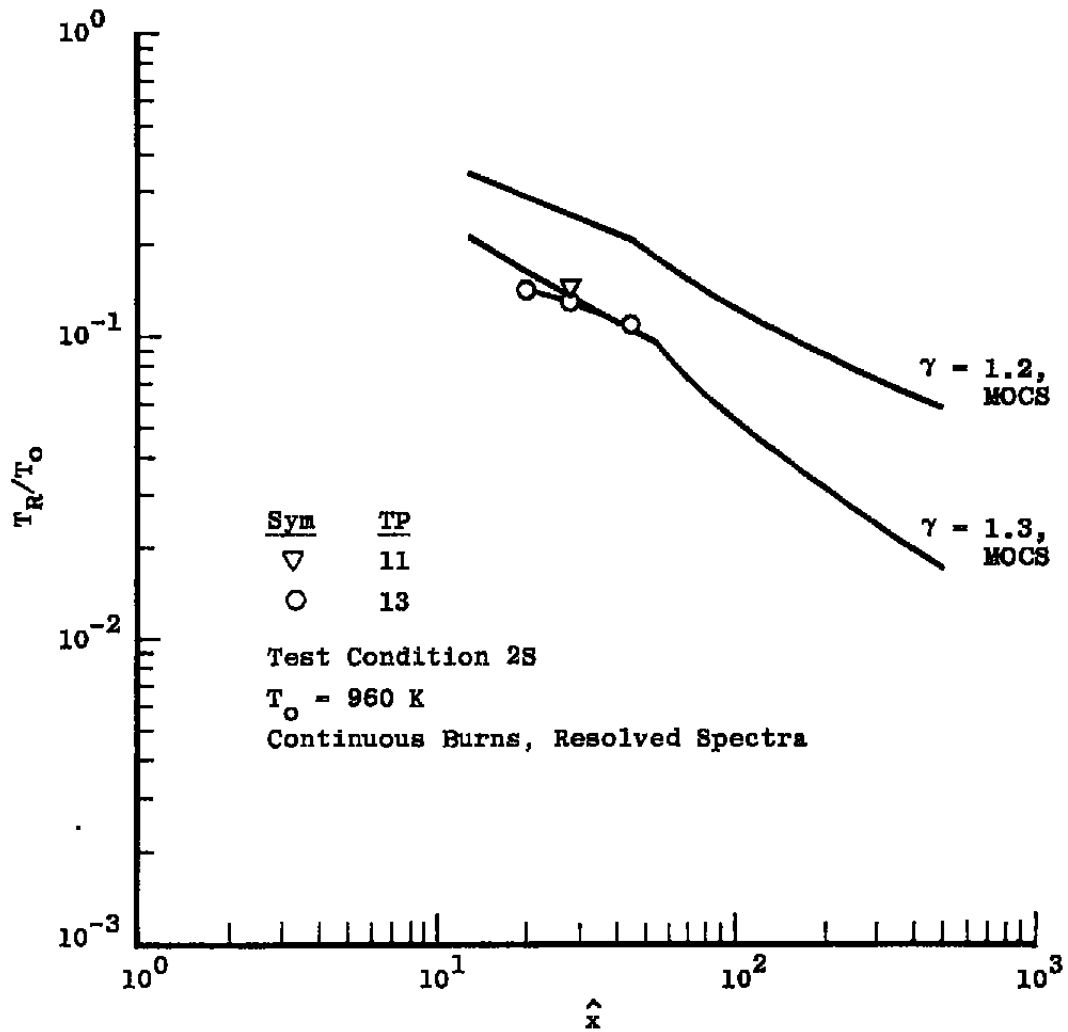
Figure 33. Axial variation of rotational temperature, test condition 2S, test periods 11 and 13.
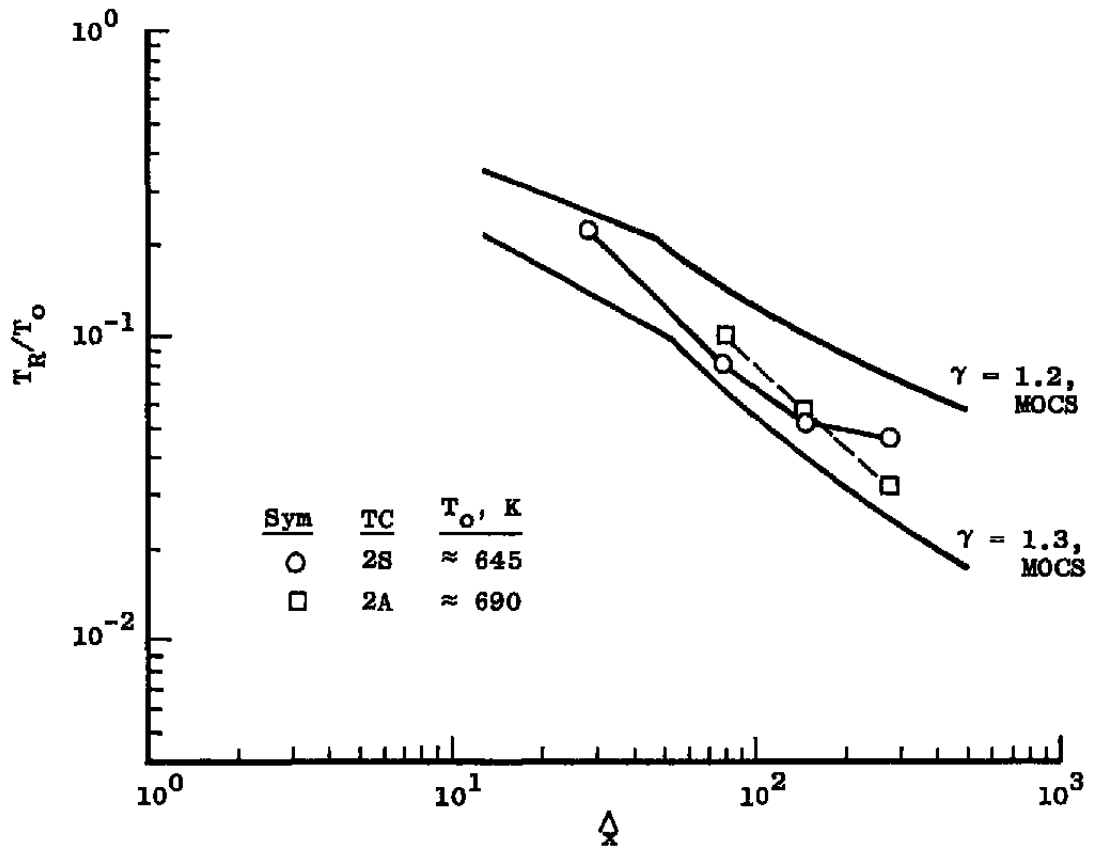
Figure 34. Axial variation of rotational temperature, test conditions 2S
and 2A, test period 18.
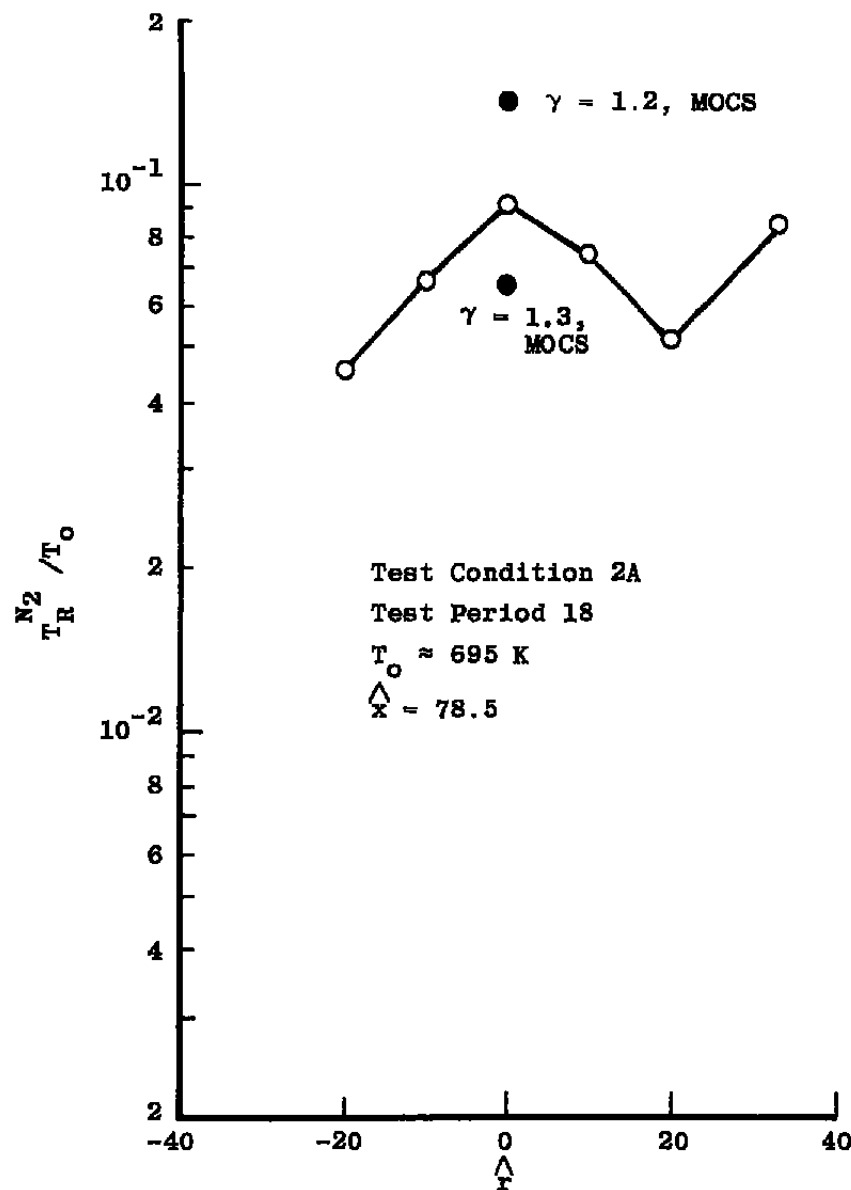
Figure 35. Radial variation of rotational temperature, $\hat{x}$ = 78.5, test condition 2A, test period 18.
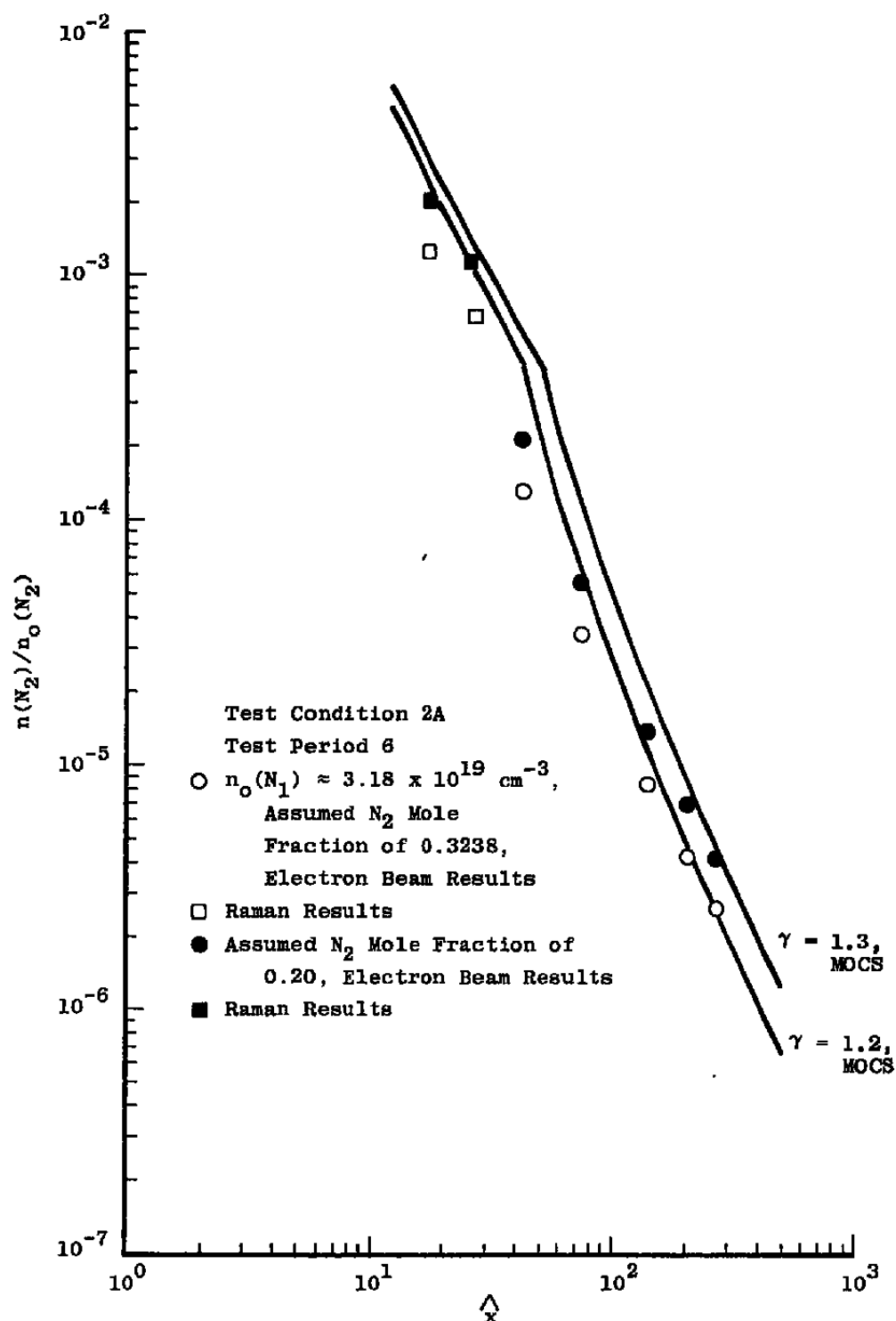
Figure 36. Axial variation of N_2 number density, test condition 2A, test period 6.
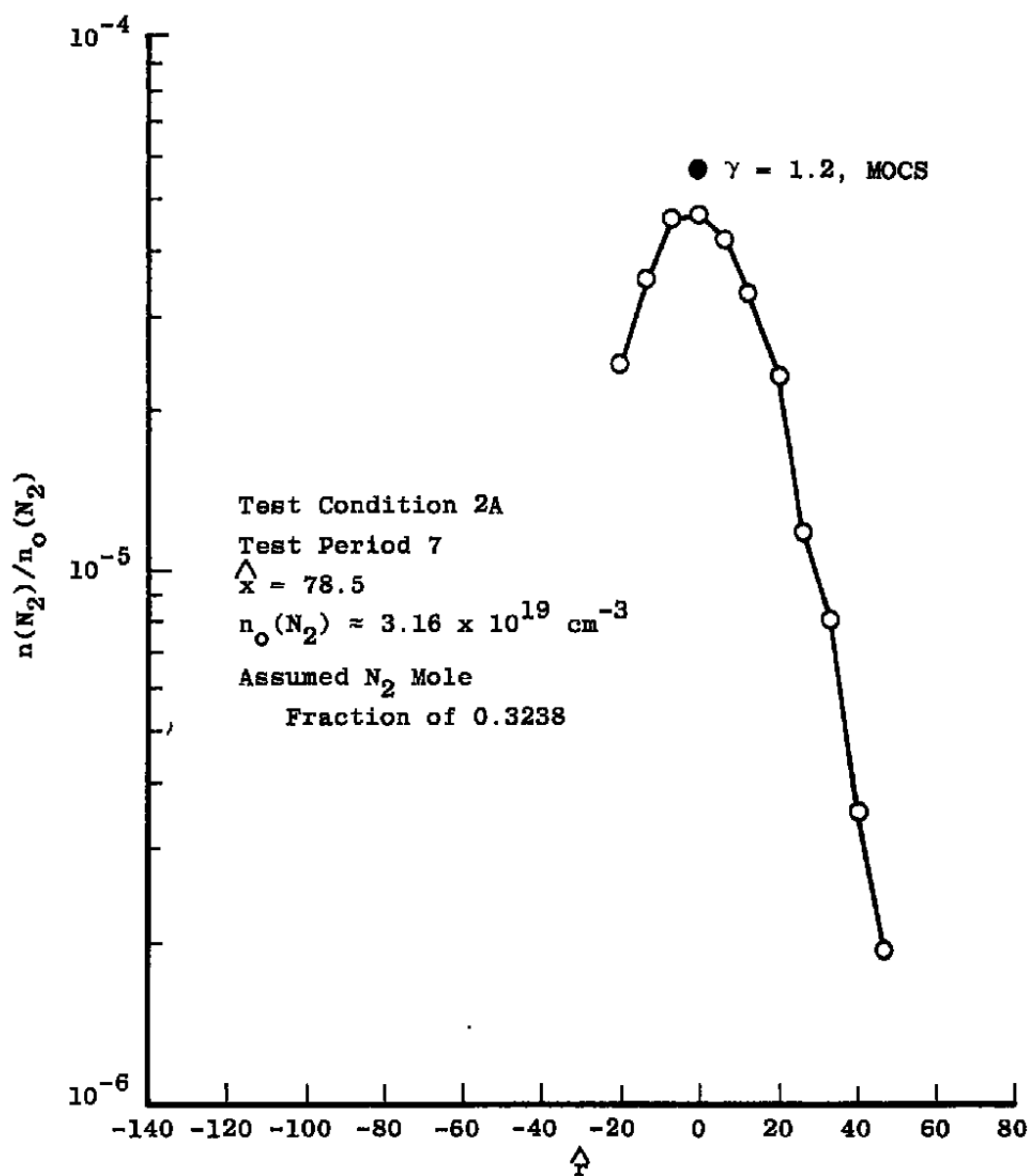
Figure 37. Radial variation of N_2 number density, $\hat{x}$ = 78.5, test condition 2A, test period 7.
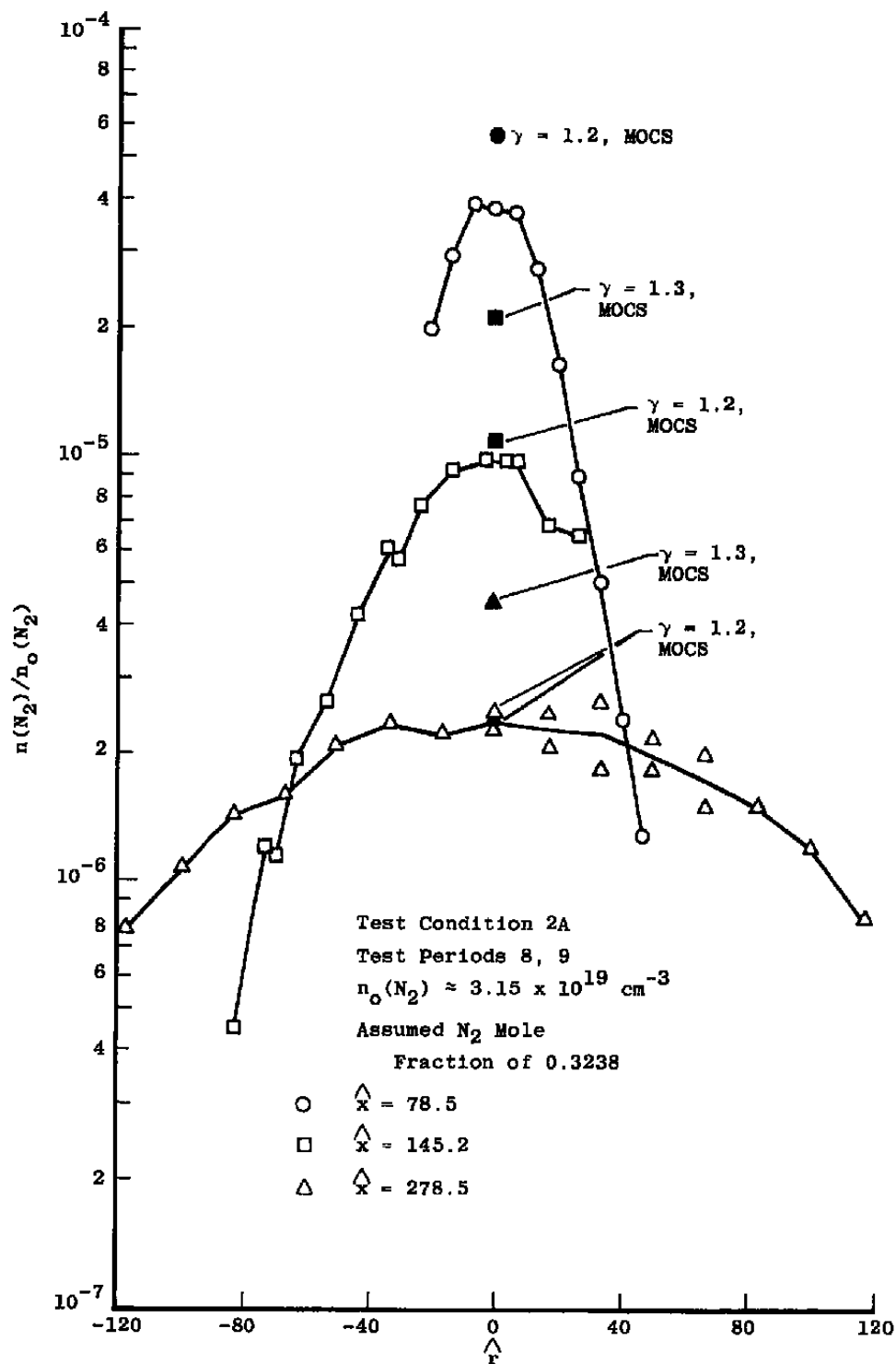
Figure 38. Radial variation of N_2 number density, $\widehat{x} = 78.5$, 145.2, and 278.5, test condition 2A, test periods 8 and 9.
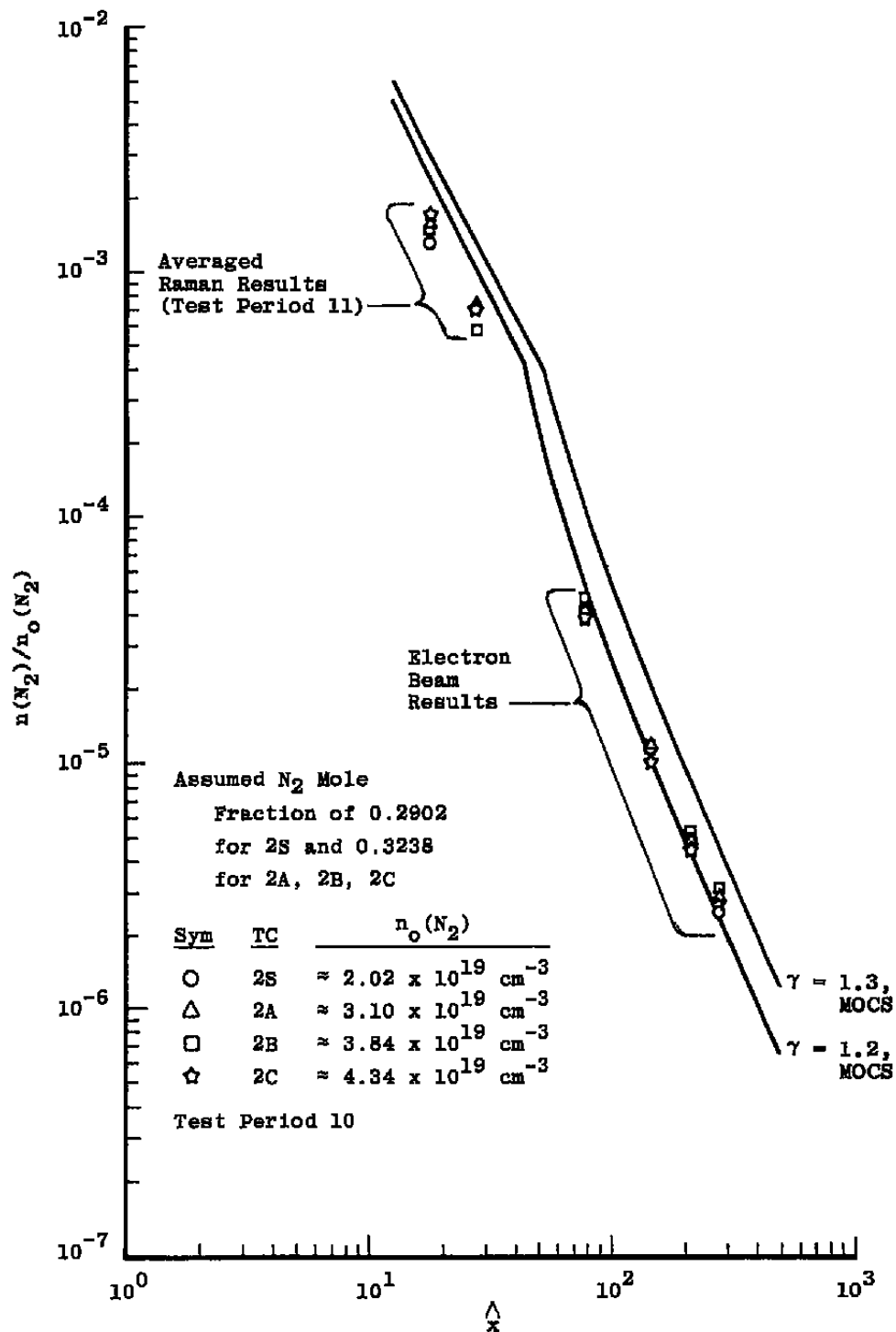
Figure 39. Axial variation of N_2 number density, test conditions 2S, 2A, 2B, and 2C, test period 10.
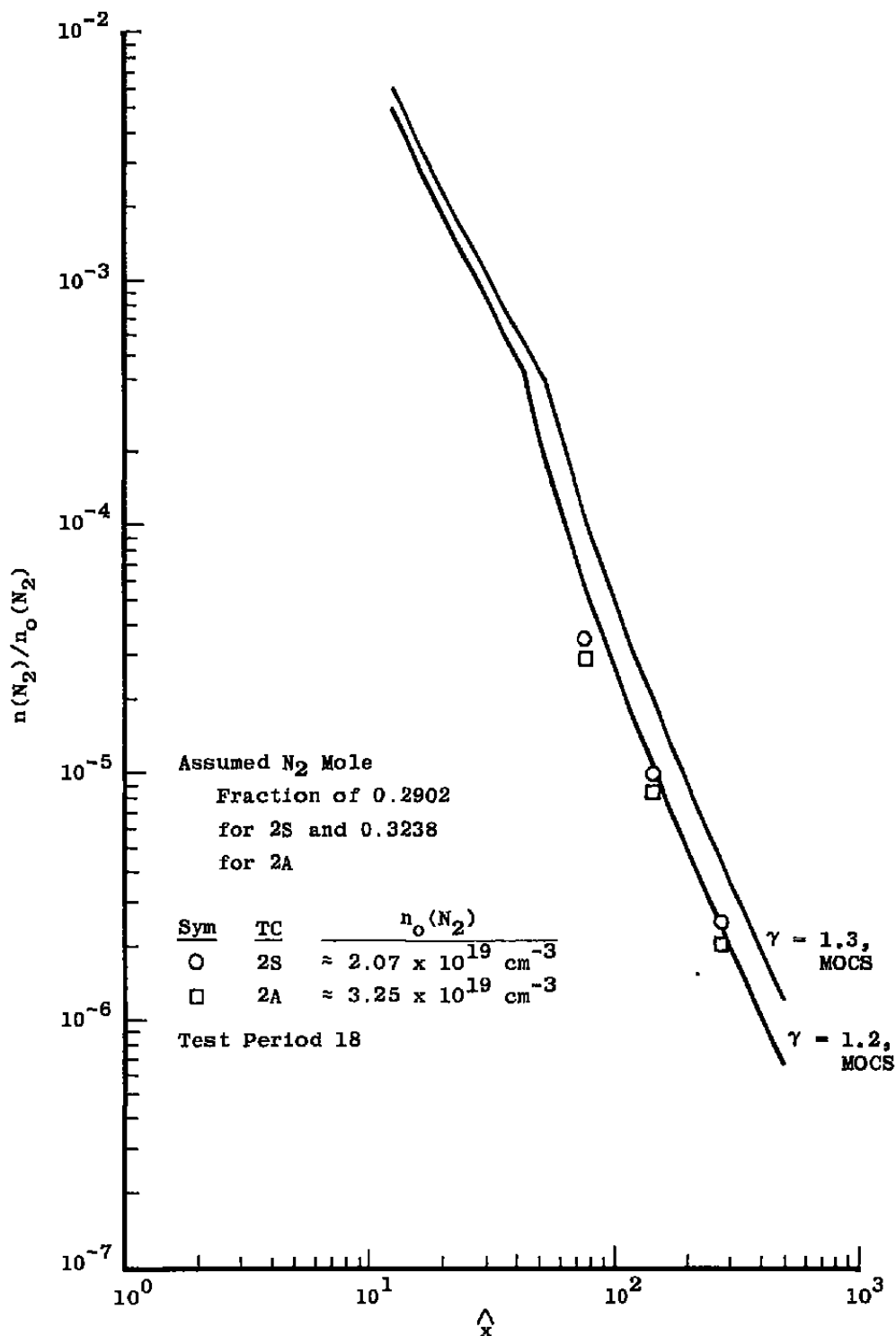
Figure 40. Axial variation of N_2 number density, test conditions 2S and 2A, test period 18.
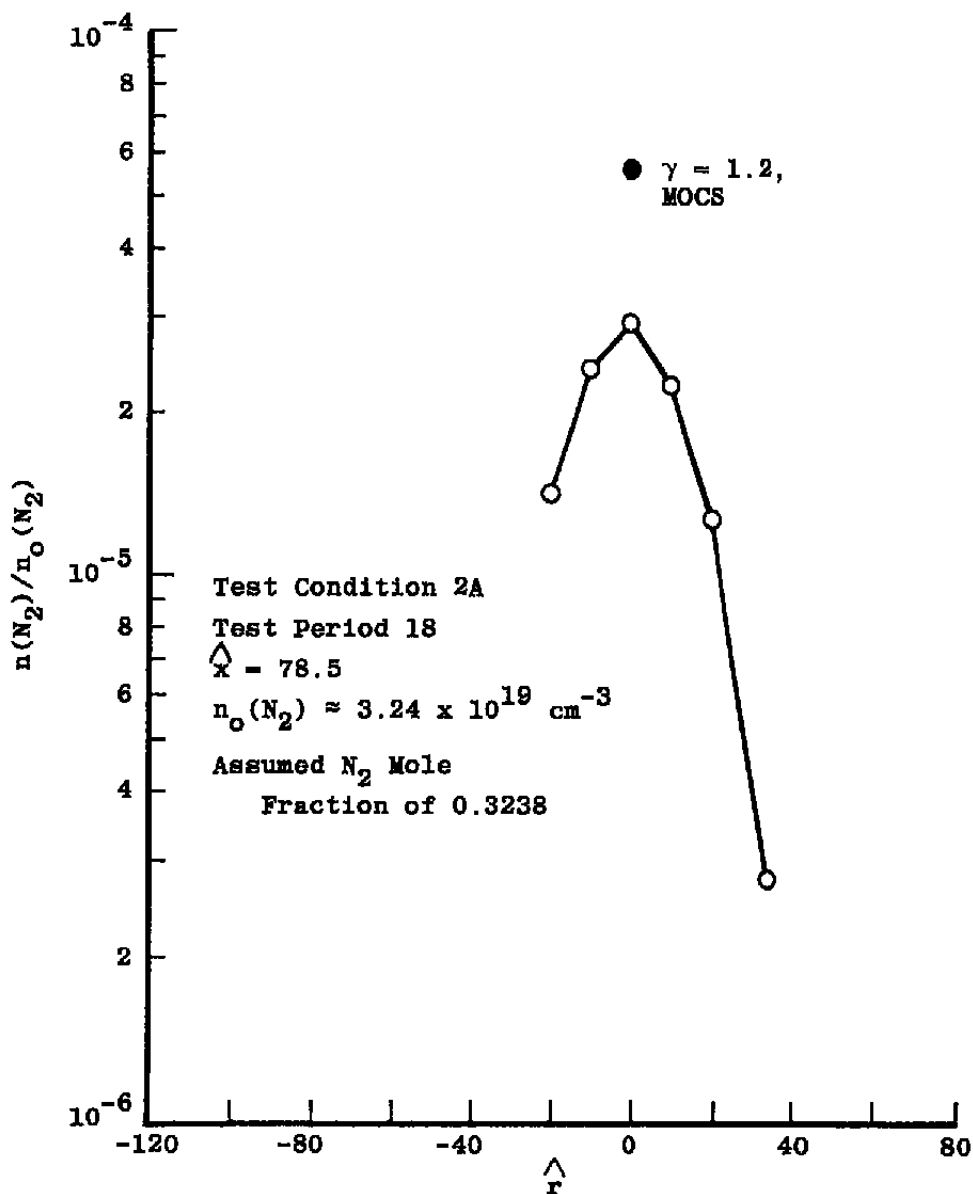
Figure 41. Radial variation of N_2 number density, $\hat{x} = 78.5$, test condition 2A, test period 18.
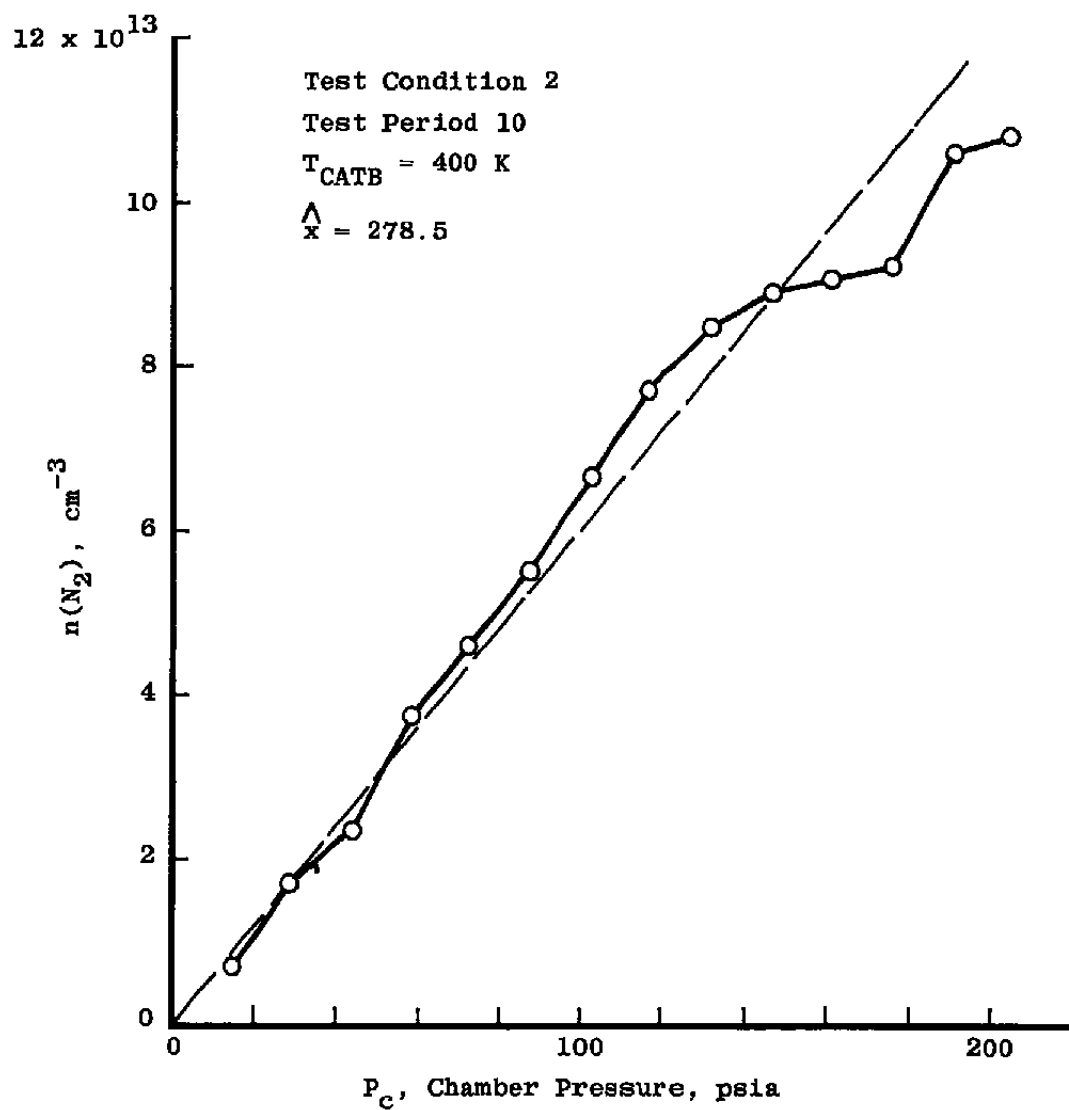
Figure 42. N_2 number density at $\hat{x}$ = 278.5 as a function of combustion chamber pressure.
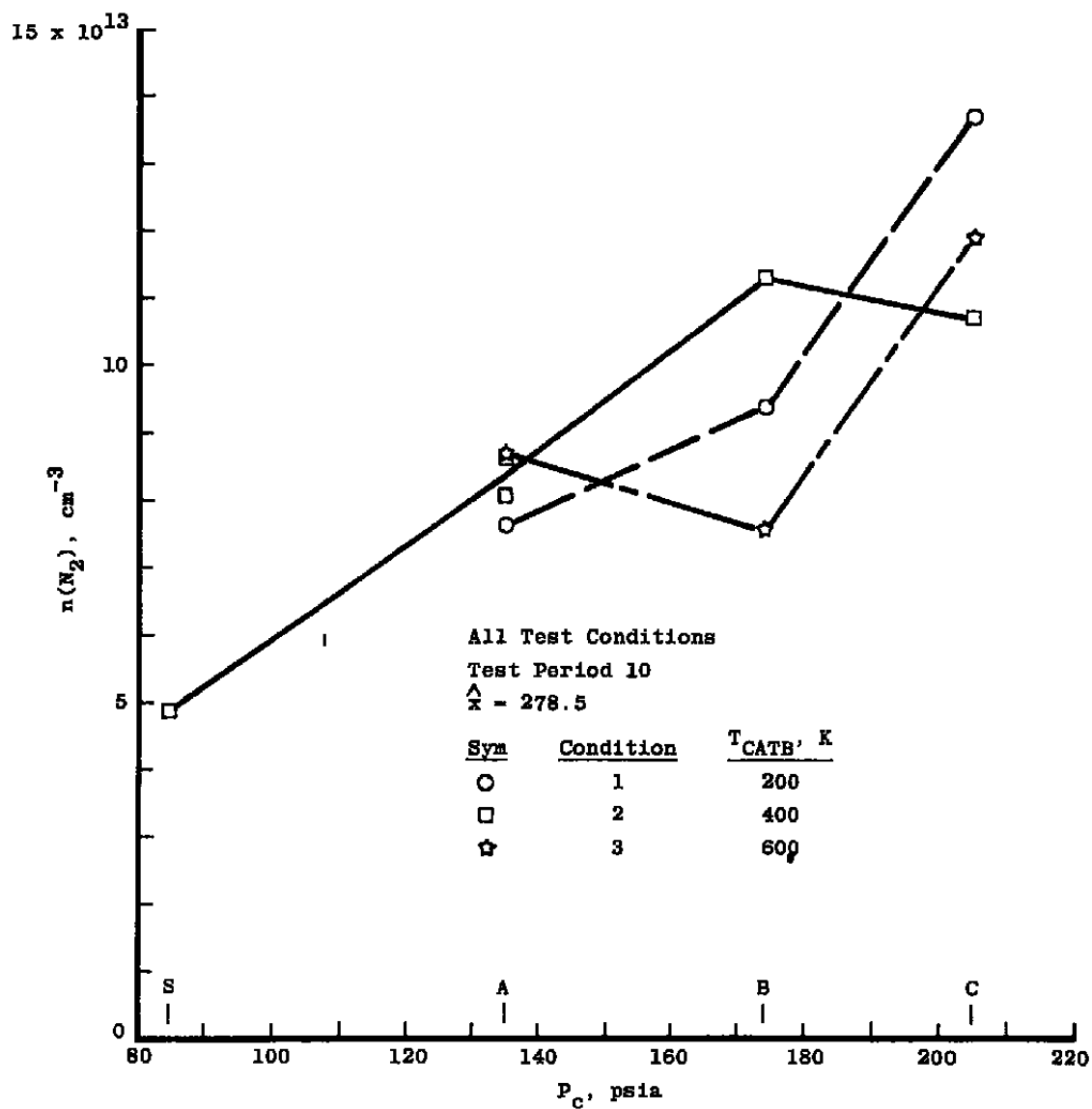
Figure 43. N_2 number density at $\widehat{x} = 278.5$ as a function of test condition.
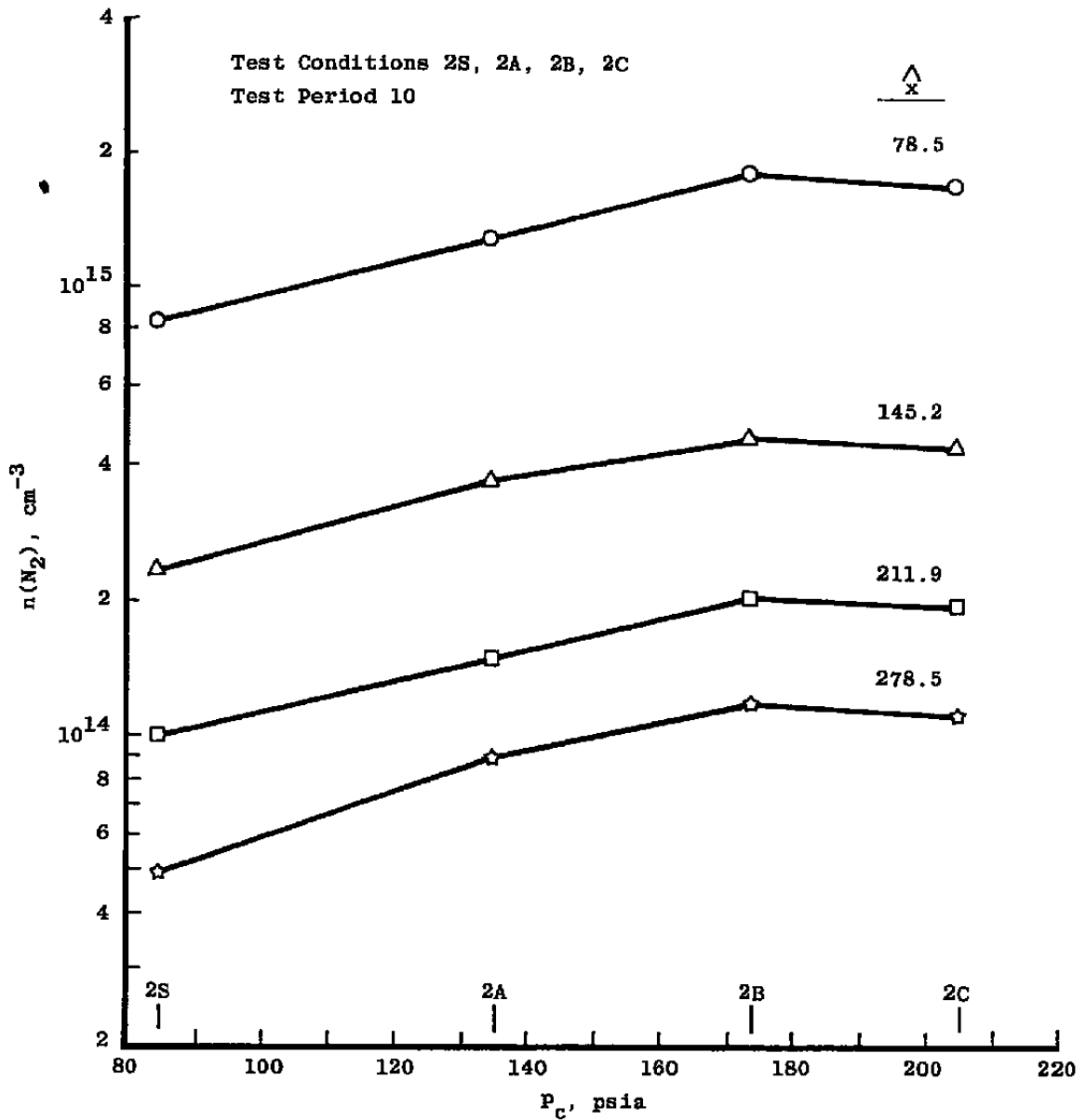
Figure 44. N_2 number density as a function of test condition for various values of axial position.
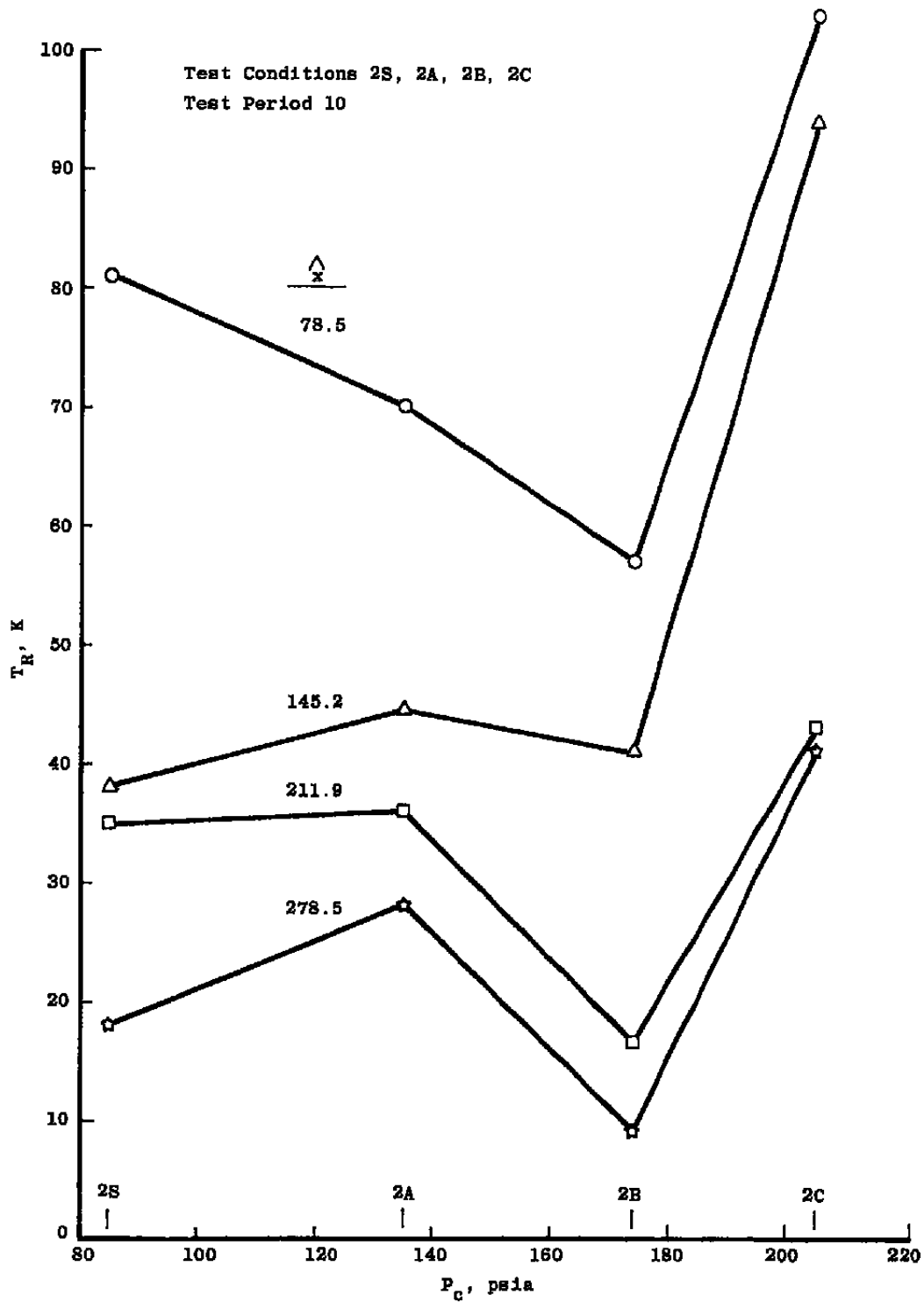
Figure 45. Rotational temperature as a function of test condition for various
values of axial position.
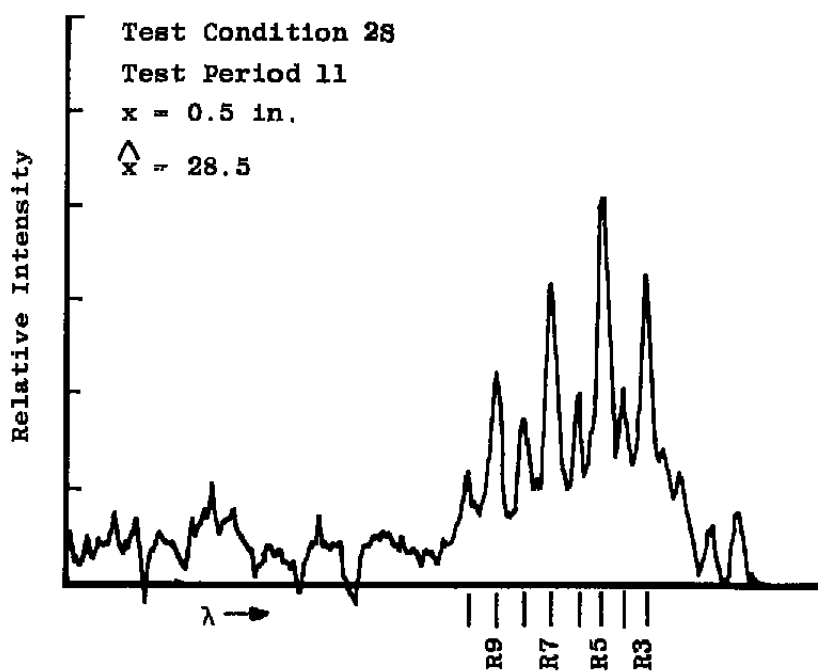
Figure 46. $N_2^+(1^-)(0,1)$ R-branch rotational spectrum, $\hat{x}$ = 28.5, test condition 2S.
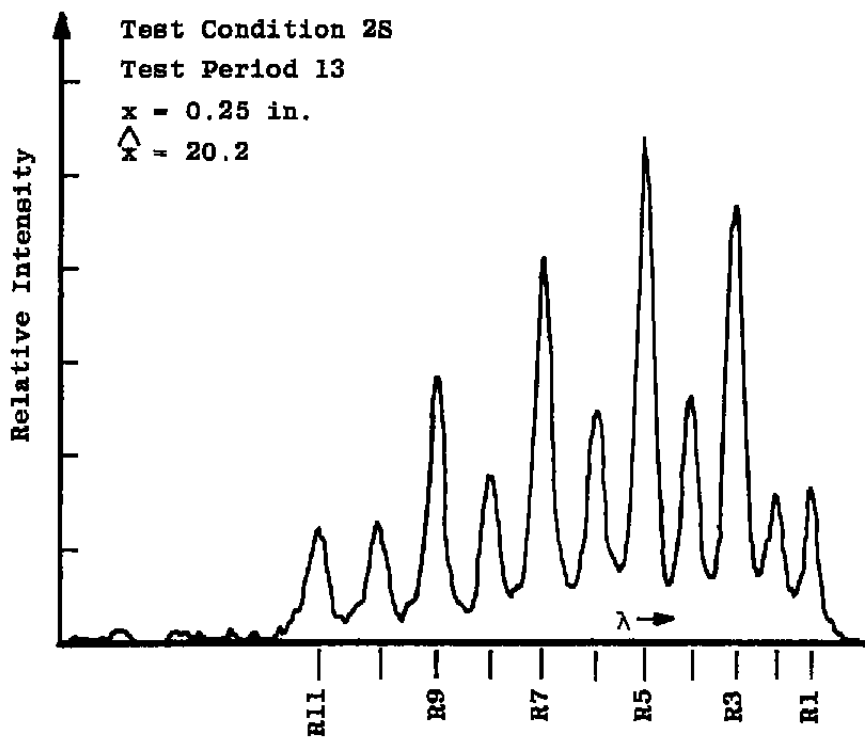
Figure 47. $N_2^+(1^-)(0,1)$ R-branch rotational spectrum, $\hat{x} = 20.2$, test condition 2S.
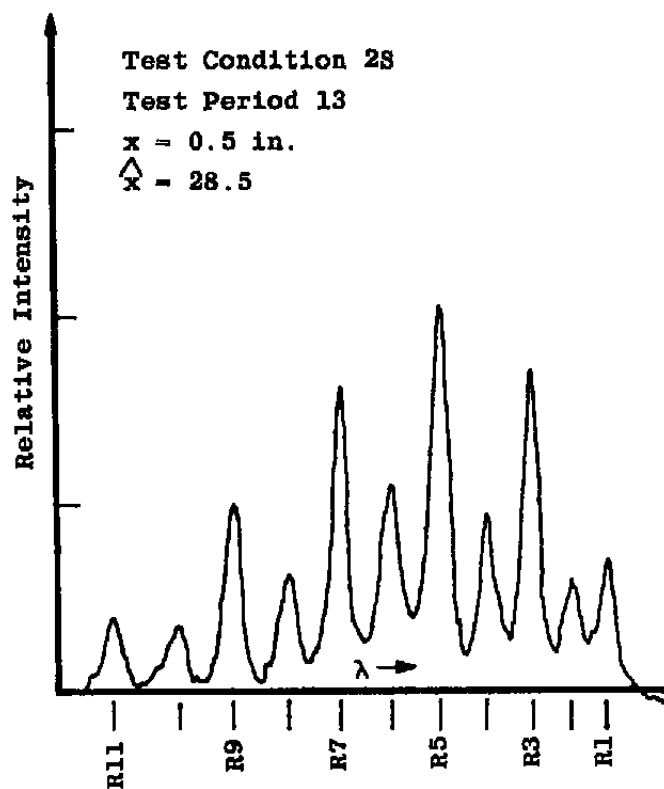
Figure 48. $N_2^+(1^-)(0,1)$ R-branch rotational spectrum, $\widehat{x} = 28.5$, test condition 2S.
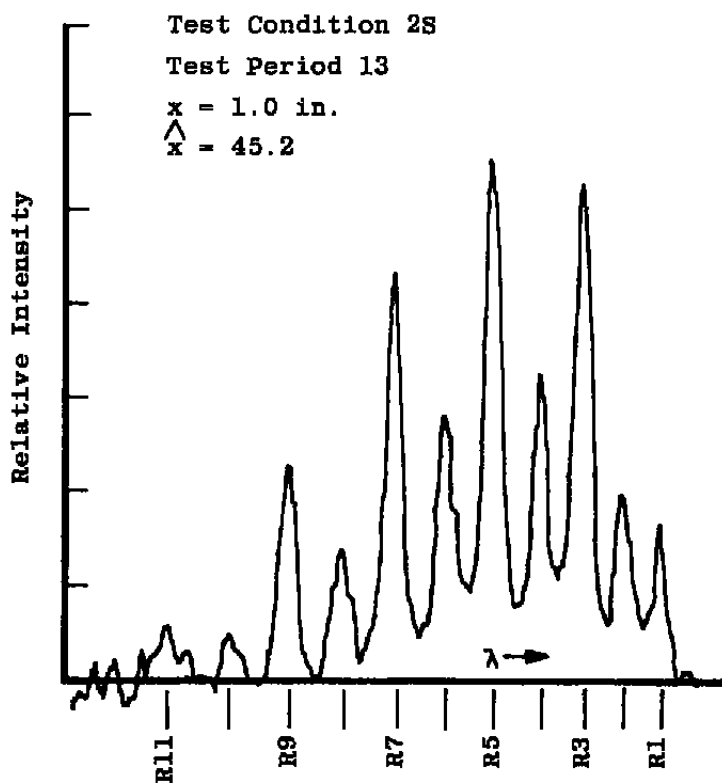
Figure 49. $N_2^+(1^-)(0,1)$ R-branch rotational spectrum, $\widehat{x}$ = 45.2, test condition 2S.
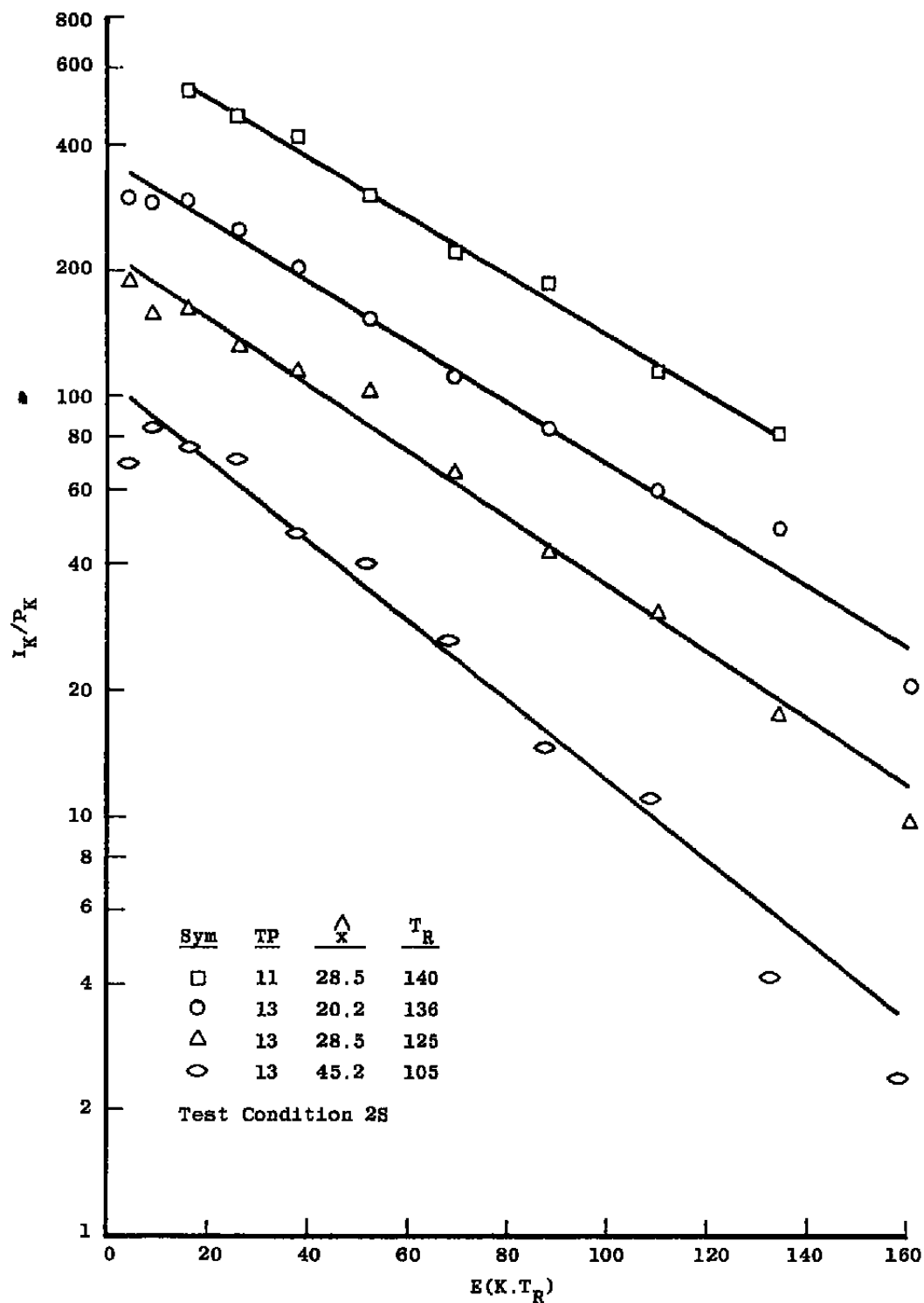
Figure 50. Boltzmann plots of $N_2^+(1^-)(0,1)$ R-branch rotational line peak height intensities.

113
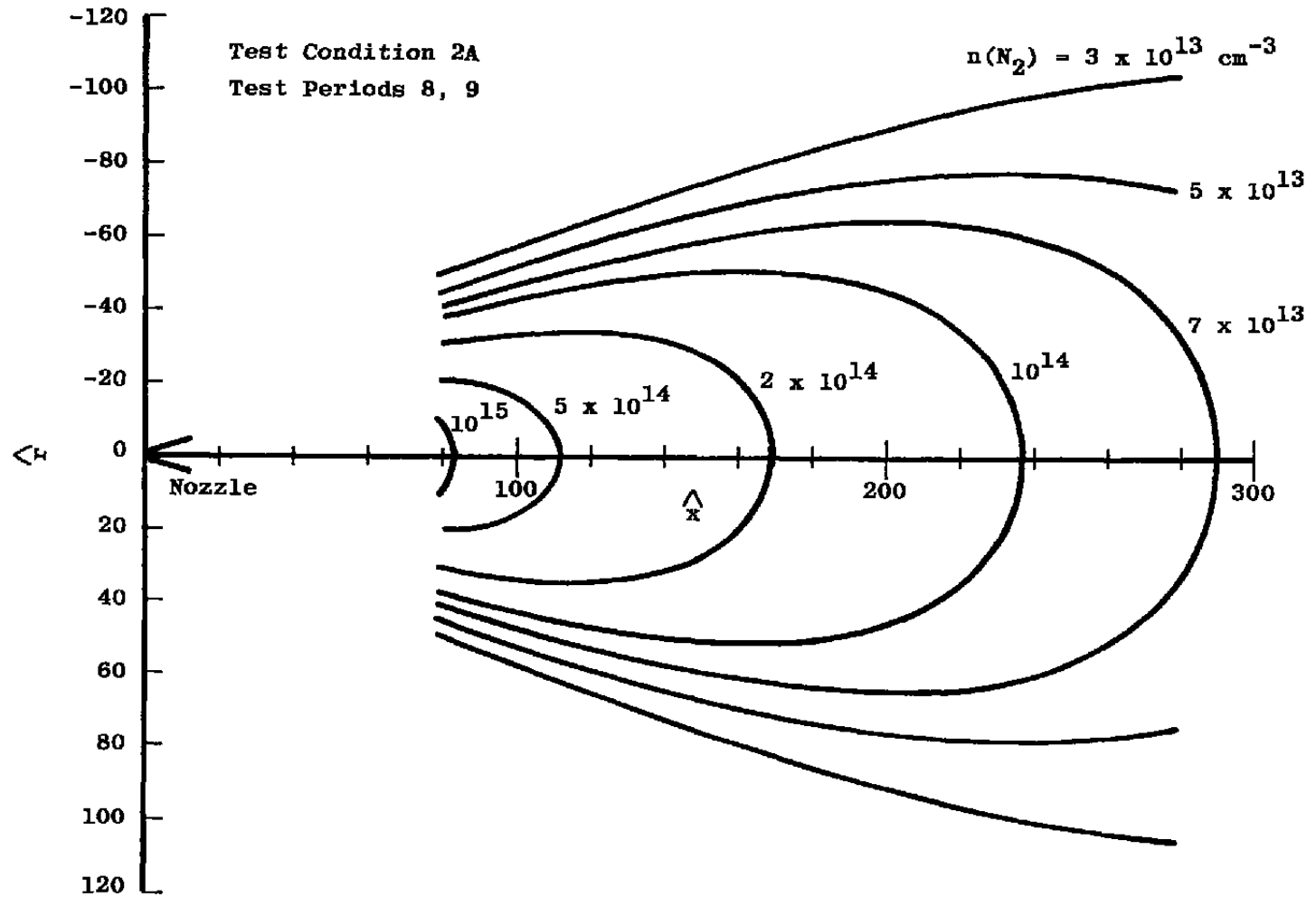
Figure 51. N_2 isodensity map, test condition 2A.
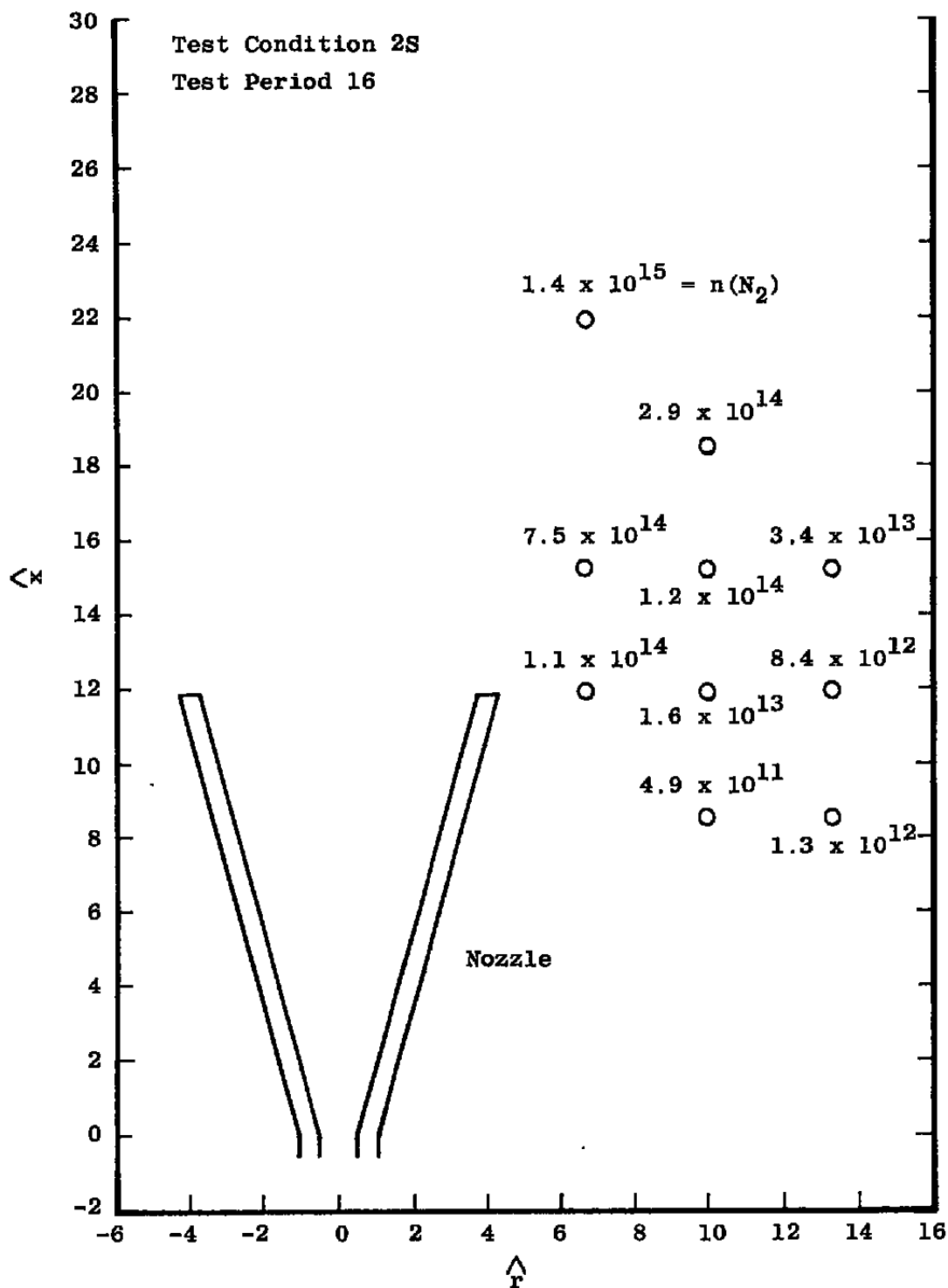
Figure 52. N_2 number density in backflow region.
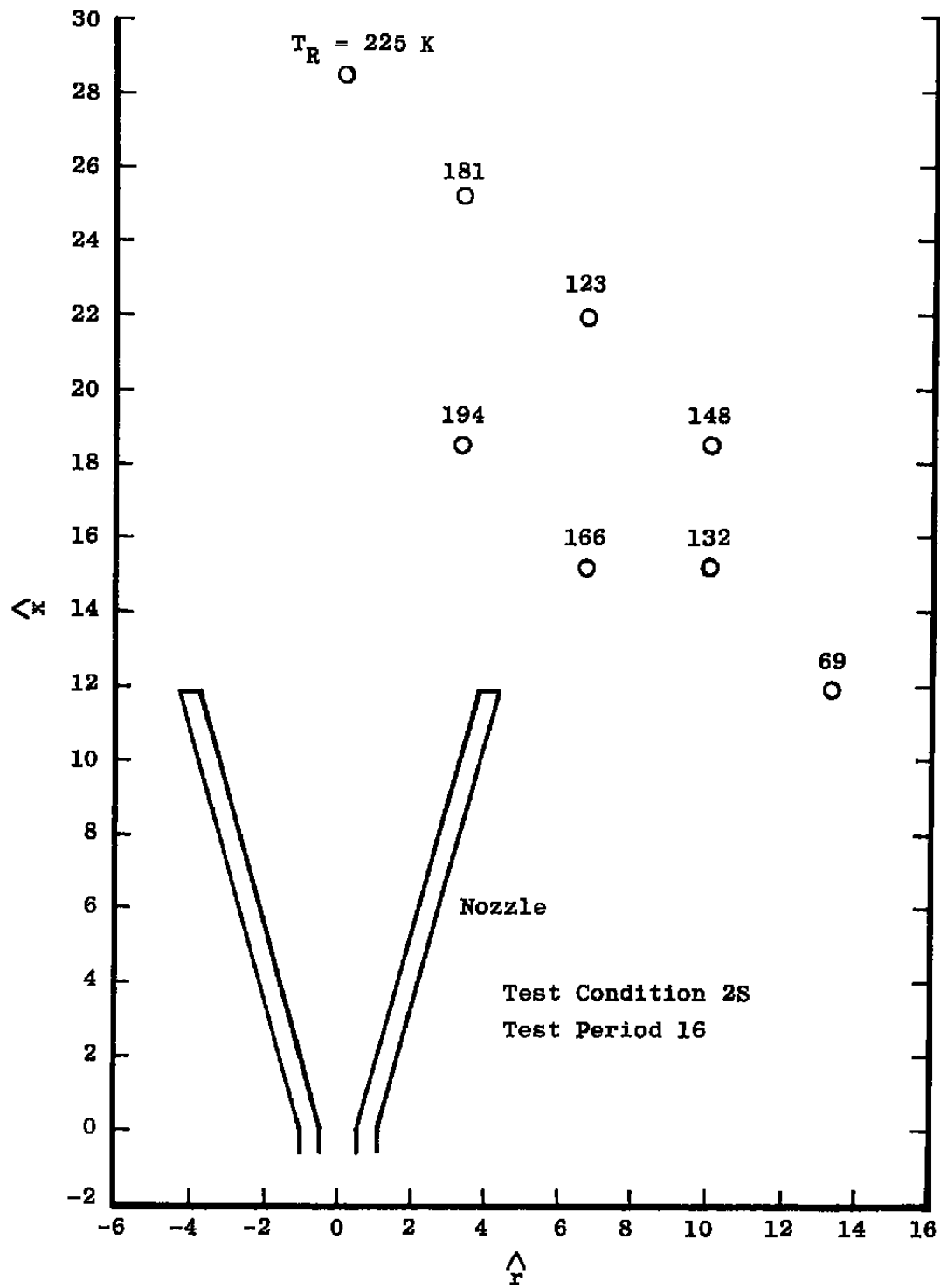
Figure 53. Rotational temperature in backflow region.
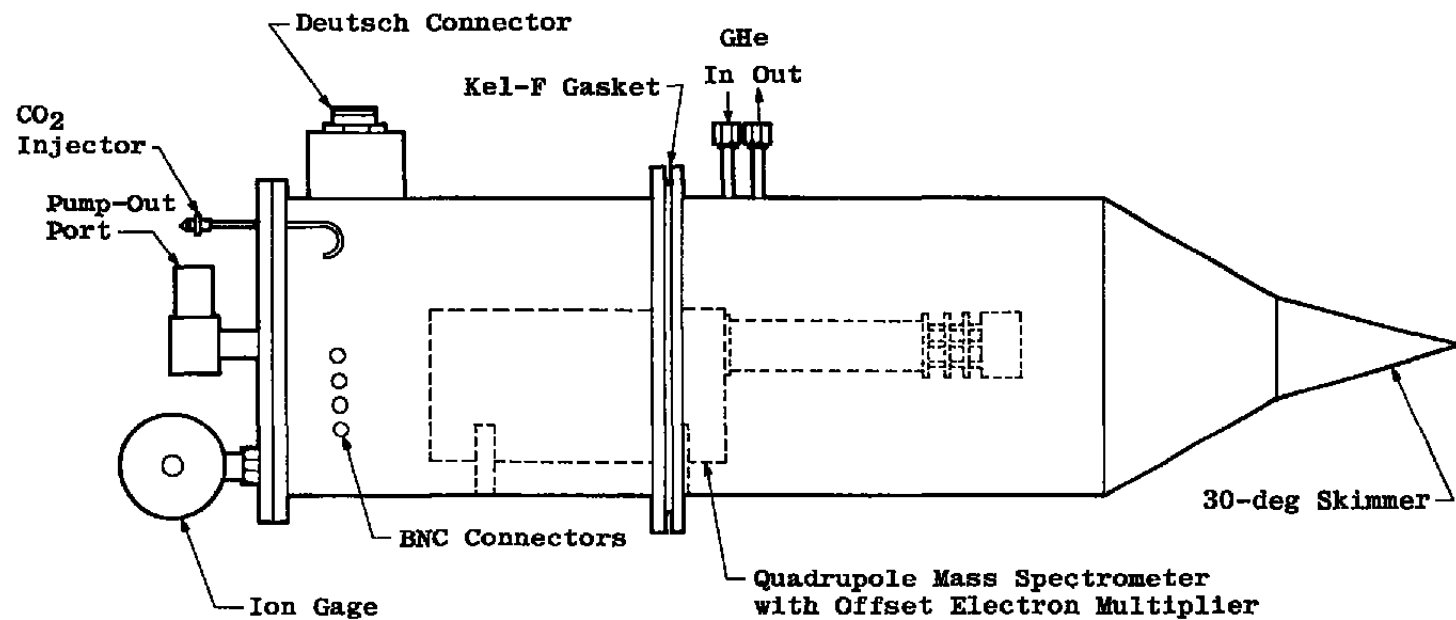
Figure 54. Schematic of mass spectrometer probe.
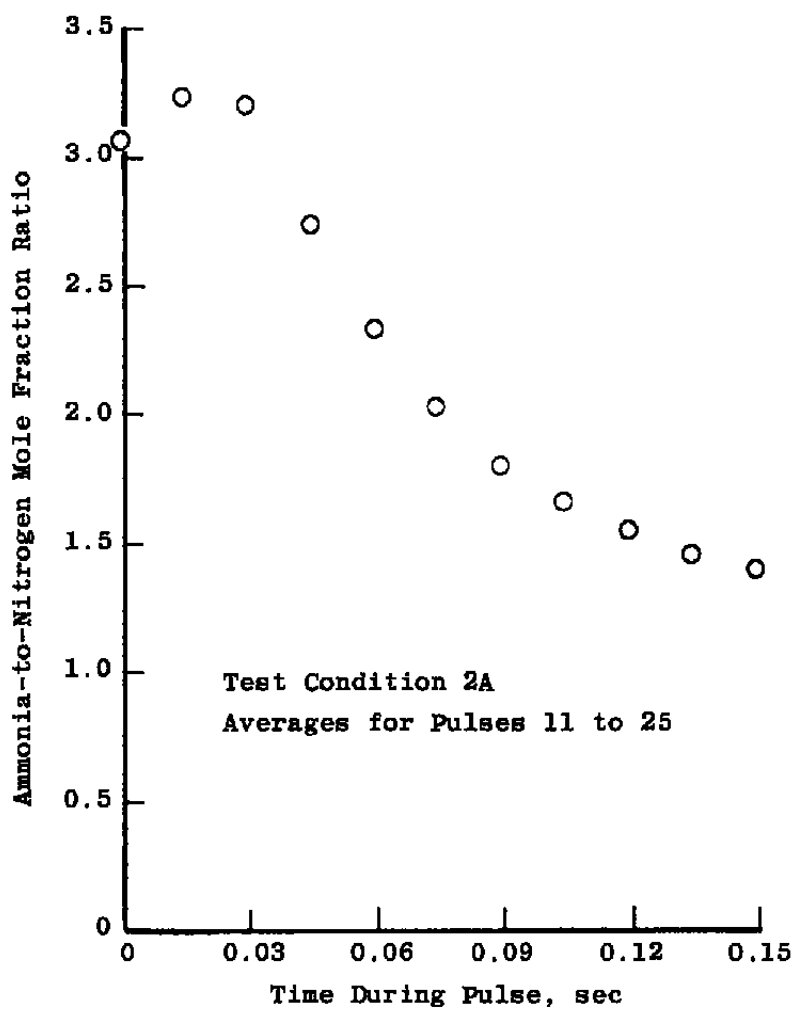
Figure 55. Variation of mole fraction ratio [NH_3/N_2] within a thruster pulse.
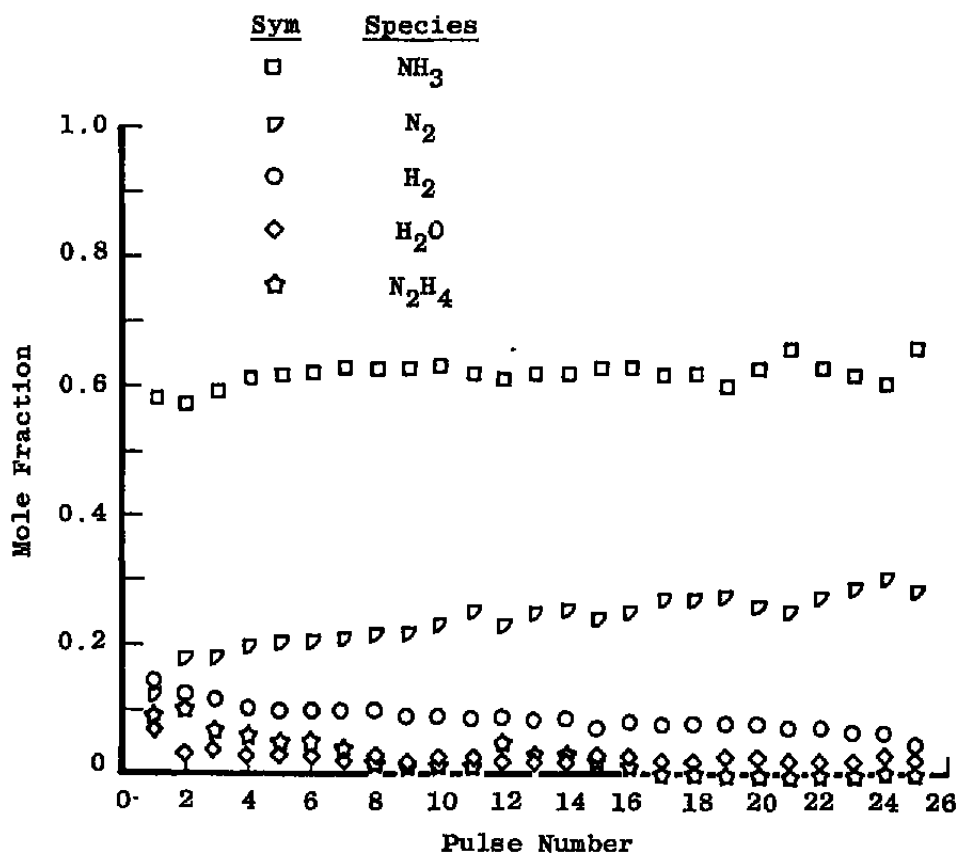
Figure 56. Species variation with pulse, condition 2A.
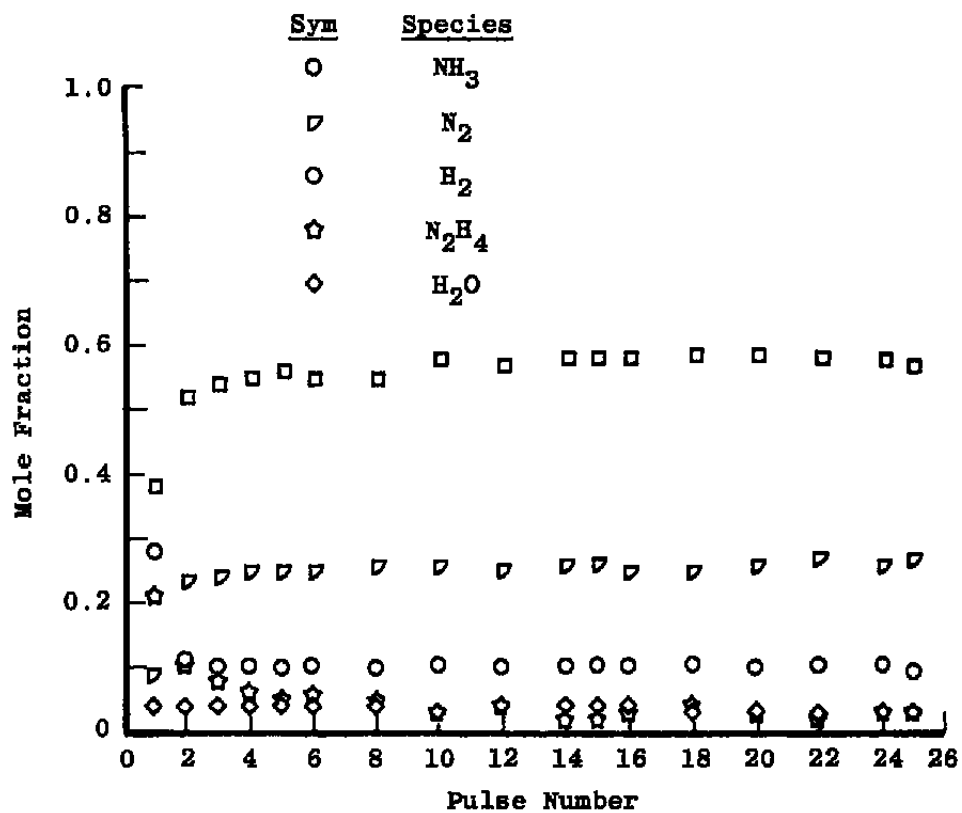
Figure 57. Species variation with pulse, condition 2B.
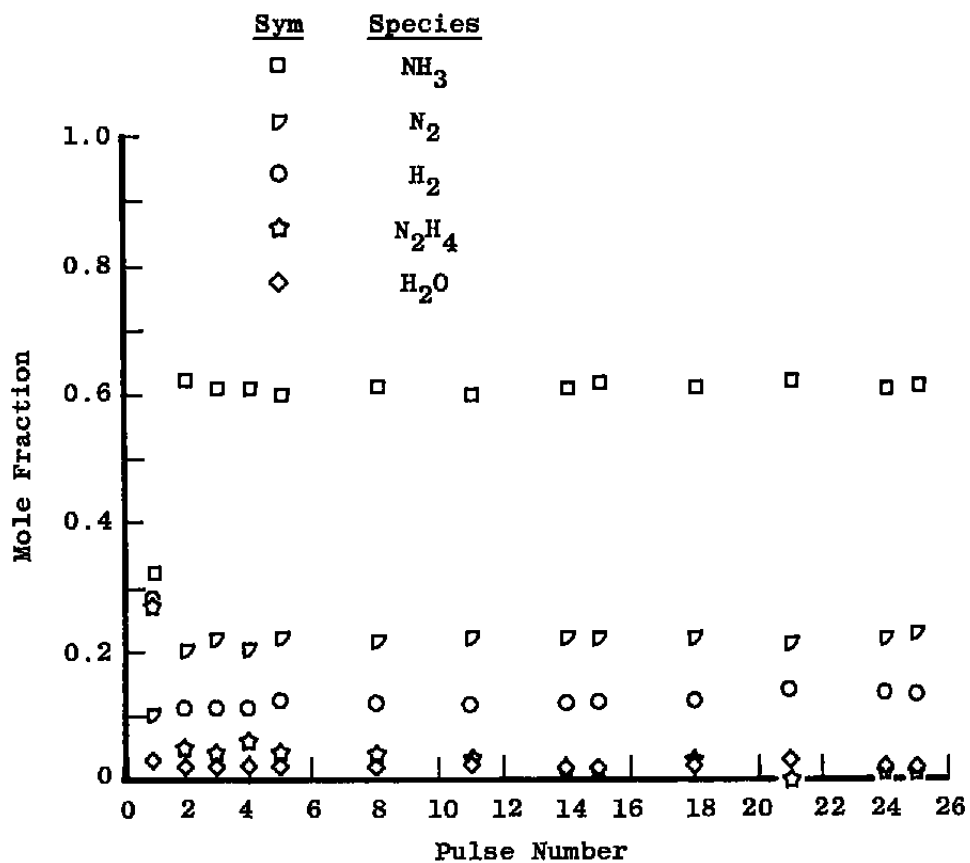
Figure 58. Species variation with pulse, condition 2C.
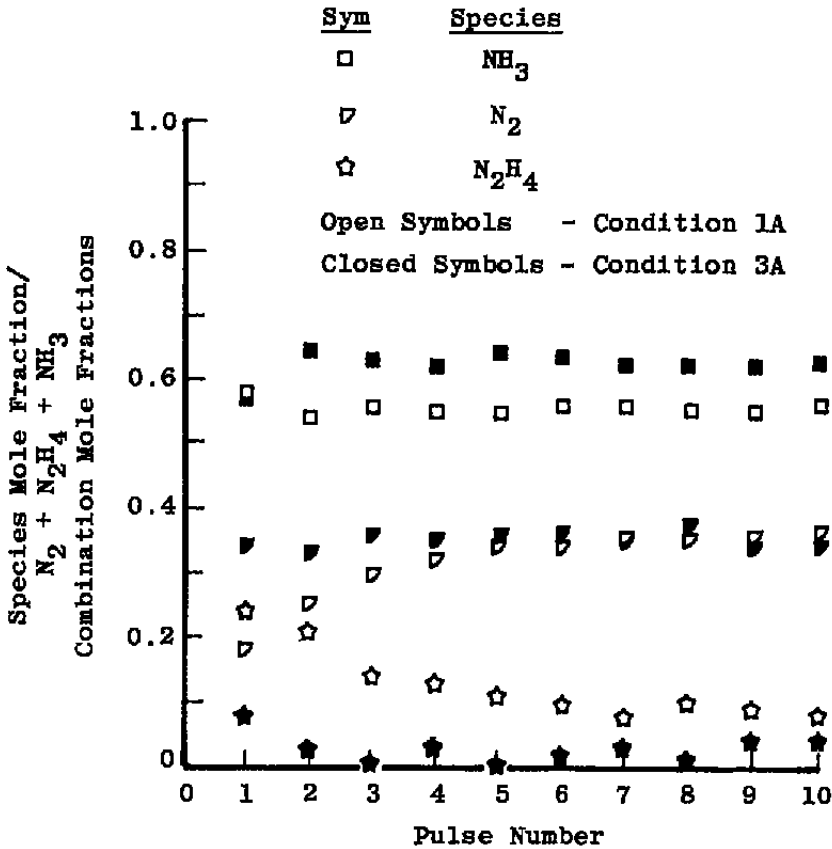
Figure 59. Species variation with pulse, conditions 1A and 3A.
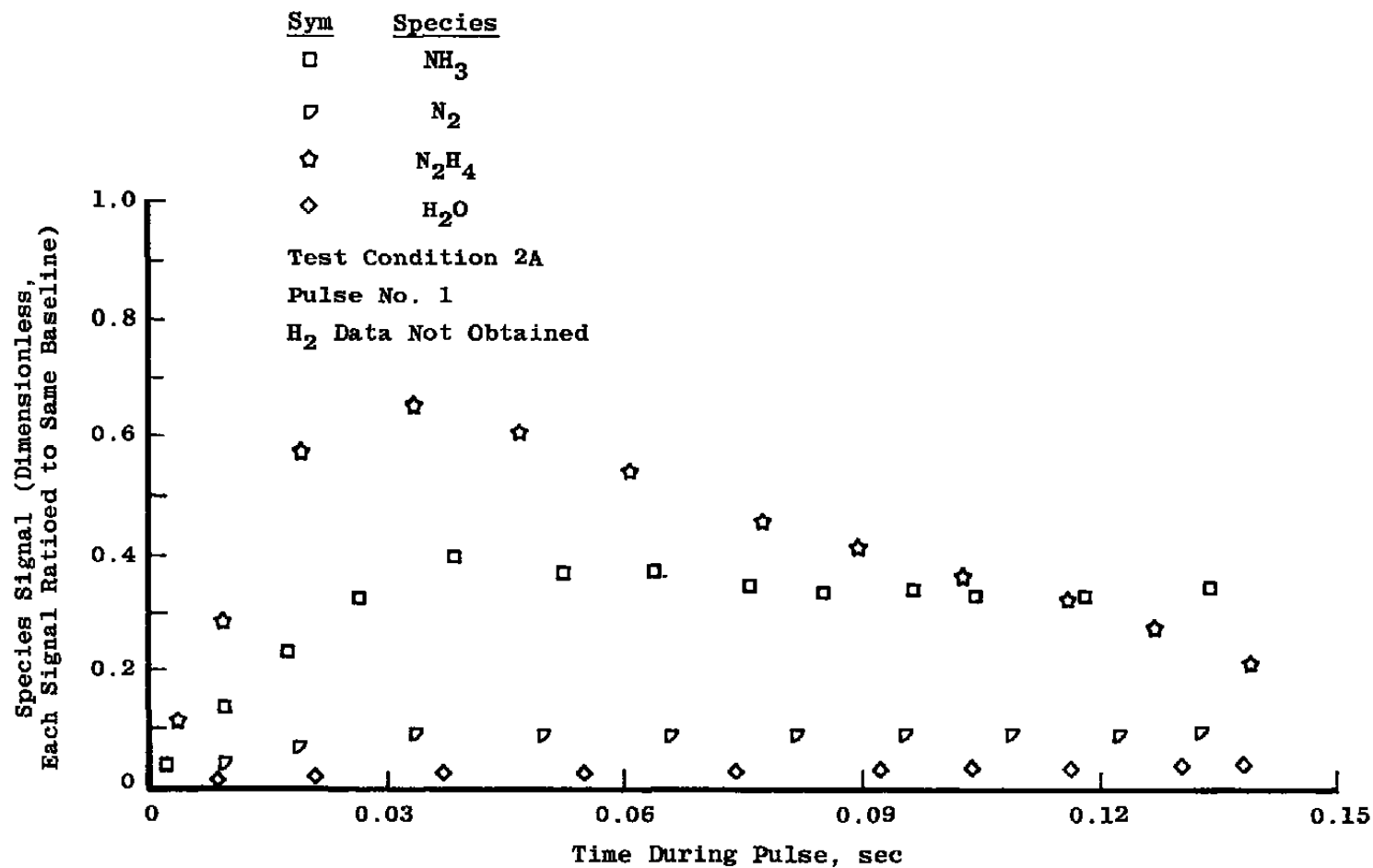
Figure 60. Species variation within pulse No. 1, condition 2A.
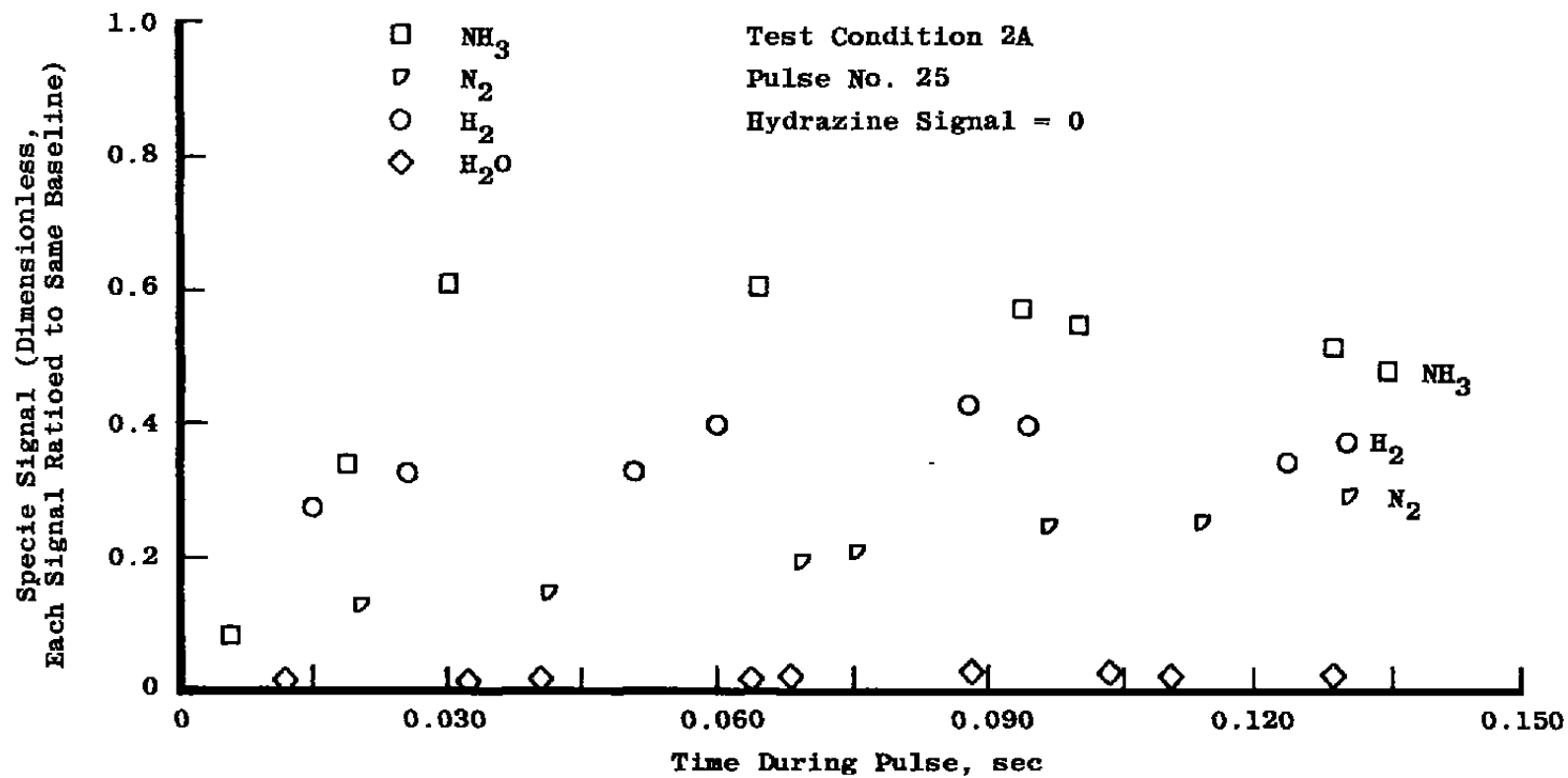
Figure 61. Species variation within pulse No. 25, condition 2A.
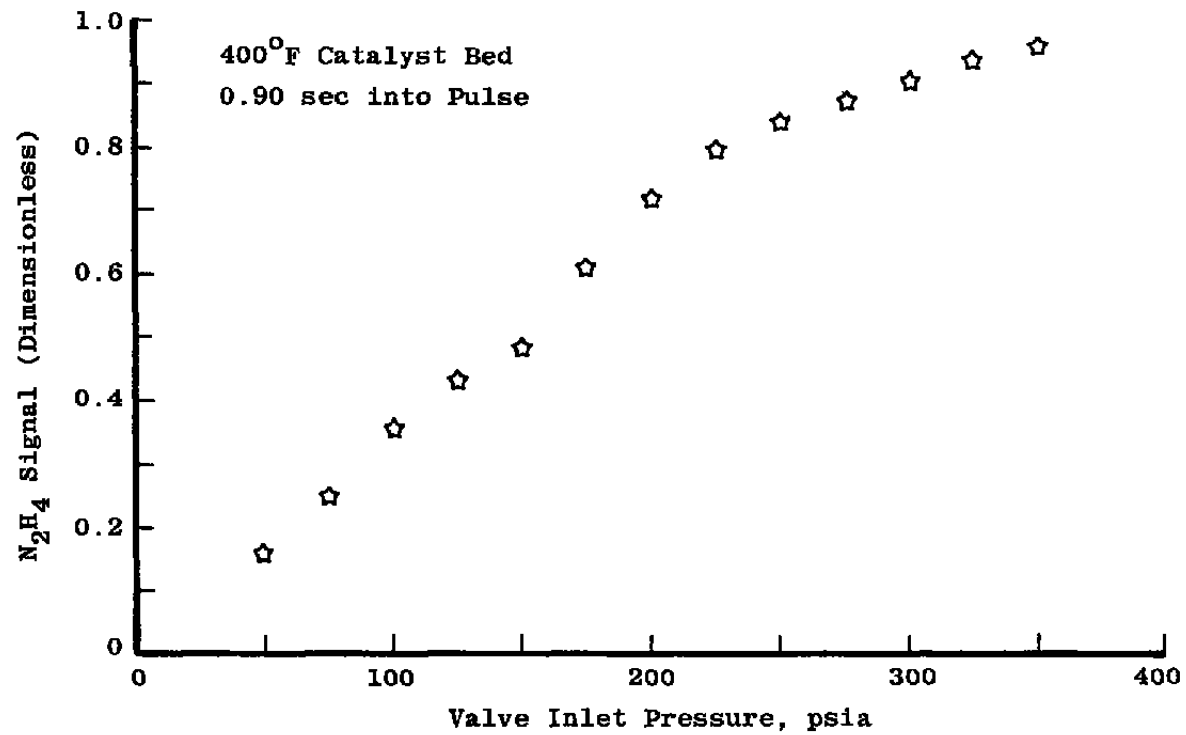
Figure 62. Hydrazine in plume for pulse No. 1 as a function of inlet pressure.

Common Electrode

2.54 cm (1.0 in.)

1.9 cm (0.75 in.)

3.5 cm (1.4 in.)

2.54 cm (1.0 in.)

1.9 cm (0.75 in.)

1.28 cm (0.5 in.)

2.3 cm (0.9 in.)

3.8 cm (1.5 in.)

Crystal Thermocouple

3.5 cm (1.4 in.)

5.85 cm (2.3 in.)

3.8 cm (1.5 in.)

Crystal Doublet

Hair Brush Mounting

Crystal Mounting Block

Connector

Electronics

Mounting Block
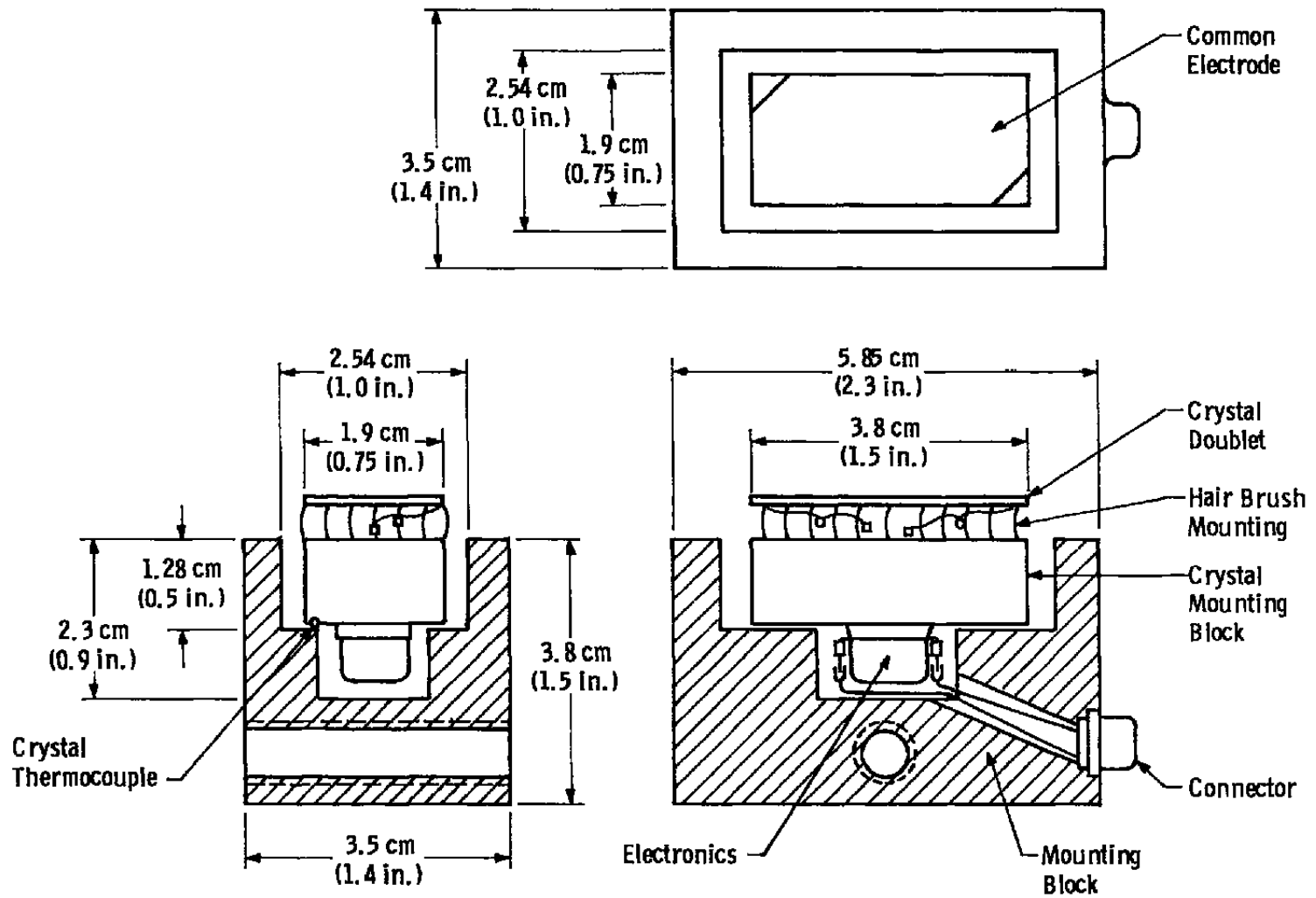
From Ref. 19

Figure 63. Schematic diagram of a variable temperature QCM unit.

Mass
Spectrometer

QCM
Surface

15.25 in.

30 deg

Laser
Beam

Axial
Penetration

Thruster
Exit Plane

Thruster Cart
Extreme
Position

Chamber Axis

Mass
Spectrometer

QCM
Surface

44-5/8 in.

Thruster Exit
Plane; Cart
in Extreme
Position

Chamber Axis
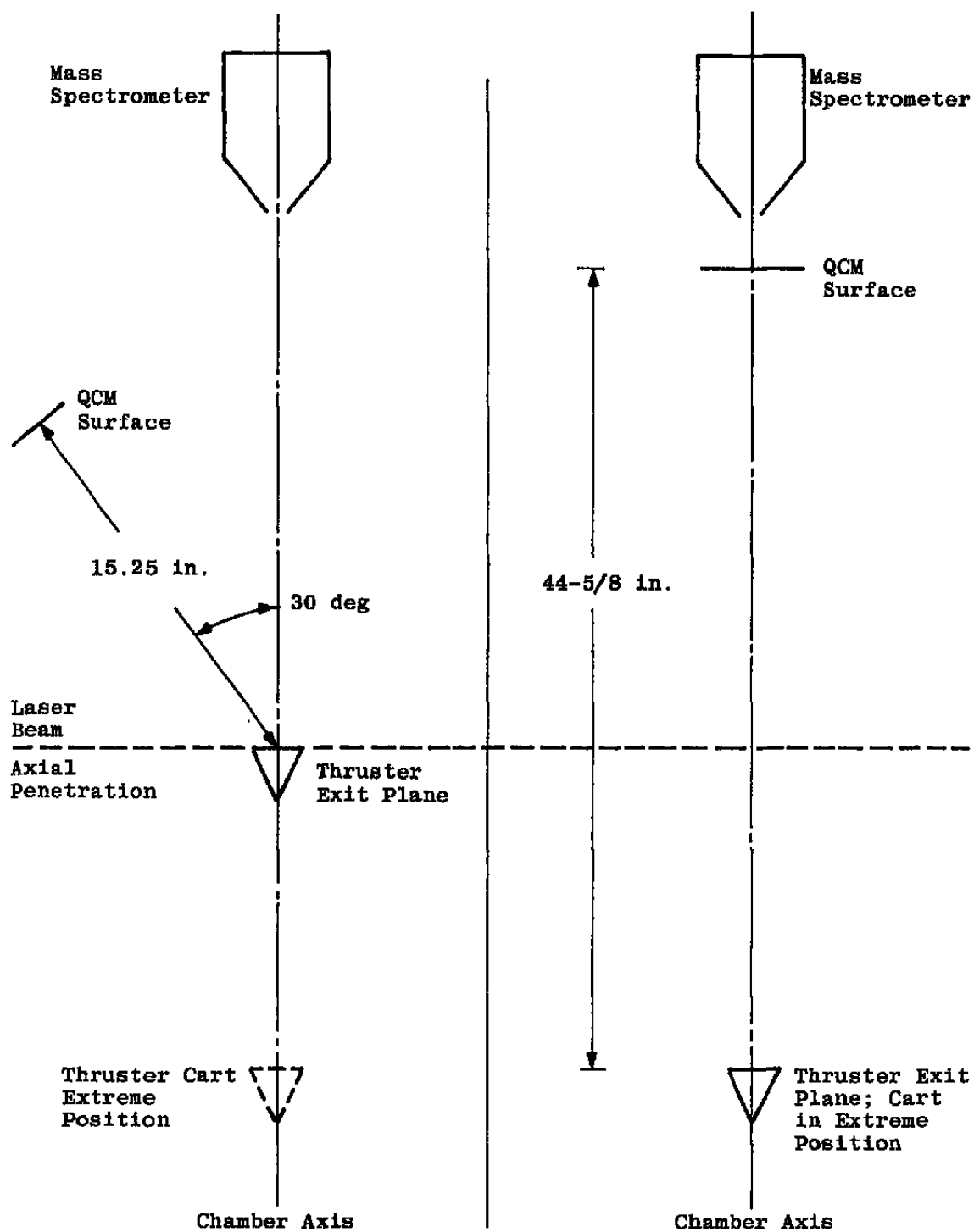
Figure 64. QCM-mass spectrometer configuration for test phases A and B.

Figure 65. QCM reference position in thruster plume.
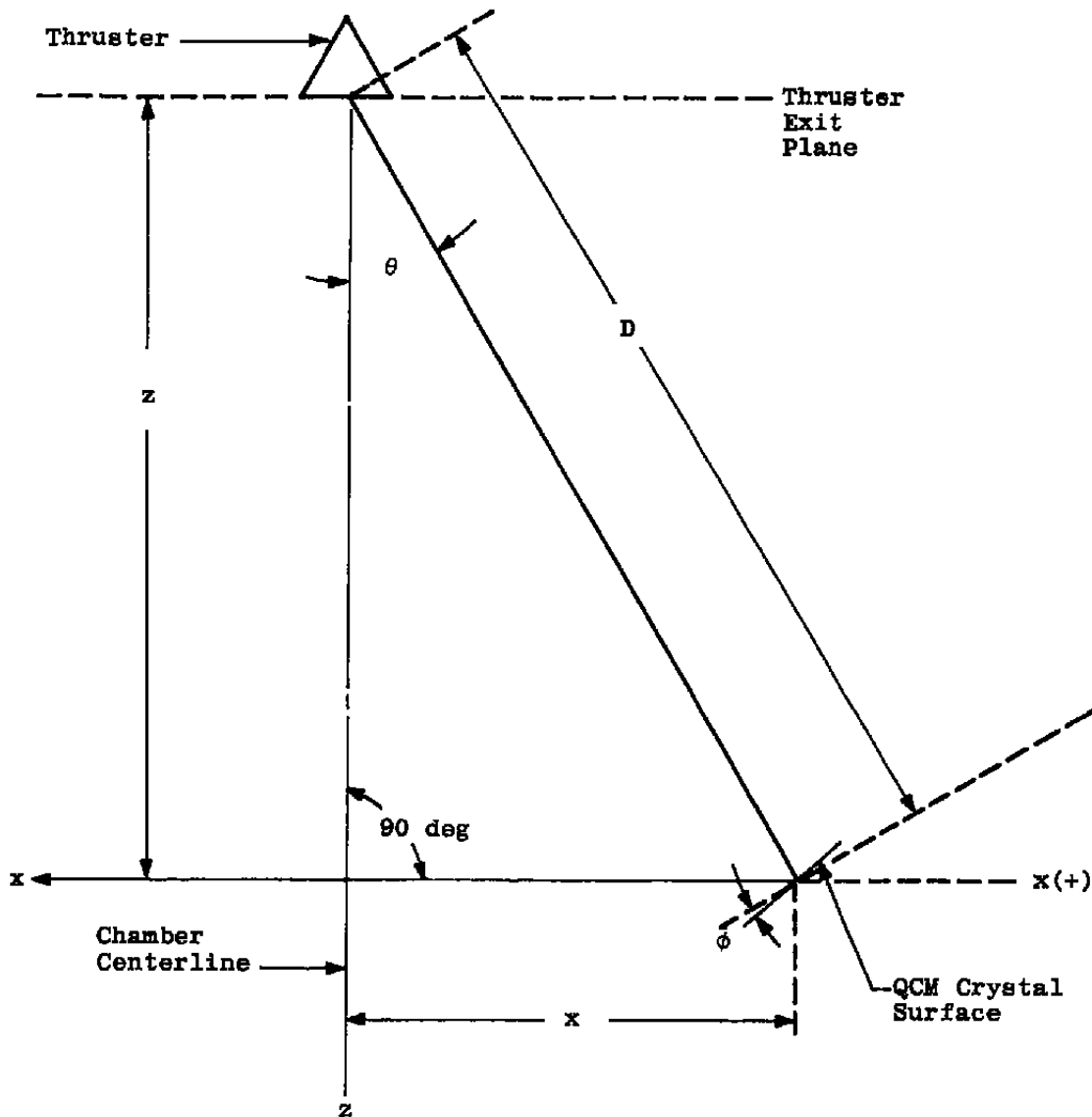
Test Phase A TP:1-11

QCM position in thruster plume is given by (z, x) where:

z = distance along the thruster/chamber center measured from nozzle exit plane.

x = perpendicular distance from thruster centerline to the center of the crystal surface. (Note: x is positive in direction of crystal surface.)

$\phi = 30 \deg - \theta$

Test Phase B TP:13-16

QCM surface is perpendicular to and centered on the chamber/thruster centerline.

a. Block diagram
Figure 66. QCM data acquisition system.
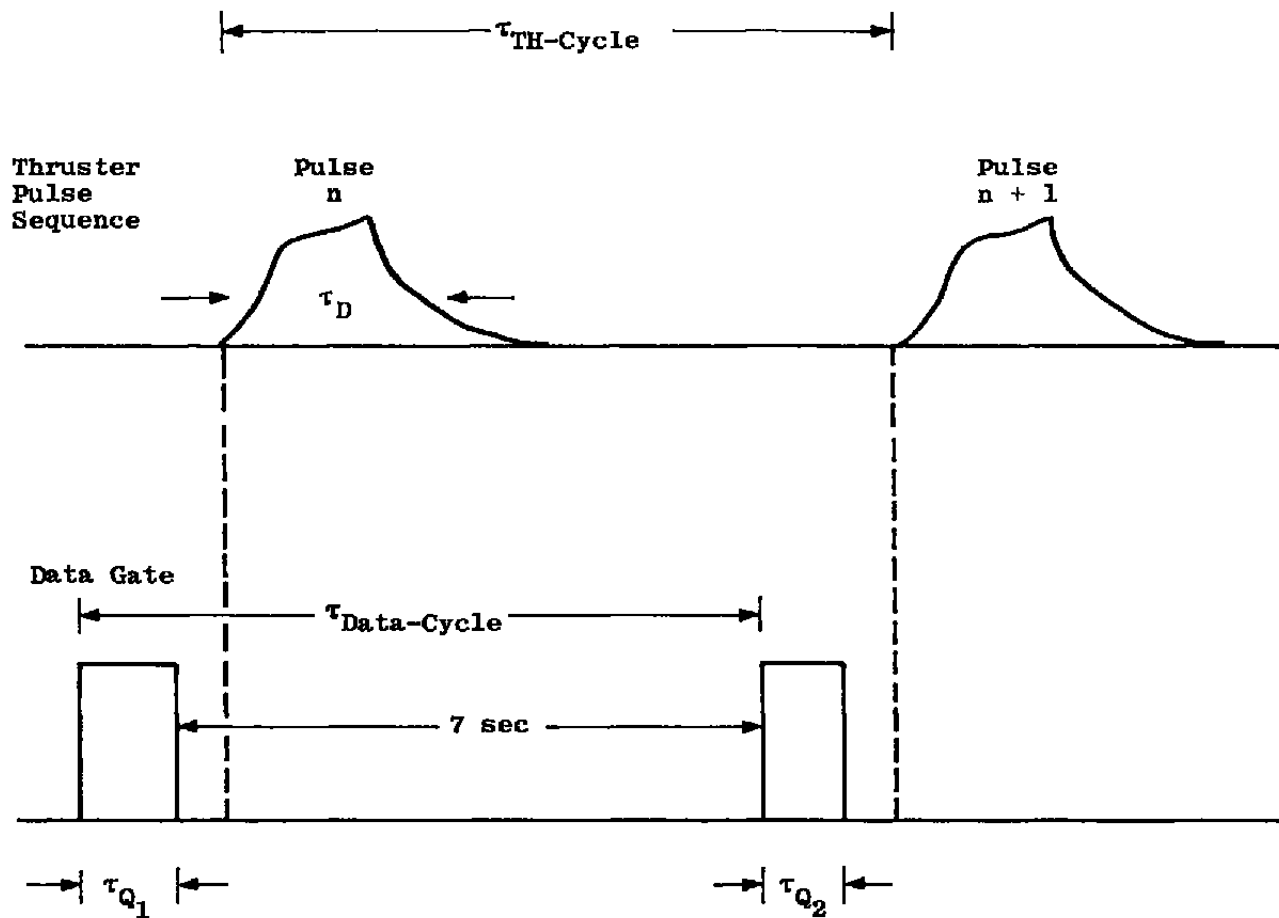
b. QCM data sequence
Figure 66. Concluded.
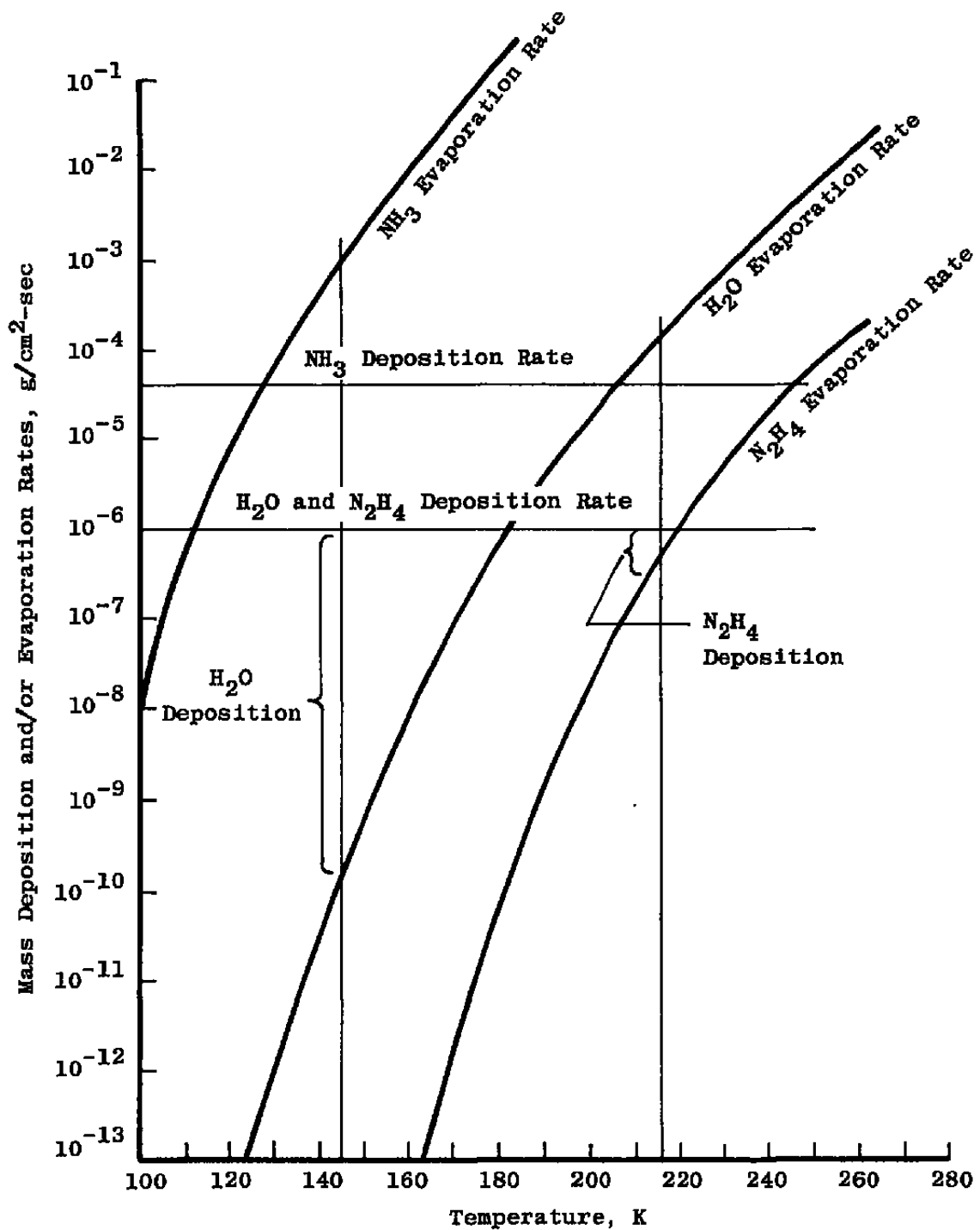
Figure 67. Deposition and/or evaporation rates versus temperature.
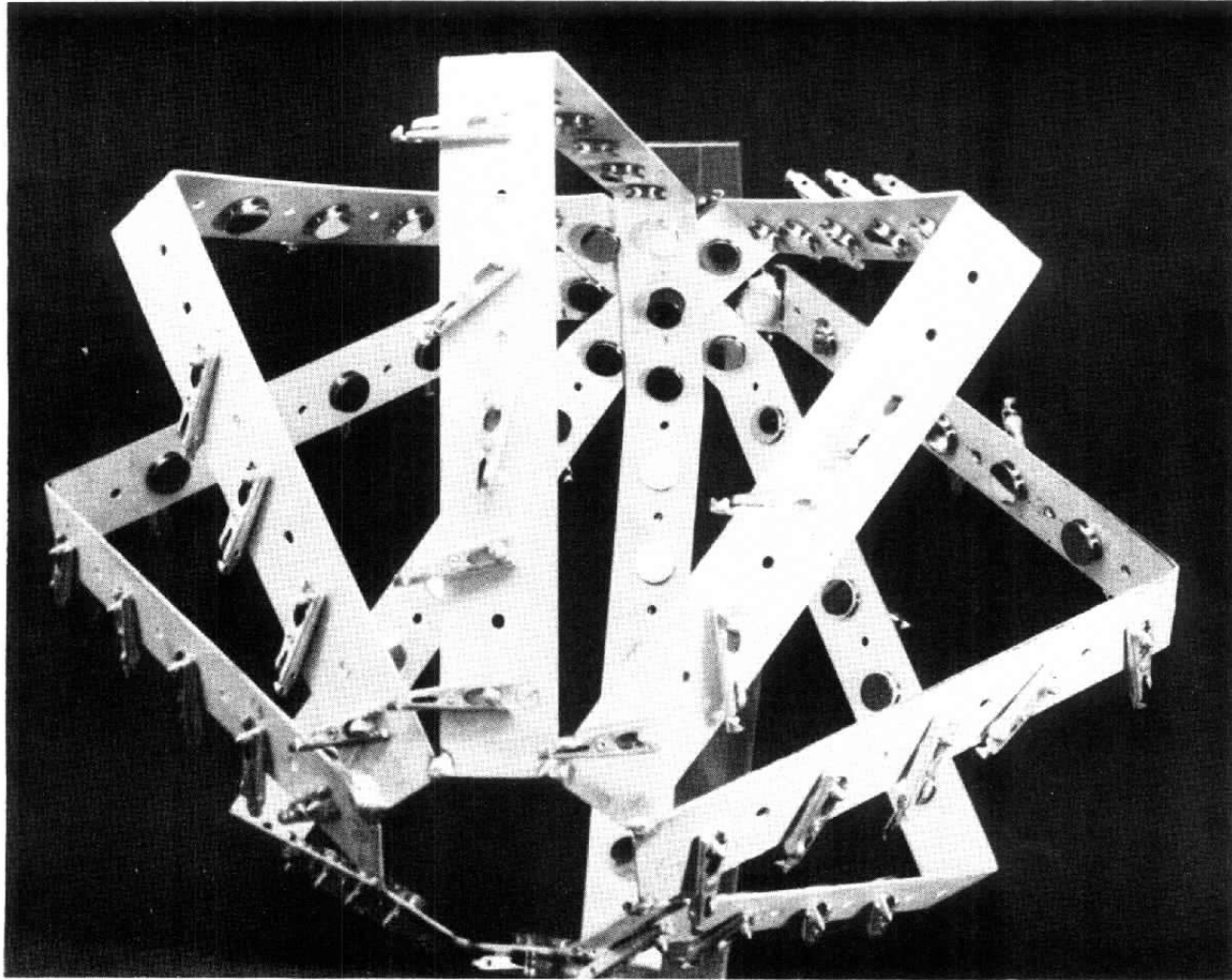
Figure 68. Particle collector.
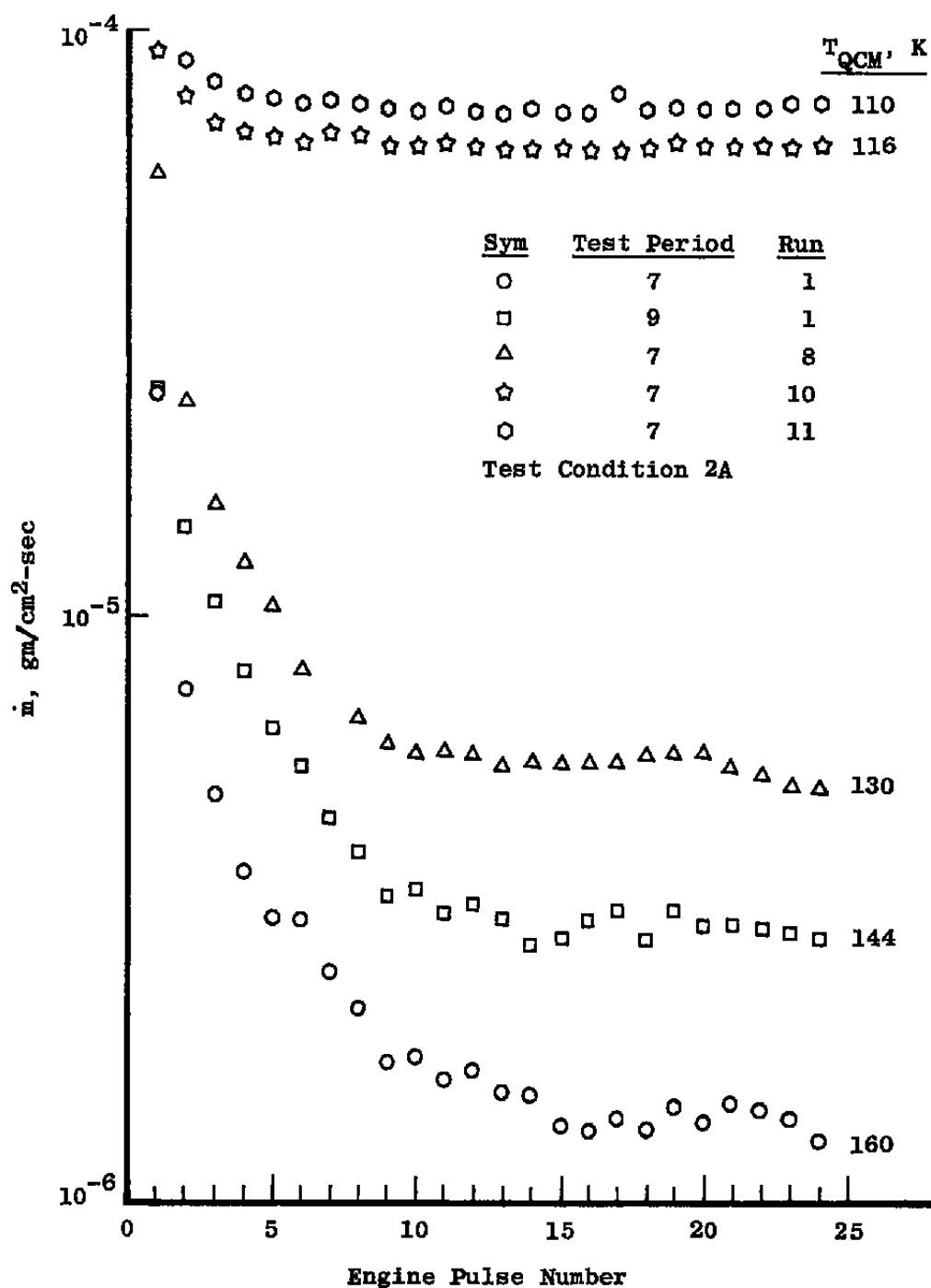
Figure 69. Mass deposition rate versus pulse number for various QCM temperatures, test condition 2A.
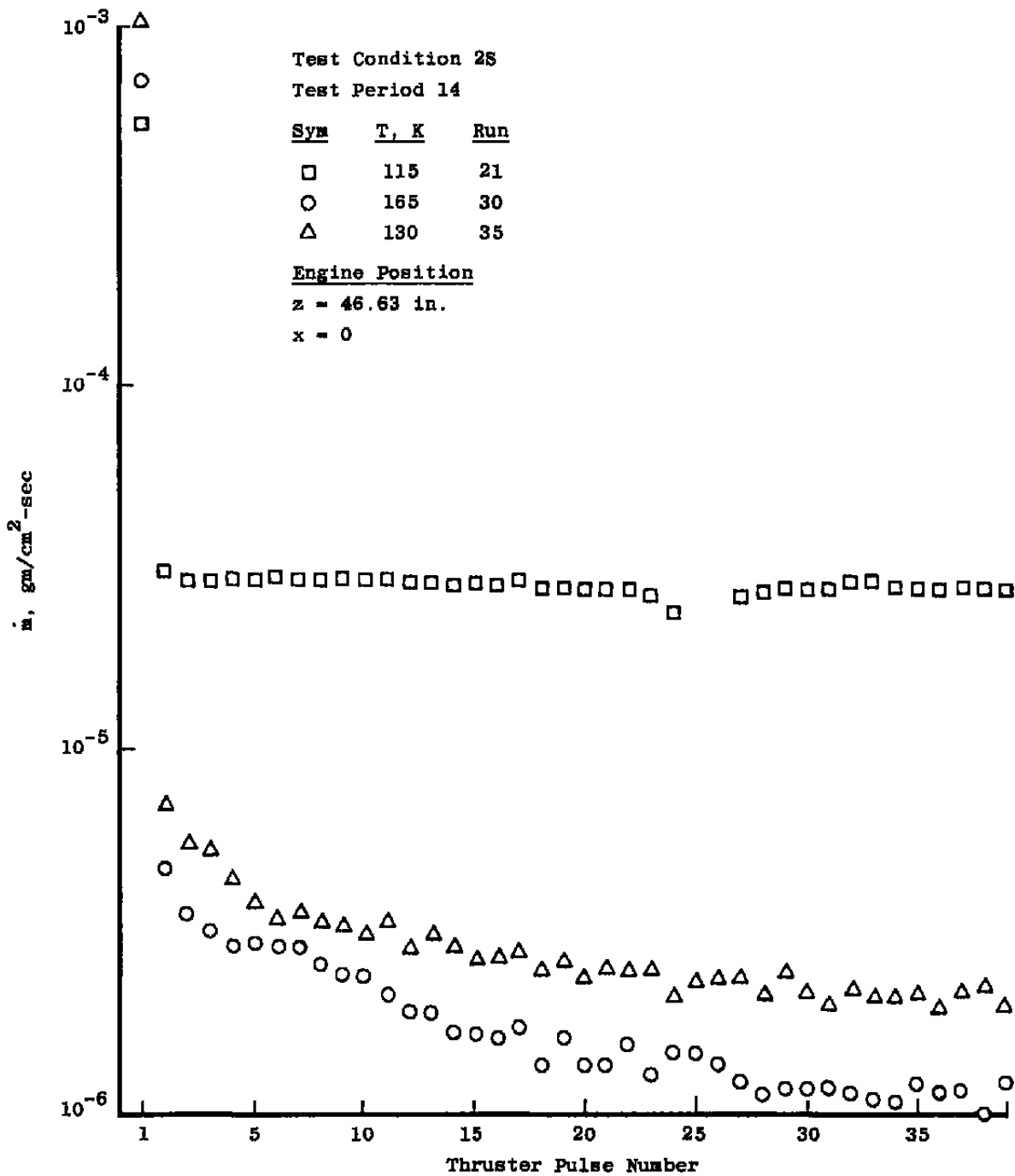
Figure 70. Mass deposition rate versus pulse number for various QCM temperatures, test condition 2S.
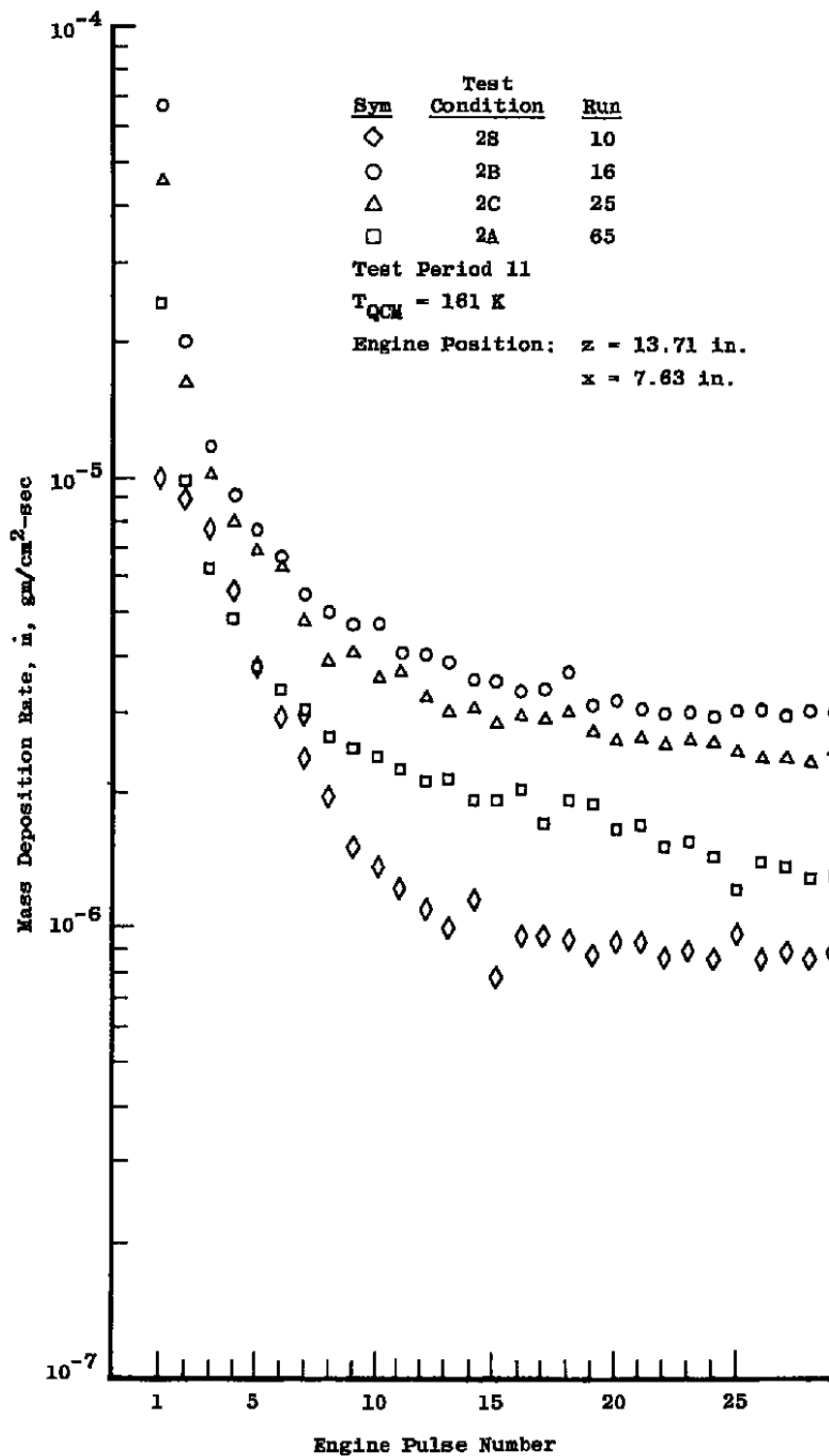
Figure 71. Mass deposition rate versus pulse number for several test conditions, $T_{QCM} = 161$ K; test conditions 2S, 2A, 2B, and 2C.
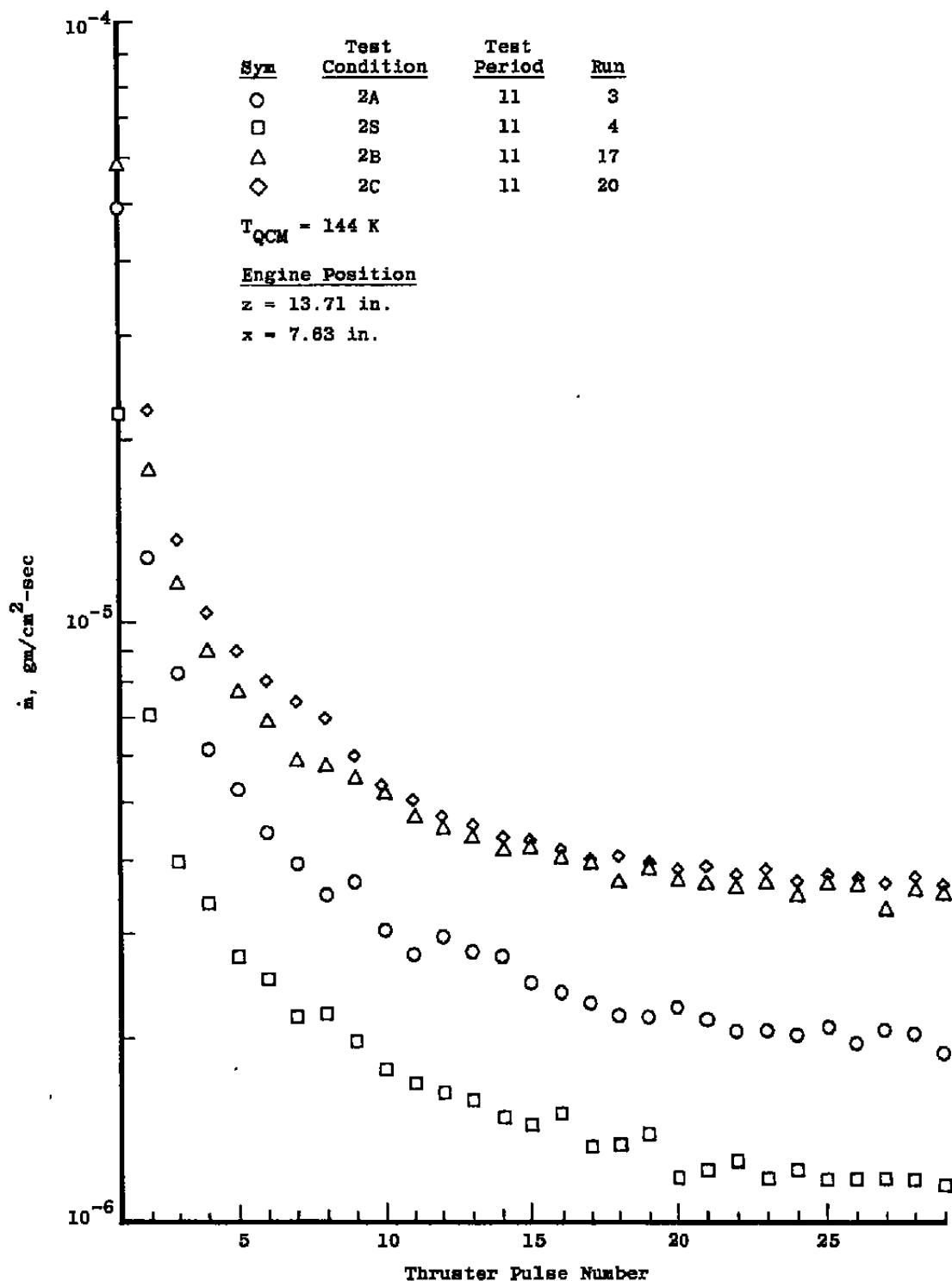
Figure 72. Mass deposition rate versus pulse number for several test conditions,
T_{QCM} = 144 K; test conditions 2S, 2A, 2B, and 2C.

136
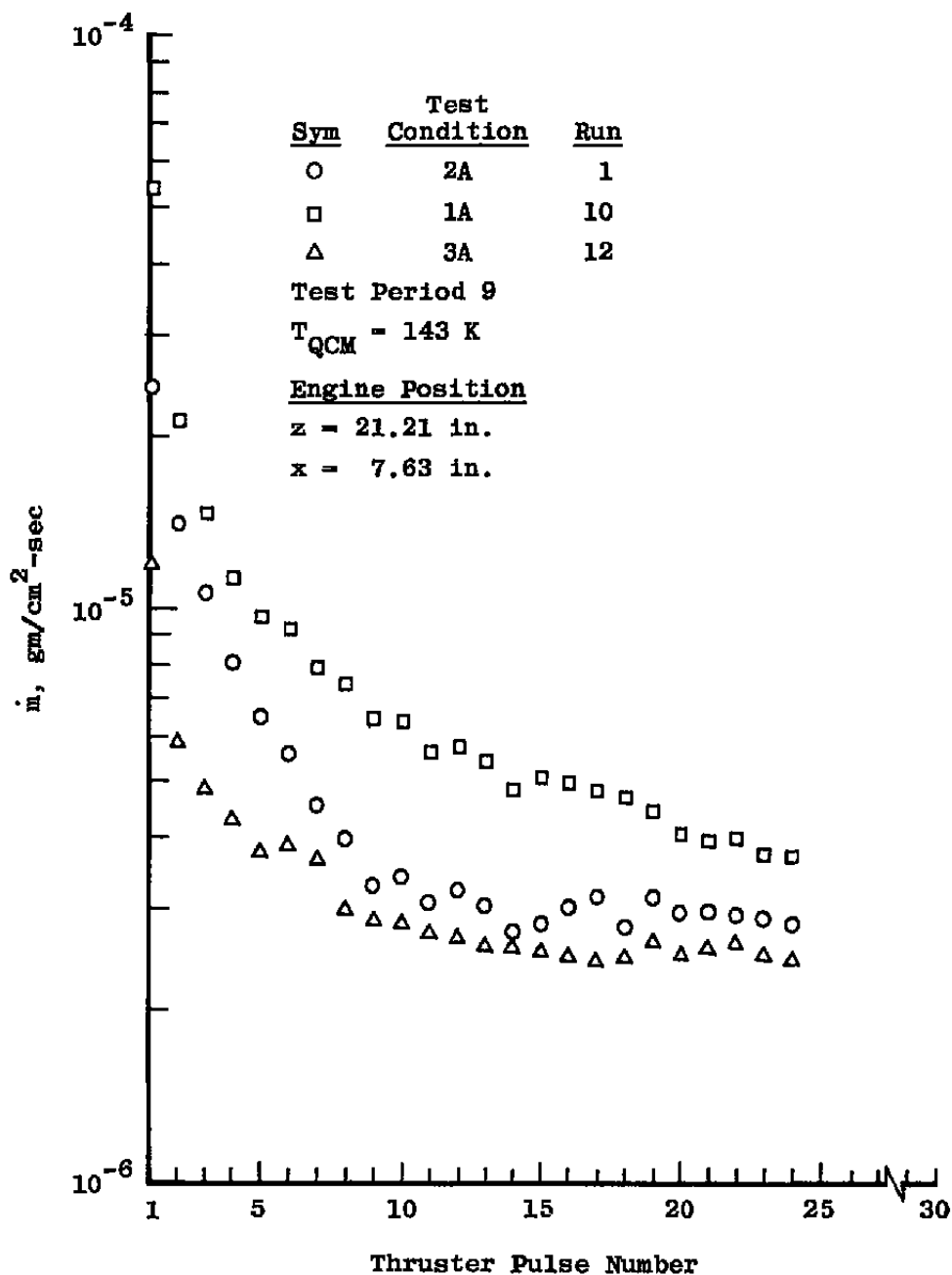
Figure 73. Mass deposition rate versus pulse number for several test conditions, T_{QCM} = 143 K; test conditions 1A, 2A, and 3A.

137
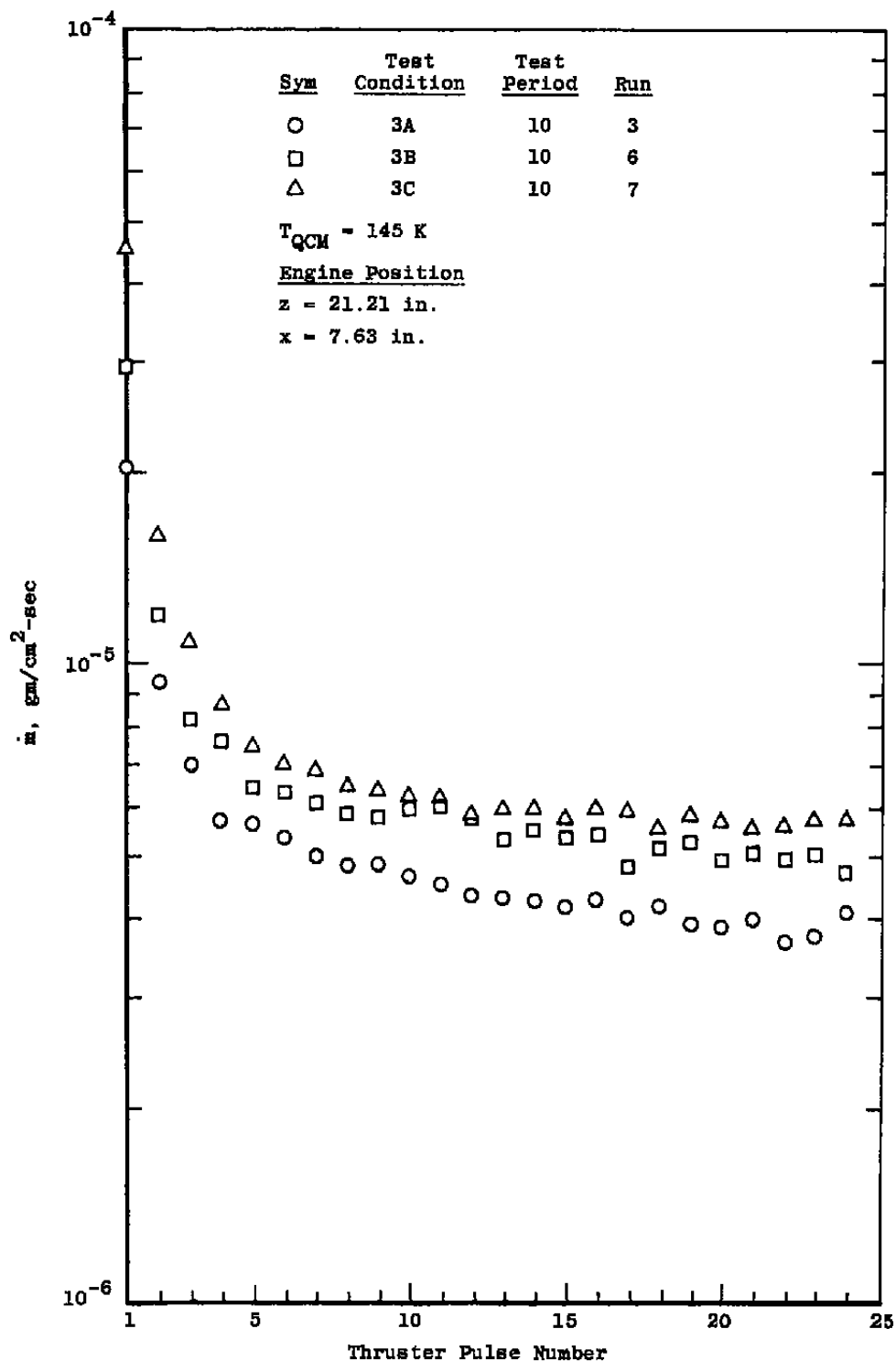
Figure 74. Mass deposition rate versus pulse number for several test conditions,
$T_{QCM} = 145$ K; test conditions 3A, 3B, and 3C.
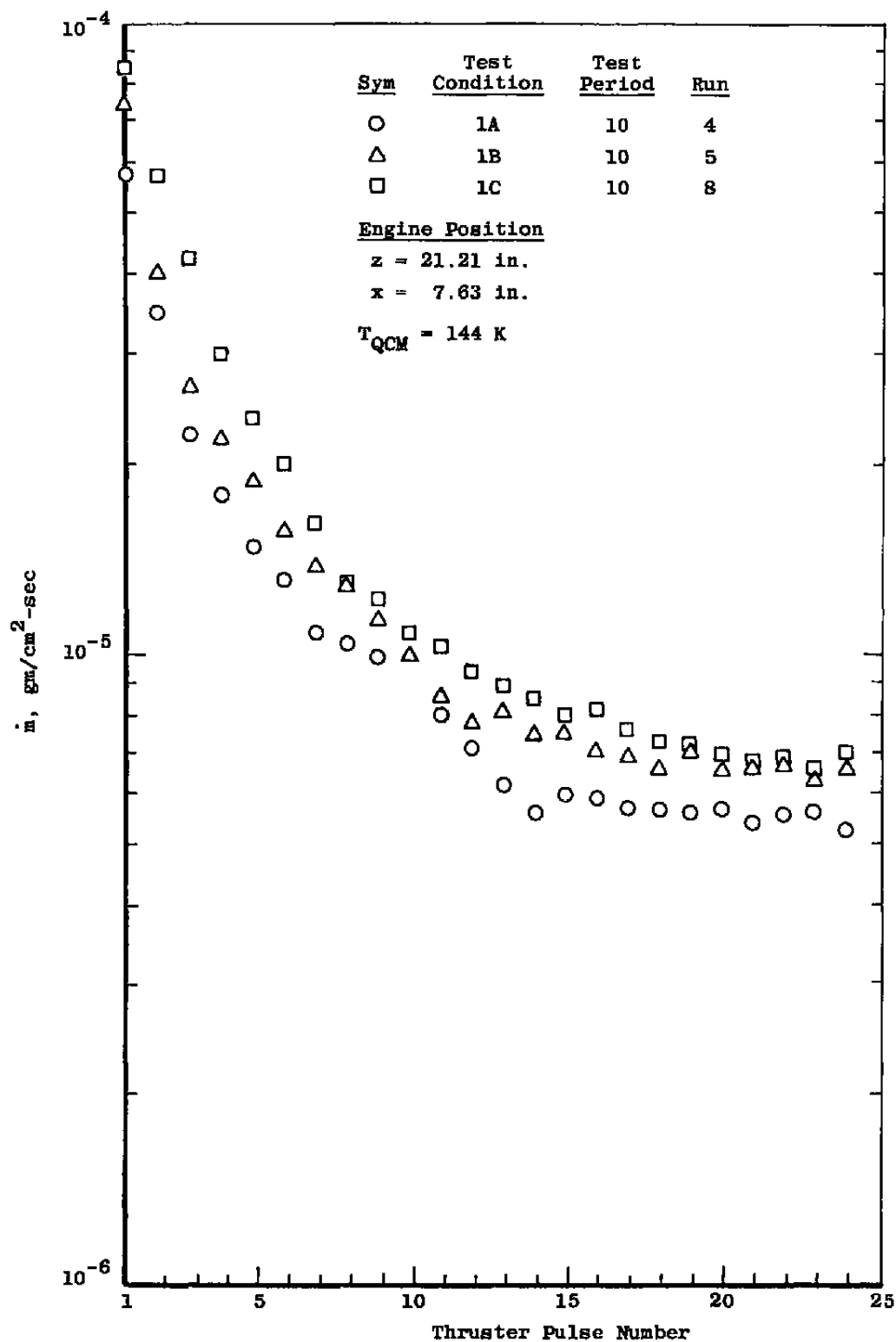
Figure 75. Mass deposition rate versus pulse number for several test conditions, T_{QCM} = 144 K; test conditions 1A, 1B, and 1C.
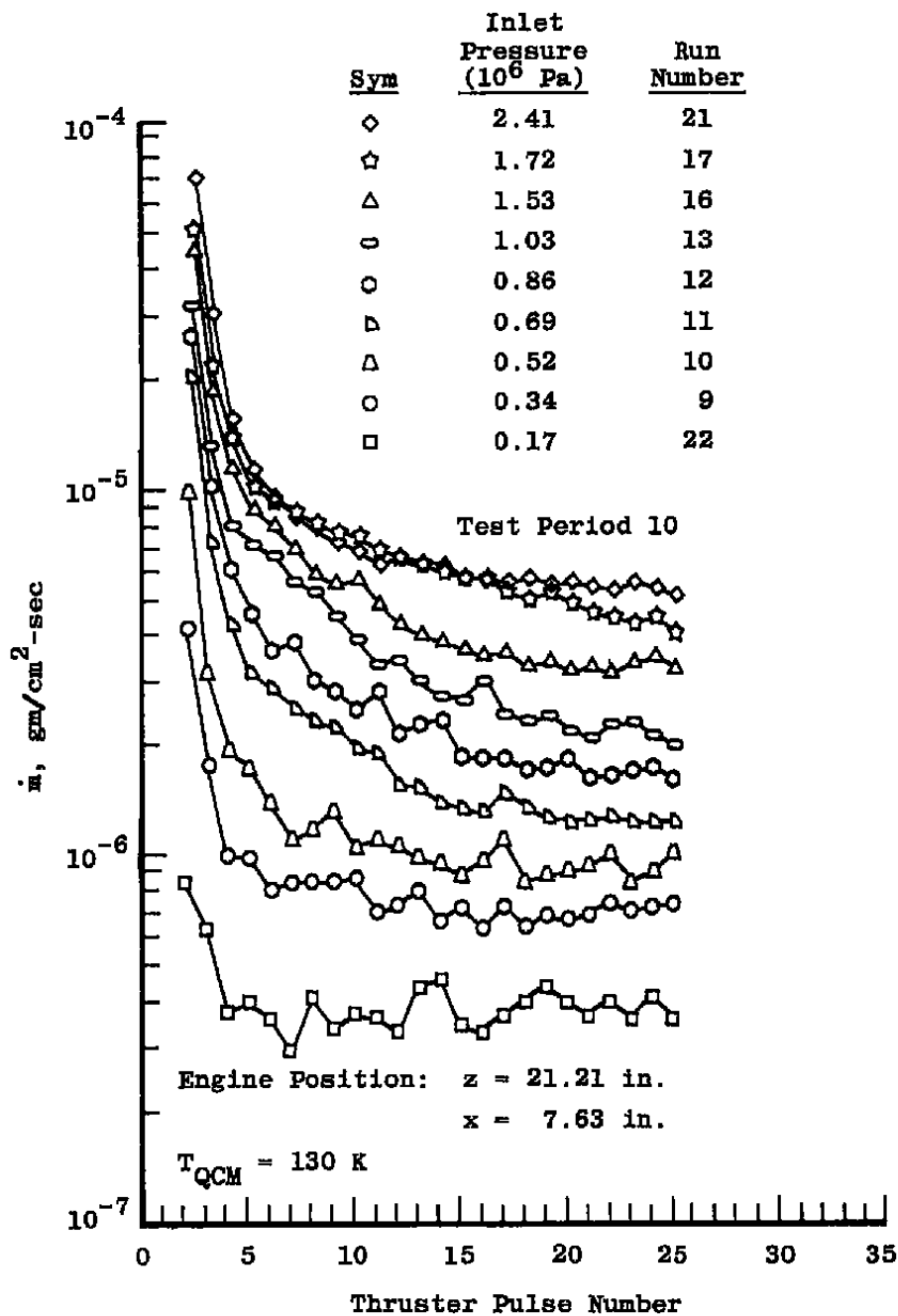
Figure 76. Mass deposition rate versus pulse number for several values
of inlet pressure, T_{QCM} = 130 K.
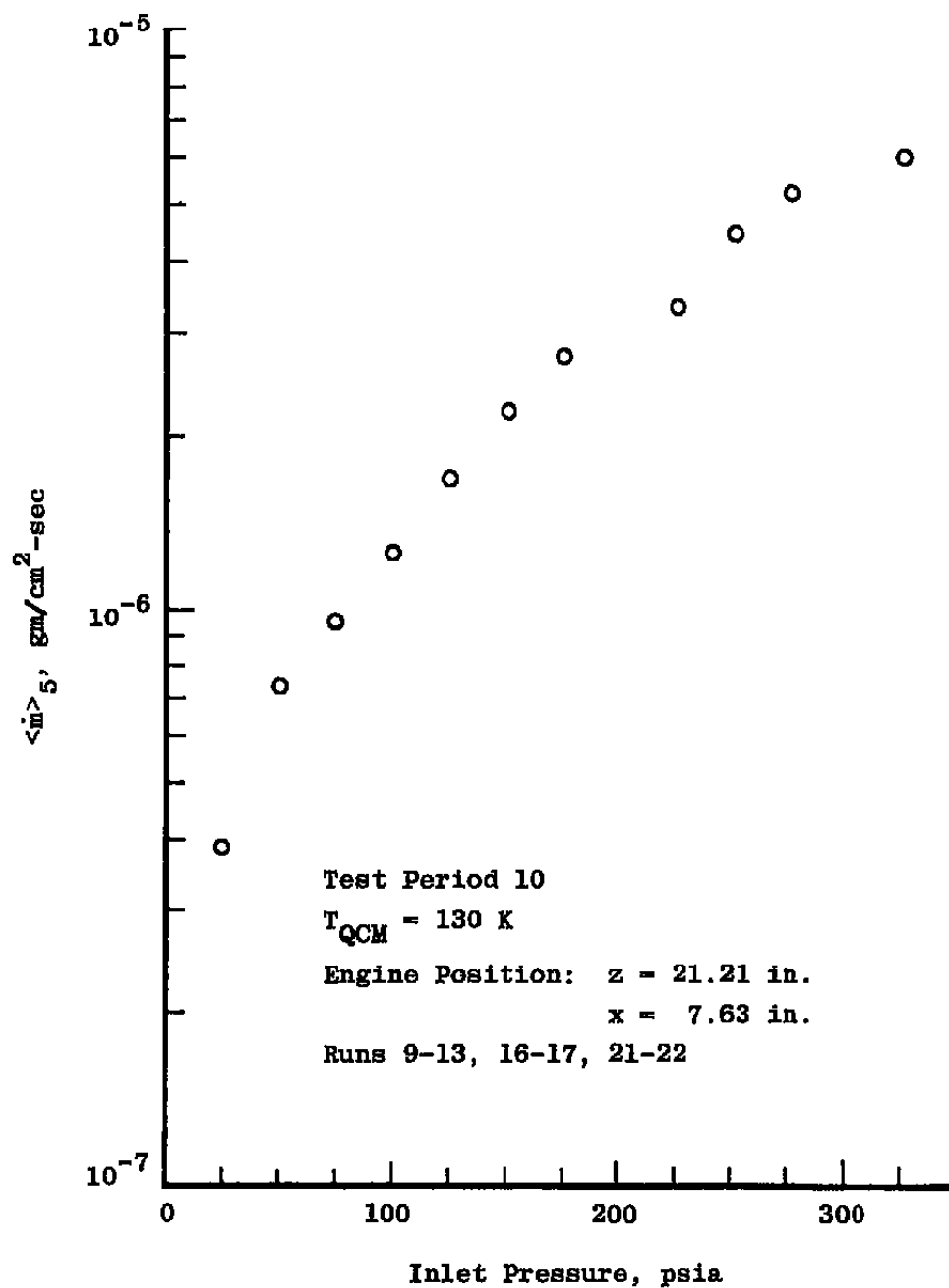
Figure 77. Average mass deposition rate versus inlet pressure, T_{QCM} = 130 K.

Graph labels:

Y-axis: $\langle \dot{m} \rangle_5$, gm/cm^2-sec, with values 10^{-5}, 10^{-6}, 10^{-7}

X-axis: Inlet Pressure, psia, with values 0, 100, 200, 300

Test Period 10

T_{QCM} = 130 K

Engine Position: z = 21.21 in.

x = 7.63 in.

Runs 9-13, 16-17, 21-22
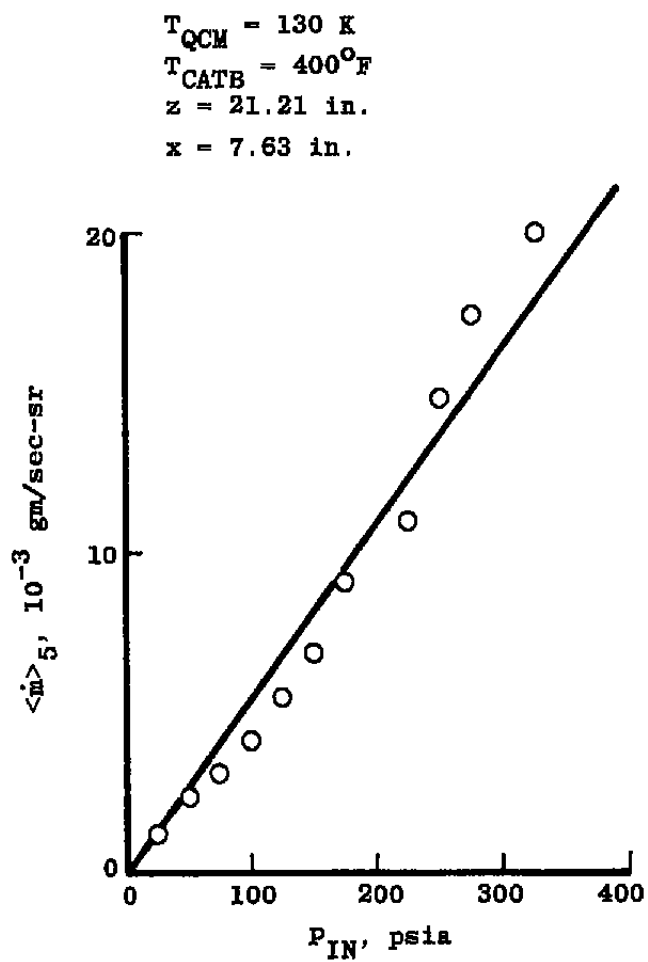
Figure 78. Average mass deposition rate versus inlet pressure, T_{QCM} = 130 K (linear plot).
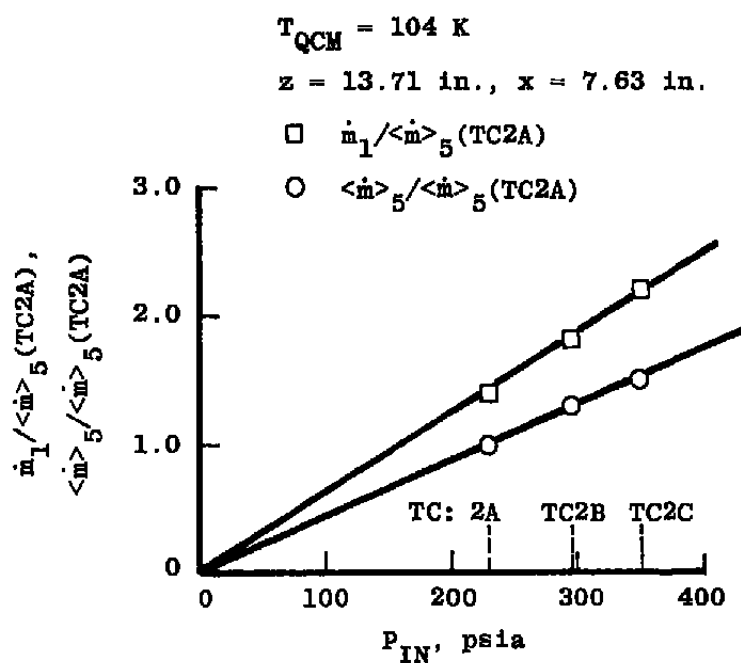
Figure 79. Normalized mass deposition rate as a function of inlet pressure, T_{QCM} = 104 K.
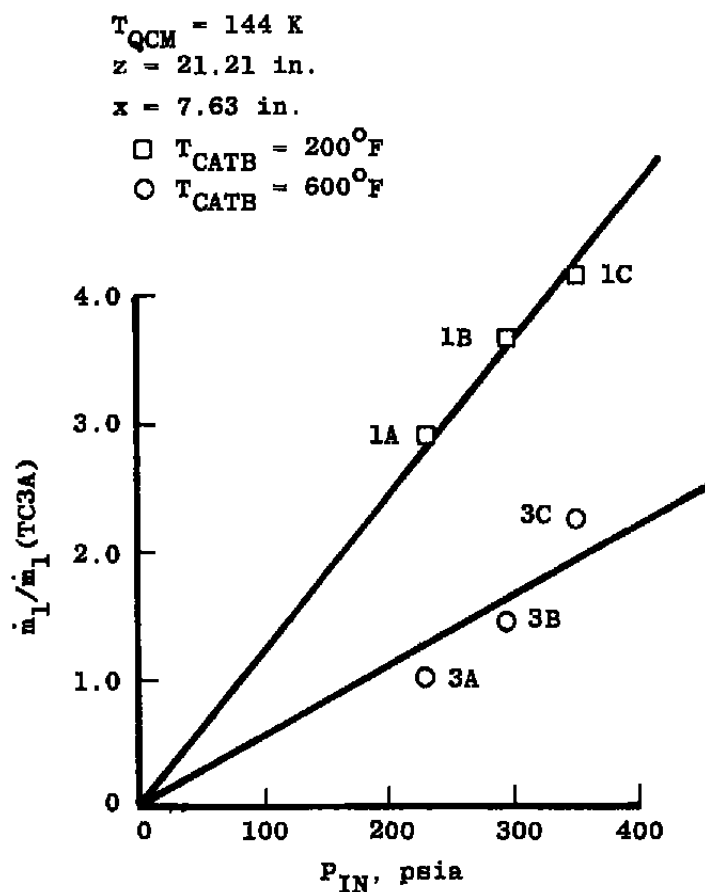
Figure 80. Normalized first-pulse mass deposition rates as a function of inlet pressure, T_{QCM} = 144 K.
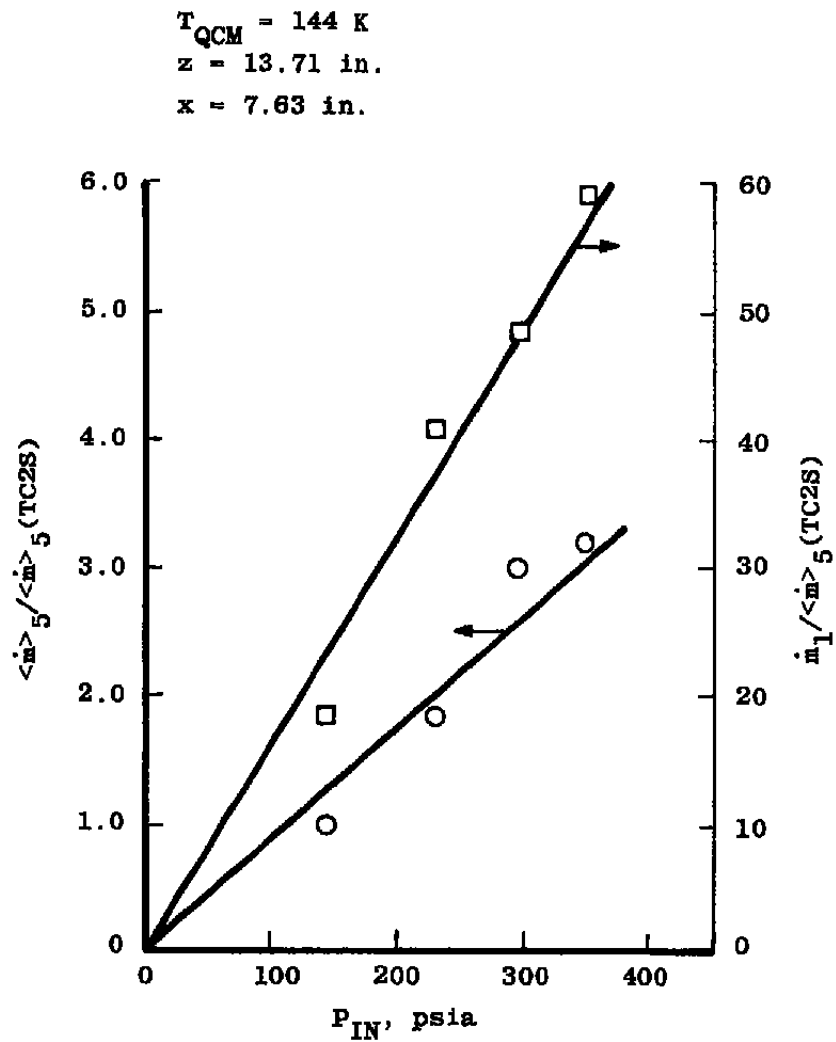
Figure 81. Normalized mass deposition rate as a function of inlet pressure, T_{QCM} = 144 K, θ = 29.1 deg.
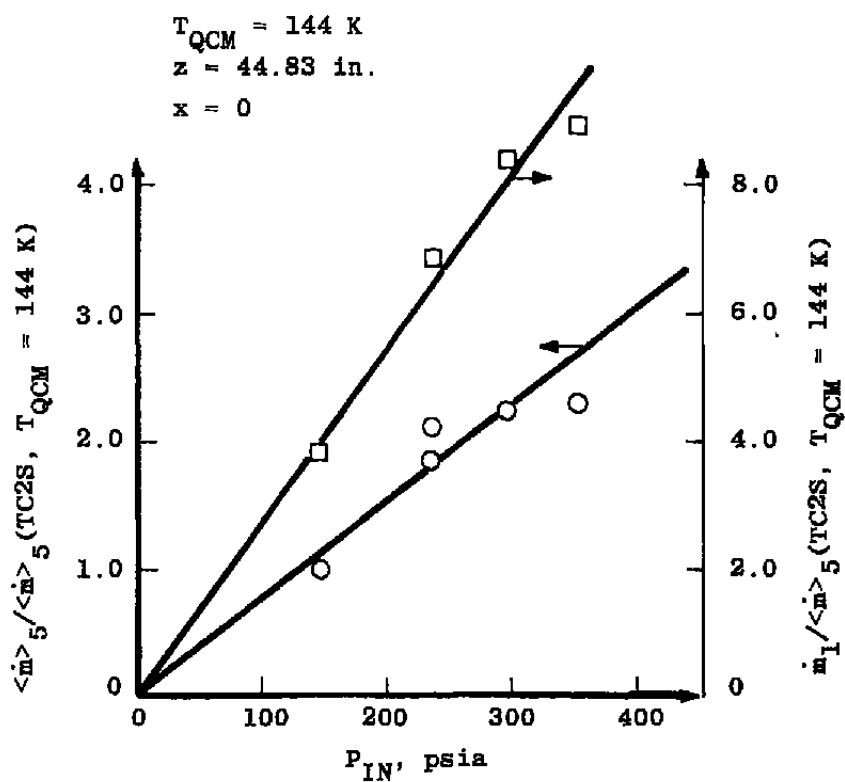
Figure 82. Normalized mass deposition rate as a function of inlet pressure, $T_{QCM} = 144$ K, $\theta = 0$.
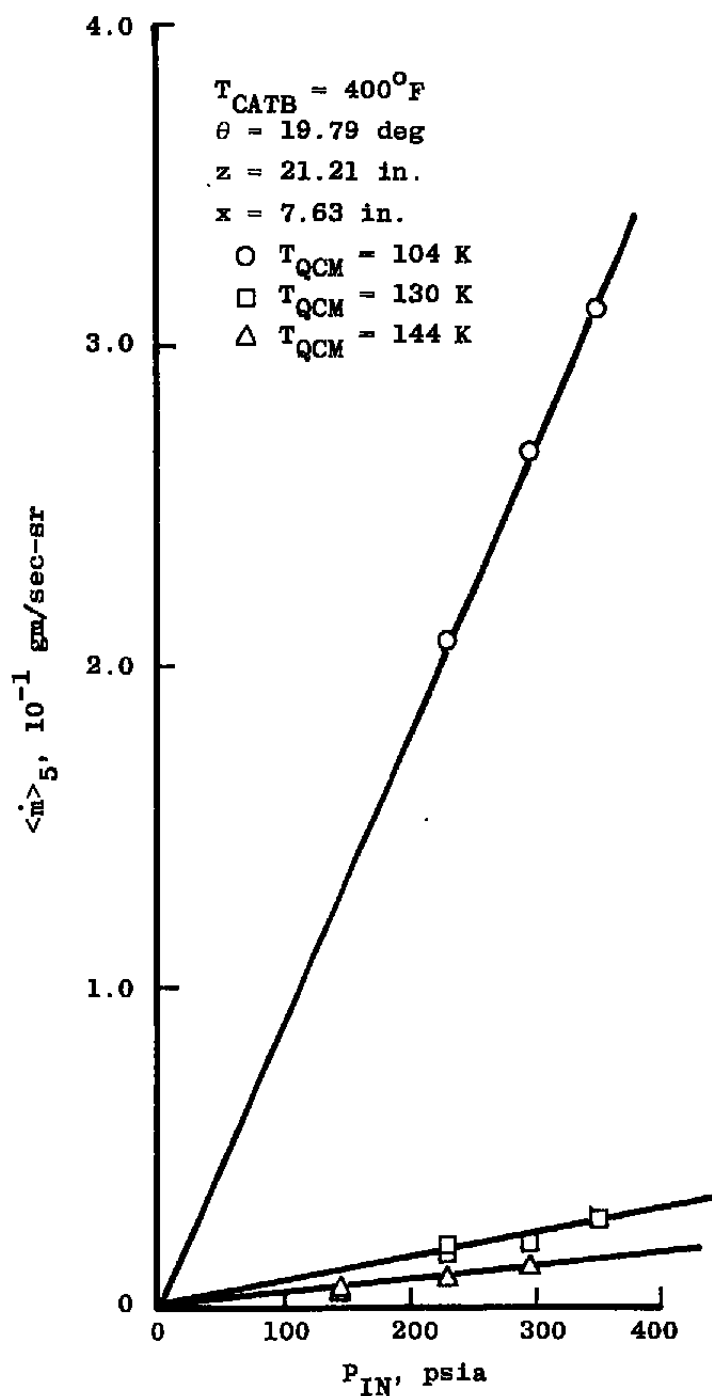
Figure 83. Average mass deposition rate as a function of inlet pressure for various T_{QCM} values.

$T_{QCM} = 144$ K, $T_{CATB} = 400^{O}F$

○ $\theta = 19.79$ deg, $z = 21.21$ in.,
    $x = 7.63$ in.

□ $\theta = 29.1$ deg, $z = 13.71$ in.,
    $x = 7.63$ in.
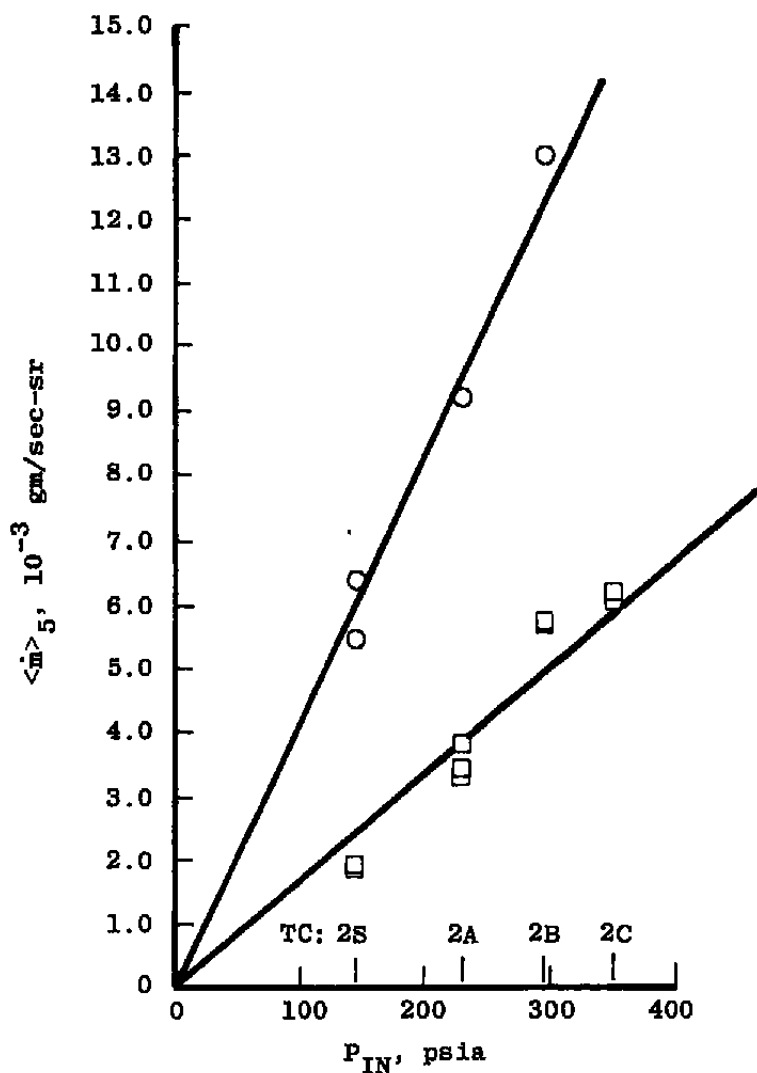
Figure 84. Average mass deposition rate as a function of inlet pressure
for $\theta = 29.1$ and 19.8 deg.

148
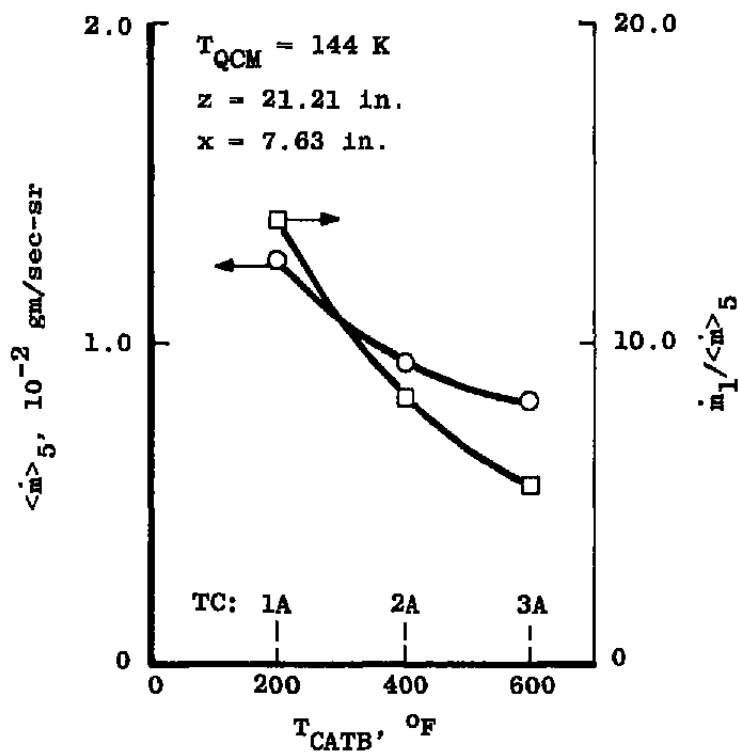
Figure 85. Average mass deposition rate and normalized first-pulse mass deposition rate as a function of initial catalyst bed temperature, T_{QCM} = 144 K, θ = 19.8 deg.
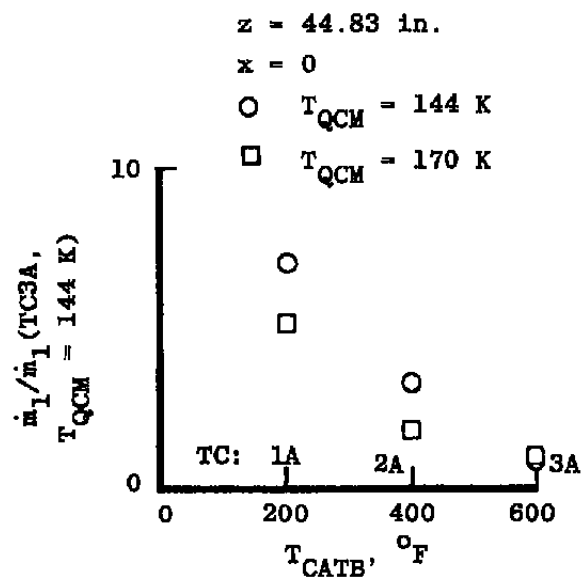
Figure 86. Normalized first-pulse mass deposition rate as a function of initial catalyst bed temperature for T_{QCM} = 144 and 170 K, θ = 0.
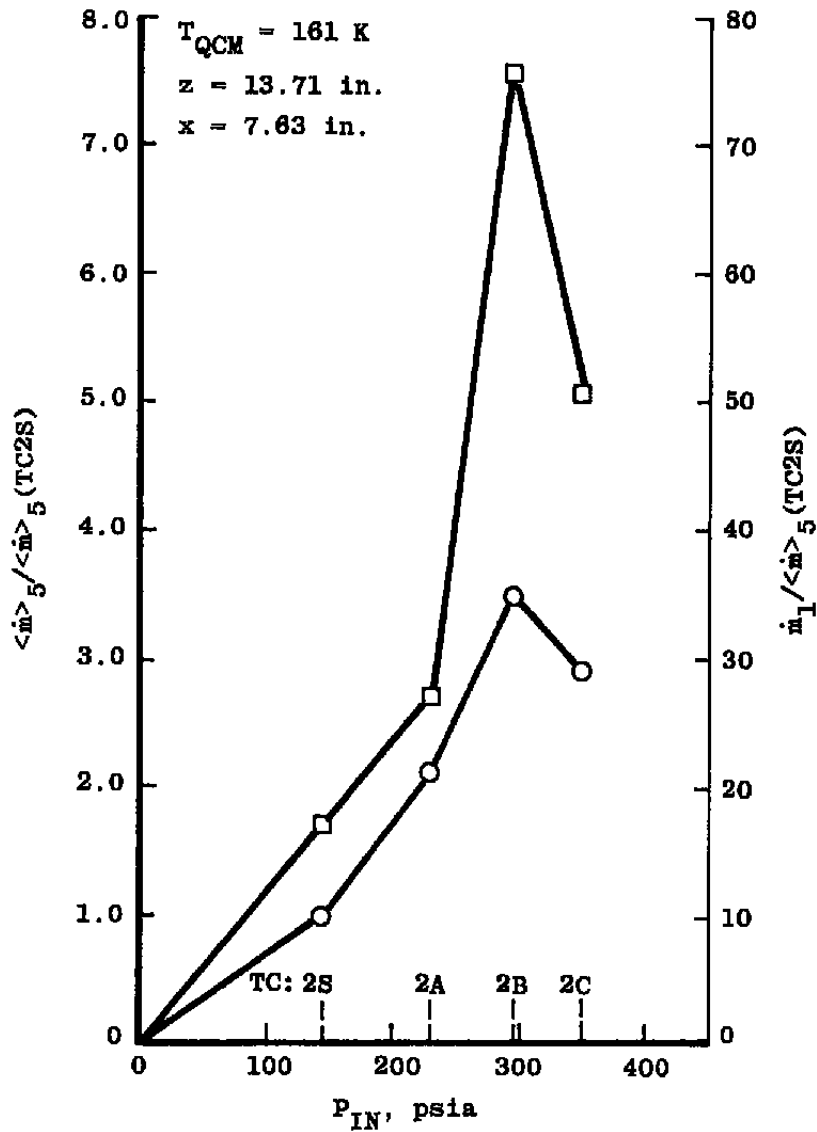
Figure 87. Normalized mass deposition rate as a function of inlet pressure, T_{QCM} = 161 K, θ = 29.1 deg.

151
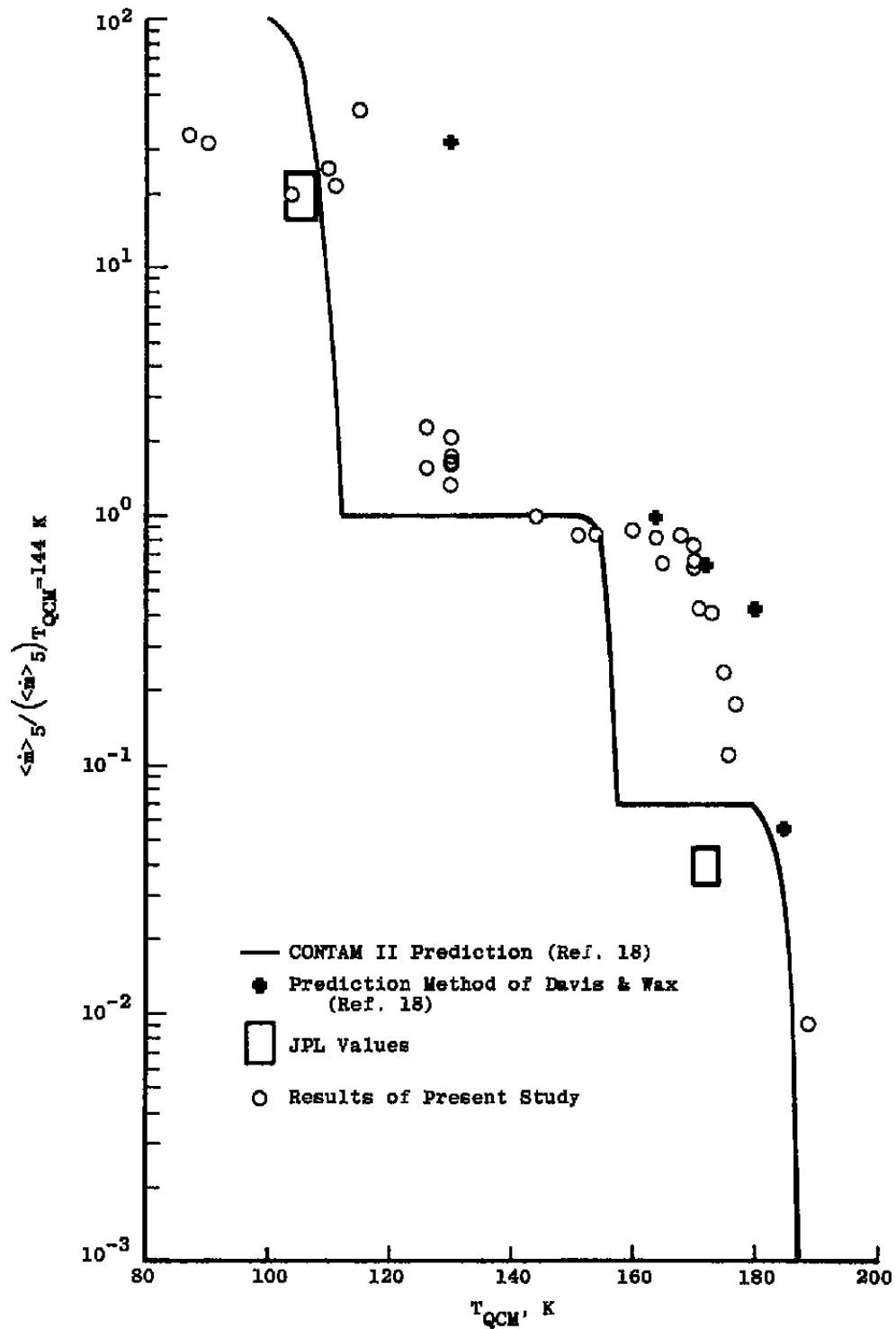
Figure 88. Normalized mass deposition rate as a function of T_{QCM}.
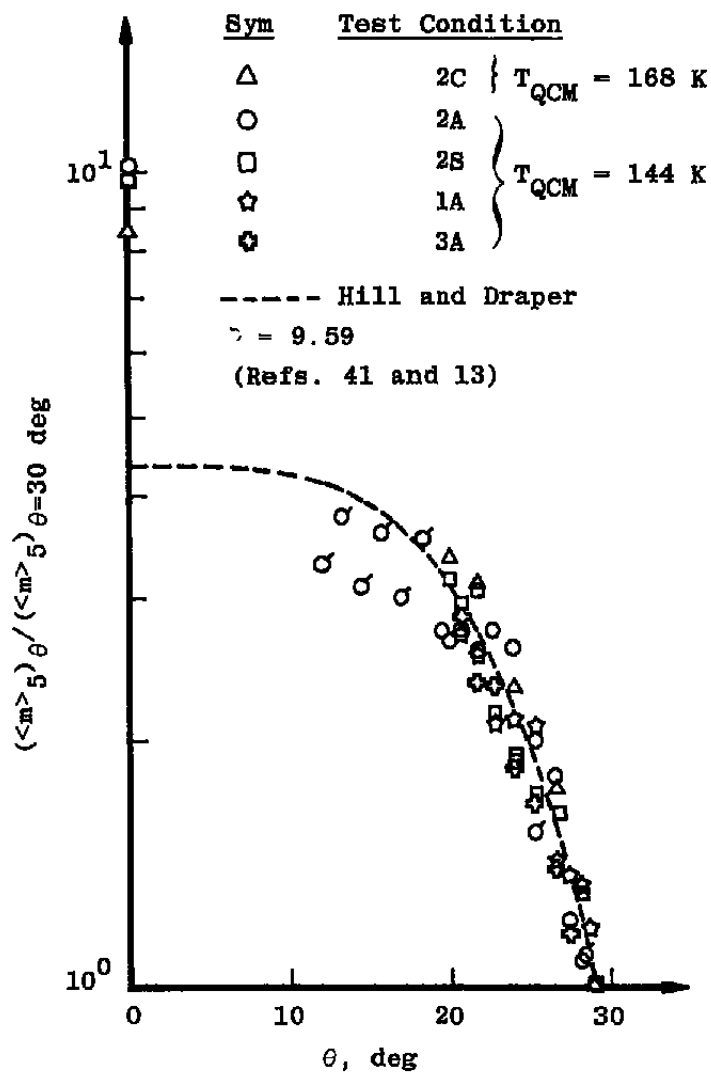
Figure 89. Normalized angular variation of mass deposition rate.
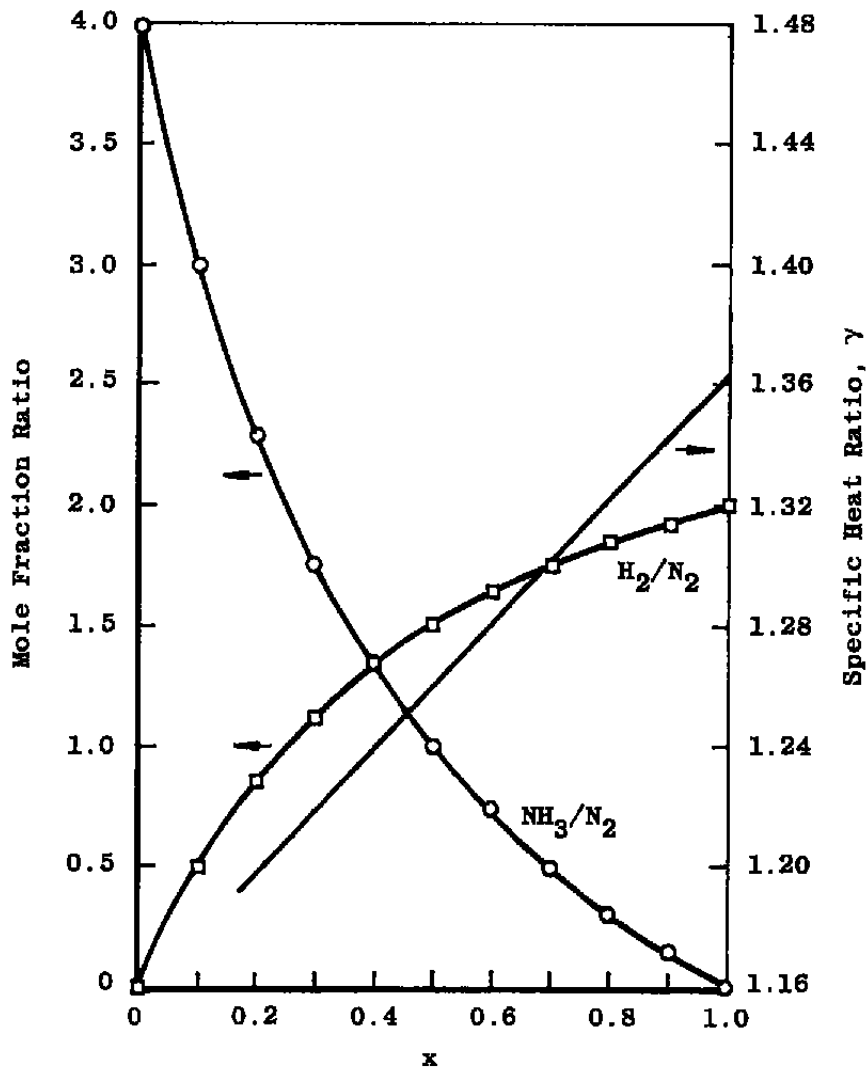
Figure 90. Mole fraction ratios and specific heat ratio, γ, as a function of ammonia dissociation fraction, x.
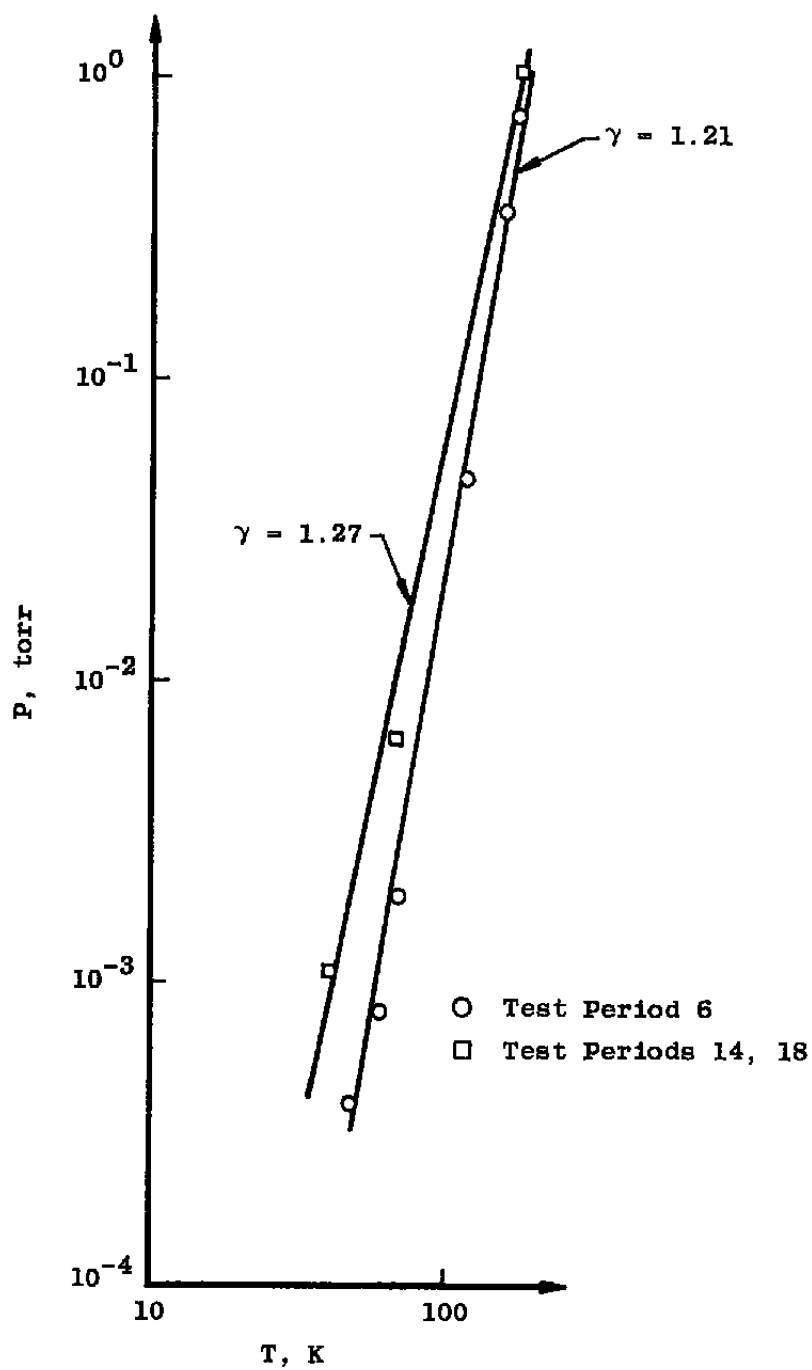
Figure 91. Pressure-temperature variation.
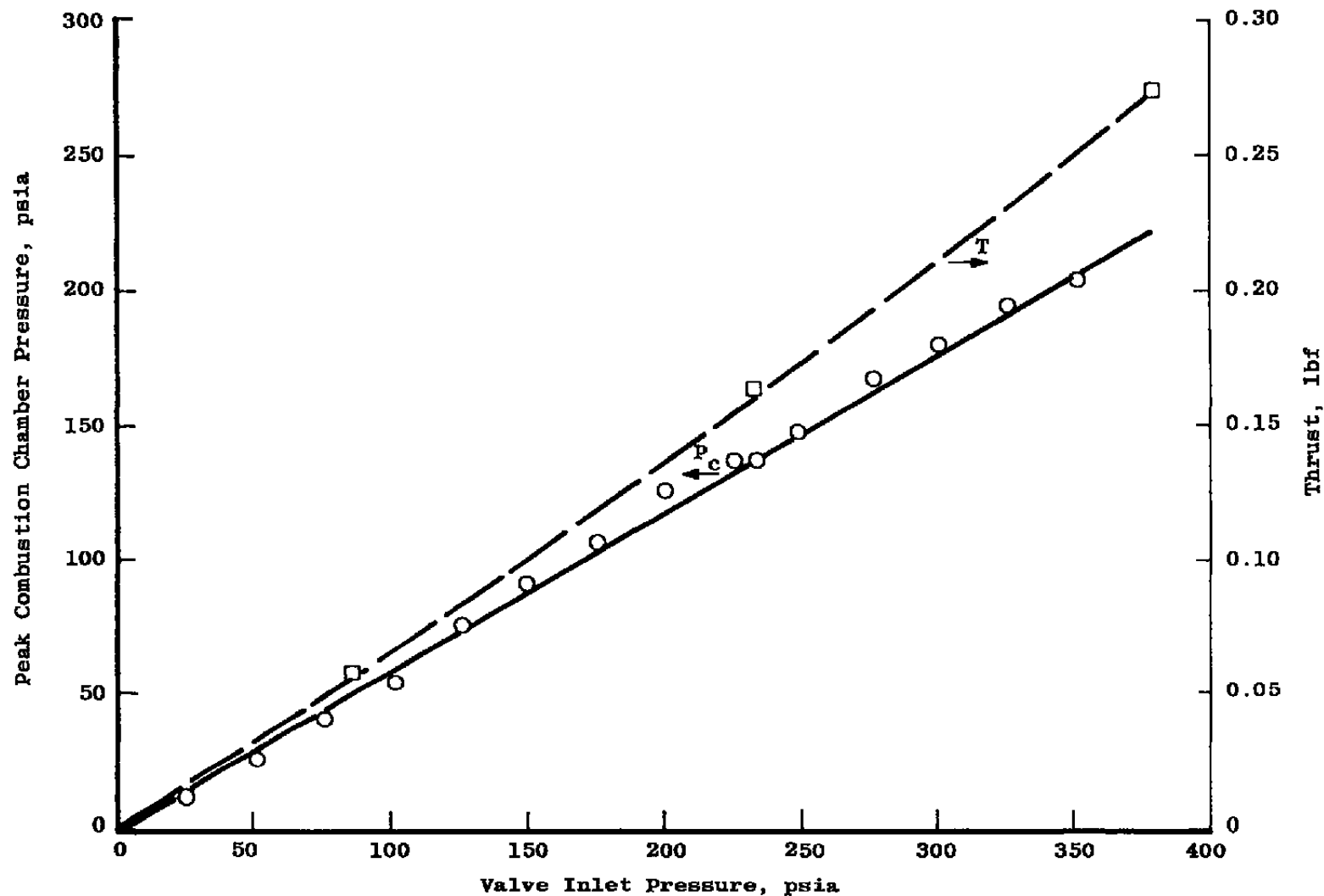
Figure 92.   Thruster calibration, $T_{CATB} = 400°$ F, pulsed mode, 11 Nov 76.
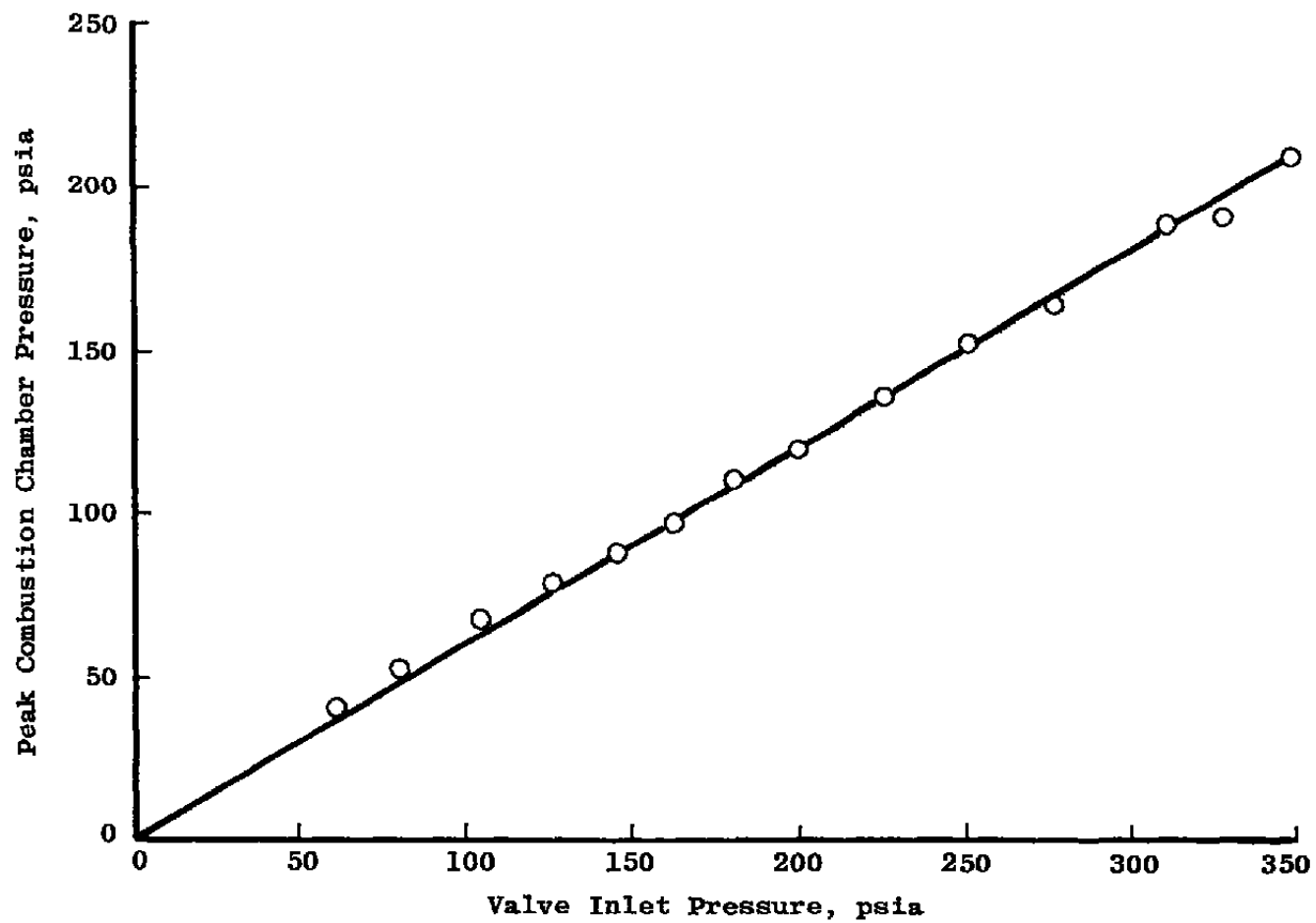
Figure 93. Thruster calibration, $T_{CATB} = 400°\,F$, pulsed mode,
29 March '77.
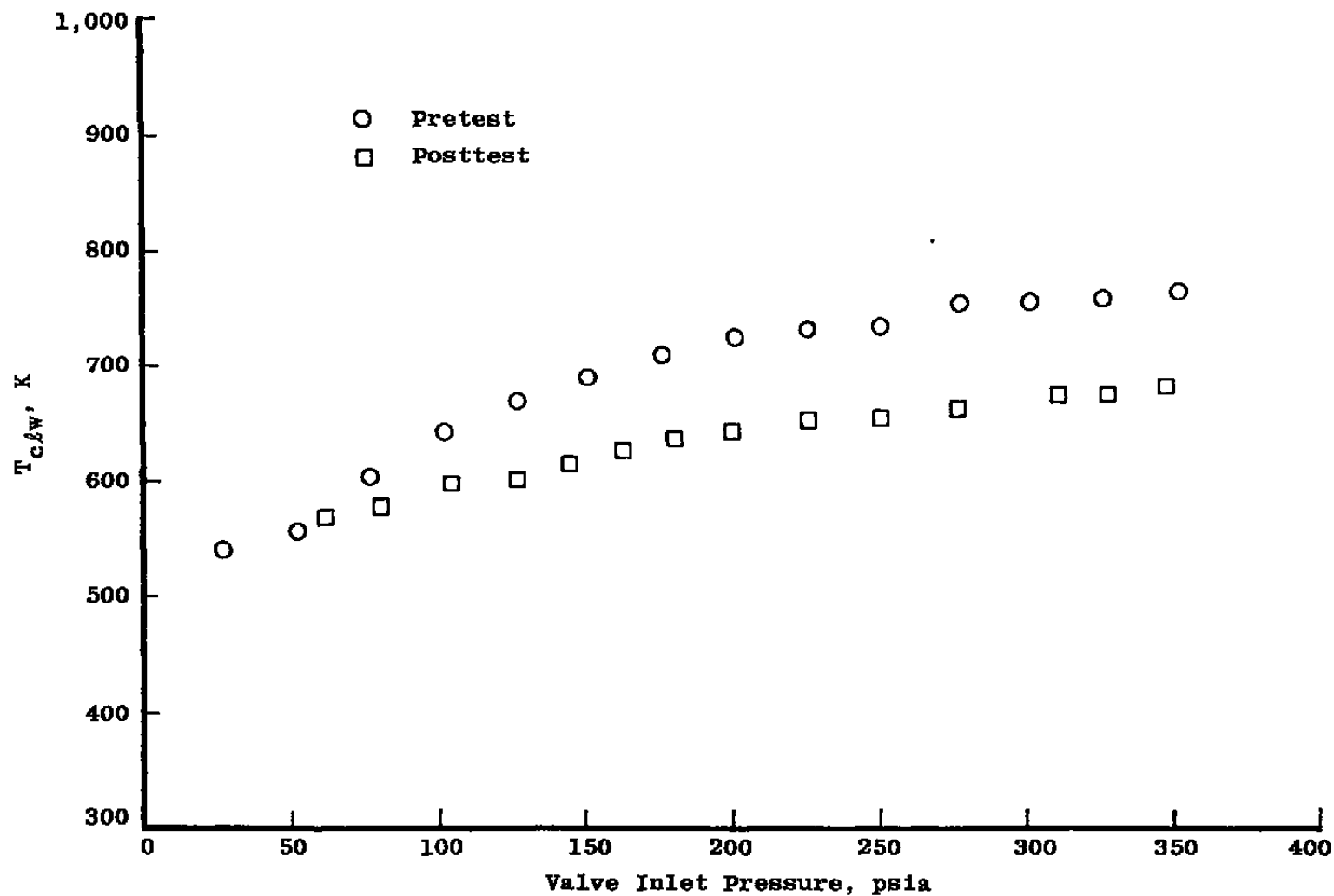
Figure 94. Variation of catalyst bed lower wall temperature with inlet
pressure, 25th pulse.
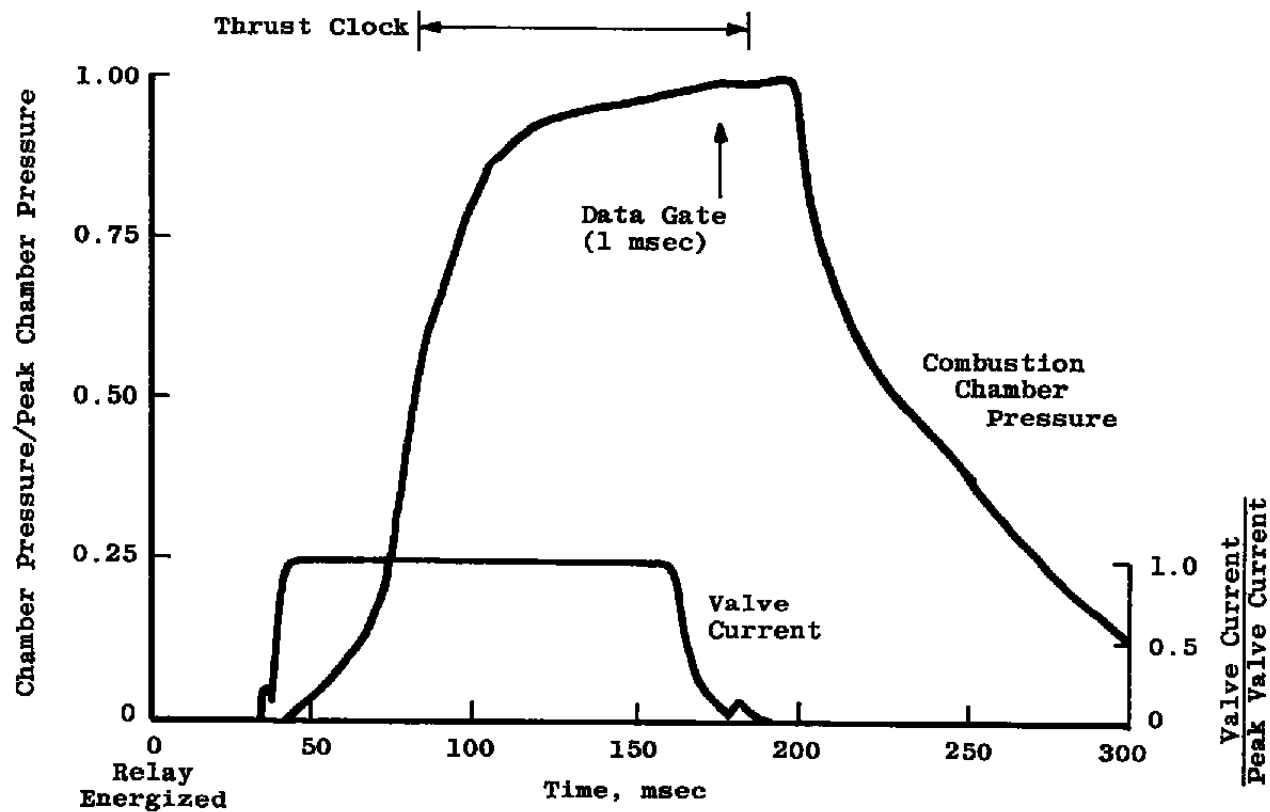
Figure 95. Typical sequence of events for a thruster pulse.
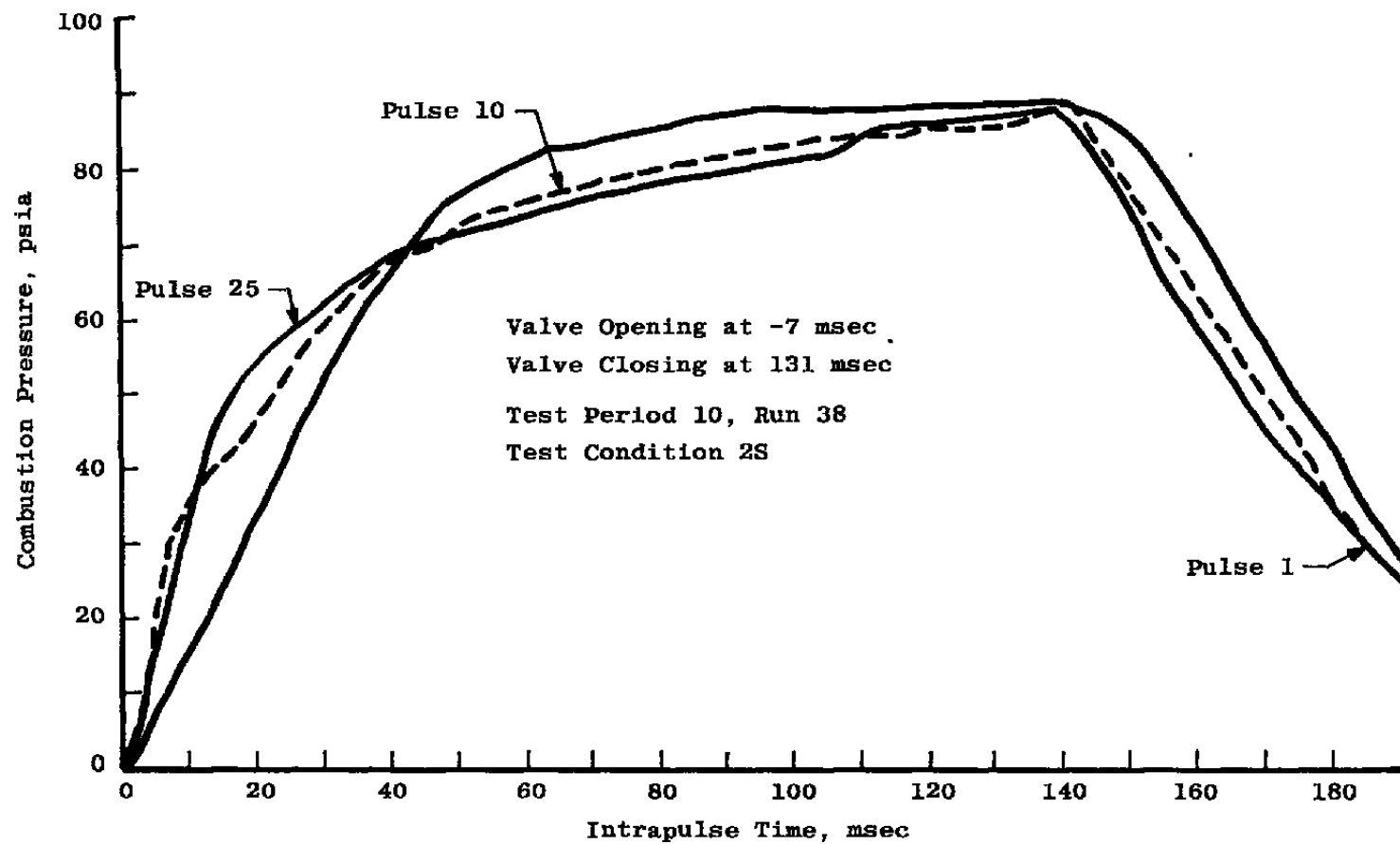
Figure 96. Combustion pressure, condition 2S.
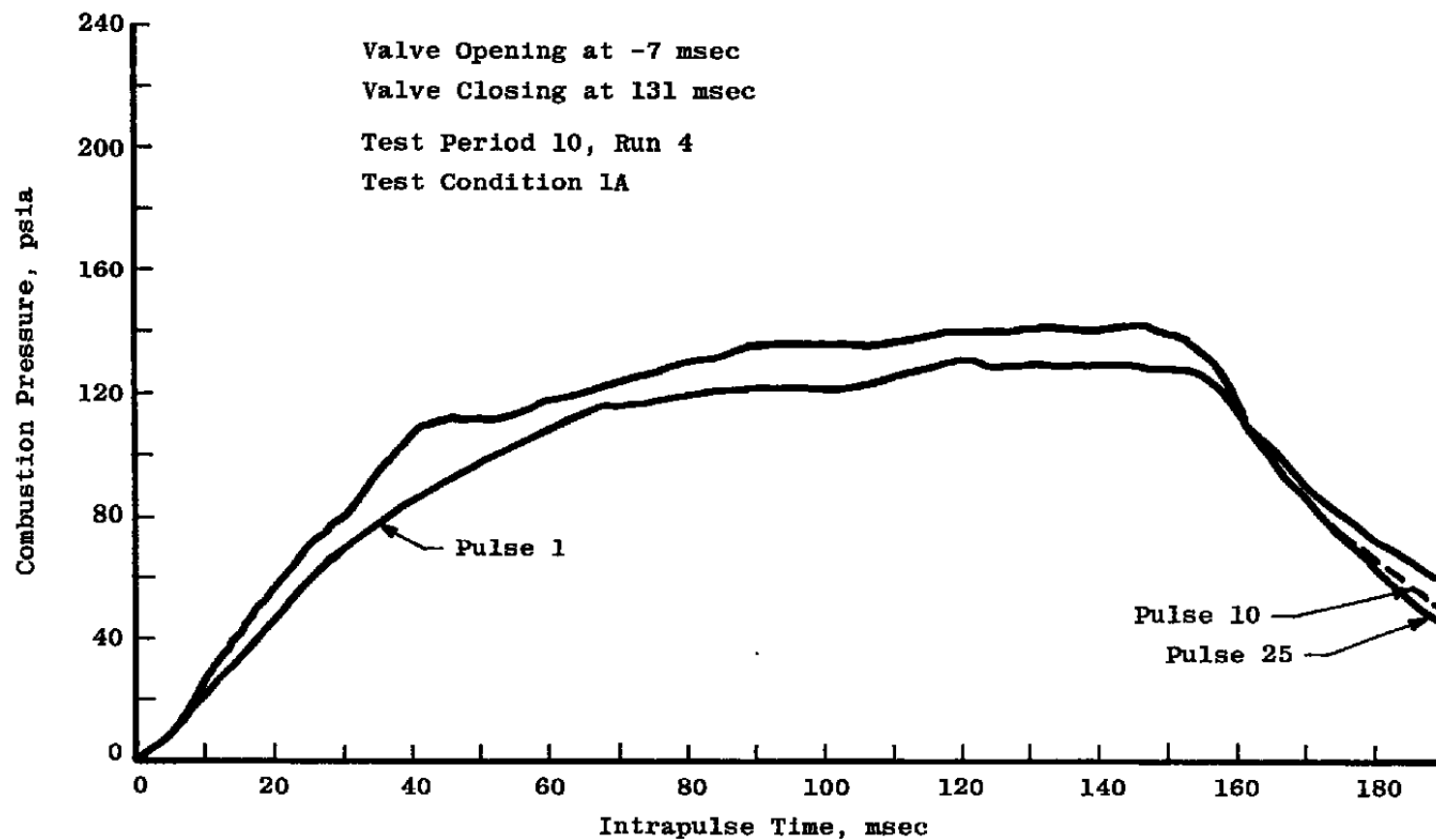
Figure 97. Combustion pressure, condition 1A.
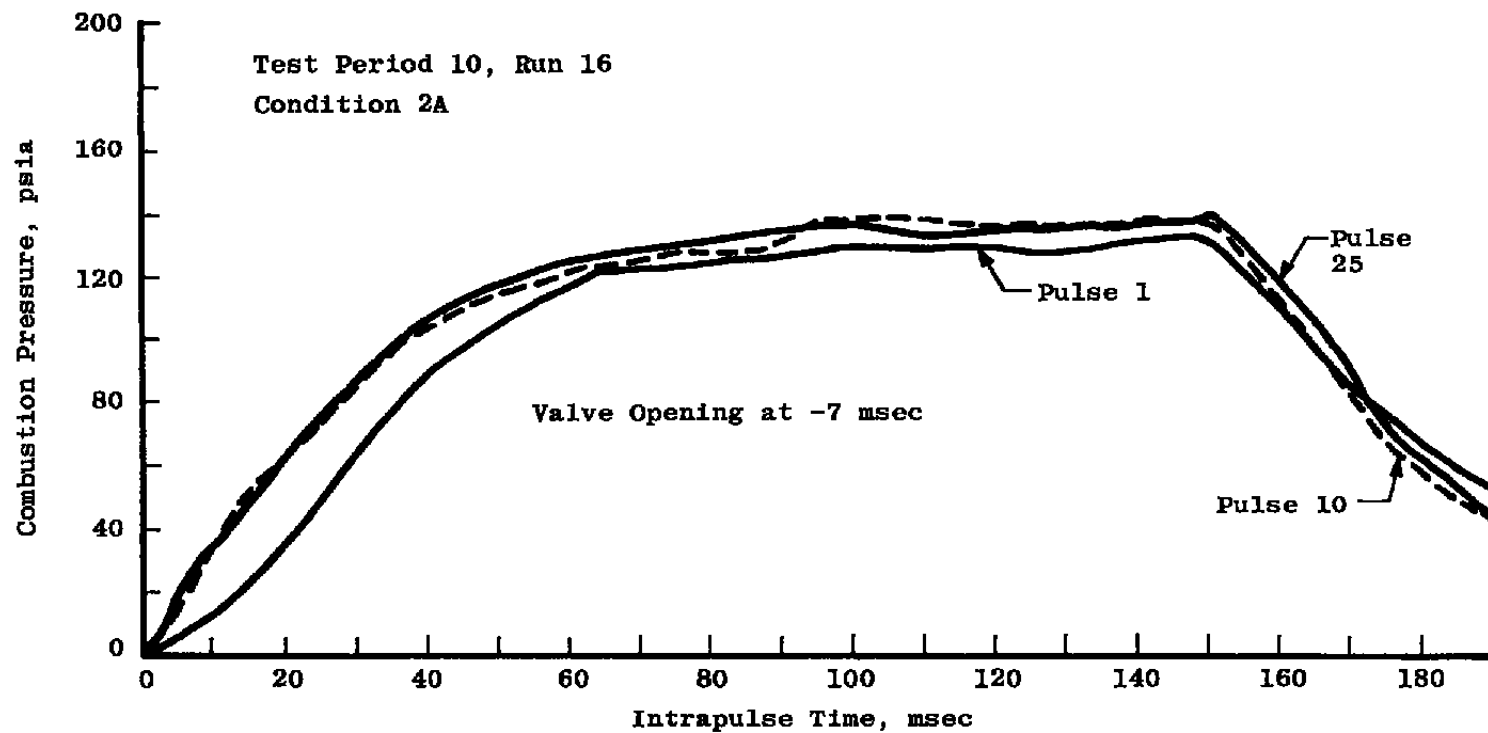
Figure 98. Combustion pressure, condition 2A.
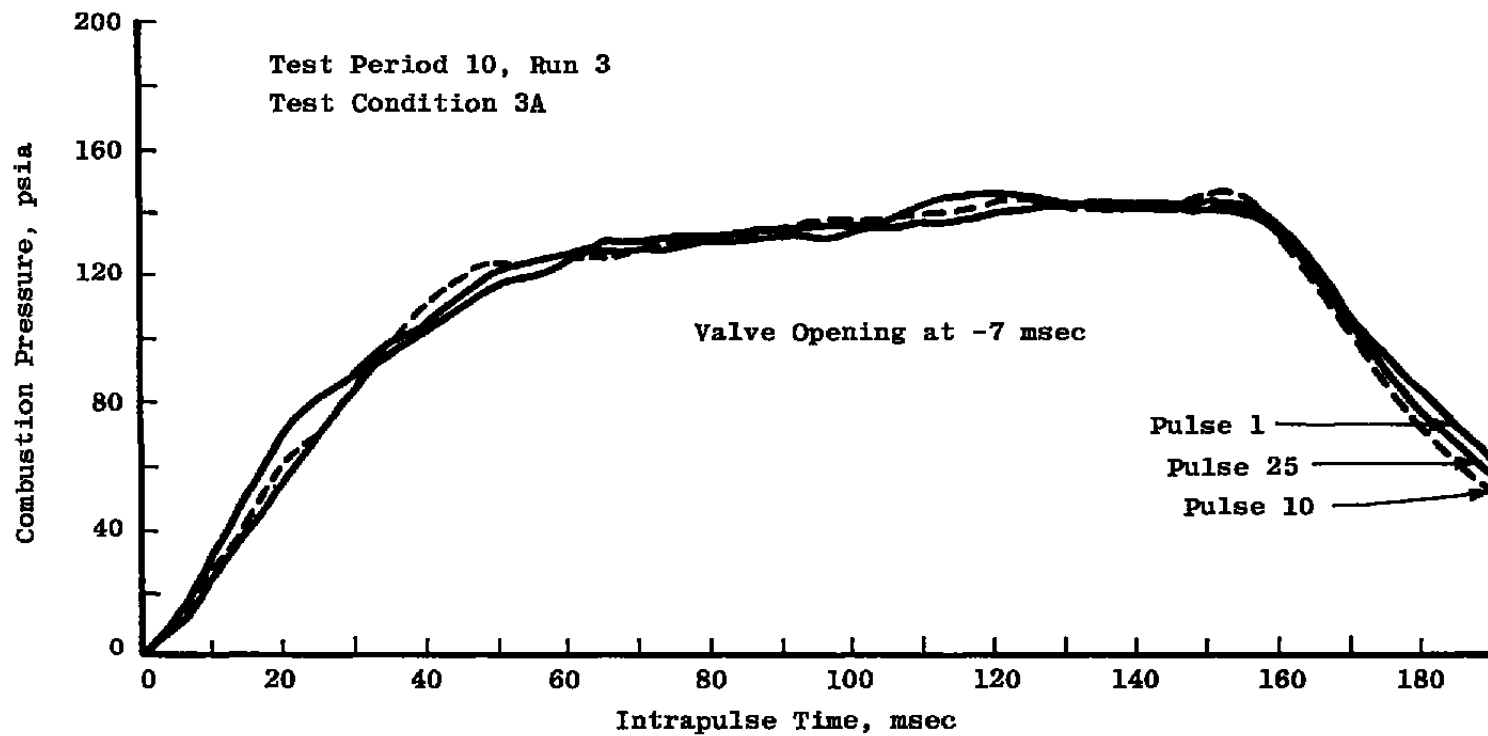
Figure 99. Combustion pressure, condition 3A.
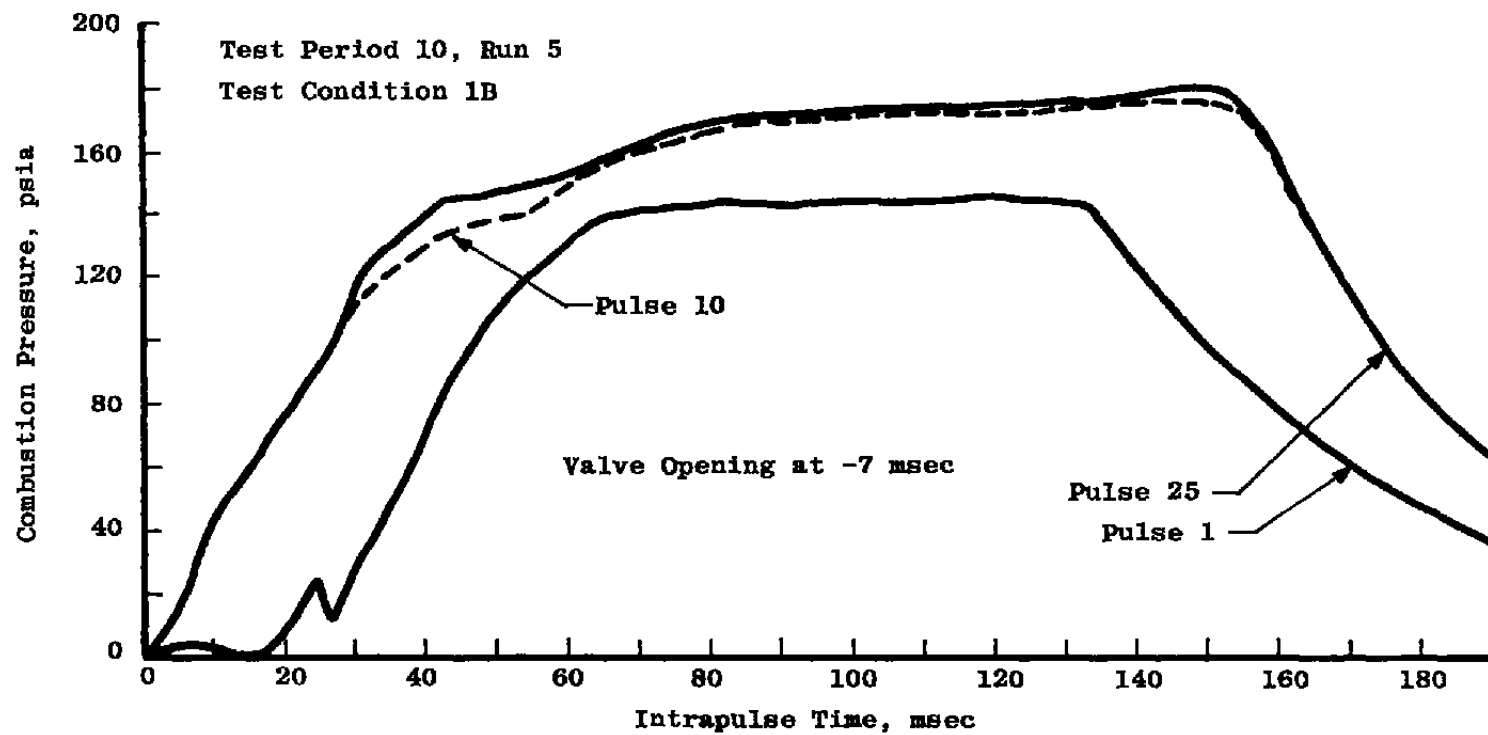
Figure 100. Combustion pressure, condition 1B.
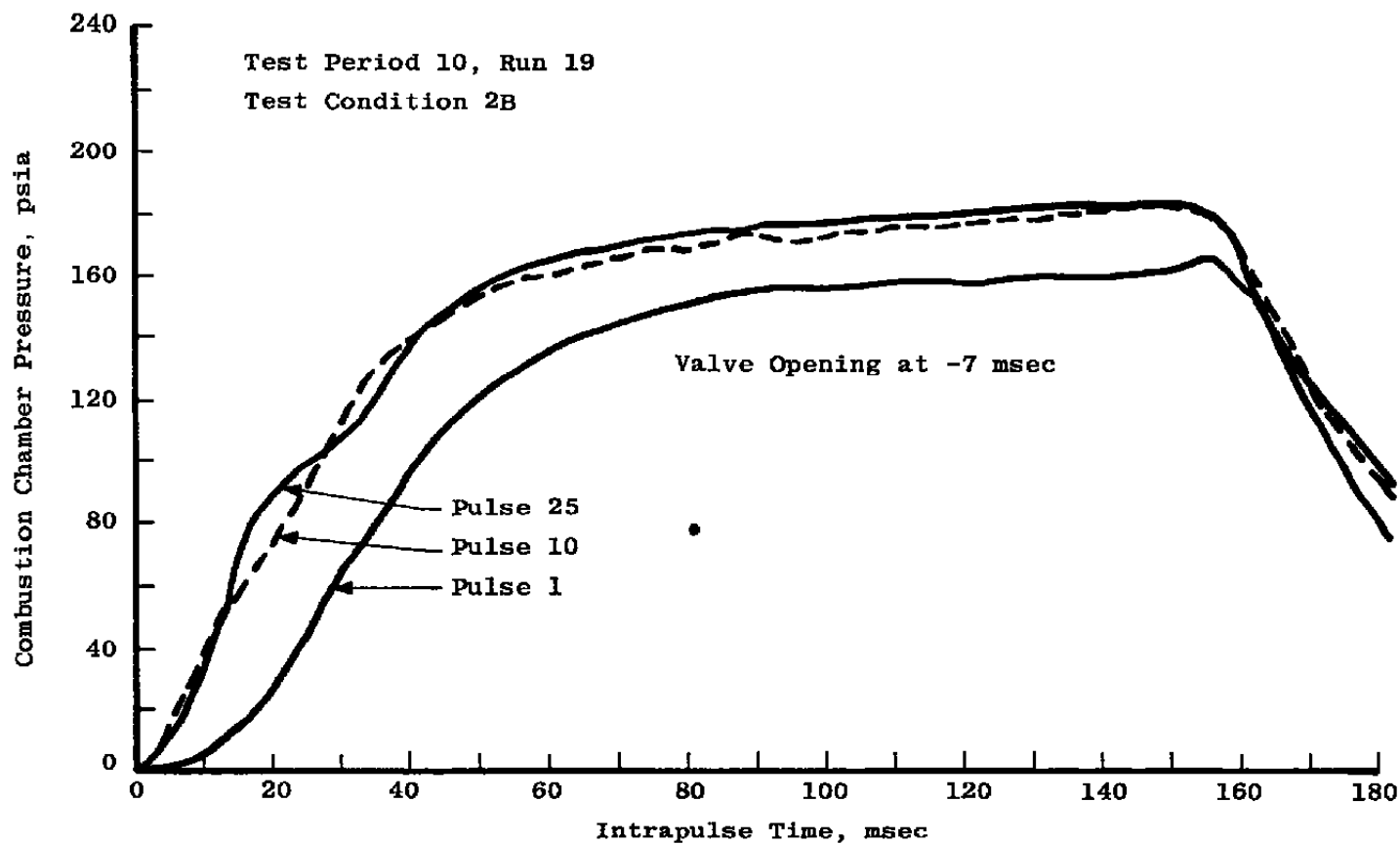
Figure 101. Combustion pressure, condition 2B.
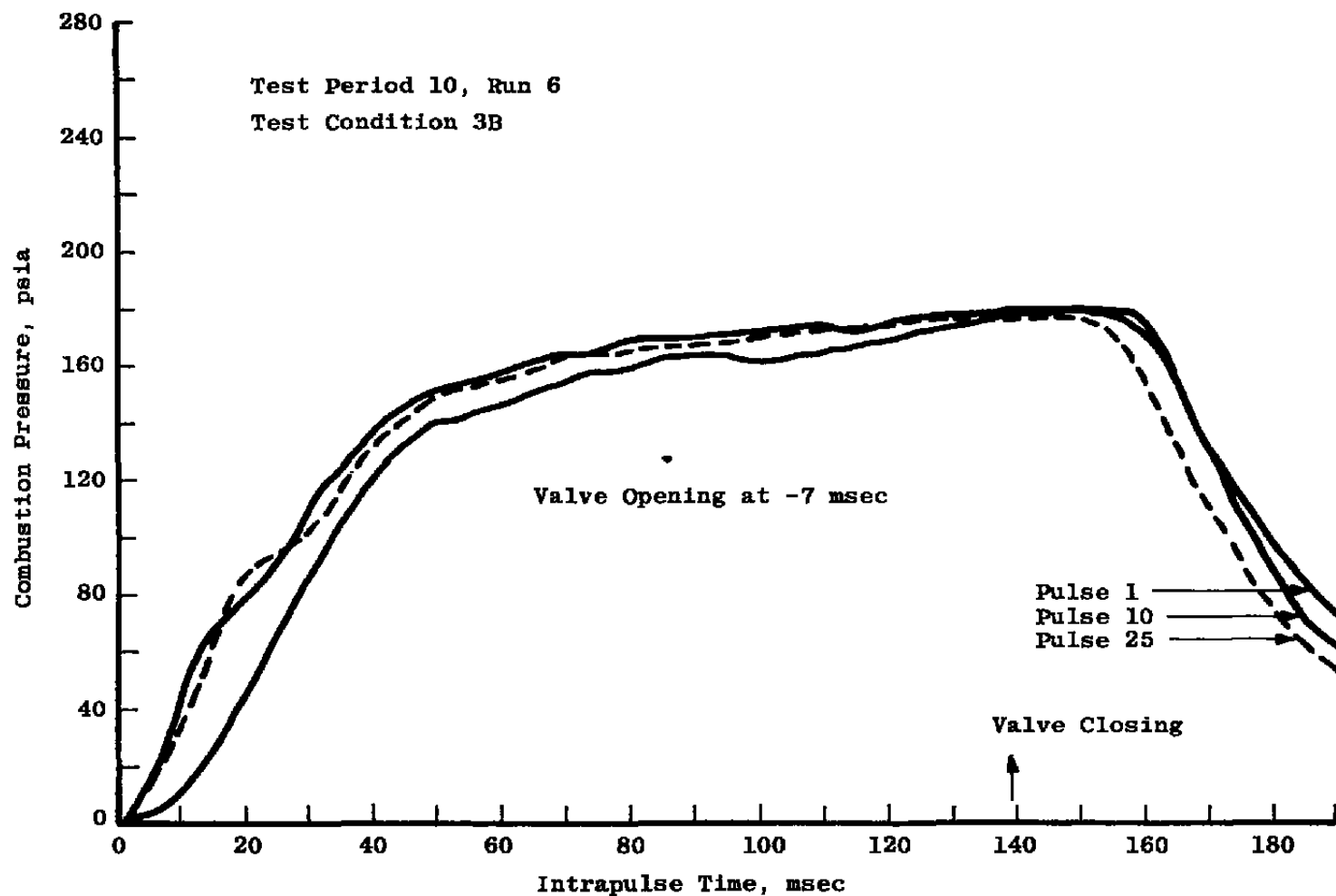
Figure 102. Combustion pressure, condition 3B.
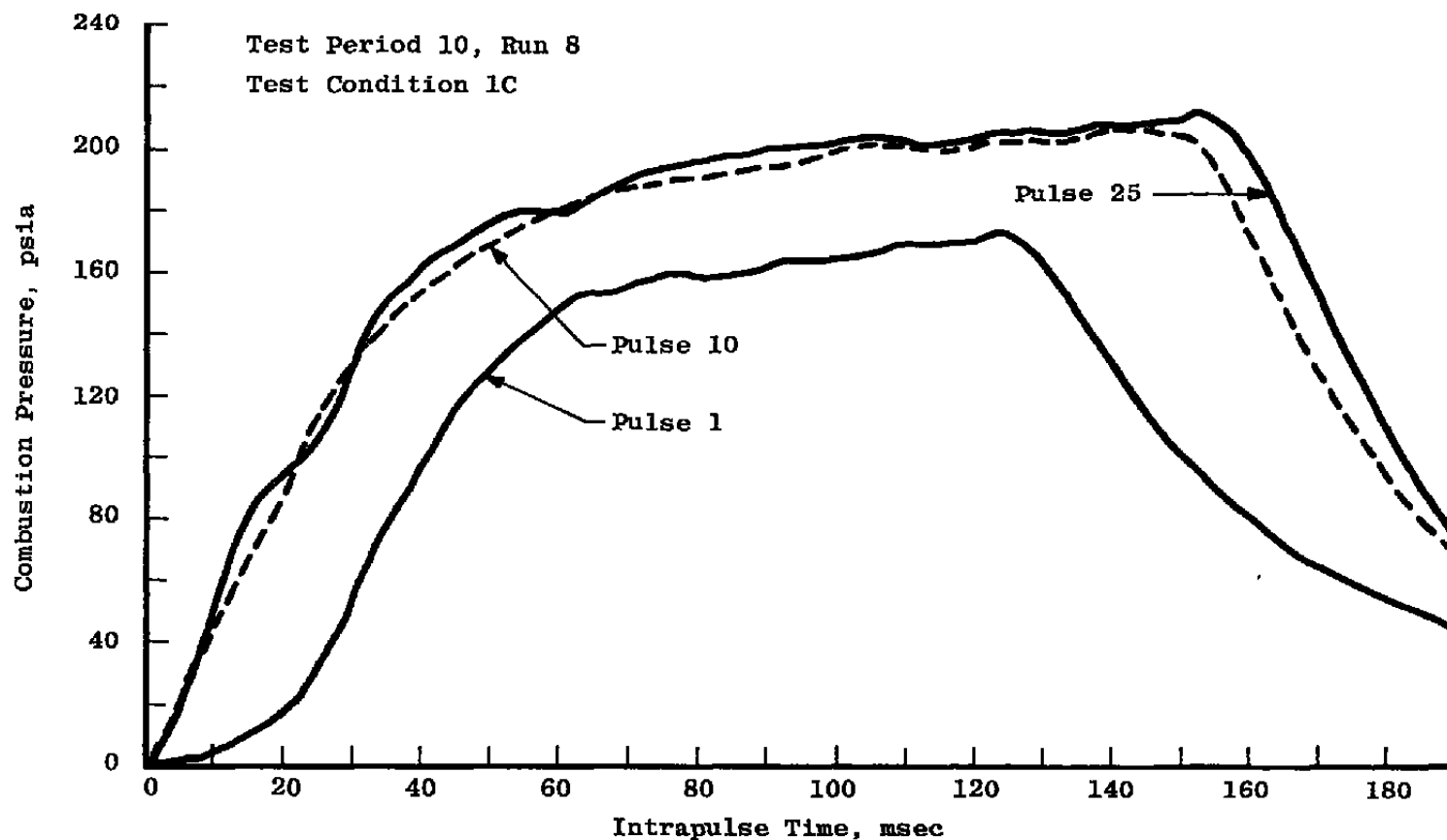
Figure 103. Combustion pressure, condition 1C.
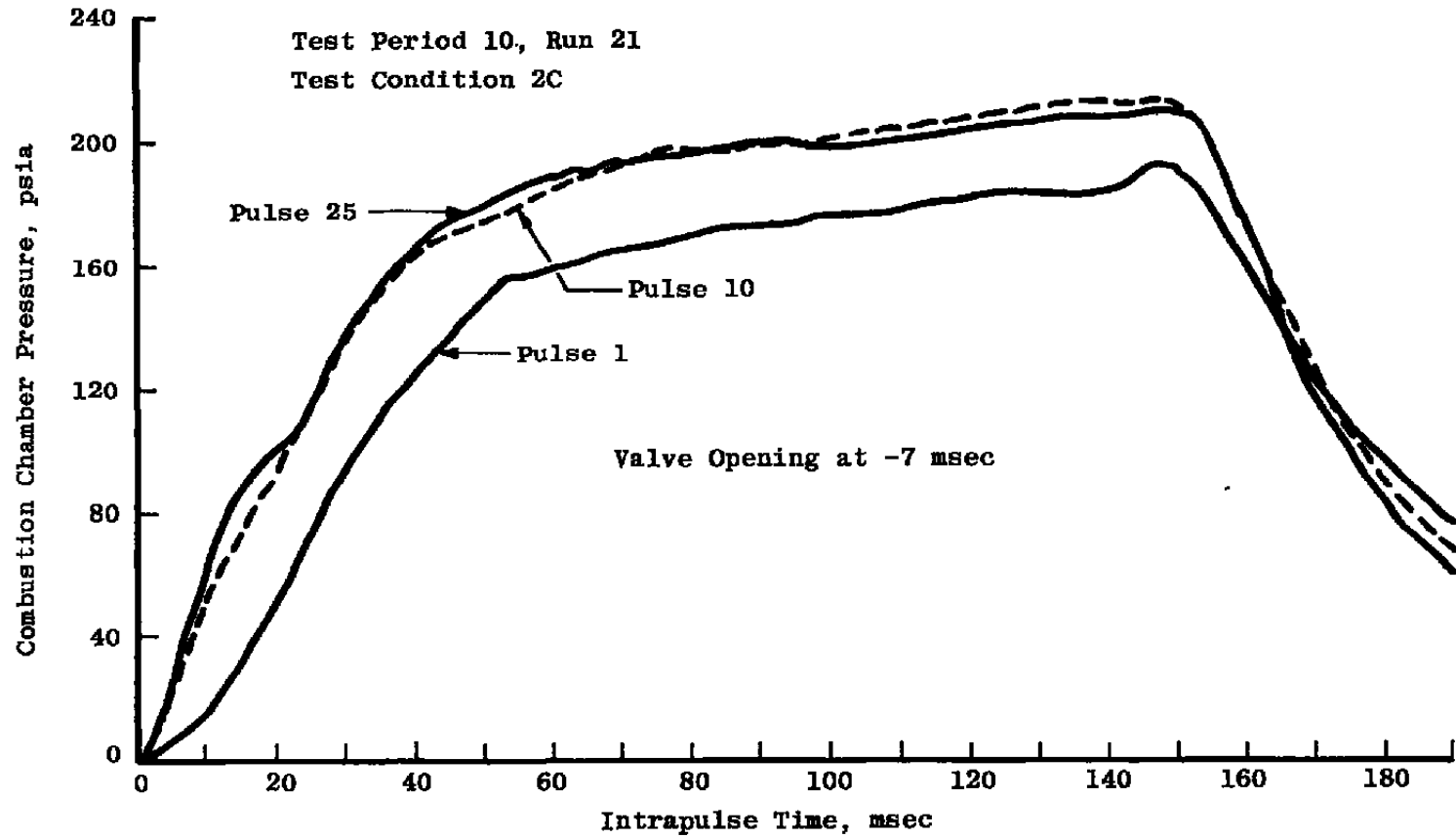
Figure 104. Combustion pressure, condition 2C.
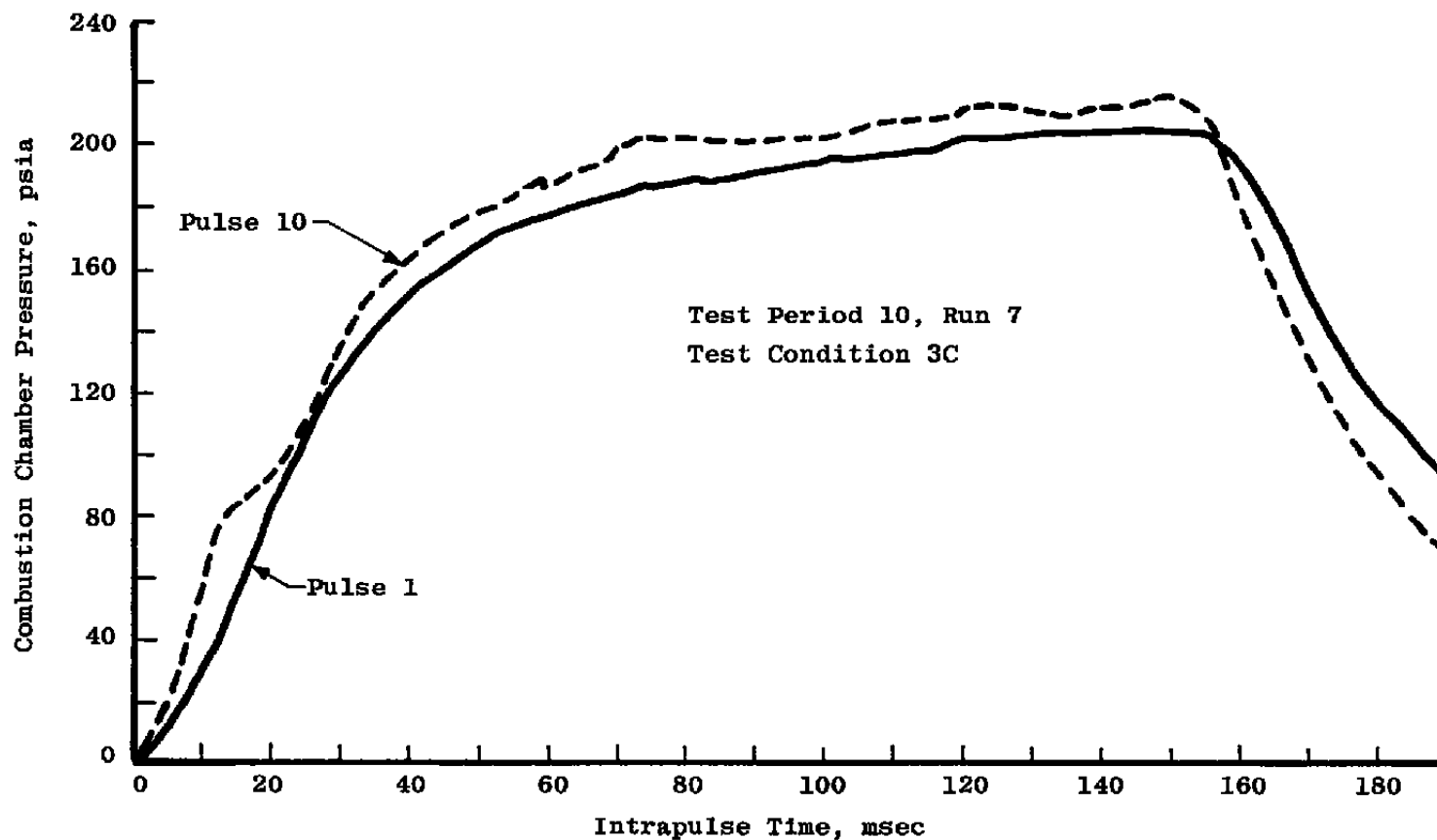
Figure 105. Combustion pressure, condition 3C.
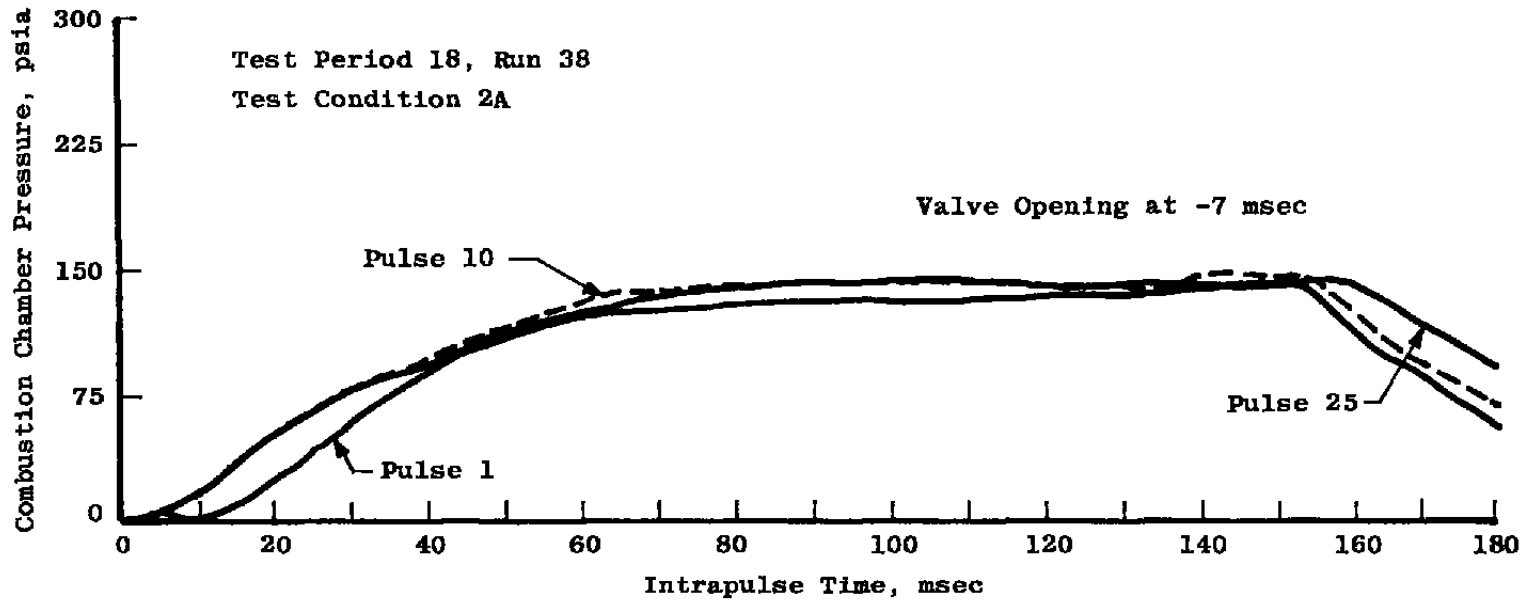
Figure 106. Combustion pressure, condition 2A, post-"catastrophe".
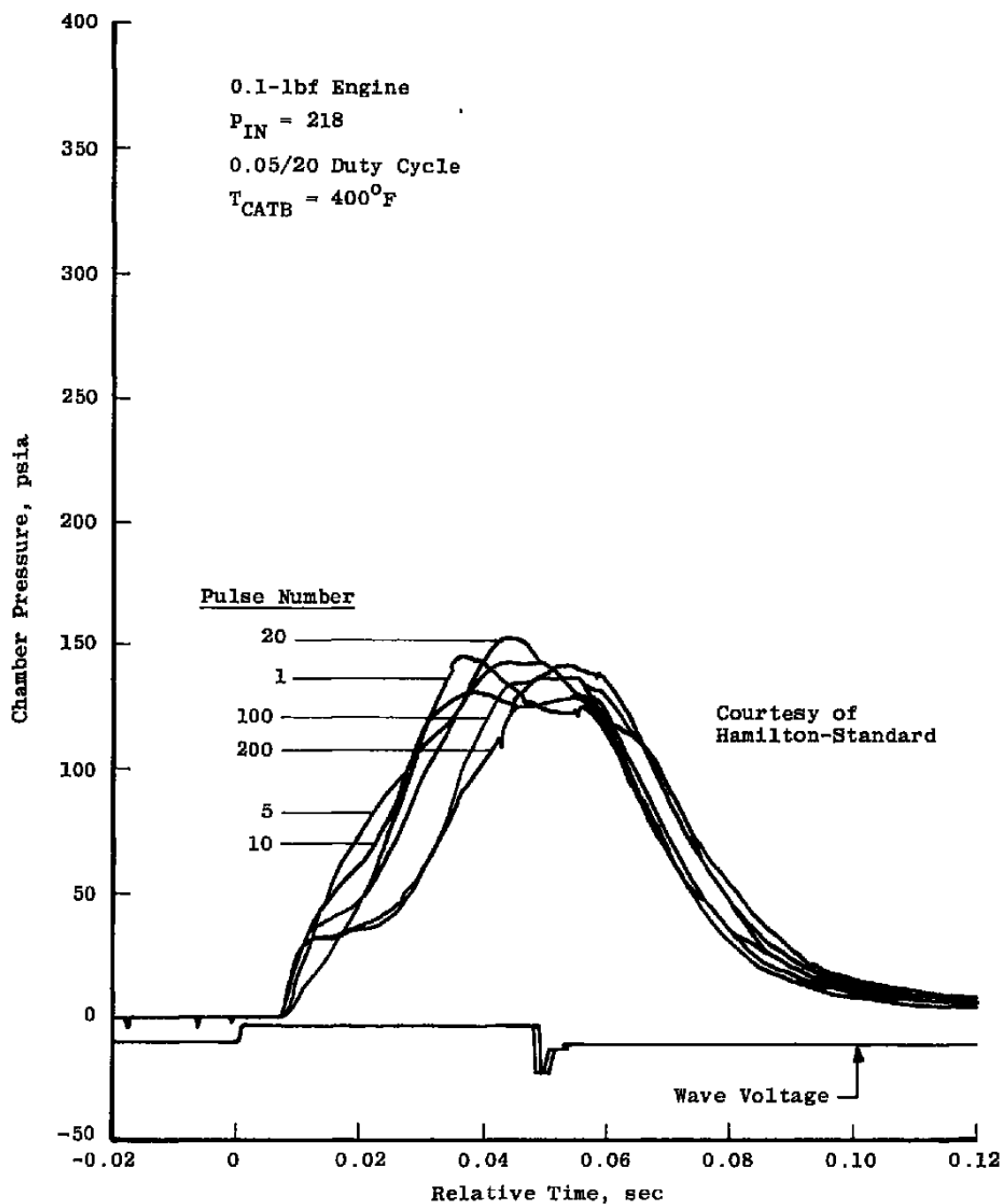
Figure 107. Hamilton-Standard combustion chamber pressure results.
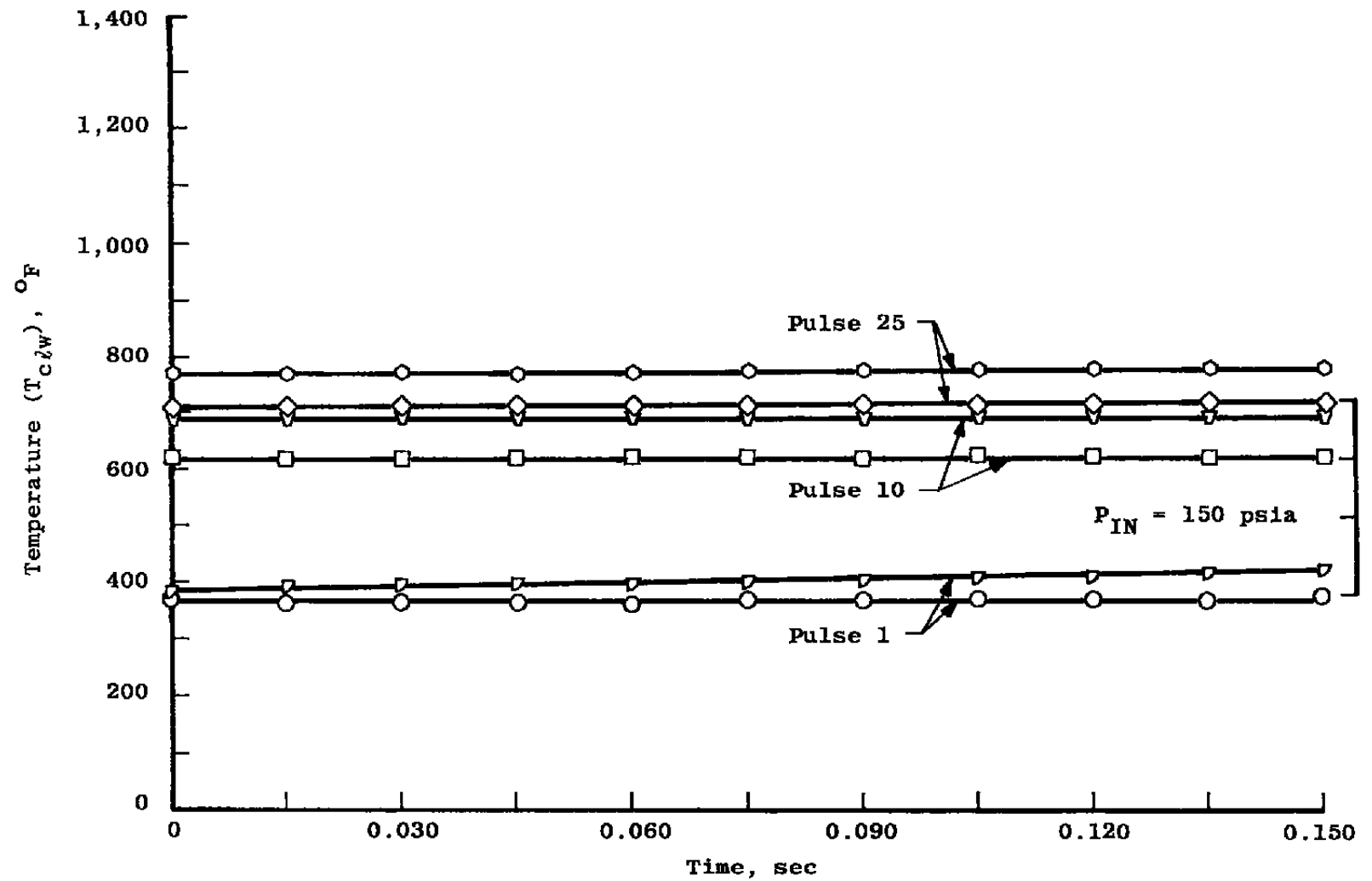
Figure 108. Response of combustion chamber lower wall temperature during pulse.
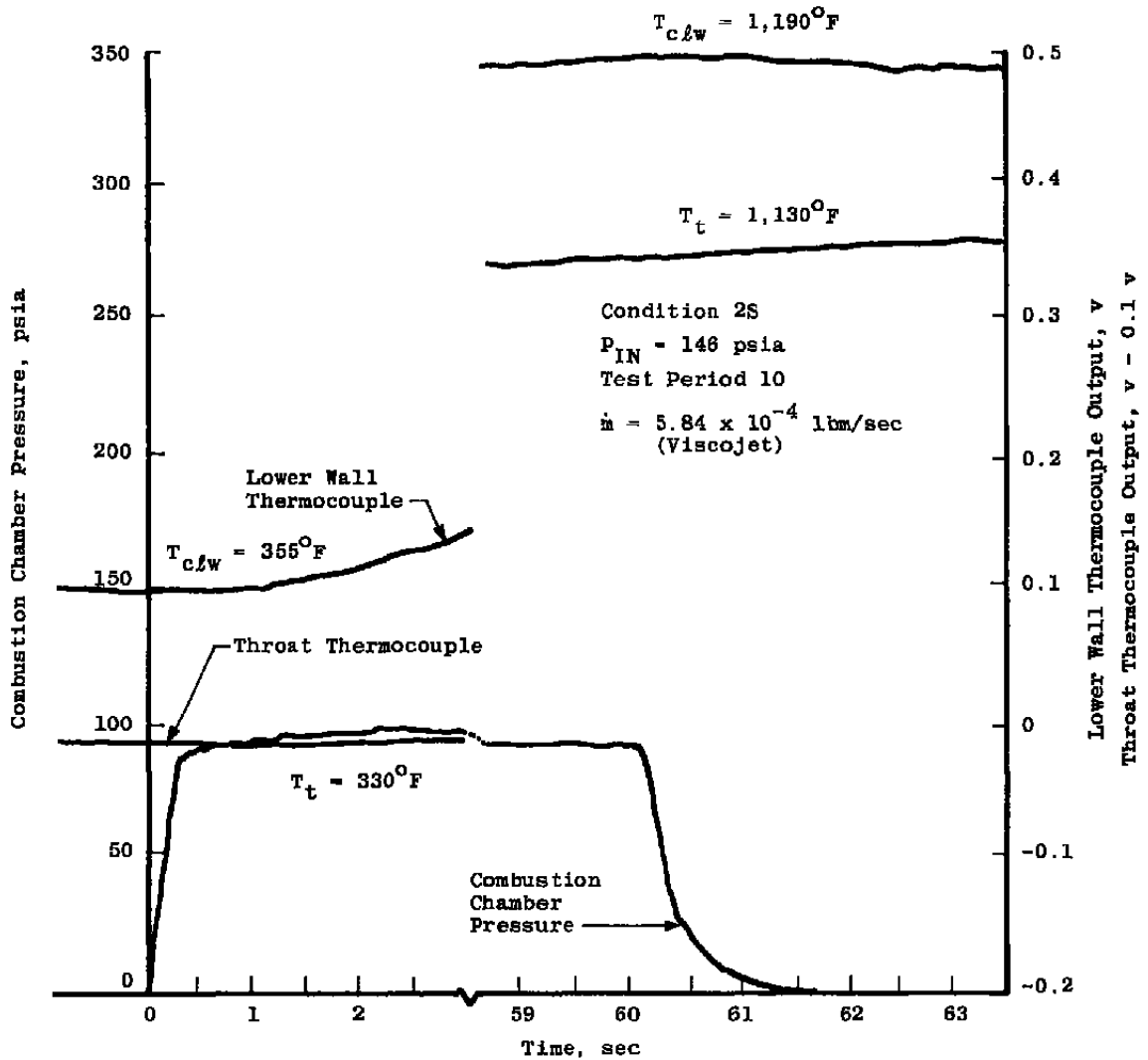
Figure 109. Condition 2S, 60-sec firing.
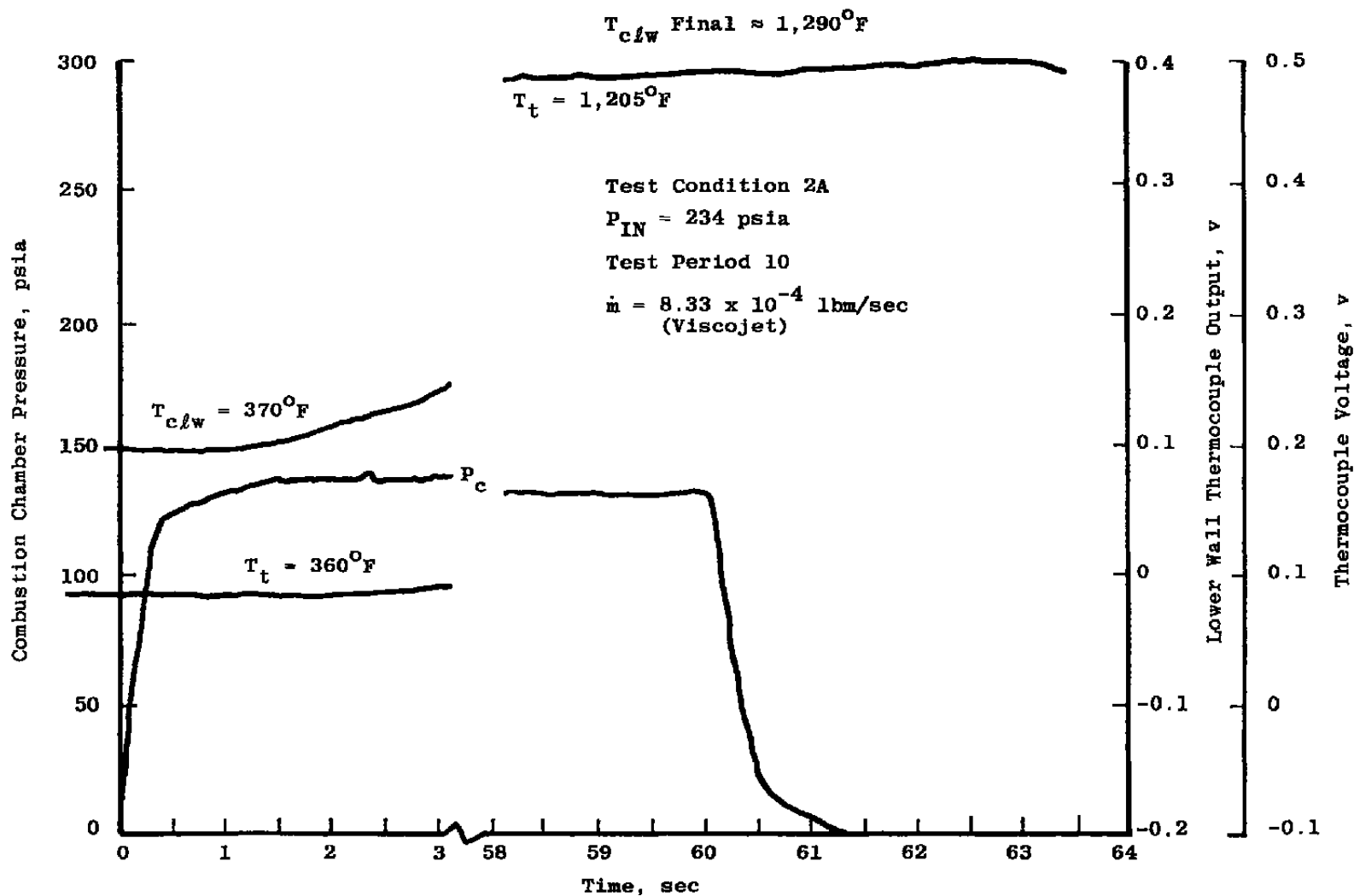
Figure 110. Condition 2A, 60-sec firing.
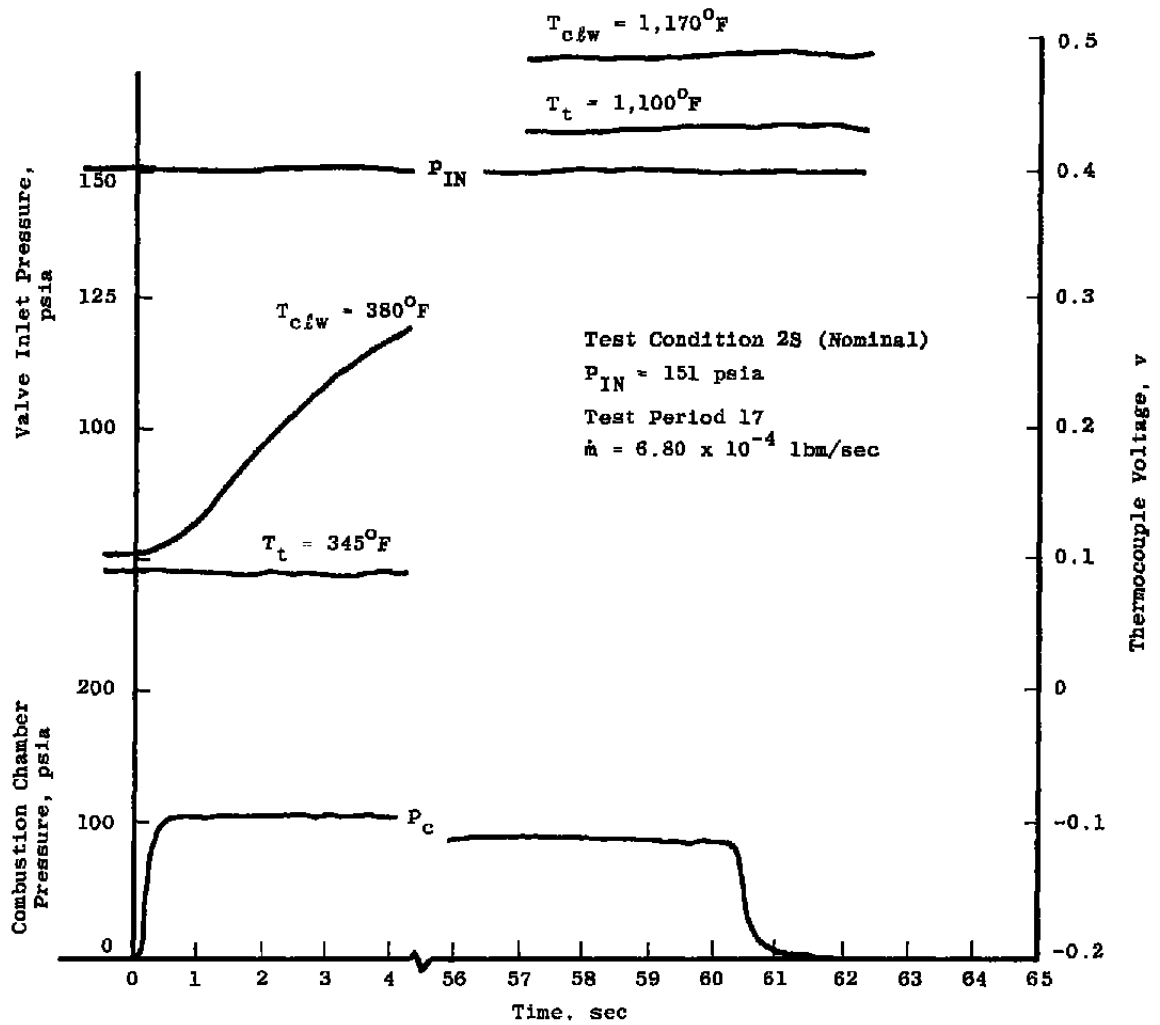
Figure 111. Condition 2S (nominal), 60-sec firing, post-"catastrophe".

Figure 112. Viscojet mass flow calibration.

The chart shows:

Viscojet Calibration for JP-4 at 74°F

Y-axis: Reynolds Number, $\dfrac{4}{\pi d_e} \dfrac{\dot{m}}{\mu}$

X-axis: Pressure Modulus, $\dfrac{g_c \rho d_e^3}{\mu^2 N_s d_s} \Delta P$
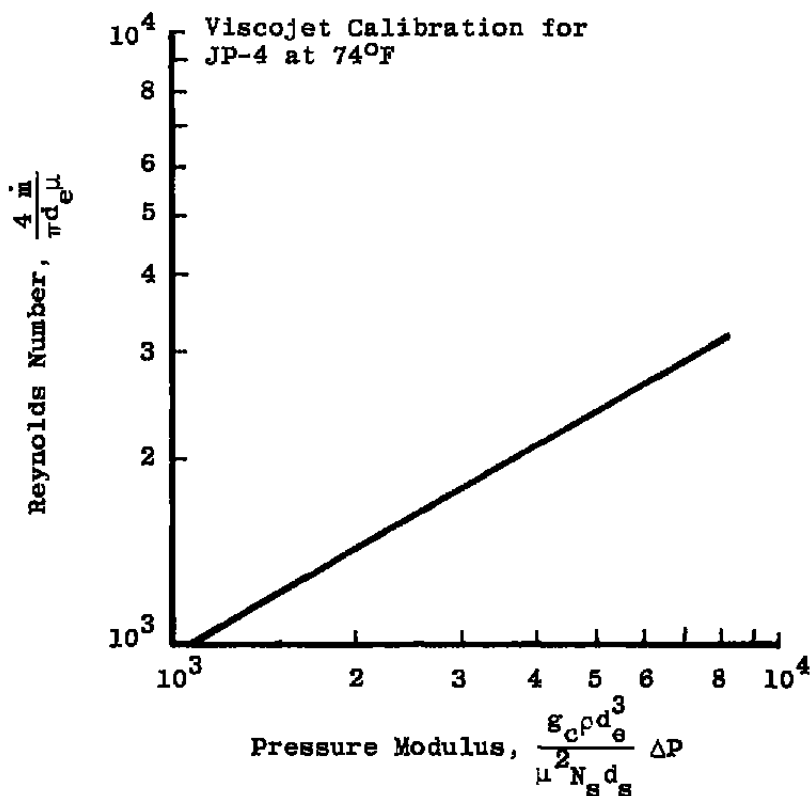
N_2H_4 Equation: $\dot{m}_{N_2H_4} = 1.527 \times 10^{-5} (\Delta P)^{0.575}$

(ΔP in psia, $\dot{m}$ in lbm/sec)

g_c = Newton's Constant

ρ = Fluid Density

d_e = Effective Orifice Passage Diameter

ΔP = Viscojet Differential Pressure

μ = Fluid Viscosity

N_s = Number of Viscojet Elements

d_s = Measured Diameter of Viscojet Element

$\dot{m}$ = Mass Flow Rate

176

Figure 113. Chromel-Alumel calibration curve for thruster data.
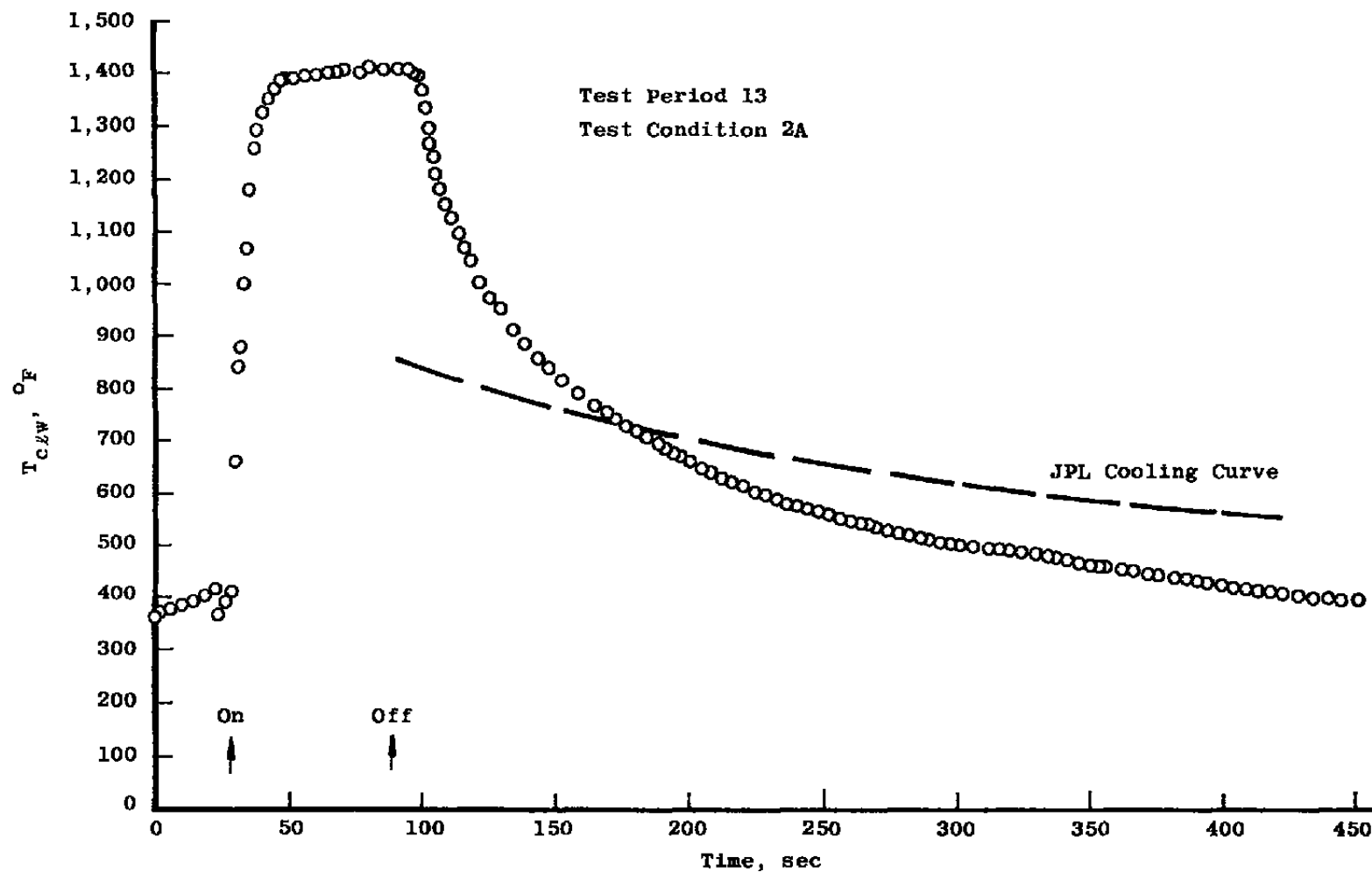
Figure 114. Engine cooling curve, $T_{c\ell w}$ versus time.
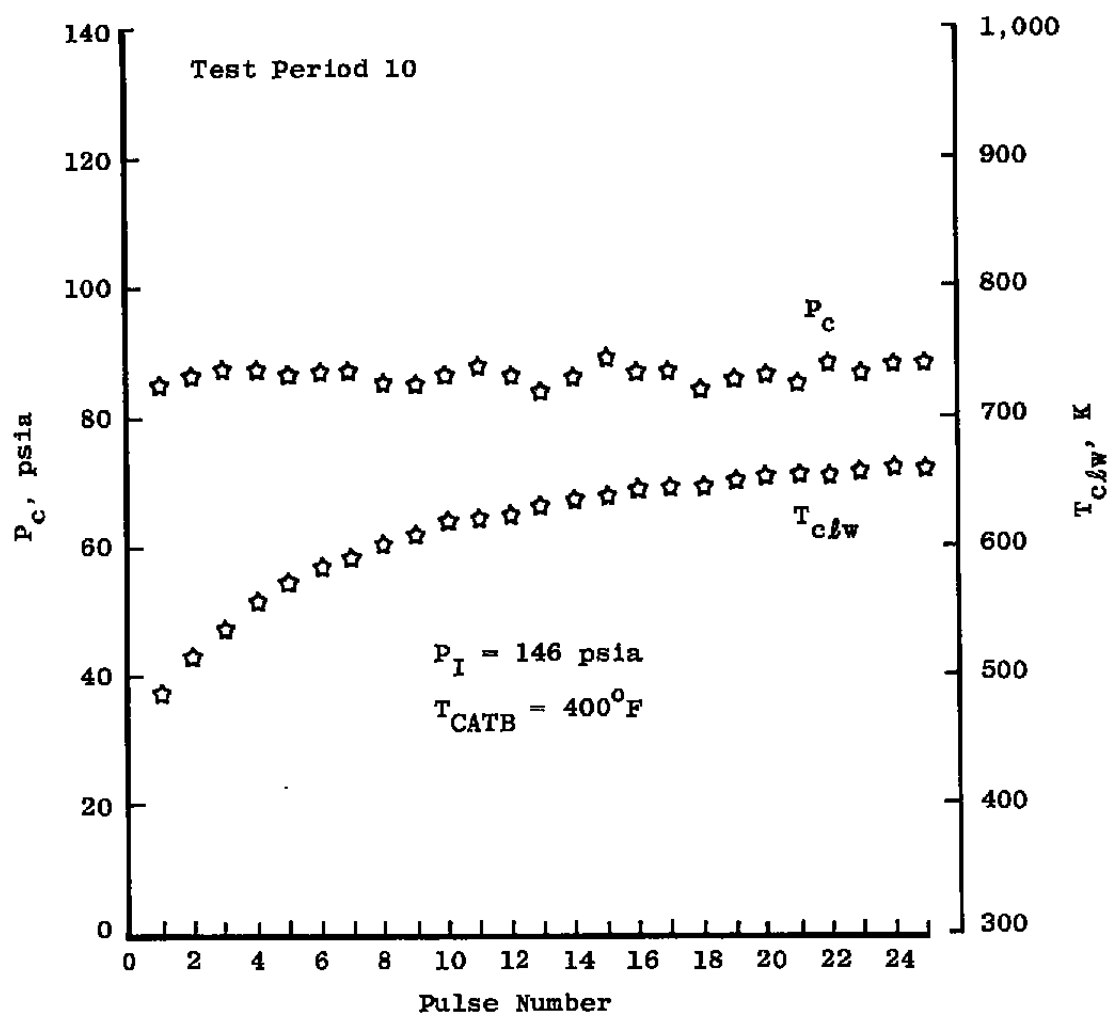
Figure 115. Thruster chamber properties for P_{IN} = 146 psia.
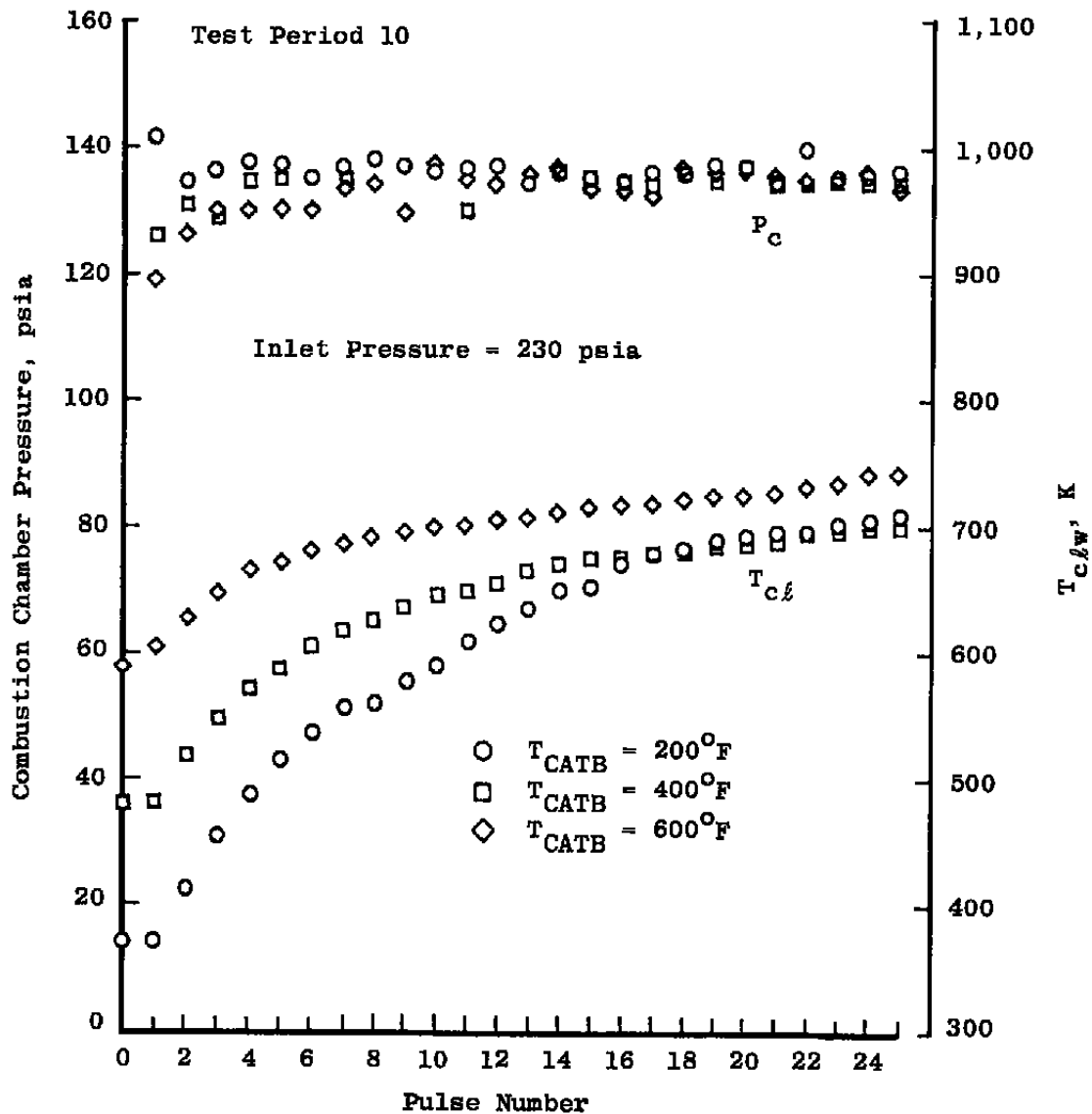
Figure 116. Combustion chamber property variation with pulse number for P_{IN} = 230 psia.
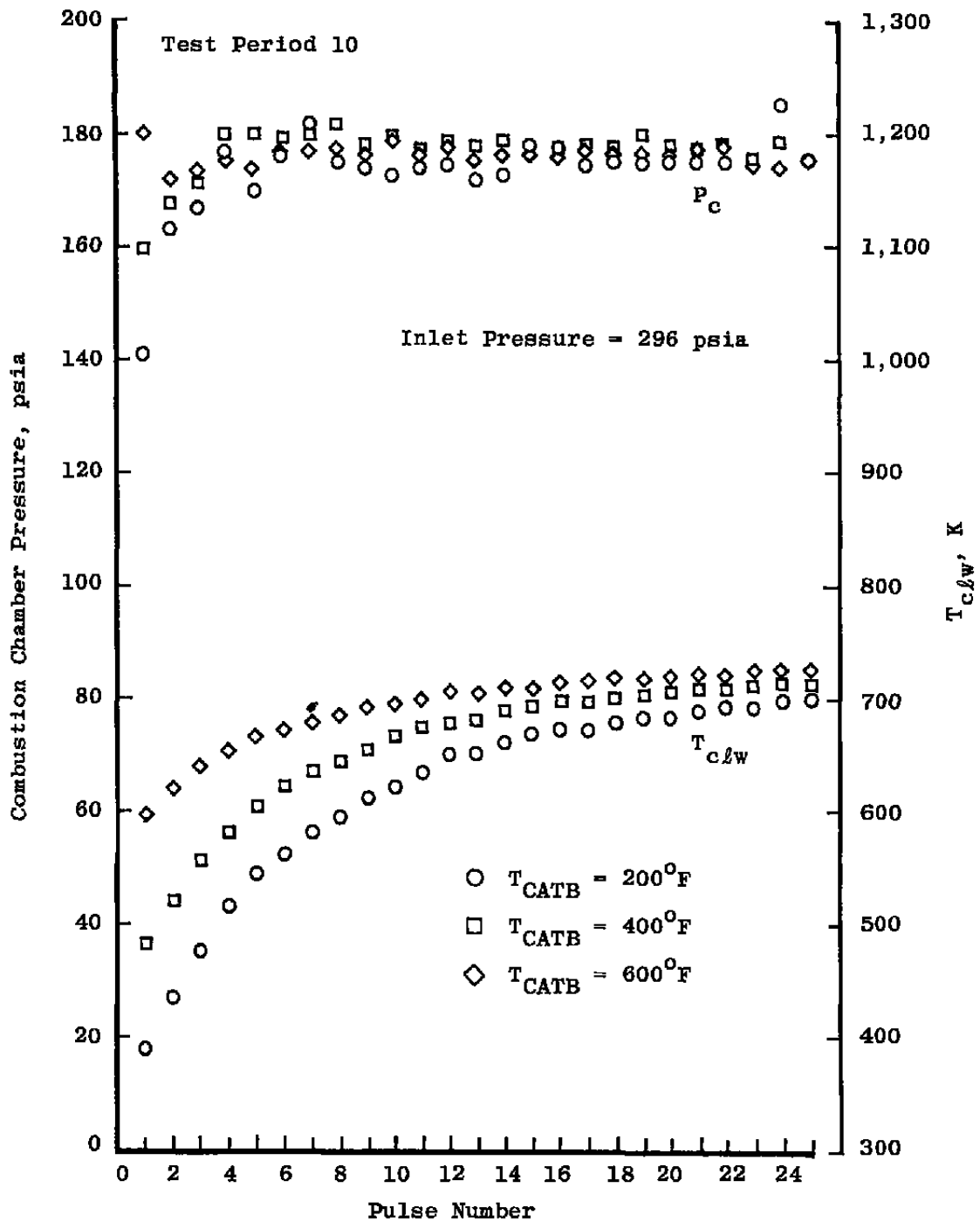
Figure 117. Thruster chamber properties for P_{IN} = 296 psia.
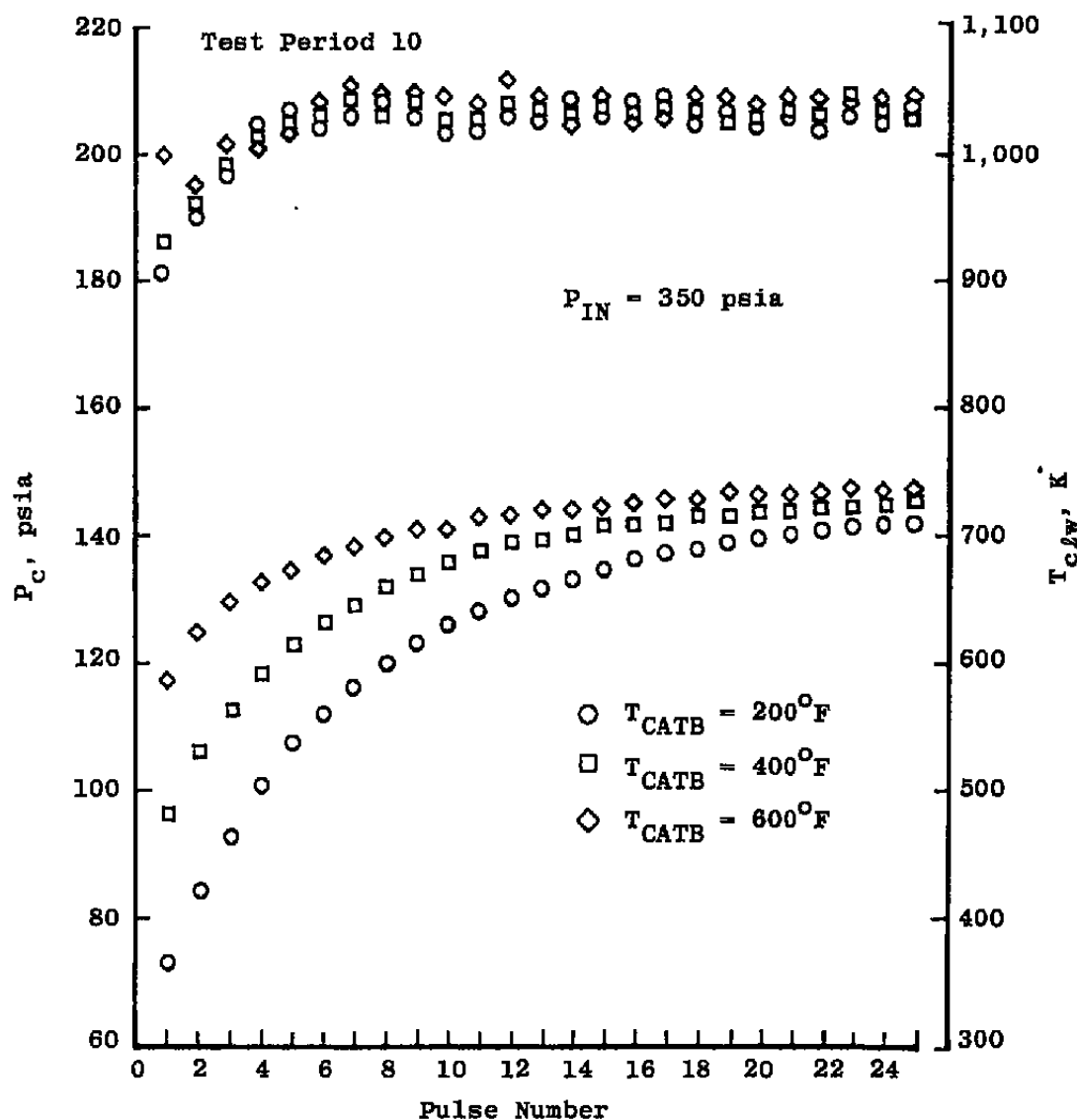
Figure 118. Thruster chamber properties for P_{IN} = 350 psia.
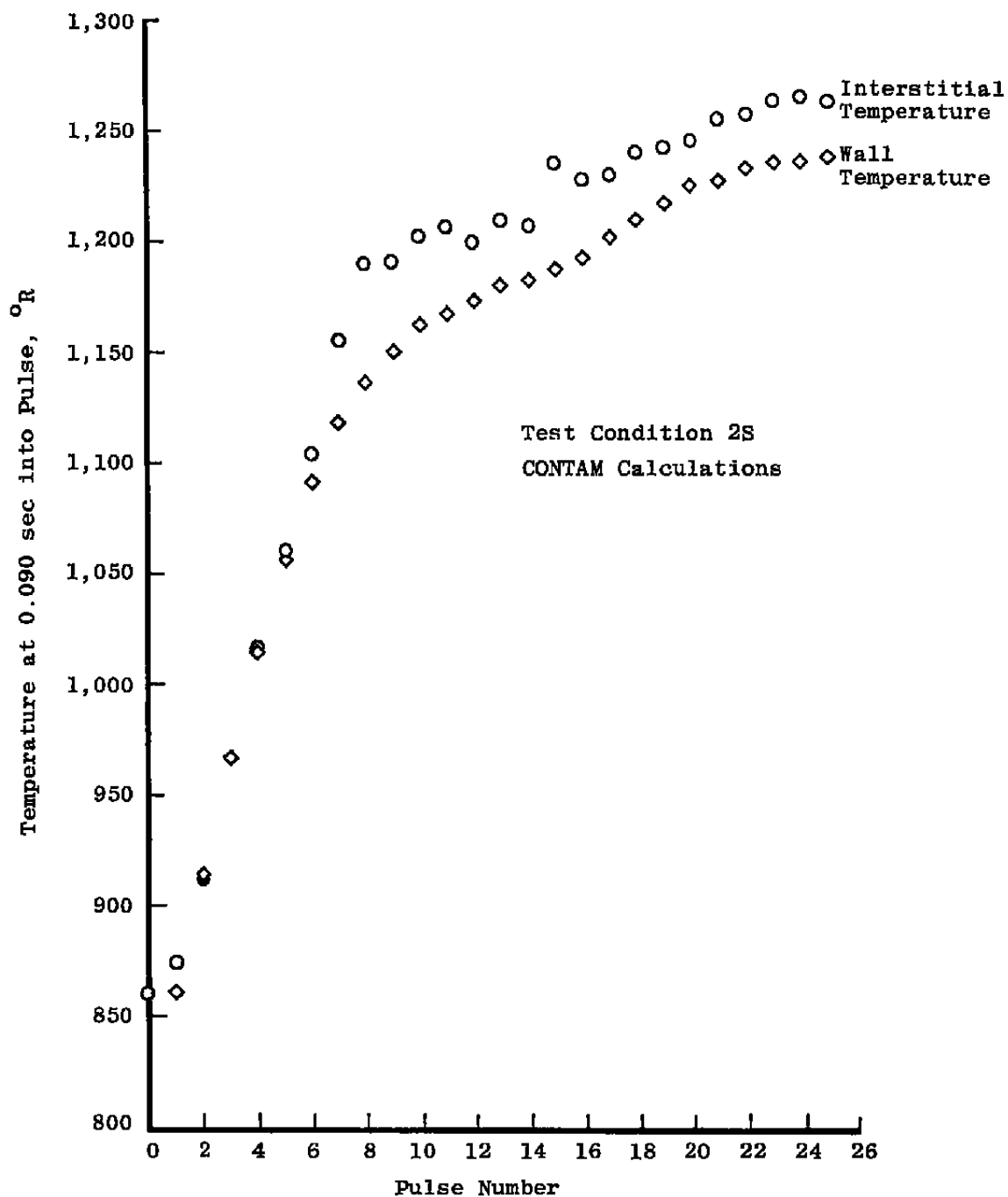
Figure 119. Comparison of wall and interstitial temperatures, condition 2S.
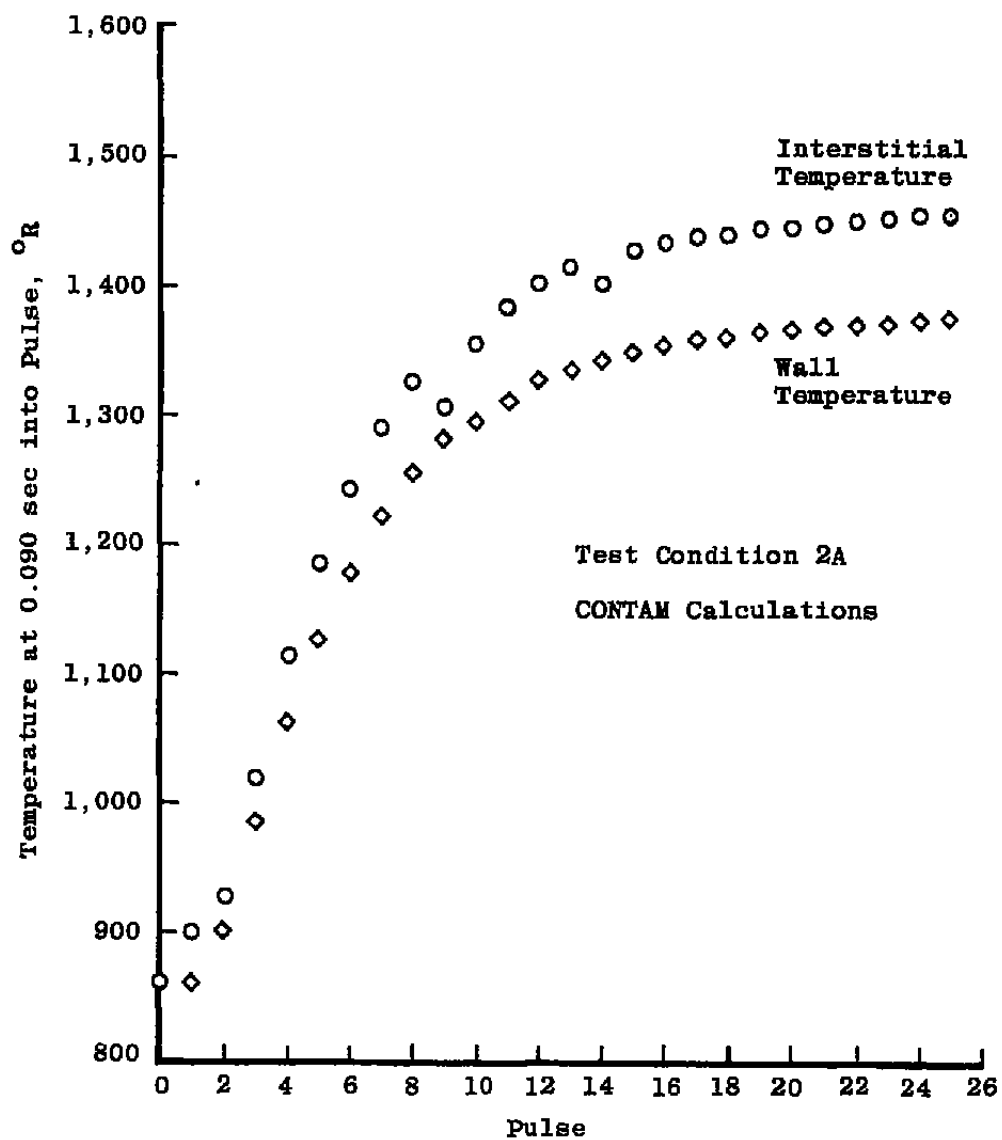
Figure 120. Comparison of wall and interstitial temperatures, condition 2A.
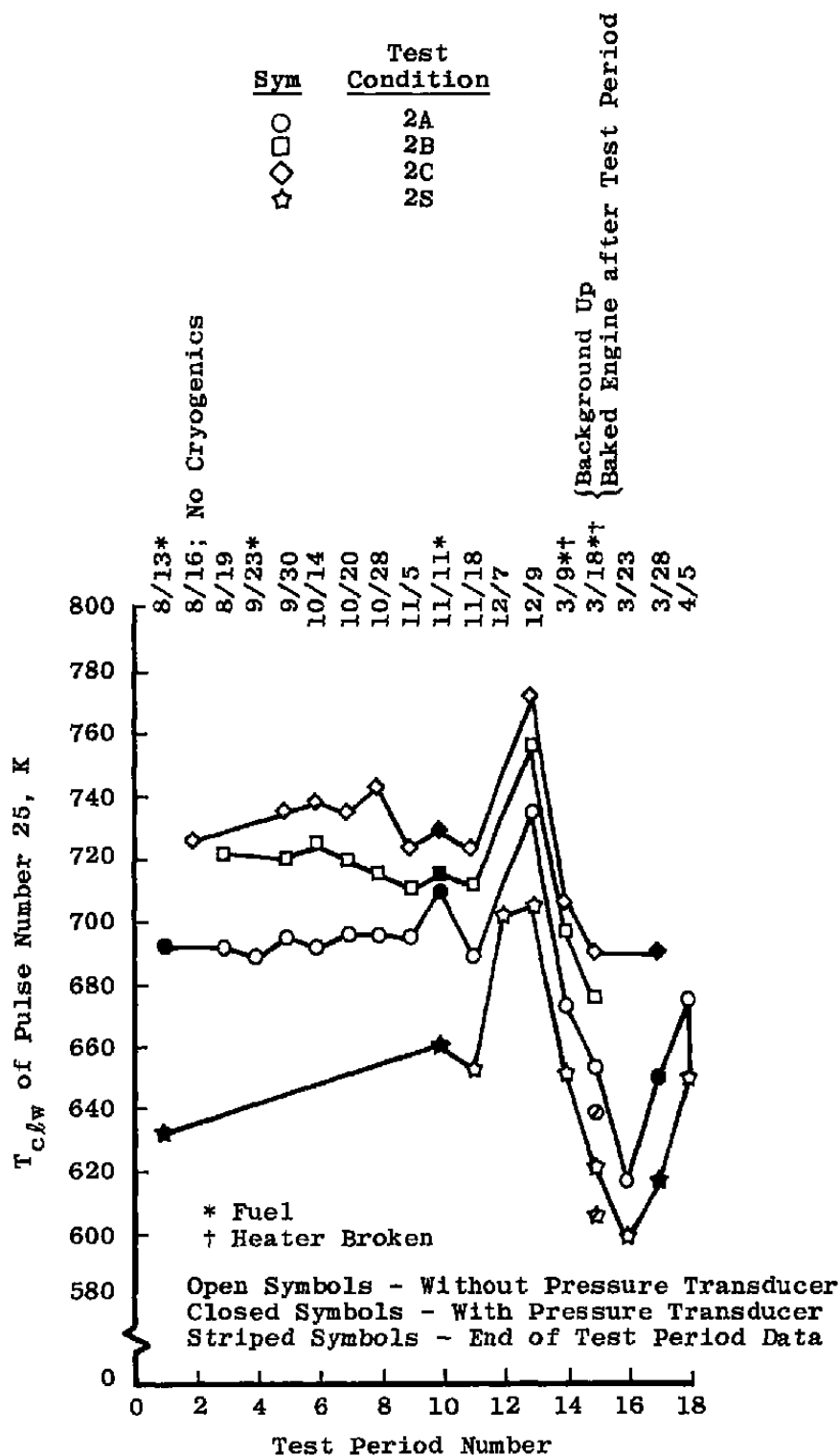
Figure 121. Lower wall temperature behavior versus test period.

185
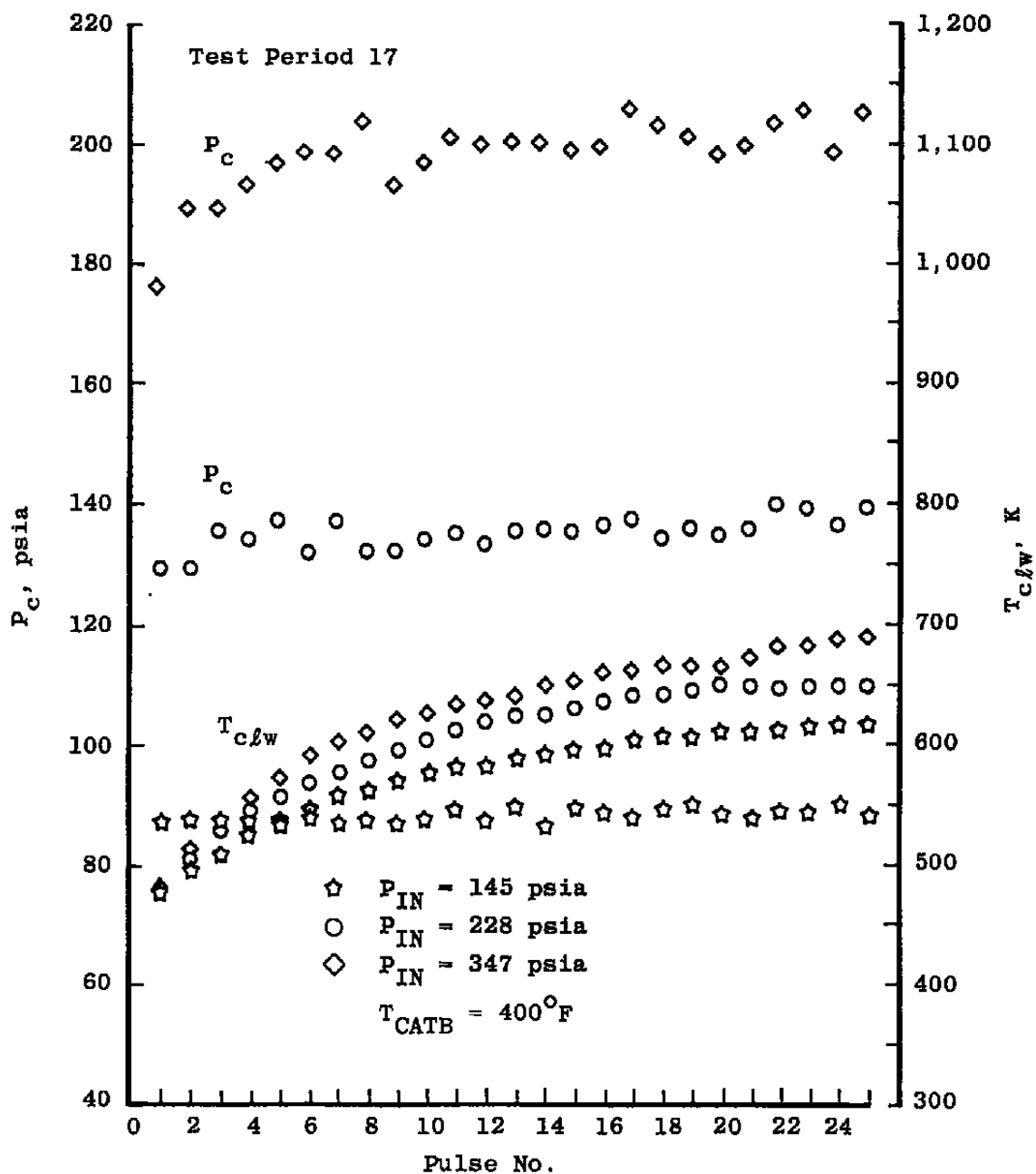
Figure 122. Combustion chamber properties for test period 17, post-"catastrophe".
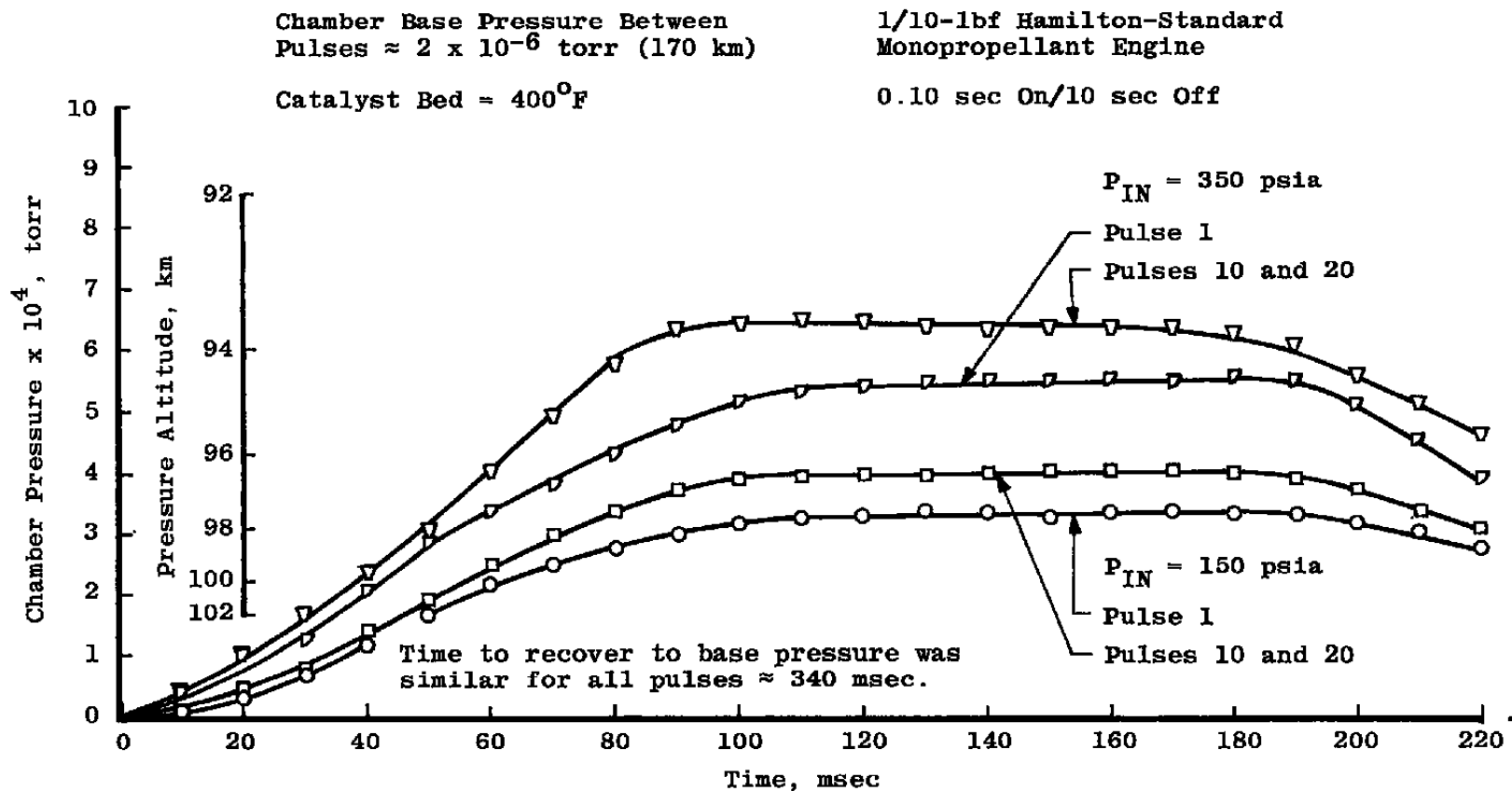
Figure 123. AEDC 4- by 10-ft RVC altitude performance.

Table 1. Thruster Test Conditions and Data Matrix

Test Case	P_{IN}, psia	P_c, psia	Initial T_{CATB}, °F	Thrust, lbf	Rayleigh Data			Near Exit Plane	Electron Beam Data			Mass Spectrometer Data	QCM Data		Flow Visualization			
					Near Exit Plane Raman Data	Axial Scan	Radial Scan		Axial Scan	Radial Scan	Backflow		Phase A	Phase B	Electron Beam Black and White	Color	Laser Black and White	Particle Sampling
1A	230	135	200	0.165	x	x		x				x	x					
1B	298	173	200	0.212								x	x					
1C	349	205	200	0.255								x	x					
2S	145	85	400	0.1	x	x	x	x	x		x	x	x	x	x	x	x	x
2A	230	135	400	0.165	x	x	x	x	x	x		x	x		x	x		
2B	296	175	400	0.212	x			x	x			x	x		x			
2C	349	205	400	0.255	x			x	x			x	x		x			
3A	230	135	600	0.165	x	x		x				x	x					
3B	296	175	600	0.212								x	x					
3C	349	205	600	0.255								x	x					

Table 2. 0.1-lbf Thruster Characteristics (Design)

Thrust, lbf	0.28
Bed Loading, lbm sec/in.^{2}	0.0221
Inlet Pressure, psia	340
Chamber Pressure, psia	225
Catalyst Bed Diameter, in.	0.268
Bed Length, in.	0.337
Steady-State Flow Rate, lbm/sec	0.00124
Sieve Size	30-35
Dribble Volume, in.^{3}	0.0002
Injector Tube I.D., in.	0.0102
Number of Injectors	1
Nozzle Area Ratio	55
Standoff Thermal Resistance, °F hr Btu	167
Stability Ratio	0.44
Diffuser Inner Screen	80 x 80
Diffuser Outer Screen	325 x 325
Nozzle Type	Conical
Valve/TCA Joint	Welded
Valve/Manufacturer	Wright
Valve Type	Solenoid
Chamber Material	Inconel 600
Standoff Material	Inconel 625
Nozzle Material	Inconel 600
Injector Tube Material	Inconel 600
Ret. Screen Materials	L-605
Thermal Coating	Gold

Table 3. Fuel Sample Analysis

Supplier: Olin Corporation, Lake Charles, La. Contract No. F41608-75-C-0975

Specification: MIL-P-26536C, Amendment I Schedule No. SFSR 13

Batch 122-75, Drum H-8388

Olin Corp. Analysis of Batch 122-75 (30 June 1975)

	Percent N_2H_4	Percent H_2O	Particulates Mg/l	Percent Cl	Percent Fe	Percent Aniline	Percent NVR	Percent CO_2	Percent Volume Carbonaceous Matter
Drum H-8415	99.54	0.29	0.2	<0.0001	0.00004	0.37	0.0004	0.0004	0.009
Drum H-8406	99.42	0.34	0.2	<0.0001	0.00004	0.38	0.0032	0.0004	0.006
Military Specs.	98.5 Min	1.0 Max	1 Max	0.0005 Max	0.002 Max	0.50 Max	0.005 Max	0.02 Max	0.02 Max

Table 4. Fuel System Particulate Requirements

Particle Size, μm	Maximum Tolerable Count*
0 to 5	Unlimited
5 to 10	1,200
10 to 25	200
25 to 50	50
50 to 75	5
75 to 90	1
>90	0

*No metallic particles >50μm were tolerable.

Table 5. Wavenumber/Wavelength Settings for Raman Measurements

Plume Species Monitored	Signal		Background	
	Wavenumber, cm^{-1}	Wavelength, $\overset{o}{A}$	Wavenumber, cm^{-1}	Wavelength $\overset{o}{A}$
N_2	1,2069.6	8,285	1,2054.6	8,296
H_2	1,3811.4	7,240	1,3786.4	7,254
H_2	1,4043.7	7,121	1,4003.7	7,141
NH_3	1,4180.8	7,052	1,4160.8	7,062

Table 6. Summary of Calibration Factors for Laser-Raman/Rayleigh Measurements

Test Period	τ_D, nsec	$C_{F_{N_2}}$, cm^{-3}	C_{F_R}	C_{F_T}	B_{F_R}
4	72.7	2.19×10^{16}	---	---	---
5	72.7	2.43×10^{16}	---	---	---
6	72.7	2.21×10^{16}	0.247	0.850	---
7	74.2	2.82×10^{16}	0.234	0.893	---
8	74.2	2.88×10^{16}	0.213	0.930	2.41
9	76	2.26×10^{16}	0.276	0.938	---
11	76	3.03×10^{16}	0.216	0.928	2.36
14	76	1.26×10^{16}	0.226	0.923	2.56

Table 7. Laser-Raman Results

Test Period	Test Cond.	Axial Position x,in.	$\hat{x}$	$n(N_2)$, cm^{-3} x 10^{16}	$n(H_2)$, cm^{-3} x 10^{16}	$n(NH_3)$, cm^{-3} x 10^{16}	n_T, cm^{-3}	T_r, K	T_R/T_O	T_O, K	n_O, cm^{-3}	T_{CATB} Initial, °F
6	2A	0.5	28.5	2.19	3.42	4.69	1.03×10^{17}	139	0.200	696.4	9.82×10^{19}	400
6	2A	0.2	18.5	3.97	5.83			183	0.263			
7	3A	0.5	28.5	2.48	4.00	5.86	1.23×10^{17}	137	0.186	736.4	9.42×10^{19}	600
7	3A	0.2	18.5	3.55	6.01							
9	3A	0.5	28.5	2.98	2.62	4.41	1.00×10^{17}	117	0.160	731.5	9.35×10^{19}	600
9	3A	0.2	18.5	5.90	5.71							
11	2S	0.5	28.5	1.36	2.28	4.75	8.39×10^{16}	99	0.152	650	6.92×10^{19}	400
11	2B	↓	↓	2.24	3.49	5.52	1.13×10^{17}	119	0.164	726.5	1.198×10^{20}	400
11	2C			3.12	3.76	4.70	1.16×10^{17}	106	0.142	744.5	1.335×10^{20}	400
11	2A			2.32	3.33	5.03	1.07×10^{17}	121	0.172	702.5	9.75×10^{19}	400
11	1A	↓	↓	1.10	1.63	2.43	5.16×10^{16}	154	0.230	670.3	1.016×10^{20}	200
11	2B	0.2	18.5	5.39	6.83			148	0.203	727.8	1.182×10^{20}	400
11	2S			2.91	3.56			177	0.274	647	6.94×10^{19}	
11	2A			----	5.48			183	0.261	701	9.76×10^{19}	
11	2C			7.21	7.34			185	0.249	742.5	1.345×10^{20}	
14	2S			2.35	3.83			148	0.229	647	7.06×10^{19}	
14	2A			5.76	5.90			178	0.257	692	1.003×10^{20}	
14	2B			6.32	5.66					723	1.205×10^{20}	
14	2C			7.64	4.58					741	1.362×10^{20}	↓
14	1A			4.41	4.67					663	1.047×10^{20}	200
14	3A	↓	↓	3.97	5.89					721	9.62×10^{19}	600

Table 8. Averaged Raman Results

Test Condition	$n(H_2)/n(N_2)$	γ	$\hat{x} = 18.5$			$\hat{x} = 28.5$			
			$n(N_2)$	$n(H_2)$	T_R/T_O	$n(N_2)$	$n(H_2)$	T_R/T_O	$n(NH_3)$
2S	1.51	1.26	2.6×10^{16}	3.7×10^{16}	0.25	1.4×10^{16}	2.3×10^{16}	0.15	4.8×10^{16}
2A	1.49	1.26	4.9×10^{16}	5.7×10^{16}	0.26	2.3×10^{16}	3.4×10^{16}	0.19	5.0×10^{16}
2B	1.24	1.23	5.9×10^{16}	6.2×10^{16}	0.20	2.2×10^{16}	3.5×10^{16}	0.16	5.5×10^{16}
2C	0.94	1.21	7.4×10^{16}	6.0×10^{16}	0.25	3.1×10^{16}	3.8×10^{16}	0.14	4.7×10^{16}
3A	1.32	1.24	4.5×10^{16}	5.9×10^{16}		2.7×10^{16}	3.3×10^{16}	0.17	5.1×10^{16}

Table 9. Laser-Rayleigh Results: Test Condition 2A, Test Periods 6 and 9

Test Period	Test Condition	Axial Position (x), in.	Axial Position $(\hat{x})$	Radial Position (r), in.	Radial Position $(\hat{r})$	I_{Ry_1}, cm^{-3}	$\hat{I}_{Ry_1}$	n_o, cm^{-3}
6	2A	8	278.5	0	0	2.19×10^{17}	2.23×10^{-3}	9.82×10^{19}
		6	211.9			3.95×10^{17}	4.02×10^{-3}	
		4	145.2			4.93×10^{17}	5.02×10^{-3}	
		2	78.5			1.10×10^{18}	1.12×10^{-2}	
		1	45.2			4.26×10^{18}	4.34×10^{-2}	
		0.5	28.5			7.49×10^{18}	7.63×10^{-2}	
		0.2	18.5			1.84×10^{19}	1.88×10^{-1}	
		0.5	28.5	−0.45	−15	6.43×10^{16}	6.55×10^{-4}	
				−0.30	−10	1.33×10^{18}	1.35×10^{-2}	
				−0.15	−5	4.77×10^{18}	4.85×10^{-2}	
				0.16	5.3	3.89×10^{18}	3.96×10^{-2}	
9	2A	8	278.5	0	0	2.57×10^{17}	2.61×10^{-3}	9.86×10^{19}
		7	245.5			3.63×10^{17}	3.68×10^{-3}	
		6	211.9			4.47×10^{17}	4.53×10^{-3}	
		5	178.5			7.37×10^{17}	7.47×10^{-3}	
		4	145.2			8.39×10^{17}	8.51×10^{-3}	
		4	145.2			8.46×10^{17}	8.58×10^{-3}	
		3	111.9			1.61×10^{18}	1.63×10^{-2}	
		2	78.5			2.23×10^{18}	2.26×10^{-2}	
		1.5	61.9			5.80×10^{18}	5.88×10^{-2}	
		1	45.2			6.68×10^{18}	6.77×10^{-2}	
		0.75	36.9			1.13×10^{19}	1.15×10^{-1}	
		0.5	28.5			1.45×10^{19}	1.47×10^{-1}	
		0.35	23.5			2.07×10^{19}	2.10×10^{-1}	

Table 10. Laser-Rayleigh Results: Test Conditions 1A and 3A, Test Period 9

Test Period	Test Condition	Axial Position (x), in.	Axial Position ($\hat{x}$)	Radial Position (r), in.	Radial Position ($\hat{r}$)	I_{Ry_1}, cm^{-3}	$\hat{I}_{Ry_1}$	n_o, cm^{-3}	ρ_L
9	3A	0.35	23.5	0	0	8.82×10^{18}	9.45×10^{-2}	9.34×10^{19}	—
		0.5	28.5			6.51×10^{18}	6.97×10^{-2}		—
		0.75	36.9			5.02×10^{18}	5.38×10^{-2}		—
		1.0	45.2			3.52×10^{18}	3.77×10^{-2}		—
		1.5	61.9			1.82×10^{18}	1.95×10^{-2}		—
		2.0	78.5			1.44×10^{18}	1.54×10^{-2}		—
		3.0	111.9			4.87×10^{17}	5.21×10^{-3}		—
		4.0	145.2			2.99×10^{17}	3.20×10^{-3}		—
		6.0	211.9			1.29×10^{17}	1.38×10^{-3}		—
9	1A	0.5	28.5			1.03×10^{20}	1.0	1.03×10^{20}	—
		1.0	45.2			7.25×10^{19}	0.703		—
		2.0	78.5			3.20×10^{19}	0.310		—
		3.0	111.9			1.99×10^{19}	0.193		—
		4.0	145.2			1.09×10^{19}	0.106		—
		6.0	211.9			4.97×10^{18}	0.483		—
		8.0	278.5			3.23×10^{18}	0.314		—
9	3A	0.5	28.5			—	—		8.32×10^{-2}

Table 11. Laser-Rayleigh Results: Test Conditions 2S, 2A, 2B, 2C, and 1A; Test Period 11

Test Period	Test Condition	Axial Position (x), in.	Axial Position ($\hat{x}$)	Radial Position (r), in.	Radial Position ($\hat{r}$)	I_{Ry_1}, cm^{-3}	$\hat{I}_{Ry_1}$	n_o, cm^{-3}	ρ_L
11	2S	8	278.5	0	0	8.32×10^{17}	1.20×10^{-2}	6.99×10^{19}	——
		7	245.2			9.37×10^{17}	1.35×10^{-2}		—
		6	211.9			1.31×10^{18}	1.88×10^{-2}		—
		5	178.5			1.36×10^{18}	1.96×10^{-2}		—
		4	145.2			2.25×10^{18}	3.25×10^{-2}		—
		3	111.9			4.86×10^{18}	7.01×10^{-2}		—
		2	78.5			7.23×10^{18}	1.04×10^{-1}		—
		1	45.2			1.39×10^{19}	2.0×10^{-1}		—
		0.5	28.5			3.41×10^{19}	4.91×10^{-1}		2.74×10^{-2}
		2.0	78.5	−0.6	−20	4.06×10^{16}	5.86×10^{-4}		
				−0.4	−13.3	2.01×10^{17}	2.90×10^{-3}		
				−0.2	−6.67	2.09×10^{18}	3.01×10^{-2}		
				0.2	6.67	2.98×10^{18}	4.30×10^{-2}		
	2A	0.5	28.5	0	0	3.96×10^{19}	4.06×10^{-1}	9.75×10^{19}	2.57×10^{-2}
	2B					7.05×10^{19}	5.89×10^{-1}	1.198×10^{20}	4.03×10^{-2}
	2C					8.57×10^{19}	6.56×10^{-1}	1.335×10^{20}	5.05×10^{-2}
	1A					1.23×10^{20}	1.21	1.016×10^{20}	1.37×10^{-2}

Table 12. Electron Beam Results

Test Period	Test Condition	$\hat{x}$	$\hat{r}$	T_R	$n(N_2)$
6	2A	28.5	0	177	---
		45.2		117	3.85E + 15
		78.5		105	1.04E + 15
		145.2		70	2.62E + 14
		211.9		60	1.29E + 14
		278.5		48	7.92E + 13
7	2A	78.5	−19.5	---	7.53E + 14[a]
			−12.9	---	1.06E + 15[a]
			−6.3	---	1.38E + 15[a]
			0.5	---	1.39E + 15[a]
			7.1	---	1.26E + 15[a]
			13.8	---	9.87E + 14[a]
			20.5	---	7.05E + 14[a]
			27.2	---	3.08E + 14[a]
			33.9	---	2.45E + 14[a]
			40.5	---	1.14E + 14[a]
			47.1	---	5.98E + 13[a]
8	2A	78.5	−20.0	62	6.09E + 14
			−13.2	68	9.03E + 14
			−6.6	76	1.19E + 15
			0	86	1.17E + 15
			6.8	80	1.15E + 15
			13.3	74	8.37E + 14
			20.1	72	5.04E + 14
			26.7	60	2.73E + 14
			33.4	50	1.53E + 14
			40.1	53	7.48E + 13
			46.7	58	3.93E + 13
		278.5	−33.0	47	7.23E + 13
			−16.7	18	6.81E + 13
			0.1	28	6.97E + 13
			16.8	---	6.45E + 13[a]

Table 12. Continued

Test Period	Test Condition	$\hat{x}$	$\hat{r}$	T_R	$n(N_2)$
8	2A	278.5	33.5	---	5.60E + 13[a]
			50.0	---	6.66E + 13[a]
			66.7	---	6.15E + 13[a]
			83.3	---	4.68E + 13[a]
			100.0	---	3.75E + 13[a]
			116.7	---	2.49E + 13[a]
			-116.7	38	2.37E + 13
			-99.9	54	3.25E + 13
			-83.2	42	4.55E + 13
			-66.7	34	4.93E + 13
			-50.0	49	6.40E + 13
			0	28	7.71E + 13
			16.7	---	7.65E + 13[a]
			33.3	---	8.08E + 13[a]
			50.0	---	5.73E + 13[a]
			66.7	---	4.64E + 13[a]
		145.2	-83.3	---	1.42E + 13[a]
			-73.3	---	3.78E + 13[a]
			-63.2	---	6.25E + 13[a]
			-53.4	---	8.26E + 13[a]
			-43.2	---	1.30E + 14[a]
			-33.4	---	1.83E + 14[a]
			-23.2	---	2.28E + 14[a]
			-13.4	---	2.82E + 14[a]
			-3.4	---	2.90E + 14[a]
			6.9	---	2.84E + 14[a]
			16.6	---	2.06E + 14[a]
			26.7	---	1.95E + 14[a]
9	2A	145.2	-70.1	23	3.63E + 13
			-30.0	16	1.77E + 14
			3.4	42	2.94E + 14
10	2A	278.5	0	---	8.05E + 13[a]
10	3A	278.5	0	---	8.70E + 13[a]

Table 12. Continued

Test Period	Test Condition	$\hat{x}$	$\hat{r}$	T_R	$n(N_2)$
10	1A	278.5	0	----	7.62E + 13[a]
	1B			----	9.37E + 13[a]
	3B			----	7.55E + 13[a]
	3C			----	1.19E + 14[a]
	1C			----	1.37E + 14[a]
	2/25 psia[b]	278.5	0	----	7.08E + 12[a]
	2/50			----	1.71E + 13[a]
	2/76			----	2.36E + 13[a]
	2/101			----	3.75E + 13[a]
	2/126			----	4.60E + 13[a]
	2/150			----	5.51E + 13[a]
	2/175			----	6.66E + 13[a]
	2/200			----	7.71E + 13[a]
10	2/225			----	8.49E + 13[a]
	2/250			----	8.90E + 13[a]
	2/276			----	9.07E + 13[a]
	2/300			----	9.23E + 13[a]
	2/326			----	1.06E + 14[a]
	2/350			----	1.08E + 14[a]
	2/2A	78.5	0	70	1.24E + 15
		145.2		44	3.59E + 14
		211.9		36	1.44E + 14
		278.5		28	8.66E + 13
	2S	78.5		81	8.16E + 14
		145.2		38	2.28E + 14
		211.9		35	9.77E + 13
		278.5		18	4.86E + 13
	2B	78.5		57	1.71E + 15
		145.2		41	4.43E + 14
		211.9		16	1.98E + 14
		278.5		9	1.13E + 14
	2C	78.5		103	1.63E + 15
		145.2		94	4 26E + 14
		211.9		43	1 91E + 14
		278.5		41	1.07E + 14

Table 12. Concluded

Test Period	Test Condition	$\hat{x}$	$\hat{r}$	T_R	$n(N_2)$
10	2A	145.2	0	---	3.85E + 14 [a]
11	2S	28.5	0	140 [c]	----
13	2S	20.2	↓	136 [c]	----
		28.5		125 [c]	----
↓	↓	45.2		105 [c]	----
16	2S	28.5	↓	225	----
		25.2	3.3	181	----
		21.9	6.7	123	1.38E + 15
		18.5	10.0	148	2.86E + 14
		15.2	13.3	---	3.35E + 13 [a]
		11.9	↓	69	8.39E + 12
		8.5	↓	---	1.27E + 12 [a]
		8.5	10.0	---	4.93E + 11 [a]
		11.9	10.0	---	1.55E + 13 [a]
		15.2	6.7	166	7.52E + 14
		15.2	10.0	132	1.22E + 14
↓	↓	11.9	6.7	---	1.14E + 14 [a]
16	2S	18.5	3.3	194	----
18	2S	28.5	0	141	----
		78.5		52	7.12E + 14
		145.2		34	2.07E + 14
	↓	278.5		30	4.92E + 13
	2A	28.5		---	----
		78.5		68	9.24E + 14
		145.2		40	2.64E + 14
		278.5	↓	22	6.47E + 13
		78.5	-20.0	32	4.55E + 14
			-10.0	47	7.53E + 14
			0	64	9.11E + 14
			10.0	52	6.93E + 14
			20.0	36	4.09E + 14
↓	↓	↓	33.3	59	8.93E + 13

[a] Calculation includes temperature-dependent band correction factor using an estimated T_R.

[b] Inlet pressure

[c] Continuous burn scan

Table 13. Averaged Electron Beam Results

x	Test Condition	$\overline{T}_{R,K}$	$\overline{n(N_2)}$, cm^{-3}
28.5	2S	158	----
45.2		105	----
78.5		67	7.6×10^{14}
145.2		36	2.2×10^{14}
211.9		35	9.8×10^{13}
278.5		24	4.9×10^{13}
28.5	2A	177	----
45.2		117	3.9×10^{15}
78.5		79	1.1×10^{15}
145.2		51	3.4×10^{14}
211.9		48	1.8×10^{14}
278.5		31	7.6×10^{13}
78.5	2B	57	1.7×10^{15}
145.2		41	4.4×10^{14}
211.9		16	2.0×10^{14}
278.5		9	1.1×10^{14}
78.5	2C	103	1.6×10^{14}
145.2		94	4.3×10^{14}
211.9		43	1.9×10^{14}
278.5		41	1.1×10^{14}

Table 14. Far-Field Ammonia-to-Nitrogen Mole Fraction Ratios

Pulse Number	Thruster Test Condition							
	2S	1A	2A	3A	1B	2B	3B	2C
1	3.40	3.42	3.58	3.10	3.43	2.64	2.97	3.35
5	2.08	2.36	2.17	1.72	2.57	2.21	2.03	2.43
10	1.94	1.93	1.91	1.58	1.90	1.80	1.64	1.66
15	2.02	1.77	1.82	1.74	1.91	1.73	1.64	1.65
25	1.82	1.58	1.78	1.61	1.65	1.64	1.63	1.73

Table 15. Equilibrium Values of Ammonia Dissociation Fractions:
Mass Spectrometer Results

Pulse Number	$[NH_3]/[N_2]$	Corresponding Equilibrium x
1	3.24	0.072
5	2.20	0.214
10	1.80	0.289
15	1.79	0.292
25	1.68	0.299

Table 16. Average Mass Deposition Rates: Test Condition 1A, Test Phase A

T_{QCM}, K	z, in.	x, in.	Test Period	Data Run	n	$<\dot{m}>_n$, gm/cm²-sec
144	21.21	7.63	10	4	5	5.49×10^{-6}
166	13.71	7.63	11	41	10	1.52×10^{-6}
144	20.21	7.63	9	39	5	4.71×10^{-6}
144	19.21	7.63	9	40	5	4.26×10^{-6}
144	18.21	7.63	9	41	5	4.61×10^{-6}
144	17.21	7.63	9	42	5	4.04×10^{-6}
144	16.21	7.63	9	43	5	4.05×10^{-6}
144	15.21	7.63	9	44	5	3.70×10^{-6}
144	14.21	7.63	9	45	5	3.24×10^{-6}
144	13.71	7.63	9	46	5	3.14×10^{-6}

Table 17. Average Mass Deposition Rates: Test Conditions 1B and 1C, Test Phase A

Test Condition	T, K	z, in.	x, in.	Test Period	Data Run	n	$<\dot{m}>_n$, gm/cm²-sec
1B	144	21.21	7.63	10	5	5	6.49×10^{-6}
1C	144	21.21	7.63	10	8	5	6.77×10^{-6}

Table 18. Average Mass Deposition Rates: Test Condition 2S, Test Phase A

T, K	z, in.	x, in.	Test Period	Data Run	n	$\langle \dot{m} \rangle_n$, gm/cm^2-sec
144	21.21	7.63	11	75	5	1.97×10^{-6}
	20.21			76		1.88×10^{-6}
	19.21			77		2.09×10^{-6}
	18.21			78		1.64×10^{-6}
	17.21			80		1.59×10^{-6}
	16.21			81		1.58×10^{-6}
	15.21			82		1.65×10^{-6}
	14.21			83		1.47×10^{-6}
	13.71			84		1.21×10^{-6}
	15.21	6.23		85		3.51×10^{-6}
		6.43		86		2.80×10^{-6}
		6.63		87		3.08×10^{-6}
		6.83		88		2.57×10^{-6}
		7.03		89		2.50×10^{-6}
		7.23		90		2.15×10^{-6}
		7.43		91		1.97×10^{-6}
		7.63		92		1.45×10^{-6}
		7.83		93		1.68×10^{-6}
	21.21	7.63		1		1.69×10^{-6}
164	21.21		10	40		1.44×10^{-6}
169	13.71		11	11		9.13×10^{-7}
164	15.21		10	39		1.43×10^{-6}
164	16.21		10	68		9.79×10^{-6}
164	18.21		10	36		1.69×10^{-6}
144	13.71		11	4	10	1.19×10^{-6}

Table 19. Average Mass Deposition Rates: Test Condition 2A, Test Phase A

T, K	z, in.	x, in.	Test Period	Data Run	n	$\langle \dot{m} \rangle_n$, gm/cm^2-sec
130	21.21	7.63	6	32	5	6.08×10^{-6}
	19.21			34		6.50×10^{-6}
	17.21			35		4.79×10^{-6}
	15.21			36		5.94×10^{-6}
	14.21			37		4.33×10^{-6}
	13.71			38		3.19×10^{-6}
144	21.21		9	1		2.93×10^{-6}
	20.21			14		3.29×10^{-6}
	19.21			15		3.40×10^{-6}
	18.21			16		3.59×10^{-6}
	17.21			17		4.13×10^{-6}
	16.21			19		3.49×10^{-6}
	15.21			20		3.53×10^{-6}
	14.71			21		2.45×10^{-6}
	14.21			22		2.30×10^{-6}
	13.71			24		2.41×10^{-6}
	17.21	7.41		64		4.59×10^{-6}
		5.21		65		9.50×10^{-6}
		6.41		67		7.66×10^{-6}
		4.98	8	59		8.57×10^{-6}
		---		---		---
		5.58		61		9.30×10^{-6}
		7.98		70		2.56×10^{-6}
	21.21	9.98		36		1.57×10^{-6}
		11.48		37		1.05×10^{-6}
		10.98		40		1.18×10^{-6}
		---		49		---
		9.48		50		1.96×10^{-6}

Table 19. Concluded

T, K	z, in.	x, in.	Test Period	Data Run	n	$\langle \dot{m} \rangle_n$, gm/cm^2-sec
144	21.21	----	8	51	5	----
		4.48		52		3.97×10^{-6}
		4.98		53		4.49×10^{-6}
		5.48		54		3.62×10^{-6}
		5.98		55		4.19×10^{-6}
		6.48		56		3.43×10^{-6}
		6.98		57		4.01×10^{-6}
		7.48		58		3.02×10^{-6}
169	15.21	6.88		17		2.92×10^{-6}
		7.08		18		2.04×10^{-6}
		7.28		19		1.86×10^{-6}
		7.48		20		1.42×10^{-6}
		7.88		23		2.16×10^{-6}
		8.08		24		1.46×10^{-6}
		8.48		26		1.43×10^{-6}
176		7.63		9		4.34×10^{-7}
		7.88		10		7.57×10^{-7}
		8.28		12		3.20×10^{-7}
		8.68		15		4.83×10^{-7}
		7.48		16		3.45×10^{-7}
144	13.71	7.63	11	61		2.17×10^{-6}
130			7	49		3.89×10^{-6}
164			11	45		1.97×10^{-6}
110	21.21		7	11		7.48×10^{-5}
111				10		6.35×10^{-5}
159				1		1.40×10^{-6}
130				9		5.07×10^{-6}

Table 20. Average Mass Deposition Rates: Test Condition 2B, Test Phase A

T, K	z, in.	x, in.	Test Period	Data Run	n	$\langle \dot{m} \rangle_n$, gm/cm^2-sec
158	21.21	7.63	7	2	5	1.74×10^{-6}
143				9	5		4.04×10^{-6}
126				6	2		6.30×10^{-6}
104	↓			8	2	↓	8.15×10^{-5}
173	13.71			11	13	10	1.48×10^{-6}
170					14	10	2.23×10^{-6}
151					16	10	3.04×10^{-6}
144	↓	↓	↓		19	10	3.61×10^{-6}

Table 21. Average Mass Deposition Rates: Test Condition 2C, Test Phase A

T, K	z, in.	x, in.	Test Period	Data Run	n	$\langle \dot{m} \rangle_n$, gm/cm^2-sec
168	17.21	7.63	10	56	5	4.05×10^{-6}
	21.21			58		4.13×10^{-6}
	19.21			60		4.52×10^{-6}
	15.21		↓	63		3.74×10^{-6}
↓	13.71		11	25	↓	2.51×10^{-6}
144				22	10	3.90×10^{-6}
165				24		2.54×10^{-6}
154	↓	↓	↓	69	↓	(3.29×10^{-6})[a]
104	21.21		8	3	5	9.55×10^{-5}
130			5	6		8.25×10^{-6}
163	↓	↓	7	3	↓	1.46×10^{-6}

[a]Includes one large pulse.

Table 22. Average Mass Deposition Rates: Test Condition 3A, Test Phase A

T, K	z, in.	x, in.	Test Period	Data Run	n	$\langle \dot{m} \rangle_n$, gm/cm^2-sec
145	21.21	7.63	10	3	5	3.86 x 10^{-6}
144	20.21			27		3.27 x 10^{-6}
	19.21			28		3.35 x 10^{-6}
	18.21			29		3.04 x 10^{-6}
	17.21			30		3.37 x 10^{-6}
	16.21			31		3.64 x 10^{-6}
	15.21			32		2.76 x 10^{-6}
	14.71			33		2.79 x 10^{-6}
	14.21			34		2.89 x 10^{-6}
	13.96			35		2.61 x 10^{-6}
	13.71			36		2.29 x 10^{-6}

Table 23. Average Mass Deposition Rates: Test Conditions 3B and 3C, Test Phase A

Test Condition	T, K	z, in.	x, in.	Test Period	Data Run	n	$\langle \dot{m} \rangle_n$, gm/cm^2-sec
3B	144	21.21	7.63	10	6	5	4.96 x 10^{-6}
3C	144	21.21	7.63	10	7	5	5.64 x 10^{-6}

Table 24. Average Mass Deposition Rates: Test Condition 1A, Test Phase B

T, K	z, in.	x, in.	Test Period	Data Run	n	$\langle \dot{m} \rangle_n$, gm/cm^2-sec
144	44.83	0	14	43	10	2.10 x 10^{-6}
170				12		3.71 x 10^{-6}
160				53		2.70 x 10^{-6}

Table 25. Average Mass Deposition Rates: Test Condition 2S, Test Phase B

T, K	z, in.	x, in.	Test Period	Data Run	n	$<\dot{m}>_n$, gm/cm^2-sec
115	46.63	0	14	21	10	5.84×10^{-5}
165				30		1.18×10^{-6}
130				35		2.17×10^{-6}
160				30		1.18×10^{-6}
170				14		8.90×10^{-7}
144				47		1.34×10^{-6}
108	45.13		15	41		4.16×10^{-5}
116				42		3.32×10^{-5}
130				23		5.74×10^{-6}
179				46		2.16×10^{-6}

Table 26. Average Mass Deposition Rates: Test Condition 2A, Test Phase B

T, K	z, in.	x, in.	Test Period	Data Run	n	$<\dot{m}>_n$, gm/cm^2-sec
156	45.13	0	15	50	10	6.59×10^{-6}
144	45.13		15	65		1.00×10^{-5}
170	44.83		14	15		2.19×10^{-6}
144	44.83		14	36		2.85×10^{-6}
130	45.13		15	10		7.47×10^{-6}
160	44.83		14	31		1.63×10^{-6}

Table 27. Average Mass Deposition Rates: Test Condition 2B, Test Phase B

T, K	z, in.	x, in.	Test Period	Data Run	n	$\langle \dot{m} \rangle_n$, gm/cm^2-sec
161	44.83	0	14	56	10	3.10×10^{-6}
147				45		2.99×10^{-6}
169				17		2.50×10^{-6}
144				51		3.41×10^{-6}
187				67		7.01×10^{-7}
181				68		1.52×10^{-6}
130	45.13		15	19		8.19×10^{-6}
137	45.13		15	55		7.50×10^{-6}

Table 28. Average Mass Deposition Rates: Test Condition 2C, Test Phase B

T, K	z, in.	x, in.	Test Period	Data Run	n	$\langle \dot{m} \rangle_n$, gm/cm^2-sec
177	44.83	0	14	11	10	5.5×10^{-7}
144				46		3.1×10^{-6}
168				57		2.6×10^{-6}

Table 29. Average Mass Deposition Rates: Test Condition 3A, Test Phase B

T, K	z, in.	x, in.	Test Period	Data Run	n	$\langle \dot{m} \rangle_n$, gm/cm^2-sec
170	44.83	0	14	20	10	1.5×10^{-6}
174				29		8.2×10^{-7}
136				44		3.4×10^{-6}
151				50		2.91×10^{-6}
165				55		2.38×10^{-6}

Table 30. Averaged QCM Data

Test Condition	T_{QCM}, K	θ, deg	r^2, cm²	$\cos\phi$	$\overline{\langle\dot{m}\rangle_n}$, gm/cm²-sec	$\overline{\langle\dot{M}\rangle_n}$, gm/sec-sr	$\overline{\dot{m}}$,[a] gm/cm²-sec	$\overline{\dot{M}}$,[a] gm/sec-sr	JPL $\overline{\dot{M}}$,[b] gm/sec-sr
2S	144	19.79	3.28×10^3	0.984	1.8×10^{-6}	5.8×10^{-3}	2.8×10^{-6}		
		29.1	1.59×10^3	≈ 1	1.2×10^{-6}	1.9×10^{-3}	1.8×10^{-6}	2.9×10^{-3}	2.4×10^{-3}
		0	1.40×10^4	1.0	1.3×10^{-6}	1.8×10^{-2}	8.8×10^{-7}	1.6×10^{-3}	1.1×10^{-2}
	106	29.7	1.70×10^4	0.869^c	——	——	1.7×10^{-5c}	0.25	0.13
	106	0	1.29×10^4	1.0^c	——	——	9.5×10^{-5c}	1.22	0.32
2A	144	19.79	3.28×10^3	0.984	2.9×10^{-6}	9.4×10^{-3}	5.4×10^{-6}	——	——
		29.1	1.59×10^3	≈ 1	2.2×10^{-6}	3.5×10^{-3}	3.5×10^{-6}	——	——
		0	1.40×10^4	1.0	2.9×10^{-6}	4.1×10^{-2}	1.7×10^{-6}	——	——
	130	19.79	3.28×10^3	0.984	5.6×10^{-6}	1.8×10^{-2}	17.7×10^{-5}	——	——
	130	29.1	1.59×10^3	≈ 1	3.5×10^{-6}	5.6×10^{-3}	11.4×10^{-5}	——	——
	164	29.1	1.59×10^3	≈ 1	2.0×10^{-6}	3.2×10^{-3}	3.5×10^{-6}	——	——
	104	19.79	3.28×10^3	0.984	6.4×10^{-5}	0.21	33.3×10^{-5}	——	——
2B	144	19.79	3.28×10^3	0.984	4.0×10^{-6}	1.3×10^{-2}	——	——	——
		29.1	1.59×10^3	≈ 1	3.6×10^{-6}	5.7×10^{-3}	——	——	——
		0	1.40×10^4	1.0	3.0×10^{-6}	4.2×10^{-2}	——	——	——
	130	19.79	3.28×10^3	0.984	6.3×10^{-6}	2.0×10^{-2}	——	——	——
	104	19.79	3.28×10^3	0.984	8.2×10^{-5}	0.26	——	——	——
2C	144	29.1	1.59×10^3	≈ 1	3.9×10^{-6}	6.2×10^{-3}	——	——	——
	144	0	1.40×10^4	1.0	3.1×10^{-6}	4.3×10^{-2}	——	——	——
	130	19.79	3.28×10^3	0.984	8.3×10^{-6}	2.7×10^{-2}	——	——	——
	104	19.79	3.28×10^3	0.984	9.5×10^{-5}	0.31	——	——	——

[a] Predicted values using Ref. 18.

[b] JPL values have been multiplied by (10.1/0.15) to eliminate inclusion of thruster off time and by 3.9 to account for JPL values having been determined from thruster pulse sequences of $\approx 1,000$ (Ref. 13).

[c] For JPL data.

Table 31. Mole Fractions Used for MOCS or Predicted by CONTAM II

$[N_2]$	$[H_2]$	$[NH_3]$	$[N_2H_4]$	γ	Conditions
0.308	0.538	0.154	0	1.3	MOCS
0.246	0.216	0.538	0	1.2	MOCS
0.2902	0.1808	0.5287	0.0003	1.199	CONTAM II, Cond. 2S
0.3238	0.2529	0.4217	0.0016	1.218	CONTAM II, Cond. 2A

Table 32. Tabulation of MOCS Plume Predictions

γ	$\hat{x}$	n/n_o	T/T_o
1.3	18.5	2.9×10^{-3}	1.71×10^{-1}
	28.5	1.3×10^{-3}	1.34×10^{-1}
	45.2	5.45×10^{-4}	1.05×10^{-1}
	78.5	1.1×10^{-4}	6.5×10^{-2}
	145.2	2.04×10^{-5}	3.95×10^{-2}
	211.9	8.4×10^{-6}	3.0×10^{-2}
	278.5	4.4×10^{-6}	2.48×10^{-2}
1.2	18.5	2.35×10^{-3}	2.99×10^{-1}
	28.5	1.03×10^{-3}	2.51×10^{-1}
	45.2	4.35×10^{-4}	2.10×10^{-1}
	78.5	5.40×10^{-5}	1.41×10^{-1}
	145.2	1.10×10^{-5}	1.01×10^{-1}
	211.9	4.4×10^{-6}	8.4×10^{-2}
	278.5	2.3×10^{-6}	7.5×10^{-2}

Table 33. Average Combustion Chamber Number Density and Temperature

Test Condition	$\overline{n}_o,$ cm^{-3}	$\overline{T}_o,$ K
2S	6.97×10^{19}	648
2A	9.84×10^{19}	698
2B	1.195×10^{20}	726
2C	1.347×10^{20}	743
1A	1.031×10^{20}	667
3A	9.43×10^{19}	730

APPENDIX A
SYSTEM INSTRUMENTATION AND PDP-8 DATA ACQUISITION SYSTEM

A.1 Engine/Test Chamber Instrumentation

Shown in Table A-1 is a list of all the engine/test chamber parameters measured and their sequence within the data acquisition. A specific parameter was identified according to the time within the engine sequence that acquisition of the channel of data was accomplished. In particular, the parameters were assigned according to prefire, burn, and postfire, which are defined as:

    a)   prefire: time of initial startup before first ignition and between permanent tape data storage and engine ignition for subsequent engine pulses

    b)   burn: time during thrust envelope

    c)   postfire: time from thruster shutdown until completion of tape storage

The identification in Table A.1 is according to when the the data were acquired by the computer and not when the instrument acquired the data. For example, counters and integrators are storage devices and, as such, need not be computer inputs at the time of the measurement event. Pressure and temperature events obviously had to be read instantaneously. During thruster burn considerable attention was paid to assuring that the data acquisition occurred as rapidly as possible for more meaningful data. To this end the data channels were placed in priority sequences (e.g., catalyst bed temperature sequence being of greater significance than fuel valve temperature). Storage devices were read during the postfire interval to allow the computer to return to an end-of-thrust interval check as quickly as possible.

An obvious omission from the list was the combustion chamber pressure, but it was normally monitored by the Visicorder system only. For some runs the mass spectrometer was eliminated from the system, and the MPS was used to record 100 pressure values during the interval of the burn profile.

The catalyst bed, combustion chamber, and nozzle throat temperatures were provided by Chromel-Alumel thermocouples referenced to 150°F. In addition, a controller was used for the thermocouples for temperature control. A contactor control was used with a variable voltage power supply to control the excitation of the catalyst bed heater. Other engine-oriented thermocouples on the fuel lines were also temperature controlled and visually monitored but were not read by the computer. Copper-constantan thermocouples were used for the QCM crystal temperatures, and they were similarly controlled and handled by the computer.

217

The engine pressure transducer data handling included conventional excitation techniques (Endevco Transducer Excitation System, Model 4402) and data amplifiers (Preston, Model 8300-B, Wideband Floating Differential Amplifiers) as multiplexer inputs. The transducers were 0 to 34 atm (500 psia) (Tabor Model 226) on the fuel system with the exception of the combustion chamber, which was 0 to 250 psia (Tabor Model 185) and the Viscojet, which was 0 to 20.4 atm (300 psid) (Tabor Model 226).

Shown also in Table A-1 are the parameters designated for Visicorder presentation. The Visicorder was a Honeywell Model 1858. In addition to the combustion chamber pressure, data clock gate or thrust gate and the mass spectrometer sweep control voltage and spectral output were recorded. The recorder drive was initiated from the trailing edge of the counter background occurring 1 sec before thruster ignition. Delay was inserted of such a magnitude as to insure that drive speed was obtained before ignition. A drive duration compatible with thrust tailoff was provided.

Chamber pressure and cryogenic temperatures were the principle 4- by 10-ft chamber parameters of interest. Thermocouples were used principally to evaluate the cooldown states of the chamber and were not read into the computer. The thermocouples were strategically located at points on the chamber liners, on the cryogenic feed and return lines, and on the liquid helium pump. Standard temperature readouts were utilized.

Chamber pressures were read by an ion gage and Alphatron to cover the entire chamber pressure range and were input parameters to the computer. These devices were often sampled as a limit criterion for determining whether an abort was required. The chamber pressure ion gage was a General Electric Model 229T103 with readout and controller. The chamber pressure Alphatron was an NRC Model 530 with readout. Mass spectrometer probe pressure was read with a Veeco Model R-75 ion gage RG-31XM controller. All vacuum pressure outputs were processed through Preston amplifiers and a PDP-8 analog multiplexer and scaled such that there existed a one-to-one correspondence between computer input and controller meter reading. Range scale factors were required as inputs through the teletype keyboard during system setup. In general the General Electric ion gage was more representative of the vacuum chamber performance unless, of course, hydrogen pumping problems were being experienced. Both the Alphatron and General Electric gages were located in the warm section of the chamber, on the end flange, behind the thruster.

A.2 PDP-8 Data Acquisition System

As implied by previous discussion, there are multiple subsystems involved in the overall organization of the instrumentation, control, and data acquisition system which is described here. Shown in Fig. A-1 is a block diagram of the basic system showing the data-handling scheme for the principle parameters of interest. Certain control functions are also required. The integrated system had to perform individually the following:

1. Engine and fuel system:

    a. Measure certain critical parameters

    b. Control engine operation in preassigned firing sequence with appropriate safety interlocks

2. Measure certain vacuum chamber parameters

3. Laser or electron beam system:

    a. If applicable, fire ruby laser system at appropriate time

    b. Recharge and monitor laser capacitor as required

    c. Sweep electron beam during thruster burn interval for flow visualization purposes

4. Mass spectrometer system:

    a. Sweep mass spectrometer through preassigned mass numbers

    b. Record intensity of designated plume constituents

    c. Monitor mass spectrometer probe pressure and terminate mass spectrometer operation as required

5. Measure QCM frequency during interval between thruster pulses

6. Optical spectrometer measurements:

    a. Gate photon counters at the appropriate time relative to the engine thrust profile and/or the laser energy pulse

    b. Monitor spectrometer wavelength via encoder

    c.   Drive spectrometer to appropriate wavelength as specified

7.   Data acquisition system:

    a.   Input both counter and multiplexed analog data for A/D conversion

    b.   Monitor for safety purposes certain preselected engine, chamber, and fuel system parameters and perform corrective actions as required

    c.   Select parameters of interest for printout and permanent storage

    d.   Gate, reset, or turn on certain devices such as counters, integrators, recorders, tape system, etc. at appropriate times during the sequence

The heart of the system was a PDP-8 minicomputer. All data parameters flowed through this device and were permanently stored on an associated magnetic tape system (Dectape) and printed via a line printer. Both analog and digital parameters are input through appropriate buffers and/or multiplexers. A secondary process system (MPS) complemented the PDP-8 system and served as a supplementary control and data acquisition device for spectrometer wavelength selections and mass spectrometer mass number selection and data input. The data from the MPS moved through the PDP-8, as with the other systems, to the Dectape.

At the appropriate time the computer initiated the firing sequence. Shown in Fig. A-2 is a timing diagram for the sequence. A clock source was also used for providing a preselected data-sampling point during the thrust interval (see Fig. 5). This device accepted a trigger from the computer coincident with the initiation of a relay closure which in turn energized the engine fuel solenoid. A series of 100 clock pulses was subsequently provided after a time-out of a preselected delay. This delay was chosen to compensate for the inherent delay caused by relay and solenoid closure times. Thus a series of time pulses was provided to the computer for the duration of the thrust. The length of the pulse sequence was selected for the desired thrust interval. A gate output was also available which was sampled by the computer to note the end of the thrust interval. The computer sampled and counted each clock pulse until an accumulated total equaled a preselected pulse count. At this point data acquisition was initiated.

The counter system was a configuration of Ortec 715, 724, and 772 counter/timers with appropriate preamplifiers. These counters could be externally gated and reset as provided by the computer and/or a special laser data gate. The counter functions and read sequence was as follows:

1. Photomultiplier data

2. Gated 1 MHz clock -- data and background duration

3. QCM data

4. Thruster pulse counter (display only)

5. Computer reference times (sec)

Functions 1 through 3 required reset after each read operation and were gated on during the background measurement interval and during the laser pulse (or electron beam data interval) after the designated timing pulse was received. Control pulses for the data read sequence were supplied by the PDP-8 computer.

The organization of the system required that the computer monitor selectable critical parameters and the status of the fuel console fire switch at certain appointed times, and if preassigned limits were not met, then engine firing was terminated. For example, when program operation was initiated, chamber pressure and/or fuel temperature was monitored for some value within prescribed limits such that if precondition limits were not met, the thruster fire switch was not closed by the computer. The startup procedure is shown in the initial steps of Fig. A-3. The general features of this procedure were as follows:

1. Read system inputs and check preassigned parameter for prescribed limits before countdown sequence was started. If any parameter was outside the specified limits, the data run was aborted and error message provided.

2. Required fuel and computer console fire selections to initiate countdown sequence. Either function could abort the data run at any time.

3. Background and prefire measurements were made at 1 sec before engine firing on specified parameters.

4. The teletype (TTY) bell was rung every second of countdown and on thruster ignition to indicate status.

5. Visicorder was turned on at 0.25 sec before firing.

6. Status of laser was checked for full charge. The ignition waited for charge flag transition.

These same features generally apply for each prefire sequence.

The postfire features are also noted in Fig. A-3 and detailed to some degree in Fig. A-2. The general features of this sequence are as follows:

1. Check reference time for prescribed repetition rate.

2. Perform relay closure for energizing fuel solenoid.

3. Trigger Delay in Thrust Clock Generator. Required for synchronization of thrust gate with thruster chamber pressure profile.

4. Count clock pulses until prescribed pulse number for data acquisition is acknowledged.

5. Acquire either electron beam or laser/Raman data.

6. Detect end of thrust gate and accomplish engine shutdown.

Postfire features noted in Fig. A-3 generally concern the following:

1. Acquisition of postfire data

2. Scaling all acquired data.

3. Transfering to buffer, data to be retained in permanent storage.

4. Transfering from MPS all mass spectrometer data.

5. Flagging MPS for wavelength change if required.

6. Transfering from buffer to Dectape for permanent storage and future access and data reduction.
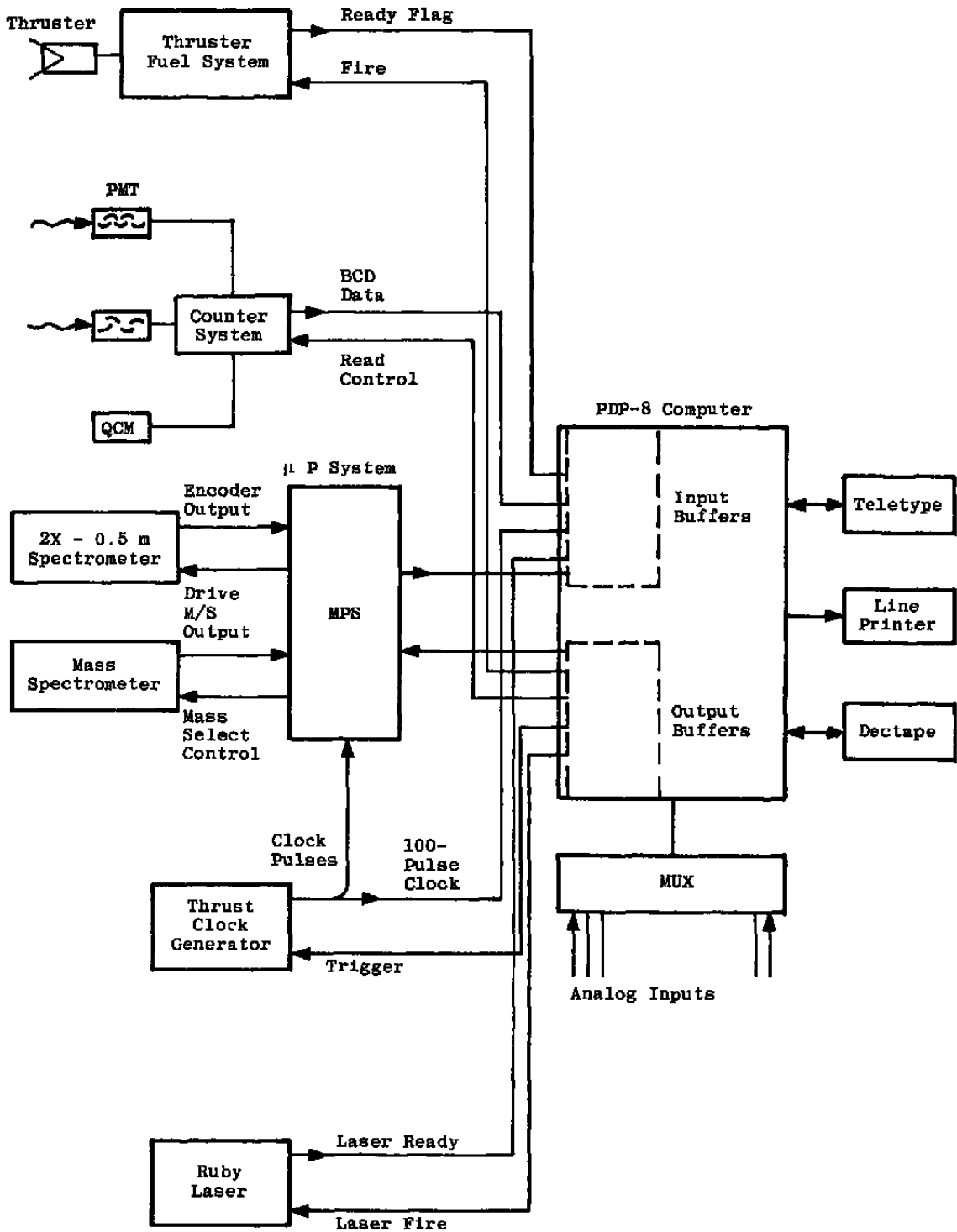
Figure A-1. Block diagram of basic data acquisition system.

Data Read A — MUX/A-D Counters
Data Read B — Counters
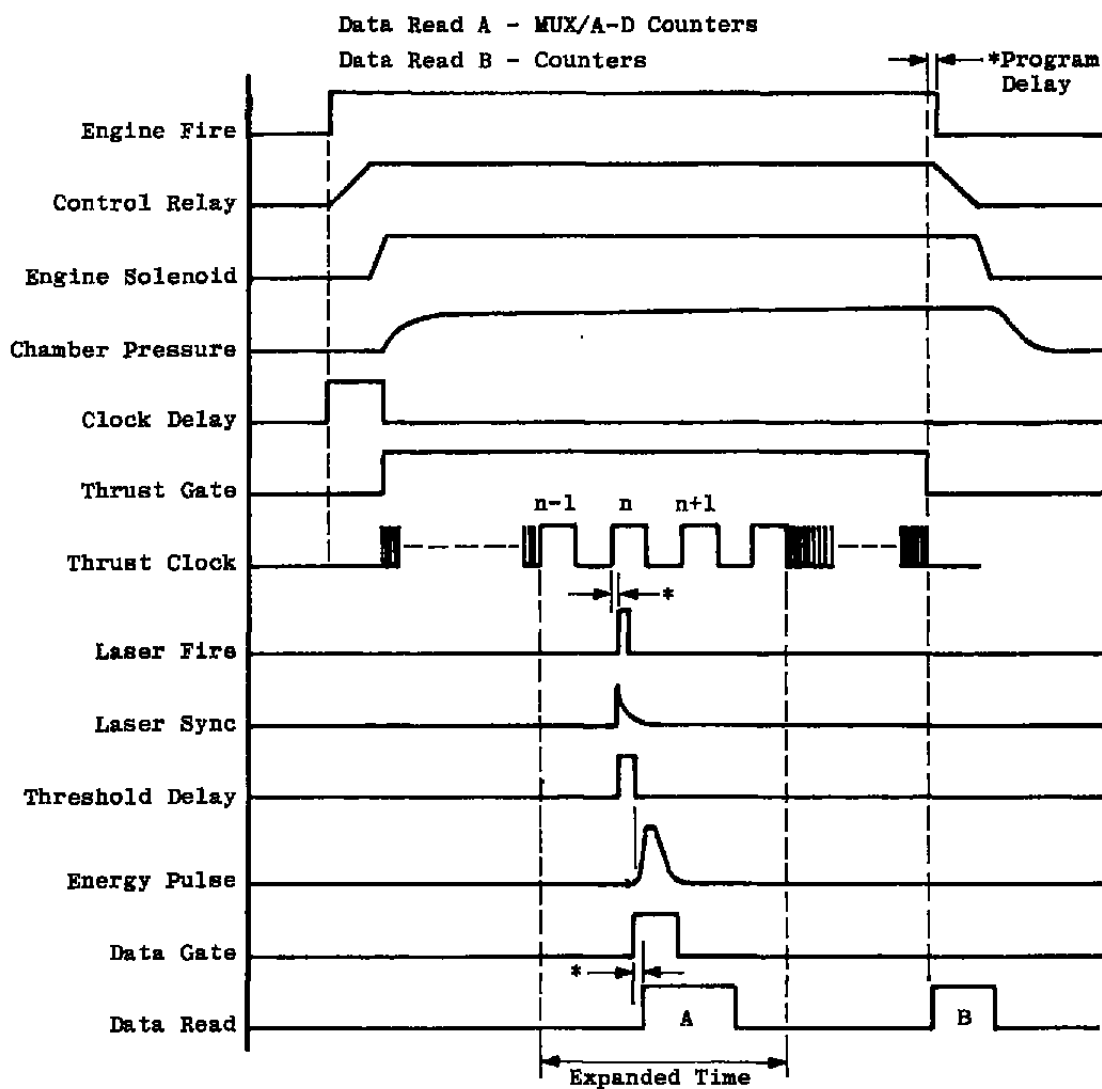
Figure A-2. Timing diagram of firing sequence.
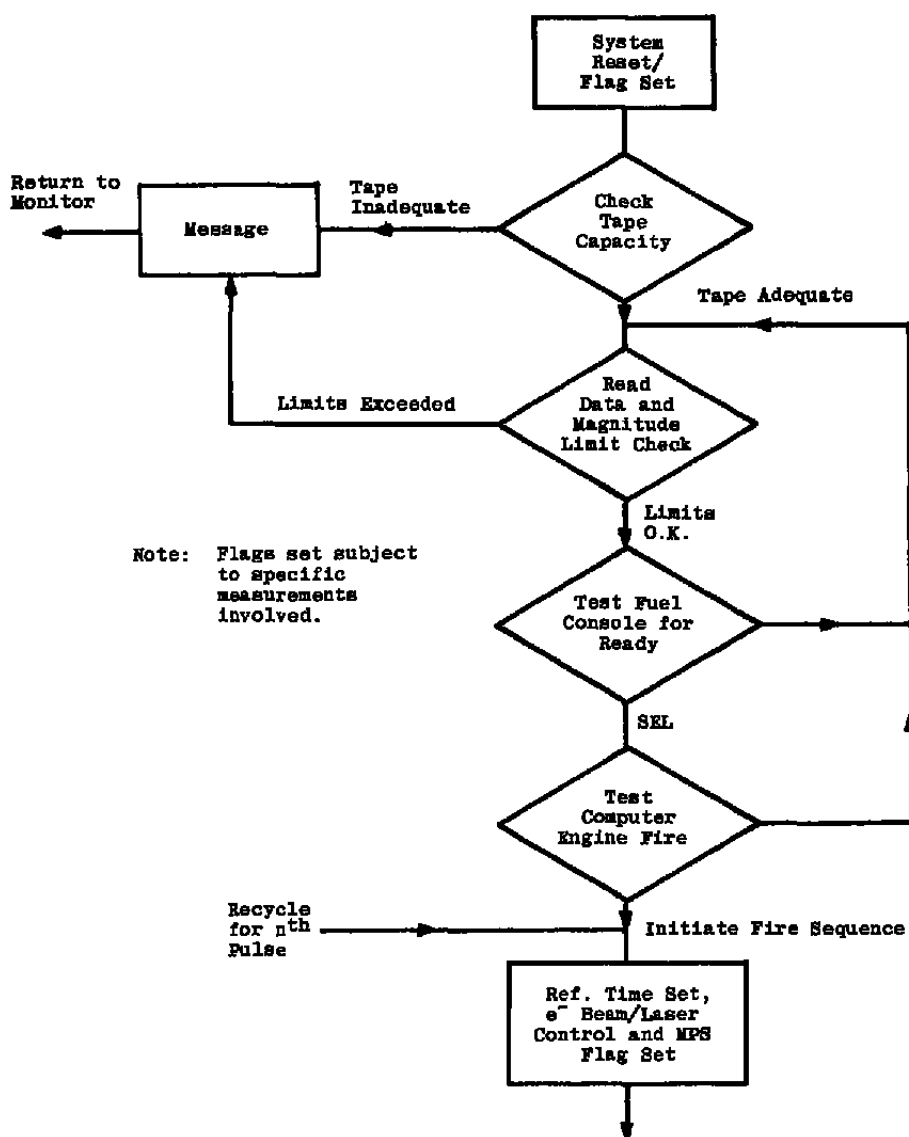
Figure A-3. System reset and flag adjustment sequence.
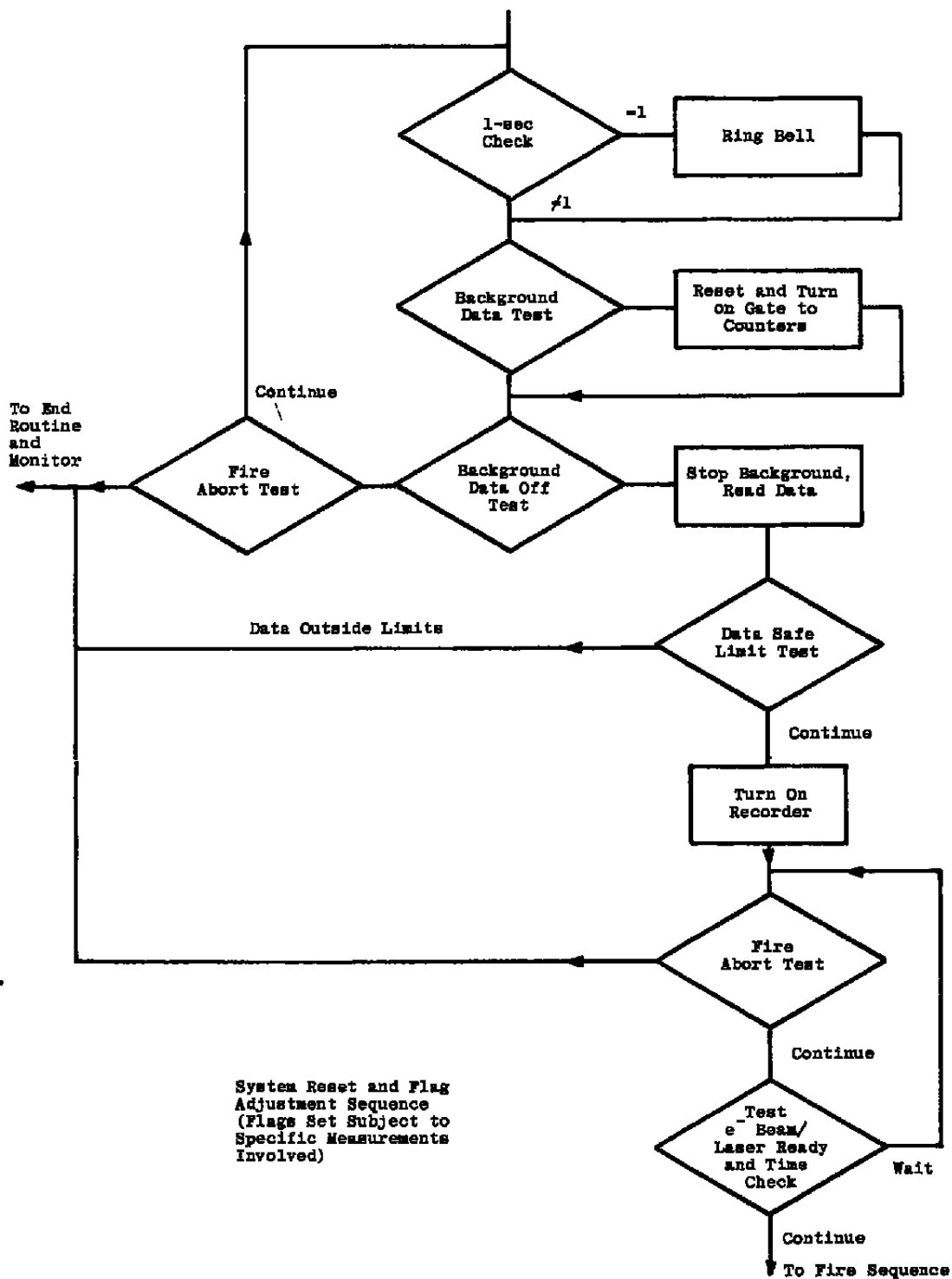
Figure A-3. Continued.
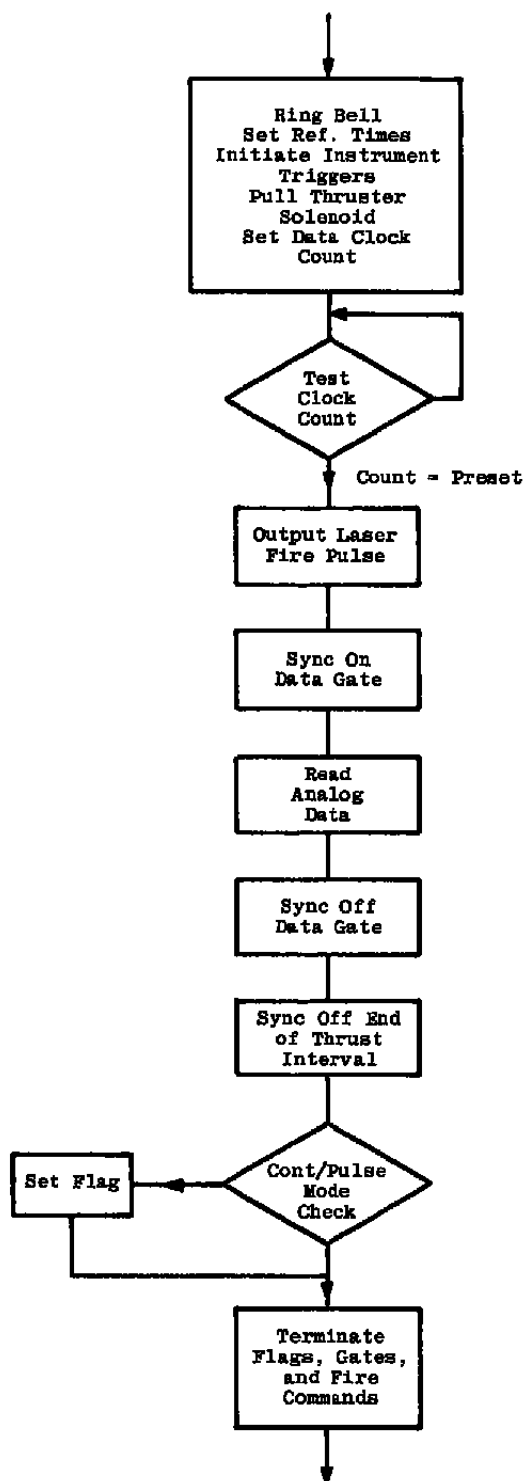
Figure A-3. Continued.
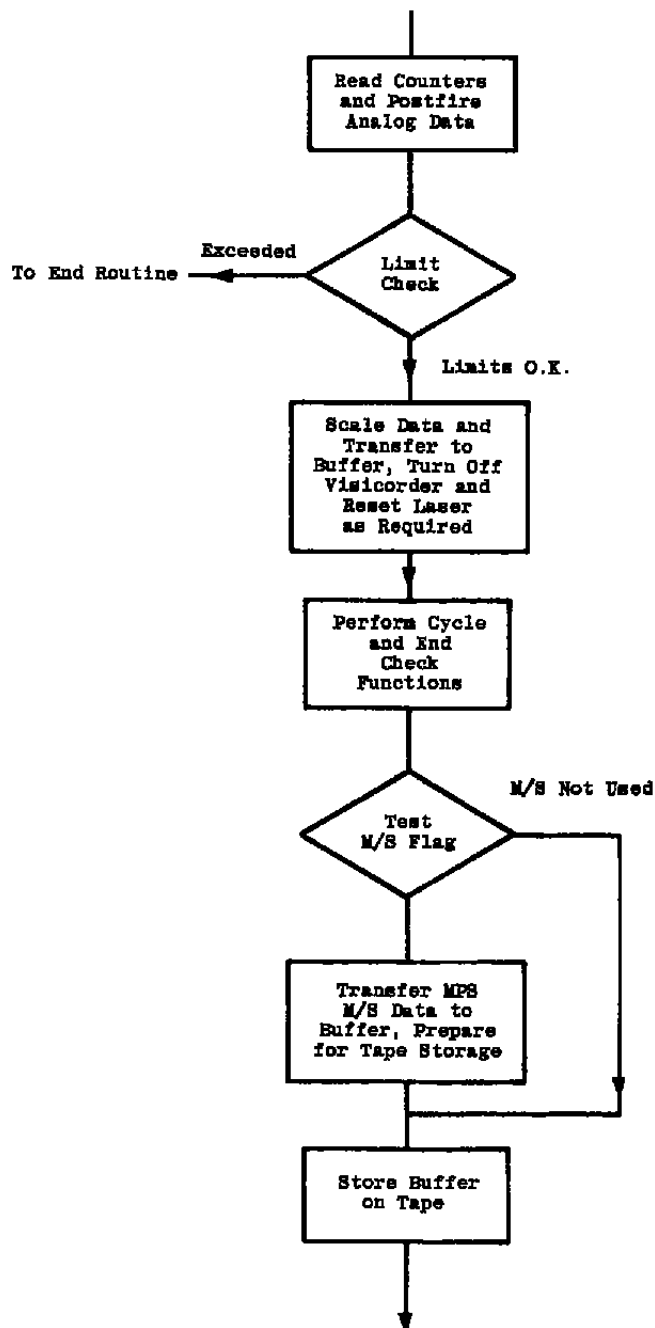
Figure A-3. Continued.
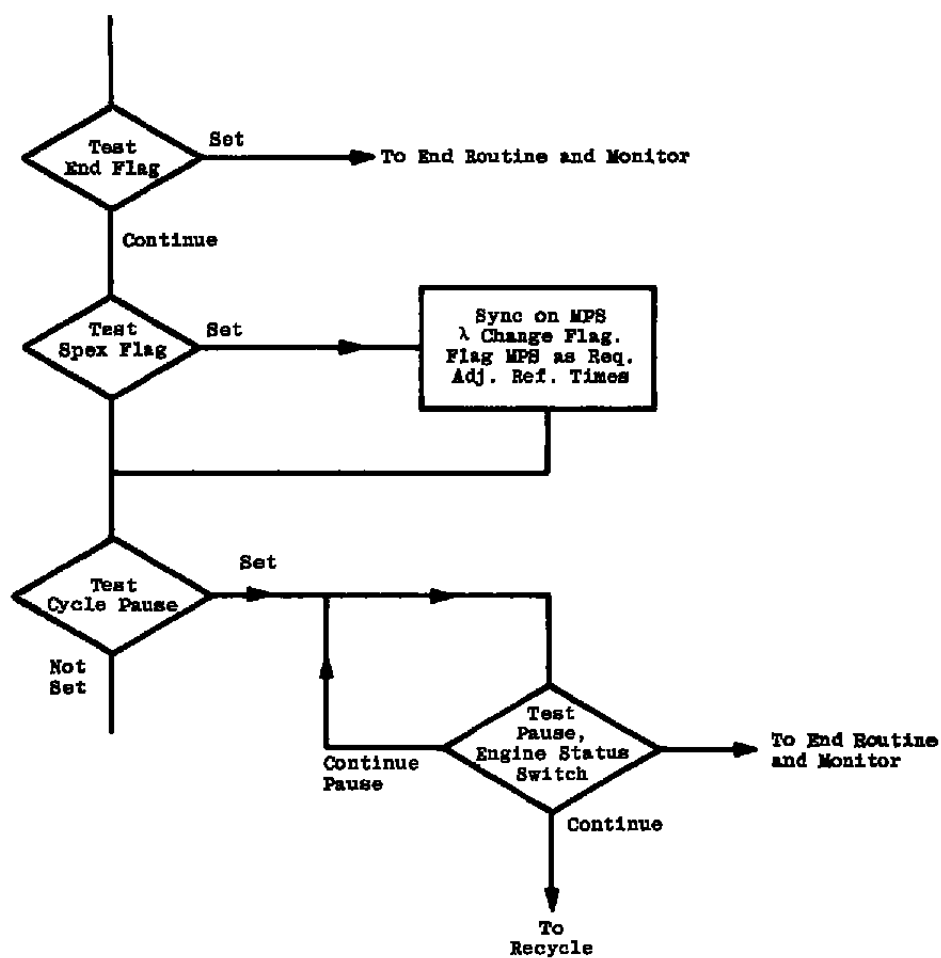
Figure A-3. Concluded.

Table A-1. Parameter List and Data Acquisition Sequence

Parameter		Sequence			
No.	Name	Pre-Fire	Burn	Post-Fire	Visi-corder
1	Catalysis Bed Temperature	1	8		x
2	Valve Inlet Pressure	2	1		x
3	M/S Probe Pressure	3	5		x
4	Combustion Chamber Temperature	4	2		
5	Fuel Valve Inlet Temperature	5	9		
6	Alphatron Pressure	6	4		x
7	Electron Beam Current	7	3		
8	Quartz Crystal (QCM) Temperature	8			
9	Ion Gage (G.E.) Vacuum Pressure	9	12		
10	Photoelectric Multiplier Counts	10		2	
11	Counter Gate Time	11		3	
12	Quartz Crystal Counts	12			
13	Rayleigh Integrator Output	13		1	
14	Laser Energy Integrator Output	14		6	
15	Horizontal Cart Position	15			
16	Vertical Cart Position	16			
17	Viscojet Inlet Pressure	17	6		
18	Viscojet Delta Pressure	18	7		x
19	Nozzle Throat Temperature		10		x
20	Fuel Valve Temperature		11		
21	Thruster Firing Counts			4	
22	Reference Time Counts			5	

APPENDIX B
PHOTON-COUNTING DEAD-TIME CORRECTION PROCEDURE

Inherent in most pulse-counting experiments are nonlinearities between the observed rate and the true rate. When the dominant cause for pulse pileup error is external electronics (discriminator, etc) as was the case for these experiments, the photon counting system may be referred to as non-paralyzable (Ref. 42). That is, every recorded pulse causes the counting system to be inoperative for a fixed dead time, τ_D; however, subsequent pulses which enter the system during τ_D neither extend the dead time nor are they counted. The relationship between the true counting rate (R^*) and the observed rate (R) may be written as

$$R^* = R/(1 - R\tau_D) \tag{B-1}$$

or

$$R = R^*/(1 + R^*\tau_D) \tag{B-2}$$

Calibration of the variation of Raman scattered intensities as a function of laser energy was accomplished before each test period. In terms of the true count rate,

$$R^* = C_o E_o \tag{B-3}$$

where C_o is proportionality constant and E_o is the laser energy in joules per pulse. In terms of actually measured values obtained during the energy variation calibration,

$$R = [I_T/\tau_g - I_D/\tau_{dg}] \tag{B-4}$$

where I_T is the total counts observed during the gate time interval, τ_g (nominally 1.0 msec), and I_D is the dark counts observed during the dark counting interval, τ_{dg} (nominally 3 sec). Substituting Eq. (B-3) into Eq. (B-2) gives

$$E_o/R = 1/C_o + E_o\tau_D \tag{B-5}$$

Therefore, a plot of E_o/R as a function of E_o gives a straight line, the slope of which yields τ_D. For Raman scattering the nominal dead time was 75 nsec.

The dead time, τ_D, of the detector and electronics when used for electron beam diagnostics was determined from two sets of measurements using neutral density filters. With a standard tungsten strip lamp used as the light source, the transmissions of seven

neutral density filters and a number of combinations of those filters were carefully measured at conditions in which no dead-time corrections were needed. Then the optical and electronics systems were adjusted for the conditions to be used for the electron beam diagnostics, except for a reduced photomultiplier tube high voltage, until a large, but unsaturated, count rate, R_m^o, was obtained with no filter. Thus the count rates R_m as functions of the filter transmission, T_x, were measured. The equation defining dead time, τ_D, is

$$R_m = a\,T_x/(1 + \tau_D\,a\,T_x) \tag{B-6}$$

where a is a proportionality constant. This equation may be written as that of a straight line:

$$1/a + \tau_D\,T_x = T_x/R_m$$

or

$$T_x R_m^o/R_m = \tau_D\,T_x\,R_m^o + R_m^o/a \tag{B-7}$$

From a plot of $T_x R_m^o/R_m$ versus T_x, the dead time equals the slope of the least-squares fit of the values divided by R_m^o. The results were $\tau_D = 28.0 \times 10^{-9}$ sec and 24.8×10^{-9} sec, and, the latter value being favored because of a better coefficient of determination of the least-squares fit, the value of 25.0×10^{-9} sec was used.

It should be noted for electron beam data acquisition and dead-time determination that the photon rate incident at the PMT is essentially constant during the data gate time. However, for the laser-Raman measurements the photon rate varies significantly during the 1-msec data gate as a characteristic result of the conventional mode laser pulse in which the major portion of the energy is concentrated in the first half of the pulse. This can easily account for the difference in dead times employed for the two diagnostic techniques.

APPENDIX C
MEASUREMENT UNCERTAINTIES OF SPECIAL DIAGNOSTIC SYSTEMS

C.1 MASS SPECTROMETER DATA

As stated in Section 5.3 and reiterated here, no good evaluation of the uncertainty in the mass spectrometer measurements can be offered because of the lack of detailed calibration data and large variations due to engine fluctuations. An analysis of the variations in measured species proportions does indicate a precision of ±20 percent for species other than H_2. The accuracy of the values for H_2 is undefinable at present, but a credibility level of ±50 percent is probably reasonable.

C.2 QCM DATA

Evaluation of the QCM data uncertainty will follow closely a similar analysis in Ref. 43. Random error of the average mass deposition rates can be estimated from the data which indicate a maximum of ±10-percent deviations from the average over the last five pulses. Therefore, from Beers (Ref. 44) the standard deviation of the average mass deposition rates can be estimated as

$$\sigma_R(<\dot{m}>_5) = \frac{\pm 10\%}{\sqrt{5}} \approx \pm 4.5\% \tag{C-1}$$

Systematic error in the measured values of $\dot{m}$ can be estimated by differentiating the functional relationships between $\dot{m}$ and its parameters.

$$\dot{m} = \dot{m}\left(C_{m_1} \cdot \Delta f, r_d, T_{QCM}, P_c\right) \tag{C-2}$$

$$\frac{1}{\dot{m}} \frac{\partial \dot{m}}{\partial C_{m_1}} \Delta C_{m_1} = 0.5 \tag{C-3}$$

The error in frequency measurement,

$$\Delta f = \Delta\left[\frac{C_2}{r_{Q_2}} - \frac{C_1}{r_{Q_1}}\right] \tag{C-4}$$

is estimated to be 1 Hz or less. A noise equivalent mass flux can be estimated to be

$$NE\dot{m} = \frac{1.524 \times 10^{-8} \ (f = 1)}{138 \ msec} = 1.1 \times 10^{-7} \ gm/cm^2 \cdot sec \tag{C-5}$$

Since all $\dot{m}$ values were one or two orders of magnitude larger than $NE\dot{m}$, the error due to frequency measurement error is estimated to be no larger than

$$\frac{1}{\dot{m}} (NE\dot{m}) = 0.1 \tag{C-6}$$

The error in thruster pulse duration, $\Delta\tau_d$, is not assumed to be negligible, since a fixed value of $\tau_d = 138$ msec was used to reduce all data regardless of thruster test condition and pulse number. Since little change in τ_d is expected over the last 5 to 10 pulses over which average values are obtained, this error is considered negligible for the average $\dot{m}$ values. However, an examination of Figs. 96 through 106 in Section 7.4 indicates a ±12-msec variation in τ_d as test conditions are varied over the full range. Therefore, the error due to $\Delta\tau_d$ is estimated as

$$\frac{1}{\dot{m}} \frac{\partial\dot{m}}{\partial\tau_d} \Delta\tau_d = \frac{12 \text{ msec}}{138 \text{ msec}} = 0.087 \qquad \text{(C-7)}$$

It should be noted, however, that the pulse-to-pulse values of $\dot{m}$, especially the first 5 to 10 pulse values, can be expected to systematically give $\dot{m}$ values too low since the actual τ_d values for the first few pulses are roughly 10 msec less than the final pulse values. This amounts to approximately -7-percent error.

The error attributable to variations in T_{QCM} values is most difficult to evaluate. Condensed mass does indeed depend strongly on crystal temperature near those temperatures where major plume species have sufficiently high vapor pressure to evaporate. For these experiments these temperatures are 130 and 172 K (see Fig. 67). During data acquisition at these T_{QCM} values the QCM was frequently monitored for ₋pproximately 200 sec after a thruster firing sequence, and no significant evaporation rate was observed. Error attributable to T_{QCM} variations will therefore be ignored.

Error attributable to combustion chamber pressure variations can be easily evaluated since average mass depostion rate has been observed to be a nearly linear function of inlet pressure. Inlet pressure was always set to within ±2 psia; therefore, for the 2S condition,

$$\frac{1}{\dot{m}} \frac{\partial\dot{m}}{\partial P_c} \Delta P_c = \frac{2}{85} = 0.024 \qquad \text{(C-8)}$$

The total systematic error in the average values of $\dot{m}$ is obtained as follows:

$$\sigma_s(<\dot{m}>_5) = [(0.5)^2 + (0.1)^2 + (0.087)^2 + (0.024)^2]^{1/2} \qquad \text{(C-9)}$$

$$\sigma_s(<\dot{m}>_5) = \pm52\% \qquad \text{(C-10)}$$

Therefore, the total uncertainty estimate for average values of $\dot{m}$ is

$$\sigma(<\dot{m}>_5) = \pm57 \text{ percent} \qquad \text{(C-11)}$$

When $\dot{m}$ values in $gm/cm^2 \cdot sec$ are converted to $\dot{M}$ values in $gm/sec \cdot sr$, additional systematic errors must be considered since

$$\dot{M} = \dot{M}\left(C_{m_1}, \Delta f, r_d, T_{QCM}, P_c, r^2, \cos \phi\right) \tag{C-12}$$

$$\frac{1}{\dot{M}} \frac{\partial \dot{M}}{\partial r} \Delta r = \frac{(2)(0.3 \text{ cm})}{39.9 \text{ cm}} = 0.015 \tag{C-13}$$

The error due to $\Delta(\cos \phi)$ can be neglected. However, it should be noted that it has been assumed that accommodation coefficients are unity and remain unity as angle of incidence is changed. Whether or not this assumption is justified cannot presently be evaluated. The total uncertainty for average $\dot{M}$ values is therefore essentially the same as for average $\dot{m}$ values.

C.3 RAYLEIGH SCATTERING DATA

Random error can be estimated from typical thruster data sequences which indicate ±80-percent variations in I'_{Ry} average values over the last 25 pulses in a 30-pulse sequence. From Beers (Ref. 44) the standard deviation of the average I'_{Ry} can be estimated as

$$\sigma_R \left(\langle I'_{Ry} \rangle\right) = \frac{\pm80\%}{\sqrt{25}} = \pm16 \text{ percent} \tag{C-14}$$

Because the Rayleigh scattering data is presented as $\widehat{I}_{Ry_1}$, the systematic error must be evaluated using Eq. (4). Therefore,

$$\widehat{I}_{Ry_1} = \widehat{I}_{Ry_1}\left(I'_{Ry}, C_{F_{Ry}}^{N_2}, n_o\right) \tag{C-15}$$

The systematic error of $\widehat{I}_{Ry_1}$ can be readily estimated at ±3 percent for the pulse integration system used. The variation of n_o is estimated at ±2 percent as judged from the spread of tabulated n_o values in Tables 7, 9, 10, and 11.

Evaluation of error associated with the calibration factor $C_{F_{Ry}}^{N_2}$ involves determination of the total uncertainty of $C_{F_{Ry}}^{N_2}$. As shown in Eq. (3),

$$C_{F_{Ry}}^{N_2} = C_{F_{Ry}}^{N_2}\left(n_{N_2}^o, I_{Ry}^o\right) \tag{C-16}$$

The nitrogen number density values used during calibrations $(n_{N_2}^o)$ were known within ±2 percent, and the I_{Ry}^o values were determined within ±5 percent. Therefore, the total uncertainty in $C_{F_{Ry}}^{N_2}$ is

$$\sigma\left(C_{F_{Ry}}^{N_2}\right) = \sqrt{(0.02)^2 + (0.05)^2} = 0.054 \tag{C-17}$$

The systematic error in $\widehat{I}_{Ry_1}$ is then

$$\sigma_s\left(\widehat{I}_{Ry_1}\right) = \sqrt{(0.03)^2 + (0.05)^2 + (0.054)^2} = 0.065 \tag{C-18}$$

The total uncertainty in $\widehat{I}_{Ry_1}$ values is then evaluated as ±22.5 percent.

C.4 RAMAN SCATTERING DATA

The random error for nitrogen number density values, $n(N_2)$, can be determined using the data and the photon counting error formulas of Beers (Ref. 44) as used in Ref. 17. In this manner. a random error of ±14 percent is assigned to $n(N_2)$ values. Determination of systematic error requires evaluation of the error involved in determination of $C_F^{N_2}$. The calibration number density is known within ±2 percent, and the calibration intensity values are known within ±3.6 percent. However, the effect of uncertainty in τ_D must be evaluated, because the calibration intensities are at a high level that requires significant correction for dead time losses. The uncertainty in τ_D is estimated at ±10 percent, and this gives an additional uncertainty in calibration intensities of ±3 percent. Therefore, the total uncertainty in $n(N_2)$ values is

$$\sigma[n(N_2)] = \left[0.14 + \sqrt{(0.02)^2 + (0.036)^2 + (0.03)^2}\,\right] 100 \tag{C-19}$$

$$\therefore \sigma[n(N_2)] \approx \pm19 \text{ percent} \tag{C-20}$$

The total uncertainty for hydrogen number density is evaluated in the same manner as

$$\sigma[n(H_2)] = \left[0.05 + \sqrt{2[(0.02)^2 + (0.036)^2 + (0.03)^2]}\,\right] 100 \tag{C-21}$$

$$\therefore \sigma[n(H_2)] \approx \pm12 \text{ percent} \tag{C-22}$$

The reason for the $\sqrt{2}$ increase in systematic error is that two calibration factors are involved in reduction of $n(H_2)$ data [see Eqs. (16) and (17)].

The total uncertainty for ammonia number density is evaluated similarly as

$$\sigma[n(NH_3)] = \left[0.44 + \sqrt{(0.02)^2 + (0.054)^2 + (0.01)^2}\,\right] 100 \tag{C-23}$$

$$\sigma[n(NH_3)] \approx \pm50 \text{ percent} \tag{C-24}$$

236

Measurement of rotational temperature, T_R, requires determination of an intensity ratio. The random error associated with this ratio measurement is ±9.4 percent, and the assumption is made that the variation of intensity ratio is linear over the range of temperatures of interest. Inspection of Fig. 11 reveals this to be a reasonable assumption. Evaluation of the systematic error requires determination of the error involved in measuring C_{F_T} [see Eq. (19)]. It will be assumed that negligible error is involved in calculating $R^c(T_R)$. The error associated with R_m^o is evaluated thus:

$$\sigma(R_m^o) = \sqrt{2[(0.02)^2 + (0.03)^2 + (0.03)^2]} = 0.066 \qquad (C-25)$$

where the $\sqrt{2}$ enters because of a ratio of two values of practically identical uncertainty. The total uncertainty of the T_R values is then

$$\sigma(T_R) = \pm 16 \text{ percent} \qquad (C-26)$$

C.5 ELECTRON BEAM DATA

The major random error was ±1 to ±6 percent for each set of about 25 pulses that defined one measurement. These random variations were caused primarily by engine pressure and temperature fluctuations. As for the Raman scattering measurements, the variation in exact wavenumber of the spectrometer as it was periodically changed caused negligible error in density measurements because of the large slit widths employed.

Pressure and temperature measurements defining the sonic orifice calibration flow result in a density error of ±2 percent. The MOCS predictions of the sonic orifice flow field are assumed accurate within ±1 percent, and the electron beam current measurement is accurate within ±2 percent. Assumption of a ±10-percent error in the dead time results in a negligible density error, and this was assured by the use of neutral density filters at high count rates. The effect of a ±10-percent error in the nitrogen mole fraction employed for the quenching corrections results in a ±1-percent error in density. Therefore, the resultant systematic error in number density measurements is ±3 percent, and the overall uncertainty range of the number density measurements is ±4 to ±9 percent.

In the determination of a nitrogen rotational temperature, the ratio of two sets of pulse counts was used, and the combined random error was ±6 to ±25 percent. The large value of this error typically occurred in plume areas of low number density. Assumption of a random error in spectrometer wavenumber of ±0.5 cm^{-1} results in a temperature error of ±5 percent. This error is enhanced in relation to that of the number density measurement because of the rapidly changing photon rate as a function of wavenumber in the R-branch tail of the $N_2^+(0,1)$ band. The combined random error is ±8 to ±25

percent. Most of the systematic errors encountered in the number density measurements are not applicable to the rotational temperature measurements because of the need to ratio sets of pulse counts. A systematic error of ± 0.5 cm^{-1} in wavenumber would, however, cause a ± 5-percent error in rotational temperature. The total uncertainty range in the temperature measurements is ± 13 to ± 30 percent.

NOMENCLATURE

| A | A rotational constant for NH_3, cm^{-1} |

| $A(T_R)$ | A temperature-dependent correction factor defined by Eq. (25) |

| a | Scatterer radius, cm or Å |

| B | A rotational constant for NH_3, cm^{-1} |

| B_{FR} | Ratio of ammonia to nitrogen number density calibration factors |

| b | A proportionality constant defined by Eq. (23) |

| C_{FN_2} | Calibration constant for determining $n(N_2)$ from Raman scattered intensities, v/count · cm^3 |

| C_{FNH_3} | Calibration constant for determining $n(NH_3)$ from Raman scattered intensities, v/count · cm^3 |

| C_{FH_2} | Calibration constant for determining $n(H_2)$ from Raman scattered intensities, v/count · cm^3 |

| $C_F(T_R)$ | Temperature-dependent correcting factor defined by Eq. (15) |

| C_{FR} | Ratio of hydrogen to nitrogen number density calibration factors |

| C_{FT} | A correction factor for the hydrogen line intensity ratio as defined by Eq. (19) |

| $C_{FRy}, C_{FRy}^{N_2}$ | Proportionality constant defined by Eq. (1), calibration factor for Rayleigh scattering defined by Eq. (3), count · cm/v or v/count · cm^3, respectively |

| C_J | A quantum number-dependent parameter used in Eq. (11) |

| C_m, C_T | Mass coefficient and temperature coefficient of a quartz crystal, H_z/gm or H_z/K, respectively |

| C_1, C_2 | Contents of QCM frequency counter before and after each thruster pulse, counts |

$C[(v',v_2'')]$	A function describing the spectral intensity variation of the v'-to-v_2'' transition
c	Speed of light in vacuum, cm/sec
D_L	Diameter of laser beam at input to laser focusing lens, cm
d	Diameter of laser beam focal volume, cm
E_o	Energy of laser beam, J
$E(K',T_R)$	A function of K' and T_R, and related to the Muntz G factor (see Ref. 16)
e_p^-, e_s^-	Primary electron and secondary electron, respectively
$F(T_R), F(T_R^o)$	A temperature-dependent correction factor and the value of the factor at calibration conditions, respectively
F_L	Focal length of laser focusing lens, cm
F_T	Engine thrust value, lbf
$f(T_R,L)C_L$	The relative intensity of the even L-th numbered rotational lines of ammonia defined by Eq. (22)
$f(\theta)$	Hill-Draper function
GHe	Gaseous helium (20 K)
g_M	A statistical weighting factor used in Eq. (22)
h	Planck's constant, erg/sec
I_K'	Intensity of K' rotational line
$I_m(N_2,Q), I_m^o(N_2,Q)$	Raman-scattered intensity of the N_2 Q-branch; value of $I_m(N_2,Q)$ at calibration conditions, respectively, counts/v
$I_m(J,H_2), I_m^o(J=1,H_2)$	Raman-scattered intensity of the j-th rotational line of H_2 and the value of $I_m(J,H_2)$ at calibration conditions for J=1, respectively, counts/v

$I_{Ry}, I_{Ry}^o, I_{Ry}^l, I_{Ry1}$	Rayleigh-scattered intensity normalized to incident laser beam intensity; calibration value of I_{Ry}; raw data value of I_{Ry}; raw data value of I_{Ry} normalized to thruster combustion chamber number density, respectively, counts/v
$I_m(L, NH_3)$	Raman-scattered intensity of the L-th numbered rotational line of NH_3, counts/v
$I_m^l(L = 10, NH_3)$, $I_m^o(L = 10, NH_3)$	Raman-scattered intensity of the L = 10 ammonia line measured in the plume and at calibration conditions, respectively, counts/v
$I_m^l(J = 1, H_2)$, $I_m^l(J = 0, H_2)$	Raman-scattered intensities measured in the thruster plume for the J = 1 and J = 0 lines of H_2, respectively, counts/v
i_B	Electron beam current, electrons/sec, or ma
J	Rotational level quantum number
K'	Upper rotational quantum number, R branch
k	Boltzmann's constant or collisional quenching constant used in Eq. (31), erg/K or cm^3/sec
L	Number of an ammonia rotational line
LHe	Liquid helium
LN_2	Liquid nitrogen
ℓ	Length of laser beam focal volume, cm
M	A quantum number associated with NH_3 rotational levels; also Mach number
$\dot{M}, \dot{M}_i$	Mass deposition rate and mass deposition rate of specie i in gm/sec · sr
$\dot{M}_T$	Mass flux from thruster, gm/sec · sr
MOCS	Method of Characteristics Solution
m	Relative index of refraction of a light scatterer
$\dot{m}, \dot{m}_i$	Mass deposition rate and mass deposition rate of species i in gm/cm^2 · sec

$<\dot{m}>_n$	Average mass deposition for last n pulses of a pulse sequence, $gm/cm^2 \cdot sec$
$N_2(X^1)$	Electronic ground state of N_2
$N_2^+(B^2)$	First excited electronic state of N_2^+
$N_2^+(X^2)$	Ground electronic state of N_2^+
n, n_0	Number density and combustion chamber number density, respectively, cm^{-3}
$n(N_2), n^\circ(N_2)$	Nitrogen number density and nitrogen number density during calibration, respectively, cm^{-3}
n_i, n_T	Number density of species i and total number density of all species, respectively, cm^{-3}
$n(H_2), n^\circ(H_2)$	Hydrogen number density and hydrogen number density during calibration, respectively, cm^{-3}
$n(NH_3), n^\circ(NH_3)$	Ammonia number density and ammonia number density during calibration, respectively, cm^{-3}
$n^{(1)}(N_2), n^{(2)}(N_2)$	First and second order determination of $n(N_2)$ using the electron beam fluorescence technique, cm^{-3}
$P_{IN}; P_c, P_o$	Thruster inlet pressure; combustion chamber pressures, psia
P_K'	$K'/2[3-(-1)^{K'}]$
QCM	Quartz crystal microbalance
q_r, q_{ro}, q_{rp}	Rotational partition function; and ortho and para modification values of q_r, respectively
R^c, R_m^o, R_m	Calculated ratio of the $J = 0$ to $J = 1$ hydrogen line intensities; measured value of the ratio at calibration conditions; measured value of the ratio in the thruster plume, respectively
R_1, R_2	Ratio of ammonia to nitrogen mole fraction and ammonia to hydrogen mole fractions, respectively

RVC	Research Vacuum Chamber
r	Distance from QCM surface to the center of the thruster exit plane, cm
$\hat{r}$	Radial distance from axial centerline normalized by the diameter of the throat
SEM	Scanning electron microscope
$S_{F_{N_2}}$	Calibration factor for determining $n(N_2)$ from electron beam fluorescence intensities, $cm^3 \cdot$ counts/sec $\cdot$ ma
$S_m(0,1), S_m^\circ(0,1)$	Measured photon rate from the $v'=0$ to $v_2''=1$ transition and the value of the rate at calibration conditions, respectively, counts/sec
$S(v', v_2'')$	Detected photon emission rate from electron beam excitation of N_2, counts/sec
T_o	Combustion chamber temperature, K
T_R, T_R°	Rotational temperature and the value of rotational temperature at calibration conditions, respectively, K
$T_{c\ell w}, T_{CATB}$	Temperature of the catalyst bed lower wall and the initial catalyst bed temperature, respectively, $^\circ$F
T_{QCM}	Temperature of the QCM surface, K
T_t	Temperature of the thruster throat, $^\circ$F
TC	Test condition
$T[(v', v_2'')]$	Spectrometer transmission function, counts/photon
T_v	Vibrational temperature
(v', v_2'')	Vibrational band designation for $N_2^+(B^2)$ level to $N_2^+(X^2)$ transition
(v_1'', v')	Vibrational band designation for $N_2(X^1)$ level to $N_2^+(B^2)$ transition
$[X_i]$	Mole fraction of the ith species

x   Ammonia dissociation fraction; or horizontal distance between QCM and thruster axial centerline, in.

x   Axial distance from thruster nozzle throat normalized by the diameter of the throat

z   Axial distance from QCM to thruster exit plane (see Fig. 65), in.

a_i Polarizability of a light scatterer, cm^3

$\beta(v',v_2'')$ Branching factor of the v'-to-v_2'' transition

γ Specific heat ratio

Δf Change in quartz crystal resonant frequency, Hz

ΔM Mass change, gm

ΔT Temperature change, K

ϵ_{Ry} Correction factor to I_{Ry_1} values defined by Eq. (5)

θ Off-axis angular position of the QCM relative to the thruster axial centerline, deg

λ_o,λ Wavelength of incident laser beam and light wavelength, cm or Å, respectively

ρ_L Depolarization ratio

ν_o,ν Frequency of laser beam, sec^{-1}

σ_{Ry_i} Rayleigh scattering of ith species, cm^2

$\sigma(v_1'',v')$ Excitation cross section for transition from v_1'' to v' vibrational level, cm^2/sr

τ Lifetime of $N_2^+(B^2)$ level, sec

τ_d Characteristic thruster deposit time, sec

τ_D Deadtime value of photon counting system

τ_{Q_1},τ_{Q_2} QCM data gates before and after thruster pulse, respectively, sec

ϕ Mass flux angle of incidence on the QCM surface, deg

ω Detection solid angle of an optical system, sr